

# A Novel Structural Health Monitoring Method for Full-Scale CFRP Structures

THÈSE N° 6422 (2015)

PRÉSENTÉE LE 27 MARS 2015

À LA FACULTÉ DES SCIENCES ET TECHNIQUES DE L'INGÉNIEUR  
LABORATOIRE DE MÉCANIQUE APPLIQUÉE ET D'ANALYSE DE FIABILITÉ  
PROGRAMME DOCTORAL EN MÉCANIQUE

ÉCOLE POLYTECHNIQUE FÉDÉRALE DE LAUSANNE

POUR L'OBTENTION DU GRADE DE DOCTEUR ÈS SCIENCES

PAR

Enrique René GUZMAN SOLARES

acceptée sur proposition du jury:

Prof. F. Gallaire, président du jury  
Prof. T. Gmür, directeur de thèse  
Prof. J. F. Dias Rodrigues, rapporteur  
Dr Y. Leterrier, rapporteur  
Prof. A. Schorderet, rapporteur



ÉCOLE POLYTECHNIQUE  
FÉDÉRALE DE LAUSANNE

Suisse  
2015



...making your ear attentive to wisdom and inclining your heart to understanding...  
— Proverbs 2 :2

...and you will know the truth, and the truth will make you free...  
— John 8 :32

I have never met a man so ignorant that I couldn't learn something from him.  
— Galileo Galilei

Try not to become a man of success, but rather try to become a man of value.  
— Albert Einstein

I am, and ever will be, a white socks, pocket protector, nerdy engineer.  
— Neil Armstrong



# Acknowledgements

I would like to thank all the people who helped me to achieve my objectives during these last 4 years of work, giving me assistance, motivation and support. I would like to thank Prof. John Botsis, who welcomed me at the LMAF, where I spent most of my time these last for years.

Of course, I want to thank my thesis supervisor Prof. Thomas Gmür, for his regular work of supervision, for his guidance and for the confidence he has placed in me, which have been essential to start this doctoral thesis four years ago, and finally to “make it to the top” only a few days ago. At the same time, I am really grateful with Dr. Joël Cugnoni for sharing his vast knowledge in all scientific fields, and for being constantly available, by all times and seasons, always ready with innovative suggestions and ideas.

I want to thank all the people with whom I had the pleasure to share my office, my colleagues Dr. Jeannot Frieden and Mr. Ali Motamed, and also temporarily Prof. Michel Del Pedro and Prof. Alain Curnier. All our spontaneous talks often lead me to figure out the solution to many questions I often got stuck with.

Many thanks go to the team at the ATME, especially to Mr. Marc Jeanneret, for his availability, for his help and for his patience to solve many of my practical problems, and for teaching me the kind of things that can only be learned by practice and thinking differently. Many thanks go also to Mr. Marc Salle, Mr. Stéphane Haldner and Mr. Laurent Chevalley for their meticulous and accurate work.

Special thanks to people at the HEIG-VD : to Prof. Jean-Pascal Reymondin and to Prof. Philippe Bonhôte who introduced in me to the use of PVDF film transducers. Also I want to thank the people at LTC for occasionally lending me the necessary equipment and for providing me with technical assistance to manufacture some of my first testing samples.

For my colleagues from LMAF, especially to Mr. Robin Amacher, Dr. Milad Maleki, Dr. Marco Lai and Mr. Georgios Pappas who in one moment or another have taken the time to patiently answer some of my questions or assist me to solve practical problems. I would like to thank Mrs. Viviane Magnenat for her patience, for her invaluable assistance and for helping me throughout all the administrative paperwork.

I thank the people from Weiss Technik AG, especially Mr. Alain Groell which assisted me with the difficult task to conveniently install and exploit the climatic chamber that helped me throughout most of my research.

## Acknowledgements

---

I would like to express my gratitude to the members of the jury : Prof. José Dias Rodrigues, Prof. Alain Schorderet, Dr. Yves Leterrier and Prof. Francois Gallaire, who agreed to review my work and to share their very constructive observations and suggestions, which have been invaluable and highly appreciated.

I want to acknowledge the financial support of the Swiss National Science Foundation (grants No. 200020-143968 and 200020-143968/1) that enabled this research work.

I would like to thank my students, especially Mr. Andreas Winter and Mr. Claudio Cavalli, for their collaboration mounting many test benches and for their fresh and original ideas. Your hard work has been a valuable contribution to this thesis.

I am really grateful to all the members of my family, but especially to my mother who with her dedication and sacrifice raised me all by herself, and taught me the value of honesty, hard work and humility.

I want to thank all my friends, especially the *Apéro du Lundi* team, with whom I could share moments of joy (and frustration as well), I wish them to soon achieve their academic objectives as well. I also want to thank the *Boys Band Tour* team for sharing all their professional experience and all the good moments we shared as undergrad classmates and later as friends.

My particular gratitude goes to my lovely fiancée Erika who has been there for me. From the bottom of my heart, I thank her for her understanding and for her support, in the best and in the worst of times. Many thanks also to her family, which from the first moment almost instantaneously adopted me.

Finally, I thank God for all these people, for all the courage and for all the blessings He has given to me in this hard and difficult road.

*Lausanne, October 25, 2014*

# Abstract

Polymer-based composite materials, such as the fibre reinforced plastics are used to manufacture ultra-light panels, massively introduced in the last decades in the aeronautical industry, as a potential solution to reduce the energy consumption and combustion emissions. Example applications are the civil airliners Boeing 787 and the (currently in development) Airbus 350 XWB models.

Safety being the main concern in aeronautical applications, structural monitoring is a cornerstone of the design process, and also during the life cycle of an aircraft. Aiming to this, non-destructive testing and surveillance techniques have been developed over the years. However, the standard methods currently used are not usually adapted to the use of these new materials, and potential improvements in the continuous monitoring techniques are constantly being investigated. New Structural Health Monitoring (SHM) systems have thus emerged during the last years as an interesting option. A SHM system is in general based on a precise damage detection strategy, which is a complex system itself, composed by simpler strategies to solve simpler problems : data acquisition, structure characterization, sensor placement, statistical damage/ageing models, etc. A SHM process implies also the ability to provide in real-time (or nearly real-time) information about structural integrity.

The specific problem of composite ageing evaluation is one of the most often dealt with and at the same time one of the worst understood. Indeed, in spite of their exceptionally high mechanical performances, polymer-based composite materials are more vulnerable than metallic alloys when confronted to aggressive environmental ageing factors. It is widely accepted that special caution needs be observed when using these materials.

The main motivation of this thesis is then to set the basic foundations of a novel, complete, reliable, robust, fast and low-cost SHM system and which could be applied to a general full-scale composite structure.

In order to address the ageing characterization problem, a standard method for artificial weathering has been developed. The artificial ageing protocols were inspired from results published in the literature and ASTM material testing standards. This thesis has focused on the influence of three factors on the ageing of CFRP specimens : exposure temperature (5[°C] – 135[°C]), surrounding humidity (0% - 95%RH) and UV radiation ( 3 [W/m<sup>2</sup>]). Most importantly, this thesis has dealt with the synergetic influence of these factors.

## Acknowledgements

---

The goal of artificial ageing is to subject the specimens to controlled ageing protocols, in order to observe changes in some macroscopic properties, namely the elastic moduli. A parametric mathematical model has been built in order to express the evolution of elastic moduli as a mean to monitor the ageing state and the structural health. The mathematical model has been established by means of the design of experiments (DoE) statistical techniques. This formulation includes the actions of the different ageing factors separately and combined. Outside of SHM, the model (and the method to obtain it) can be collaterally be used for ageing characterization and prediction in further applications. Depending on the protocol, the extent of the ageing can reach a degradation of 15% of the elastic moduli. Most of the degradation is reached under the influence of temperature and humidity changes.

Concerning the data acquisition, the polyvinylidene difluoride (PVDF) technology is a relatively new technology for strain measuring and offers an alternative. To prove the survivability to the ageing conditions was essential to justify their integration in a composite structure. The validation has been carried out by comparing the ability of PVDF sensors to provide quality signals, which can prove to be as accurate as those from non-aged sensors. The statistical approach is used for this comparison, giving satisfying results in the frame of the designed ageing protocols (less than 2% in relative error with respect to non-aged sensors).

In order to measure the elastic properties while following a line of thought compatible with SHM, vibrational behaviour could provide information about the internal properties of a composite structure. Indeed, the physical fundamentals are given by the wave propagation theory, which relates structural stiffness with natural frequencies, with the mass distribution as an intermediary. However, the orthotropic nature of the fibre reinforced plastics (FRP) makes this problem more complex, and an identification algorithm intervenes to solve it. The method employed here was adapted from a numerical-experimental identification algorithm previously developed by several authors, which minimizes the difference between experimental and FE simulation results in order to identify the best estimation of the elastic properties. The natural frequencies and the corresponding vibration mode shapes (named vibration modal parameters) constitute the "features" mentioned in the SHM axioms as information vehicles about the internal health of the structure. A sensitivity analysis was included in the identification process in order to determine quantitatively how the elastic properties are related to the natural modal parameters.

Concerning the acquisition of structural data and extraction of the modal parameters, output-only modal analysis (OMA) was privileged, since it carries inherently the attributes of robustness and rapidity required by the SHM axioms. Moreover, the integration of low-cost sensors carries inherently the possibility to carry out real-time (or near real-time) monitoring, which is an important step improving the monitoring capabilities on full-scale structures, especially for operational and safety reasons. In recent years, the use of OMA has been justified by the difficulty (or even impossibility) to perform classic static or dynamic tests, such as experimental modal analysis (EMA),



to extract information about the state of the structures. The frequency domain decomposition (FDD) technique was chosen because of the simplicity of its formulation and the remarkable results reported in the literature. This method uses the notion of singular value decomposition (SVD) to extract the necessary information exclusively from the output sensors. It was successfully applied using several sensor/actuator combinations. The evaluation of the performance shows a relative difference of less than 1% with the reference method (EMA).

As part of the feature extraction solution, the optimal placement problem has been extensively addressed in the current state-of-the-art in SHM. Among the different approaches, the effective independence (EI) method was adapted to this specific case. The effectiveness of the implementation was proved and validated through the experimental tests carried out, showing a significant improvement in the measurement accuracy.

Finally, taking into account the results and observations in the development of the different tools, a global SHM method has been proposed, which gathers all the elements mentioned above : the use of a multifactorial model to predict the ageing, the design of a transducer network, the feature extraction by OMA and the identification of the constitutive properties. The method was successfully applied to a series of demonstrators, in the frame of a controlled laboratory environment. The next step would contemplate the adaptation of the method to a broader range of applications (in particular *in situ* applications) and the manufacturing of operating prototypes.

**Keywords** : Structural Health Monitoring, piezoelectric sensors, optimal sensor placement, accelerated ageing, inverse methods, Operational Modal Analysis.



# Résumé

Les matériaux composites à base de polymères, tels que les plastiques renforcés par des fibres, sont utilisés pour la fabrication de panneaux ultralégers, et ont été massivement introduits ces dernières décennies dans l'industrie aéronautique. Ceux-ci représentent une solution à la volonté de réduire la consommation d'énergie et l'émission de gaz de combustion. On peut citer comme exemple d'application des avions de ligne civils de nouvelle génération tels que le Boeing 787 et l'Airbus 350 XWB (actuellement en développement).

La sécurité aéronautique étant une préoccupation constante dans l'aviation civile, la surveillance structurelle devient un pilier autant pendant le processus de conception que durant le cycle de vie de l'aéronef. Dans ce but, des techniques d'essai non destructives ont été développées au fil des ans. Cependant, les méthodes standard couramment utilisées ne sont généralement pas adaptées à ces nouveaux matériaux, et des améliorations potentielles sont constamment un objet d'étude. De nouveaux systèmes de surveillance de l'état des structures (connus sous le nom de *Structural Health Monitoring* ou SHM en anglais) ont ainsi vu le jour au cours des dernières années comme une option intéressante. Un système SHM est en général basé sur une stratégie de détection d'endommagements, et composée elle-même par des sous-stratégies pour résoudre des problèmes plus simples : acquisition de données, caractérisation de la structure, positionnement des capteurs, modèles de vieillissement/endommagements, etc. Un processus SHM implique la capacité de fournir en temps réel (ou presque en temps réel) des informations sur l'intégrité structurelle.

L'évaluation du vieillissement des composites est un des problèmes le plus souvent traités dans la littérature, et en même temps l'un des moins bien compris. En effet, malgré leurs performances mécaniques exceptionnelles, les matériaux composites polymériques sont plus vulnérables que les alliages métalliques lorsqu'ils sont confrontés aux agents naturels. Il est largement admis que des précautions spéciales doivent être mises en place lors de l'utilisation de ces matériaux.

La motivation principale de cette thèse est donc de définir les fondements d'un système SHM de nouvelle génération, complet, fiable, robuste, rapide et à faible coût qui pourrait être appliqué à une structure en composite. Afin de résoudre le problème de la caractérisation du vieillissement, une méthode standard pour vieillissement artificiel a été mise au point. Les protocoles de vieillissement artificiel ont été inspirés des résultats publiés, ainsi que par les normes ASTM d'essai des matériaux. Cette thèse

## Acknowledgements

---

s'est penchée spécifiquement sur l'influence de trois facteurs de vieillissement : la température d'exposition (5 [°C] - 135 [°C]), l'humidité ambiante (0% - 95%) et le rayonnement ultraviolet ( 3 [W / m<sup>2</sup>]). Plus important encore, cette thèse a traité de l'influence synergique de ces facteurs.

Le but du vieillissement artificiel est de soumettre les échantillons à des protocoles contrôlés, afin d'observer des changements dans certaines des propriétés macroscopiques, à savoir les modules d'élasticité. Un modèle mathématique paramétrique a été constitué, dans le but d'exprimer l'évolution de ces modules élastiques comme un moyen de surveiller l'état de vieillissement et de la santé structurelle. Le modèle mathématique a été établi à l'aide des techniques statistiques prônées par le design d'expériences (*Design of experiments*, DoE en anglais). Cette formulation comprend les actions des différents facteurs de vieillissement, séparément et combinés. En dehors du contexte de la SHM, le modèle et la méthode pour l'obtenir peuvent accessoirement être utilisés pour la caractérisation et la prédiction du vieillissement dans d'autres applications. Selon le protocole, le vieillissement ainsi mesuré peut atteindre une dégradation de 15 % des modules élastiques. Les résultats montrent que la plupart de la dégradation est atteinte sous l'influence des variations de température et d'humidité.

En ce qui concerne l'acquisition de données, le polyfluorure de vinylidène (*polyvinylidene difluoride*, PVDF en anglais) est une technologie relativement nouvelle pour la mesure et offre une alternative intéressante dû à son coût faible et sa facilité d'intégration. Prouver la capacité de survie aux conditions de vieillissement était essentiel pour justifier leur intégration dans une structure composite. La validation a été effectuée en comparant la capacité des capteurs de PVDF à fournir des signaux de qualité, pouvant se révéler être aussi précis que ceux des capteurs non soumis au vieillissement. L'approche statistique est utilisée pour cette comparaison, donnant des résultats satisfaisants le cadre des protocoles de vieillissement conçus (moins de 2 % en erreur relative par rapport à des capteurs non vieillis).

Dans le but de mesurer les propriétés élastiques, tout en suivant une ligne de pensée compatible avec SHM, le comportement vibratoire peut fournir des informations sur propriétés internes d'une structure en composite. En effet, d'après les résultats donnés par la théorie de propagation des ondes, la rigidité structurelle est directement connectée aux fréquences naturelles, avec la répartition de la masse en tant qu'intermédiaire. Cependant, la nature orthotrope des plastiques renforcés (*fibre reinforced plastics*, FRP en anglais) rend ce problème plus complexe, et un algorithme d'identification intervient dans la solution. La méthode utilisée ici a été adaptée à partir d'un algorithme d'identification numérique-expérimentale développée précédemment par plusieurs auteurs, qui minimise la différence entre les résultats expérimentaux et les simulations éléments finis, afin d'identifier la meilleure estimation des propriétés élastiques. Les fréquences propres et les formes propres correspondant (connus sous le nom de paramètres modaux de vibration) constituent les "caractéristiques" mentionnées dans les axiomes SHM, qui véhiculent l'information sur la santé interne de

la structure. Une analyse de sensibilité a été incluse dans le processus d'identification en vue de déterminer quantitativement la façon dont les propriétés élastiques sont liées aux paramètres modaux.

Pour ce qui est de l'acquisition de données structurelles et l'extraction des paramètres modaux, la relativement récente analyse modale opérationnelle (*operational modal analysis*, OMA en anglais) a été privilégiée, car elle porte intrinsèquement les attributs de la robustesse et la rapidité requises pour une méthode SHM. En outre, l'intégration de capteurs à faible coût porte en soi la possibilité d'effectuer un suivi en temps réel (ou quasi-temps réel), ce qui est une étape importante pour améliorer les capacités de surveillance des structures réelles, en particulier pour des raisons opérationnelles et de sécurité. Au cours des dernières années, l'utilisation de l'OMA a été justifiée par la difficulté (voire l'impossibilité) d'effectuer des tests statiques ou dynamiques classiques (comme l'analyse modale expérimentale) pour extraire des informations sur l'état des structures. La technique de la décomposition dans le domaine fréquentiel (*Frequency Domain Decomposition*, FDD en anglais) a été choisie en raison de la simplicité de son élaboration et des résultats remarquables dans la littérature. Cette méthode utilise la notion de décomposition en valeurs singulières (*Singular Value Decomposition*, SVD en anglais) pour extraire les informations nécessaires exclusivement des capteurs de sortie. Elle a été appliquée avec succès à l'aide de plusieurs combinaisons des capteurs /actionneurs. L'évaluation de la performance montre un écart relatif inférieur à 1 % avec la méthode de référence, l'analyse modale expérimentale (*experimental modal analysis* EMA en anglais).

Dans le cadre de l'extraction de caractéristiques, le problème du placement optimal a été largement abordé dans l'état de l'art actuel dans SHM. Parmi les différentes approches, la méthode de l'indépendance effective (effective independence, EI en anglais) a été adaptée à ce cas précis. L'efficacité de la mise en œuvre a été prouvée et validée par des essais expérimentaux, montrant une amélioration significative de la précision de mesure. Enfin, en tenant compte des résultats et des observations dans l'élaboration des différents outils, une méthode globale SHM a été proposée, qui rassemble tous les éléments mentionnés ci-dessus : l'utilisation d'un modèle multifactoriel de prédiction du vieillissement, la conception d'un réseau de transducteurs, l'extraction de caractéristiques par OMA et l'identification des propriétés constitutives. La méthode a été appliquée avec succès à une série de démonstrateurs, dans un environnement de laboratoire contrôlé. La prochaine étape serait de contempler l'adaptation de la méthode à un plus large éventail d'applications (en particulier de applications *in situ*) et la fabrication de prototypes d'exploitation.

**Mots clés** : surveillance des structures, capteurs piezoélectriques, placement optimal, analyse modale opérationnelle, vieillissement accéléré.



# Resumen

Los materiales compuestos a base de polímeros, tales como plásticos reforzados de fibras, se utilizan para la fabricación de paneles ligeros y han sido masivamente introducidos en las últimas décadas en la industria de la aviación. Estos representan una solución al deseo de reducir el consumo de energía y las emisiones gas de combustión. Se puede por ejemplo citar los más recientes aviones de línea de nueva generación, como el Boeing 787 y el Airbus 350 XWB (actualmente en desarrollo).

La seguridad aérea siendo una preocupación constante en la aviación civil, la vigilancia de las estructuras se convierte en un pilar esencial, tanto durante el proceso de diseño como durante el ciclo de vida de la aeronave. Con este propósito, diferentes técnicas de ensayo no destructivo han sido desarrolladas en el curso de los años. Sin embargo, los métodos estándar comúnmente utilizados no son adecuados para estos nuevos materiales en general, y las mejoras potenciales son siempre un sujeto de estudio. Nuevos sistemas de auscultación de estado estructural (conocido como *Structural Health Monitoring* o SHM en inglés) han surgido en los últimos años como una opción atractiva. Un sistema SHM generalmente se basa en una estrategia de detección de daños, y está a su vez compuesto por sub-estrategias para resolver problemas sencillos: la adquisición de datos, la caracterización de la estructura, el posicionamiento de los sensores, el modelo de envejecimiento/daños, etc. Un proceso de SHM implica la capacidad de proporcionar en tiempo real (o casi en tiempo real) la información sobre la integridad estructural. La evaluación del envejecimiento de los materiales compuestos es uno de los problemas tratados más a menudo en la literatura, y sin embargo uno de los menos comprendidos. En efecto, a pesar de su rendimiento mecánico excepcional, los materiales compuestos a base de polímeros son más vulnerables que las aleaciones de metales cuando frente a los agentes naturales. Es ampliamente reconocido que precauciones especiales se necesitan cuando estos materiales se utilizan.

La motivación principal de esta tesis es básicamente definir las bases de un sistema SHM de nueva generación, completo, fiable, robusto, rápido y de bajo costo, que se pueda aplicar a una estructura compuesta. Para resolver el problema de la caracterización de envejecimiento, un método estándar para el envejecimiento artificial fue desarrollado. Algunos protocolos de envejecimiento artificial se inspiraron de la literatura publicada, así como de los estándares ASTM. Esta tesis se ha centrado específicamente en la influencia de tres factores de envejecimiento: la temperatura exposi-

## Acknowledgements

---

ción (5 [° C] - 135 [° C]), humedad (0 % - 95 % C) y la radiación ultravioleta (3 [W / m<sup>2</sup>]). Más importante aún, esta tesis aborda el efecto sinérgico de estos factores. El objetivo del envejecimiento artificial es someter las muestras a protocolos controlados de envejecimiento artificial, con el fin de observar los cambios en algunas propiedades macroscópicas, a saber los módulos elásticos. Un modelo matemático paramétrico ha sido constituido, con el fin de expresar la evolución de los módulos elásticos como medio de vigilar el estado de envejecimiento y salud estructural. El modelo matemático se estableció mediante técnicas estadísticas promovidas por el diseño de experimentos (*Design of Experiments*, DoE en inglés). Esta formulación incluye acciones de diferentes factores de envejecimiento, por separado y combinados. Fuera del contexto de SHM, el modelo y el método para conseguirlo) pueden también ser utilizados para la predicción y caracterización de envejecimiento en otras aplicaciones. Según el protocolo, la degradación medida de esta manera puede alcanzar 15 % en los módulos elásticos. Los resultados muestran que la mayoría de la degradación se alcanza bajo la influencia de las variaciones de temperatura y humedad.

En cuanto a la adquisición de datos, polifluoruro de vinilideno (*polyvinylidene difluoride*, PVDF en inglés) es una tecnología relativamente nueva para la medición y ofrece una alternativa interesante debido a su bajo costo y facilidad de integración. Demostrar la capacidad de supervivencia las condiciones de envejecimiento era esencial para justificar su inclusión en un estructura compuesta. La validación fue realizada mediante la comparación de la capacidad de los sensores PVDF para proporcionar señales de calidad comparable a la de sensores que no están sujetos al envejecimiento. Se utiliza el método estadístico para esta comparación, con resultados satisfactorios en virtud de los protocolos de envejecimiento diseñados (menos de 2 % en error relativo a los sensores no envejecidos). Con el fin de medir las propiedades elásticas, y siguiendo razonamiento compatible con SHM, el comportamiento vibratorio puede proporcionar información sobre sus propiedades internas. De hecho, los resultados dados por la teoría de la propagación de ondas, la rigidez estructural está conectada directamente con las frecuencias naturales, con la distribución de la masa como intermediario. Sin embargo, la naturaleza ortotrópica del plástico reforzado (*fibre reinforced plastic*, FRP Inglés) complica este problema, y la solución toma la forma de un algoritmo de identificación. El método utilizado aquí ha sido adaptada de un algoritmo identificación numrico- experimental previamente desarrollado por varios autores. Este algoritmo minimiza la diferencia entre resultados experimentales y simulaciones en elementos finitos para estimar el mejor conjunto de propiedades elásticas. Las frecuencias naturales y las correspondientes formas propias (conocidos como parámetros modales de vibración) son las características" que se mencionan en los axiomas SHM, que transmiten la información sobre la estructura interna de la salud. Un análisis de sensibilidad fue incluido en el proceso de identificación para determinar cuantitativamente cómo las propiedades elásticas están relacionadas con los parámetros modales.

En cuanto a la adquisición de datos y la extracción de parámetros estructurales modal,



el análisis modal operacional (*Operational modal analysis*, OMA en inglés) es preferido ya que lleva intrínsecamente los atributos de robustez y rapidez requerida para el método de SHM. Además, la integración de sensores con bajo costo lleva en sí la posibilidad de rastrear los parámetros modales en tiempo real (o casi en tiempo real). Este es un paso importante para mejorar la capacidad de monitoreo de estructuras, sobre todo por razones operativas y de seguridad. En los últimos años, el uso de la OMA ha estado justificado por la dificultad (o imposibilidad) a realizar pruebas dinámicas o estáticas (como el análisis modal experimental) para extraer información sobre la salud estructural. La técnica de descomposición en el dominio de la frecuencia (*Frequency Domain Decomposition*, FDD en Inglés) fue elegido debido a su facilidad de preparación y sus resultados sobresalientes reportados en la literatura. Este método utiliza el concepto de descomposición en valores singulares (*singular value decomposition*, SVD en inglés) para extraer sólo la información necesaria de los sensores de salida. Se ha aplicado con éxito usando varias combinaciones de sensores/actuadores. La evaluación del rendimiento muestra una desviación estándar relativa inferior al 1 % con respecto al método de referencia (EMA).

Dentro de la extracción de características, el problema de la colocación óptima ha sido ampliamente discutido en el estado actual de las técnicas en SHM. Entre los diferentes enfoques, el método de la independencia efectiva (EI) se ha adaptado a este caso. La eficacia de realización se ha demostrado y validado mediante análisis experimentales que muestran una mejora significativa en la precisión de la medición. Por último, teniendo en cuenta los resultados y las observaciones en el desarrollo de diversas herramientas, un método SHM global se ha propuesto, que reúne todos los elementos ya mencionados: el uso de un modelo de múltiples factores para predecir el envejecimiento, diseño de una matriz de transductores, la extracción de características por OMA y la identificación de propiedades de los componentes. El método fue aplicado con éxito a una serie de demostradores, en un entorno de laboratorio controlado. El siguiente paso sería buscar en la adaptación del método a una gama de aplicaciones más amplia (en determinadas aplicaciones *in situ*) y la creación de prototipos operativos. **Palabras clave:** monitoreo estructural, sensores piezoeléctricos, colocación óptima, análisis modal operacional, envejecimiento acelerado.



# Contents

<b>Acknowledgements</b>	<b>v</b>
<b>Abstract</b>	<b>vii</b>
<b>List of figures</b>	<b>xxii</b>
<b>List of tables</b>	<b>xxvii</b>
<b>1 Introduction</b>	<b>1</b>
1.1 Motivation . . . . .	1
1.2 State-of-the-art . . . . .	3
1.2.1 General state-of-the-art in SHM . . . . .	3
1.2.2 Sensing and actuating technologies in SHM . . . . .	5
1.2.3 Natural and accelerated ageing protocols . . . . .	7
1.2.4 Feature extraction methods . . . . .	8
1.2.5 Identification of material properties . . . . .	10
1.2.6 Optimal sensor placement . . . . .	11
1.3 Objectives and thesis structure . . . . .	12
<b>2 Materials and methods</b>	<b>15</b>
2.1 Introduction . . . . .	15
2.2 Materials . . . . .	15
2.2.1 Carbon Fibre Reinforced Plastic (CFRP) . . . . .	15
2.2.2 PVDF film transducers . . . . .	17
2.2.3 Weiss Technik 180/40 Climatic chamber . . . . .	20
2.2.4 Excitation/Acquisition hardware . . . . .	23
2.2.5 Additional material . . . . .	26
2.3 Methods . . . . .	35
2.3.1 Modal Analysis . . . . .	35
2.3.2 Numerical-experimental identification of elastic properties from natural frequencies and vibration modes . . . . .	39
2.3.3 Sensitivity analysis and propagation of uncertainty . . . . .	41
	<b>xix</b>

## Contents

---

<b>3</b>	<b>Weathering and accelerated ageing protocols for composite structures</b>	<b>45</b>
3.1	Motivation and state-of-the-art . . . . .	45
3.2	Preliminary ageing protocols . . . . .	46
3.2.1	Isothermal diffusion in CFRP . . . . .	48
3.2.2	A model for water diffusion in isothermal conditions . . . . .	49
3.3	Design of the accelerated ageing protocols . . . . .	52
3.3.1	Justification of a factorial experiment . . . . .	54
3.3.2	Justification of dwelling times . . . . .	56
<b>4</b>	<b>Multi-factorial model for CFRP ageing</b>	<b>61</b>
4.1	Ageing protocols and experimental campaign . . . . .	61
4.2	Introduction to the experimental results . . . . .	63
4.3	Multi-factorial statistical model . . . . .	65
4.3.1	Mathematical model inspired from the Prony series . . . . .	65
4.3.2	Validation of the exponential pattern . . . . .	67
4.3.3	Interpretation of the validation . . . . .	71
4.4	Equivalent moisture absorption in cyclic ageing protocols . . . . .	71
4.4.1	Diffusion for periodic ageing protocols . . . . .	72
4.4.2	Equivalent diffusivity and equivalent saturation mass . . . . .	74
4.5	Relationship between moisture concentration and loss of stiffness . . . . .	77
4.5.1	Linear regression between mass and elastic properties . . . . .	77
4.5.2	Correlation test . . . . .	78
4.5.3	A linear model for $A_i$ . . . . .	80
4.5.4	Conclusion about the correlation tests . . . . .	81
4.6	A prediction method for composite ageing . . . . .	82
4.7	Conclusions about the ageing model . . . . .	83
<b>5</b>	<b>Survivability of integrated piezoelectric PVDF film transducers</b>	<b>85</b>
5.1	PVDF transducers survivability tests . . . . .	85
5.1.1	PVDF film sensors and integration techniques . . . . .	87
5.2	Interpretation and analysis of experimental results . . . . .	87
5.2.1	Visual inspection of the PVDF sensors . . . . .	87
5.2.2	Results interpretation . . . . .	88
5.2.3	Measurement quality differences between PVDF film sensors and accelerometer . . . . .	89
5.2.4	Statistical data analysis: ANOVA . . . . .	91
5.2.5	Conclusions on survivability of integrated PVDF sensors . . . . .	95
<b>6</b>	<b>Establishment of a transducer network: placement strategy</b>	<b>97</b>
6.1	Motivation . . . . .	97
6.2	Effective Independence method for sensor placement . . . . .	98
6.2.1	Note about optimization of PVDF transducers as actuators . . . . .	100
6.3	Transformation to strain mode shapes . . . . .	100

6.4	Example: transducer placement on rectangular composite plates . . .	102
<b>7</b>	<b>Implementation of Operational Modal Analysis using strain transducers</b>	<b>109</b>
7.1	Approach of the problem . . . . .	109
7.2	Operational Modal Analysis: a robust monitoring method . . . . .	109
7.2.1	Power spectral density (PSD) and singular value decomposition (SVD) . . . . .	110
7.2.2	Modal Extraction: AutoMAC, the peak-picking algorithm and the influence zones . . . . .	112
7.2.3	Modal Extraction: FDD upgrades . . . . .	116
7.3	Experimental campaign . . . . .	119
7.3.1	Placement strategy and specimens manufacturing . . . . .	119
7.3.2	Experimental planning . . . . .	120
7.3.3	Validation of a standing fan as actuator . . . . .	121
7.4	Results . . . . .	122
7.4.1	EMA results and identification . . . . .	122
7.4.2	Reference case: Sp/Acc and Fan/Acc . . . . .	125
7.4.3	PVDF as actuators: PVDF/Acc . . . . .	125
7.4.4	PVDF as sensors: Loud-speaker/PVDF and Fan/PVDF . . . . .	127
7.4.5	PVDF as sensors: Fan/PVDF in different configurations . . . . .	127
7.4.6	PVDF as sensors/actuators: PVDF/PVDF . . . . .	129
7.4.7	Discussion of the results . . . . .	129
7.5	Conclusions about OMA with PVDF . . . . .	132
<b>8</b>	<b>Application of the SHM method: Section of a plane wing</b>	<b>135</b>
8.1	Motivation . . . . .	135
8.2	Monitoring protocol . . . . .	136
8.3	Design . . . . .	137
8.3.1	NACA profile and structure choice . . . . .	137
8.3.2	Finite element model . . . . .	137
8.3.3	Ageing protocols . . . . .	140
8.3.4	EMA with impact hammer and Polytec interferometer . . . . .	142
8.3.5	Numerical-experimental identification using vibration modes . . . . .	145
8.3.6	Local orientation of elastic properties . . . . .	146
8.3.7	Sensitivity analysis . . . . .	147
8.3.8	Optimal placement . . . . .	149
8.3.9	Manufacture . . . . .	149
8.4	Experimental monitoring . . . . .	152
8.4.1	Online monitoring . . . . .	152
8.5	Results . . . . .	153
8.5.1	Moisture absorption . . . . .	153
8.5.2	Statistical comparison between EMA and OMA . . . . .	153
8.5.3	Ageing prediction based on the multifactorial model . . . . .	159

**Contents**

---

- 8.5.4 Sensing and actuation with PVDF transducers . . . . . 160
- 8.6 Conclusions about SHM method applied to the wing section . . . . . 163
  
- 9 Conclusions . . . . . 167**
- 9.1 Synthesis . . . . . 167
- 9.2 Concluding statements . . . . . 169
- 9.3 Recommendations . . . . . 170
  
- A Influence of sensors in the dynamic behaviour . . . . . 173**
- A.1 Experimental tests . . . . . 173
- A.2 Numerical tests . . . . . 174
  
- B Useful abbreviations . . . . . 177**
  
- Bibliography . . . . . 186**
  
- Curriculum Vitae . . . . . 187**

# List of Figures

1.1	Time chart of the increasing use of composite materials in the aeronautics industry (sources: FAA, NASA, Boeing, Airbus). . . . .	2
1.2	Flowchart showing the structure of this thesis and the relationship between chapters. . . . .	14
2.1	Fibre orientation: 1 = longitudinal direction (length $l$ ), 2 = transverse direction (width $w$ ), 3 = normal direction (thickness $h$ ). Carbon fibres are oriented along 1 in UD. . . . .	17
2.2	PVDF products as supplied by Measurement Specialties: (a) PVDF film sheet (b) DT series PVDF sensors. . . . .	20
2.3	Schemes of sensor mounting:(a) glued PVDF sensor and (b) embedded PVDF sensor. . . . .	22
2.4	Relative humidity control charts for the WK180/40 test chamber (photo courtesy of Weiss Technik GmbH ©). . . . .	23
2.5	External view of the WK180/40 test chamber. . . . .	24
2.6	Front view of the HP35670A Dynamic Signal Analyzer (photo courtesy of Hewlett-Packard©). . . . .	25
2.7	NI acquisition hardware: (a) PCI6229 acquisition board and (b) PCI-MIO-16XE with BNC2090 rack-mounted terminal block (photos courtesy of National Instruments©). . . . .	26
2.8	Example of an experimental setup including the actuation and the sensing data flows. PVDF provide the excitation source while accelerometers provide the output signal. . . . .	27
2.9	B&K tool box for data acquisition: charge accelerometers (a) 4517C and (b) 4374 (photos courtesy of Brüel&Kjaer). . . . .	28
2.10	B&K tool box for data acquisition: charge amplifiers (a) Nexus 2692 and (b) 2635 (photos courtesy of Brüel&Kjaer ©). . . . .	29
2.11	Polytec acquisition tool: (a) laser beam generator and (b) controller (photos courtesy of Polytec©). . . . .	30
2.12	(a) B&K excitation impact hammer (mainly used for EMA) (photo courtesy of Brüel&Kjaer ©), (b) Typical impact hammer excitation spectrum. . . . .	31
2.13	Pioneer loud-speakers: (a) TS-1750 and (b) TS-W253F (photos courtesy of Pioneer ©). . . . .	32

## List of Figures

---

2.14	VE5948 standing fan (photo courtesy of Cdiscount (France)©). . . . .	33
2.15	HP33120A signal generator (photo courtesy of Hewlett-Packard©). . . . .	33
2.16	Piezomechanik's SQV 1/500 piezo amplifier, capable to generate electric tension up to 500 [V] (photo courtesy of Piezomechanik©). . . . .	34
2.17	Earthworks micro system: (a) M30BX microphone and (b) LAB1 preamp. . . . .	34
2.18	Representation of excitation/response signals in modal analysis: the actuator excites the structure at input point $i$ and the sensor measures the response at output point $j$ . . . . .	35
2.19	Data handling scheme in EMA. . . . .	37
2.20	Flow chart representing the mixed-numerical identification algorithm based on the comparison between simulated and measured natural frequencies. . . . .	41
2.21	Example of sensitivity analysis between engineering constants and natural frequencies for a D-series sample. The latter are mainly influenced by the longitudinal and transverse tensile moduli $E_1$ and $E_2$ , and the transverse shear modulus $G_{12}$ . . . . .	43
3.1	Experimental results of sample weighing, for isothermal exposure at (a) 60 [°C], (b) 80 [°C] and (c) 100 [°C]. . . . .	50
3.2	Graphs of linear regressions ( $1/T, \ln M_s$ ) and ( $1/T, \ln D$ ) as in equations (3.5) and (3.7) for measured values of Aa- and Bb-series. The slopes give respectively the values of $E_D$ and $E_S$ . . . . .	53
3.3	Graphic representation of the factorial experiment in the 3D cartesian space, showing the position of the individual subject series. . . . .	56
3.4	(a) General form of an ageing protocol plot of set points: the temperature $T$ (in blue), the relative humidity $RH$ (in green) and UV radiation intensity $UV$ (in red). The mean values are in dashed line. Temperature and relative humidity profiles exhibit finite slopes in the transient phases, while UV radiation can be turned on/off instantaneously. (b) Example of actual measurements (full lines) compared to the set points (dashed lines), for an ageing protocol with $x_1 = 0.5$ , $x_2 = 0.53$ and $x_3 = 0$ . . . . .	59
4.1	Example of evolution of relative mass $\mu$ , Young's moduli $\epsilon_1, \epsilon_2$ and shear modulus $\gamma_{12}$ for (a) D-, (b) EF1-, (c) EF2- and (d) H1-series. . . . .	64
4.2	Bar diagrams for identified model coefficients $a_i$ for relative (a) mass $\mu$ , (b) Young's modulus $\epsilon_1$ , (c) Young's modulus $\epsilon_2$ and (d) shear modulus $\gamma_{12}$ . . . . .	67
4.3	Scatter plot for measurements of D-series samples (D: low $T$ , high $RH$ and $UV$ on). . . . .	69
4.4	Scatter plot for measurements of J-series samples (J: low $T$ , high $RH$ and $UV$ off). . . . .	70



4.5	Cyclic mass absorption. The variables are those described in equations (4.7) to (4.14) in subsection 4.4.1: the saturation mass in constant (isothermal) conditions is $M_s$ , while $M_\infty = M_{s,eq}$ is the equivalent saturation mass in cyclic conditions. . . . .	74
4.6	Comparative plot show the closeness of the two exponential functions $\Theta(x) = 1 - e^{-1.311x^{0.75}}$ and $1 - e^{-1.3181x}$ . . . . .	76
4.7	Comparison between the theoretical and fitted models, for (a) D-, (b) EF1-, (c) EF2- and (d) J-samples. . . . .	77
4.8	Correlation plots between the relative mass $\mu$ and (a) $\epsilon_1$ , (b) $\epsilon_2$ and (c) $\gamma_{12}$ . 79	79
5.1	Examples of integrated PVDF sensors: (a) Correctly glued (and aged) PVDF sensors; (b) Correctly embedded PVDF sensors. . . . .	89
5.2	Evolution of mass $m$ and Young's modulus $E_1$ in (a) D- and (b) EF1-groups. Error bars represent the standard deviation. . . . .	90
5.3	Evolution of $\epsilon_1$ , $\epsilon_2$ and $\gamma_{12}$ in (a) D- and (b) EF1-group. Both series were subjected to UV radiation ageing. . . . .	90
5.4	(a) FRF as measured by the accelerometer and the PVDF sensor on DIV after a 300-cycle ageing period. (b) FRF as measured by the accelerometer and the PVDF sensor on EII after a 600-weeks ageing period. (c) [ $\epsilon_1$ ; $\epsilon_2$ ; $\gamma_{12}$ ] vs. Time plot as estimated by the accelerometer and the PVDF sensor in DIV. (d) [ $\epsilon_1$ ; $\epsilon_2$ ; $\gamma_{12}$ ] vs. Time plot as estimated by the accelerometer and the PVDF sensor in EII. . . . .	92
6.1	Strain modes and strain levels for each of the 8 evaluated vibration modes. The regions with higher strain (in red) for each mode are superposed, and three of them are chosen. . . . .	105
6.2	Configuration 1: $\mathcal{S}$ -optimized placement, for 3 strain transducers. . . . .	106
6.3	Configuration 2: $\mathcal{K}$ -optimized placement, for 3 strain transducers. . . . .	107
6.4	Optimal placement of a 3-accelerometer network. . . . .	108
7.1	Example of diagonal spectra from a $\mathbf{S}_+$ resulting of a SVD. The vertical lines are the values of the specimen's natural frequencies obtained by EMA. . . . .	112
7.2	Graphic representation of time signal division in sub-signals: local Hanning windows are applied to avoid the "leakage" effect. . . . .	114
7.3	Principle behind AutoMAC: (a) The influence zone is statistically determined as a continuous frequency interval where $MAC_{mean}$ is high and $MAC_{std}$ is low. (b) A resonance peak is isolated and the modal parameters identified, assuming the SDoF hypothesis (see subsection 7.2.3). . . . .	115
7.4	Application of EFDD to a SDoF peak: (a) local peak, (b) IFFT representing the IRE. . . . .	118

## List of Figures

---

7.5	Transducer placement on the surface of the manufactured samples (the dotted lines represent the PVDF patches on the no visible side of the plate). . . . .	120
7.6	Random excitation signals coming from the Tristar fan and the TS-1750 loud-speaker, and compared to the environmental white noise: (a) time signals (zoomed in) and (b) PSD spectra. . . . .	123
7.7	Experimental mesh where the nodes are the location of the moving impact point. Accelerometers are located optimally as described in chapter 6. . . . .	124
7.8	SVD plot for Sp/Acc and Fan/Acc OMA combination. . . . .	126
7.9	SVD plot for PVDF/accelerometers OMA combinations. . . . .	127
7.10	SVD plot for Loud-speaker/PVDF and Fan/PVDF OMA combinations. . . . .	128
7.11	SVD plot for the Fan/PVDF combination, test on two different configurations: $\mathcal{S}$ -optimized and $\mathcal{K}$ -optimized. . . . .	130
7.12	SVD plot for the PVDF/PVDF and Fan+PVDF/PVDF OMA combinations, test with the $\mathcal{K}$ -optimized network. . . . .	131
7.13	OMA methods ranked by their performance, in terms of standard deviation with respect to the reference method (EMA). Red bars are the cases where $\mathcal{S}$ -optimized networks are involved for sensing or actuation, and green bars are the cases where $\mathcal{K}$ -optimized are involved for sensing and actuation. The latter show a better performance from this point of view. . . . .	132
8.1	NACA 2412 profile. . . . .	138
8.2	Above: example of the internal structure of a wing (photo source: Wikimedia). Below: numerical model of the NACA 2412 profile demonstrator, with the ribs integrated to the upper skin. . . . .	139
8.3	Coloured regions by element type. . . . .	140
8.4	Simulated numerical vibration modes of the demonstrator. . . . .	141
8.5	Example: Experimentally observed vibration modes of the demonstrator L, using the Polytec interferometer. . . . .	143
8.6	Example: Experimentally observed vibration modes of the demonstrator L, using the impact hammer. . . . .	144
8.7	Example: Experimentally measured FRF, for demonstrator L, using (a) the Polytec interferometer and (b) the impact hammer setup. . . . .	145
8.8	Local orientation frames on the upper surface: red = 1, green = 2, blue = 3. . . . .	147
8.9	Sensitivity coefficients for the demonstrators. . . . .	148
8.10	Optimal placements, as computed for the demonstrators, using (a) 3 accelerometers and (b) 5 PVDF sensors. . . . .	150
8.11	Photos of a manufactured demonstrator (L). . . . .	151

8.12	Water mass absorption prediction, and measured using separately EMA and OMA, for demonstrators (a) K, (b) L and (c) M. . . . .	154
8.13	Ageing of (a) K, (b) L and (c) M as predicted by the ageing model, and measured using separately EMA and OMA. . . . .	155
8.14	Plot of ageing prediction curves corresponding to (a) K, (b)L and (c) M, and overall measured data (includes EMA and OMA). . . . .	161
8.15	SVD for demonstrator M, where the excitation is given by the fan. . . . .	164
8.16	SVD for demonstrator M, where the excitation is given by the PVDF actuator network. . . . .	164
8.17	SVD for demonstrator M, where the excitation is given by the fan/PVDF actuators combination. . . . .	165



# List of Tables

2.1	Nominal elastic properties of the PR-UD CST 125/300 FT109 PrePreg after layup and curing. . . . .	16
2.2	Specimen dimensions and average initial masses, as experimentally measured for each series. . . . .	17
2.3	Curing protocol parameters, estimated degrees of curing (based on the supplier's datasheet), estimated starting point of the glass transition zone and lay-up configuration. The autoclave pressure was set to 3 [bar] in all cases. . . . .	18
2.4	Physical properties of the PVDF film as provided by Measurement Specialties. . . . .	21
2.5	Physical properties of the PVDF film, as provided by the supplier's datasheet.	21
2.6	Technical features of the Weiss Technik WK180/40 climatic chamber. . . . .	23
2.7	Nominal settings selected for the HP35670A. . . . .	25
2.8	B&K accelerometers operating features. . . . .	26
2.9	Calibrated equivalent sensitivities for PVDF transducers. . . . .	29
2.10	Selected cut-off frequencies for signal acquisition, for all sample series.	29
2.11	Pioneer loud-speakers features. . . . .	31
2.12	Settings for an impact hammer/accelerometer installation for performing EMA, as performed of the CFRP specimens. . . . .	36
3.1	Summary of the selected papers addressing the artificial ageing problem and its pertinence with respect to real-time ageing in aerospace applications. . . . .	47
3.2	Nominal geometric dimensions and initial mass of plates. . . . .	48
3.3	Computed diffusion coefficients in preliminary tests with test series A and B. . . . .	52
3.4	Summary of ageing protocol parameters for all the series. . . . .	57
4.1	Normalized ageing parameters $x_1$ , $x_2$ and $x_3$ and time parameters for all the series. . . . .	62
4.2	Domain of inputs for the Monte Carlo simulations . . . . .	66

## List of Tables

---

4.3	Lack-of-fit test, along with the coefficient of determination $R^2$ , for a total of $N = 193$ measurements ( $Q = 79$ averaged), and a $p = 16$ DoF model. . . . .	71
4.4	Estimated mass increase for the four series subjected to humid protocols, saturation masses, and equivalent saturation masses for each ageing protocol. . . . .	75
4.5	Comparison between theoretical and experimental estimations of the equivalent diffusivity. . . . .	76
4.6	Results of hypothesis testing on the correlation between $\mu$ and the elastic properties. If $H_0$ is accepted, there is no correlation, while if $H_0$ is rejected, there is a correlation. . . . .	80
4.7	Summary table of data $y_i = A_i(x_1, x_2, x_3)$ used to set up a linear model with interactions, along with the corresponding correlation coefficients $\rho$ . . . . .	81
4.8	ANOVA for the linear model with interactions of $y_2 = A_2(x_1, x_2, x_3)$ , corresponding to $\epsilon_2$ . . . . .	82
4.9	ANOVA for the linear model with interactions of $y_3 = A_3(x_1, x_2, x_3)$ , corresponding to $\gamma_{12}$ . . . . .	82
5.1	Summary of ageing protocol parameters for all the series: nominal values ( $T$ , $RH$ and $UV$ ), the time periods $\Delta t$ , the number of cycles $N_{cyc}$ and the number of rounds. . . . .	86
5.2	Number of sensors used simultaneously for each plate. . . . .	87
5.3	Equivalence table between real and non-dimensional factor after application of equation (5.3). . . . .	93
5.4	ANOVA tables: $SS$ = sum of squares, $DoF$ = degrees of freedom, $MS$ = mean square, $F$ = Fischer's quotient, $p$ = Fischer's probability function. For these results, the differences $y^e$ where expressed as percentages. . . . .	94
7.1	Test plan: EMA extracted natural frequencies are the reference, while OMA extracted natural frequencies are tested: IH = impact hammer, Sp = loud-speaker, Acc = accelerometer, PVDF = PVDF film transducers and Fan. . . . .	121
7.2	Natural frequencies (in [Hz]) identified by an EMA, using an impact hammer and an accelerometer. Several measurements were carried out on each sample, in order to reduce the scattering (less than 0.1% of standard deviation for each mode). . . . .	122
7.3	Summary table of the extracted natural frequencies from EMA and OMA, with the corresponding errors, with $\alpha = 5\%$ and $\nu = 7$ . . . . .	124
8.1	Identified elastic properties before the ageing process. It can be noticed that the directions 2 and 3 have been interchanged. For further details, see subsection 8.3.6 . . . . .	140

8.2	Summary of ageing protocols for the demonstrators. Monitoring rounds were carried out every 100 cycles. For all protocols, $\Delta t_+ = \Delta t_-$ . . . . .	142
8.3	Welch's t-test for $E_3$ of demonstrator K. . . . .	157
8.4	Welch's t-test for $G_{13}$ of demonstrator K. . . . .	157
8.5	Welch's t-test for $E_3$ of demonstrator L. . . . .	157
8.6	Welch's t-test for $G_{13}$ of demonstrator L. . . . .	158
8.7	Welch's t-test for $E_3$ of demonstrator M. . . . .	158
8.8	Welch's t-test for $G_{13}$ of demonstrator M. . . . .	158
8.9	F-test for demonstrator K. . . . .	160
8.10	F-test for demonstrator L. . . . .	160
8.11	F-test for demonstrator M. . . . .	160
8.12	Statistical $t$ -tests comparing EMA with OMA. The null hypothesis is accepted in all cases. . . . .	163
A.1	Experimental comparison between measurements with differently equipped samples. . . . .	174
A.2	Numerical comparison between samples when the glue is modelled and when it is not using an FE model of the sample. . . . .	174





# 1 Introduction

## 1.1 Motivation

Polymer-based composite materials belong to the family of ultra-light structural materials, which have been introduced massively in the recent years in aeronautical applications, but also in other fields like civil and automotive engineering as well. As an example, nowadays most emblematic examples in the civil aeronautical applications are the Boeing 787 and the currently in development Airbus 350 XWB models, as well as in military and space applications (see figure 1.1). Moreover, the anisotropy of the elastic properties allows optimizing the performance of the structural materials, offering countless new design possibilities.

Non-destructive testing and surveillance techniques have been developed over the years, mainly encouraged by the constant search of enhanced safety in the aeronautical industry and in civil engineering applications. However, the standard methods currently used are far from being optimal for these novel materials, and potential improvements in the continuous monitoring techniques are constantly being investigated. From this perspective, new Structural Health Monitoring (SHM) systems have thus emerged during the last years as an interesting option.

The design of a SHM system implies the implementation of a damage detection strategy around a structure, *ie* a strategy the main goal of which is to detect any changes in the geometrical or material properties of a structure or its boundary conditions. These changes are usually unwanted and prejudicial to the system performance and safety [Farrar and Worden, 2007]. The paradigm to solve structural problems and uncertainties goes through by four stages [Giurgiutiu, 2008]: (1) data acquisition and cleansing (filtering), (2) feature extraction and data compression, (3) statistical model development and (4) operational evaluation. The detection strategy is a complex system in itself, since it is composed by smaller strategies with different simpler tasks: periodic data acquisition, structure characterization, optimization of sensor placement, statis-

Chapter 1. Introduction

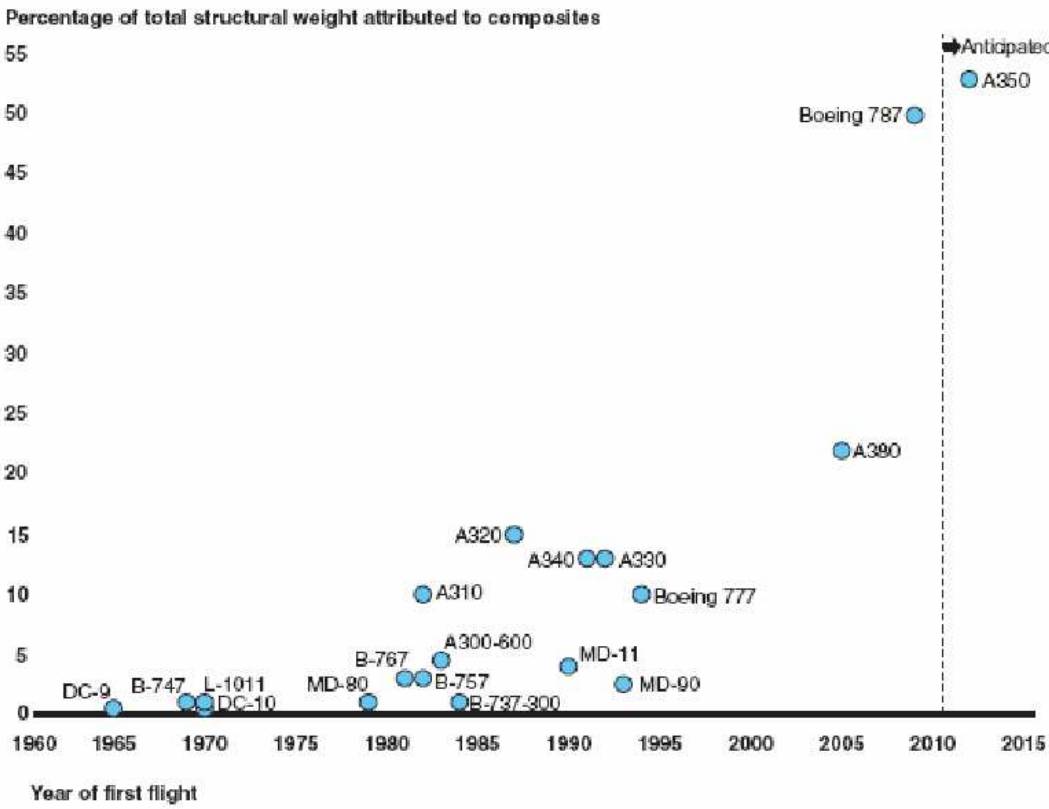


Figure 1.1 – Time chart of the increasing use of composite materials in the aeronautics industry (sources: FAA, NASA, Boeing, Airbus).

tical damage/ageing models, etc.

A SHM process implies also the ability to provide in real-time (or nearly real-time) information about structural integrity. Among the different methodologies of mechanical design, SHM can be inscribed in the categories of damage-tolerant and condition-based maintenance. Most advances in SHM systems come from the need to solve recurrent (and often unavoidable) damage detection problems inside aerospace and civil engineering structures, which are the most exposed to natural ageing and unusual (and sometimes catastrophic) events.

In this optic, the application of SHM on full-scale composite structures has been (and is currently) investigated. Every year new methods and technologies are proposed/developed in order to satisfy an increasing demand on fast, reliable, robust, non-destructive, low-cost monitoring systems to be applied to aircraft, bridges, windmills, skyscrapers, rotorcraft, satellites, high-performance race cars, submarines or any other application where the use of composites materials continues to gain importance.

As stated before, the specific problem of composite ageing evaluation is one of the most often dealt with and at the same time one of the least understood. Taking the example of aeronautical industry, carbon fibre reinforced plastics (CFRP) are currently the most massively used composites. In spite of their exceptionally high mechanical performances, polymer-based composite materials are more vulnerable than metallic alloys when confronted to aggressive environmental ageing factors such as vibrations, impacts, heat, cold, chemical corrosive atmosphere, moisture, fuel, solvents and ultraviolet (UV) radiation, and many aspects of their behaviour are not yet completely understood. Under these circumstances, it is widely accepted that special caution needs be observed when using these materials to manufacture mechanically critical airframe components inside a full-scale structure.

The main motivation of this thesis is then to set the basic foundations of a complete SHM system with all the performance attributes enumerated above, and which could be applied to a general full-scale composite structure, although some times with more emphasis to the specific case of aeronautical structures.

## 1.2 State-of-the-art

### 1.2.1 General state-of-the-art in SHM

The first recorded SHM to be qualified as such can be tracked back to the 19<sup>th</sup> century, when impact hammers were frequently used to recognize damage inside the long steel rail roads, only by hearing the quality of sound propagation [Farrar and

Worden, 2007].

SHM has evolved such that some efforts for the systematisation of the research have been attempted, among which can be found a set of several "axioms" of SHM. Those general principles mention the elements composing a SHM system and the usefulness of each one in the extraction of information about the health of a structure. The axioms are listed as follows [Worden et al., 2007]:

- Axiom I: All materials have inherent flaws or defects.
- Axiom II: The assessment of damage requires a comparison between two system states.
- Axiom III: Identifying the existence and location of damage can be done in an unsupervised learning mode, but identifying the type of damage present and the damage severity can generally only be done in a supervised learning mode.
- Axiom IVa: Sensors cannot measure damage. Feature extraction through signal processing and statistical classification is necessary to convert sensor data into damage information.
- Axiom IVb: Without intelligent feature extraction, the more sensitive a measurement is to damage, the more sensitive it is to changing operational and environmental conditions.
- Axiom V: The length- and time-scales associated with damage initiation and evolution dictate the required properties of the SHM sensing system.
- Axiom VI: There is a trade-off between the sensitivity to damage of an algorithm and its noise rejection capability.
- Axiom VII: The size of damage that can be detected from changes in system dynamics is inversely proportional to the frequency range of excitation.

After lecture of the list, it can be stated that there is a few recurrent generic elements that should necessarily be part of any SHM system. Nowadays, available scientific literature is abundant in scientific papers related to these SHM methods/technologies [Hurlebaus and Gaul, 2006], covering all aspects of a complete SHM process, such as:

1. Sensing technologies: from classical strain gauges, to more innovative optical like:
  - Fibre Bragg gratings (FBG) [Wood et al., 2000, Kister et al., 2004, Tang et al., 1999, Frieden et al., 2012],
  - Piezoceramic transducers [Lin and Giurgiutiu, 2006, Grisso and Inman, 2005],
  - Piezo polymers transducers [Chen et al., 2007, Jeon et al., 2009, Wegener et al., 2009, Guzman et al., 2013]
  - Wireless technology [Lynch and Loh, 2006, Mascarenas et al., 2007].
2. Ageing characterization: most of the research has been centred about the effects of mechanical fatigue and chemical corrosion [Pupurs and Varna, 2009, White, 2006, Fox et al., 2004]. However, polymer-based composite behaviour remains

quite unpredictable in some other usual operating conditions: high temperatures [White, 2006, Fox et al., 2004], moisture absorption [Kumar et al., 2002, Crank, 1989], UV degradation [Kumar et al., 2002, Carraher, 2010], etc.

3. Data handling and structural information extraction techniques:
  - Static methods [Hjelmstad and Shin, 1997, Sanayei and Saletnik, 1996],
  - Acoustic and ultrasound methods [Holroyd, 2000, Stephens and Pollock, 1971],
  - Electric resistance [Chung, 2001],
  - Dynamic methods: Classic experimental modal analysis (EMA) [Ewins, 2000] and output-only or operational modal analysis (OMA), including the time-domain techniques [James et al., 1992, van Overschee and de Moor, 1996] and recently frequency-domain techniques [Brincker et al., 2007, aes et al., 2008, Rainieri and Fabbrocino, 2010].
4. Optimal sensor placement (OSP): depending on the application, the optimization of sensor/actuator placement is based on one of several criteria. The most common results in the literature maximize the received/supplied energy by the transducer network [Li et al., 2007, Kammer and Tinker, 2004], maximize the observability/controllability of the structure (which is viewed as a dynamic system) [Güney and Eskinat, 2008, Nestorović and Trajkov, 2013] or use a statistical approach to minimize the error probability when detecting damages [Flynn and Todd, 2010, Guratzsch and Mahadevan, 2010]. It is also important to mention the efforts made to adapt these optimization methods to the specific case of strain sensors [Foss and Haugse, 1995, Yam et al., 1996].
5. Material characterization methods: using optimization schemes in order to "fit" a vibration model in order to estimate the elastic properties. The first identification algorithms for composite materials were based on analytical equations from the Rayleigh-Ritz theory [Deobald and Gibson, 1988, Fällström, 1991], which were later replaced by numerical models [Sol et al., 1997, Cugnoni et al., 2007].

### 1.2.2 Sensing and actuating technologies in SHM

Among the emerging sensing technologies intended to be used in embedded systems, it can be mentioned: the optical fibre Bragg gratings (FBG) [Tang et al., 1999, Wood et al., 2000, Kister et al., 2004], the wireless technology [Lynch and Loh, 2006, Mascarenas et al., 2007], the semi-conductor piezoresistive transducers [Sze, 1994, Liu, 2012], and the piezoelectric patch transducers [Park et al., 2006, Giurgiutiu et al., 2002, Lin and Giurgiutiu, 2005, Vasques and Rodrigues, 2006]. These modern technologies carry their own package of inherent advantages and drawbacks with respect to each other, in particular from economic and safety points of view.

Among common piezoelectric materials, can be mentioned some crystals (quartz, tourmaline, etc.) and some ceramics (lead zirconate titanate PZT and other niobates,

titanates). Piezoelectric transducers have many advantages as their measurement accuracy, fast reaction, and the possibility to use them alternatively as sensors or actuators. However, these classic materials are some times not suitable for a SHM application mainly because of their high cost, fragility and low mechanical compliance.

In this thesis, an interesting alternative for *in situ* monitoring and for solving the problems mentioned above is extensively studied. It concerns the use of polyvinidilene fluoride (PVDF) piezoelectric patch transducers, because of their compliance for *in situ* monitoring due to their low cost of implementation (economic benefits) and high mechanical compliance (operational benefits).

PVDF technology is based on the piezoelectric properties of PVDF, a thermo-plastic fluoropolymer that exhibits a glass transition point around  $-35$  [°C] and a melting point around  $180$  [°C]. Due to the lowness of the latter compared to other classical piezoelectric sensor materials, it is legitimate to lead a survivability study to verify the accuracy of dynamic measurements provided by the PVDF sensors, and eventually identify the operating limits under constantly changing environmental conditions. Moreover, PVDF sensors are better suited for dynamic analysis methods than some classic strain sensors like strain gauges or piezoresistive sensors due to their short response time.

However, because of their polymer-based nature, the same factors leading to the environmental ageing of composite panels could potentially affect their electromechanical and piezoelectric performances. Industrial applications in monitoring of full-scale aeronautical structures by such sensors have to be verified. Results of artificial ageing protocols applied to composite structures in previous works [White, 2006, Carraher, 2010, Brinson and Brinson, 2008, Fox et al., 1965] show the detectable extent of damage on polymer materials. These documents focus in commonly evoked factors that contribute to composite structures ageing, in particular vibrations, impacts, high/low temperature, thermo-mechanical fatigue, moisture and exposition to UV radiation. These factors, alone or combined, have been observed to have an effect on polymer-based pieces inside long-time operating aircraft and rotorcraft. The survivability of PVDF mechanical and electromechanical properties to artificial ageing protocols has been demonstrated as part of this thesis, and the results published [Guzman et al., 2013]. Moreover, PVDF sensors are better suited for dynamic analysis methods than piezoresistive sensors due to their short response time. For all these reasons, the idea of an integrated transducer network is now admissible.

As mentioned above, one of the assets of a PVDF film sensor is the possibility of an easy integration due to a high mechanical compliance. However, this comes with a drawback: the block force is reduced, on the contrary to piezoceramic patches such as PZT. Fortunately, these PVDF transducers, despite their relatively low stiffness and block force, can be used as actuators when correctly integrated, as demonstrated by

several authors [Chen et al., 2007, Wegener et al., 2009, Jeon et al., 2009]. This fact leads to a whole new perspective: the operational modal analysis (OMA) of a full-scale structure can be eventually completely carried out by a simple integrated PVDF transducer network.

### 1.2.3 Natural and accelerated ageing protocols

In the current state-of-the-art, there is in scientific literature some lack of understanding of polymer-based composite materials behaviour to environmental ageing conditions. Most of the research has been centred about the effects of mechanical fatigue [Pupurs and Varna, 2009], water absorption [Lin and Chen, 2005, Weitsman, 2012] and chemical corrosion [Liao et al., 1998, White, 2006]. A lot of experiments of the material evolution under other usual natural ageing agents such as heat, moisture or solar radiation, when applied periodically on a given sample, have been carried out [Mouzakis et al., 2008, Dao et al., 2007, Fox et al., 2004, Bondzic et al., 2006]. However, ageing characterization is a very complex problem, the solution of which depends on a lot of factors, notably the material itself.

Considering the case of CFRP, the polymer-based matrix and the fibre/polymer interface are the most vulnerable components of the composite. Specialized researchers in the field of composite ageing have described qualitatively the failure mechanisms [White, 2006, Fox et al., 2004, Bondzic et al., 2006] or presented empirical quantitative evidence of changes in constitutive properties of polymers [Mouzakis et al., 2008, Dao et al., 2007, Tong et al., 1996, Lin and Chen, 2005] when subjected to natural and/or artificial weathering. Macroscopically, these changes lead to an observable progressive degradation of the global constitutive properties of the composite (elastic moduli, strength, ductility, etc.), which could turn out to be critical if the proper safety precautions are not taken into account. In more extensive treatises [Carragher, 2010, Brinson and Brinson, 2008], most of the chemical and microscopic mechanisms that explain the degradation are reviewed.

Thus, the lessons learned from this research landscaping advise that in order to reveal any changes in stiffness due to exposition to relatively aggressive ageing factors, experimental campaigns under controlled weathering conditions should take place. Previous works can provide an idea of the approach for the ageing protocol design [Mouzakis et al., 2008, Dao et al., 2007, Fox et al., 2004, Bondzic et al., 2006] as well as by ASTM standard guidelines: D4762 for cyclic ageing protocols, C581, D1151 and D5229 for the combined hygro-thermal testing, and G151 and G154 for UV radiation testing.

These documents focus on commonly evoked factors that contribute to composite structures ageing, in particular relatively high temperature, moisture and UV radia-

tion. These factors, alone or combined, have several effects on polymer-based pieces inside long-time operating aircraft and rotorcraft: water diffusion, polymer molecules cross-linking/de-linking, alternate dilatation/contraction cycles, residual stress, photo-oxidation, post-curing, temperature gradients, and many others. The specific features of ageing protocols are discussed more in detail in section 3.3. This summary states that from the experimental point of view, cyclic conditions in specific temperature and relative humidity conditions, and periodic exposition to UV radiation are most often considered dominant. Even more important, the interaction between all these factors add a supplementary non-negligible degradation which is not often taken into account in the literature. The effect of these interactions are considered from the quantitative point of view in chapter 4.

If standard testing with quantitative results is applied to several species of structural materials, it can be used as a comparison reference for mechanical designers while trying to select a specific material by its ageing performances. The apparent usefulness of an ageing modelling method becomes clearer in the context of SHM. An ageing model would provide an initial estimation of the material degradation under given conditions. After ageing, the current state can be evaluated and a fresher prediction can be estimated. This way, it can be judged if a structure can be operated safely, by comparison with the expected ageing course/lifetime estimation.

It is missing from literature a standard method to parametrize the effects of these ageing factors on the composite structure. According to the specialized literature in the Design of Experiments (DoE) theory [Box et al., 2005, Montgomery, 2009], it is possible to create a parametric multi-factorial model, the parameters of which can be estimated by a mathematical regression from experimental data. This model can be useful from the quantitative point of view, in order to compare objectively the influence of the different weathering agents and especially the effect of their interaction.

### 1.2.4 Feature extraction methods

Feature extraction methods occupy by far most of the research efforts in SHM investigation. The goal of feature extraction is to get the necessary data to distinguish between an aged/damaged structure from a non-aged/undamaged one.

Among the most common feature extraction methods, can be mentioned:

- those based on the direct measurement of stiffness using static response tests and residual stresses [Hjelmstad and Shin, 1997, Sanayei and Saletnik, 1996],
- those using acoustic and ultrasound methods to test the quality of sound propagation through matter [Holroyd, 2000, Stephens and Pollock, 1971],
- those measuring the electric resistance (or more generally the electric impedance) along the structure [Chung, 2001, Salvia and Abry, 2006],



- and those extracting vibrational information such as the natural frequencies are compatible with the general principles of SHM, especially concerning robustness and simplicity, qualities that are highly appreciated.

It is the methods in the last category that are considered in this thesis, in particular modal analysis.

In classic modal analysis, the approach known as experimental modal analysis (EMA) is currently the most frequently used in vibration tests. Over the years, a large set of methods, techniques and technologies has been developed and commercialized to be used in industrial and scientific applications. The fundamental relationship between stiffness and natural frequencies (coming from the waves theory and its mathematical solution) are the cornerstone of modal analysis. Thus, if there were any changes in the structural elasticity, those can be directly tracked by the changes in natural frequencies. Note, that the mass also plays a part in this formulation.

Basically, EMA works on the base of an known excitation time signal (frequently called input) and a response time signal (output) to estimate the modal parameters from a transfer function. Each signal is sampled and transformed through a fast Fourier transform (FFT) algorithm, in order to obtain the discrete frequency spectra of both signals. These output-to-input ratio signal obtained like this is known as the Frequency Response Function (FRF). This function contains information about the natural frequencies, damping coefficients and the corresponding mode shapes. This set of information is known collectively as the modal parameters of the structure, and determine the dynamic and vibrational behaviour of the structure. The mathematical details of modal analysis are discussed in section 2.3.1.

Even if it is the best known modal testing technique, due to the necessary hardware and envioning conditions for correct data extraction and handling, classic EMA is frequently not adapted for measurement and experimentation outside the laboratory context. To be applicable *in situ*, alternative variants of modal analysis methods exist, more robust and stable. Operational or Output-only modal analysis (OMA) answers to this need. With respect to the classic experimental modal analysis (EMA), OMA has the particularity to assume the uncertainty about the excitation signal, making necessary to measure only output signals. As shown by several authors [Ibrahim, 1977, James et al., 1992, van Overschee and de Moor, 1996, Ventura and Horyna, 1997, Brincker et al., 2000], the information contained in the output signal only suffices for a modal extraction. Thus, a randomly (or near-randomly) excited structure can be modal-analysed as long as the excitation level is sufficient to excite enough vibration modes.

The first OMA methods to appear approached the problem using time-domain based models like the natural excitation (NExT) method [James et al., 1992] or subspace

state methods [van Overschee and de Moor, 1996, Peeters and DeRoeck, 1999]. In contrast with this, during the 2000s decade, frequency-domain methods and its applications were largely studied. Among these, it can be mentioned the least-squares complex functions (LSCF) [Peeters et al., 2004] and the frequency domain decomposition (FDD) [Brincker et al., 2007, aes et al., 2008, Rainieri and Fabbrocino, 2010]. The latter includes three generations of algorithms: the first FDD, the enhanced FDD (EFDD) and the frequency-spatial FDD (FSDD). The theoretical principles are detailed in chapter 7.

### 1.2.5 Identification of material properties

The Euler-Bernoulli beam theory, in combination with the Euler-Lagrange formulation [Euler and Truesdell, 1980], proposes analytical estimations for the natural vibration frequencies of structures in some specific cases. For example, consider a rectangular specimen, for which  $t \ll w$  and  $t \ll l$ , with  $t$  being the thickness,  $w$  the width and  $l$  the length of the sample. The natural frequencies of this free-free beam can be estimated using the equations below:

$$f_{bend,i} = \alpha_i \sqrt{\frac{Ewt^3}{ml^3}}, \alpha_i = 1.013, 2.835, 5.543, 9.180\dots \quad (1.1)$$

$$f_{tors,i} = i \sqrt{\frac{Gt^3}{mw}}, i = 1, 2, 3, 4, 5\dots \quad (1.2)$$

where  $m$  is the mass of the sample and  $E$  and  $G$  denote the longitudinal Young's modulus and transverse shear modulus respectively. In this case, the essence of material characterization based on vibration tests can be observed:  $E$  and  $G$  can be computed from the measured natural frequencies of the beam.

Unfortunately, the beam approximation diverges considerably from reality when the aspect ratio  $w/l < 0.1$  is no longer satisfied. One step ahead, the first analytic models for thin shells were developed in the frame of Rayleigh-Ritz plate solution [Reddy, 2006]. These models state a direct proportionality between the elastic moduli and the square of the natural frequencies, corresponding mainly to bending and torsional mode shapes. The first identification algorithms for composite materials were based on analytical equations from the plate theory [Deobald and Gibson, 1988, Fällström, 1991, Araújo et al., 1996, Doebling et al., 1998].

Although analytical continuous models provide a good approximation to establish the theoretical basis of properties identification, it is clear that a numerical model, like a finite element (FE) model, provides more accurate computations when the plate

approximation cannot longer be respected (complex geometries, curved plates, irregular shapes) especially concerning the influence of some deformation mechanisms (such as interactions between bending and transverse shear) that are not always included in the analytical formulation of which the solutions are similar to those in equations 1.1 and 1.2. A FE model discretises a structure into small elements, and can thus be viewed as an oscillating dynamic system with  $n$  degrees of freedom (DoF) [Gmür, 1997]. Its dynamic behaviour  $x(t)$  can be described by a matrix equation:

$$\mathbf{M}\ddot{\mathbf{x}}(t) + \mathbf{K}\mathbf{x}(t) = \mathbf{f}(t) \quad (1.3)$$

where the matrices  $\mathbf{M}$  and  $\mathbf{K}$  contain information about mass and structural stiffness respectively, and  $\mathbf{f}(t)$  is the external excitation force (non-conservative forces are neglected for the sake of clarity). So, in this formulation, the local elastic properties of each element (Young's moduli, shear moduli and Poisson's ratios) enter in the constitution of the elements of matrix  $\mathbf{K}$ . Based on a spectral transformation approach of equation (1.3) (Fourier or Lagrange for example), the free vibration problem ( $\mathbf{f}(t) = \mathbf{0}$ ) becomes:

$$(-\omega^2\mathbf{M} + \mathbf{K})\boldsymbol{\phi} = \mathbf{0} \quad (1.4)$$

which is a generalized eigenproblem, the solution of which is given by  $(\omega_k, \boldsymbol{\phi}_k)$  pairs. The  $k^{th}$  natural frequency is given by  $f_k = \frac{\omega_k}{2\pi}$ , which proves the theoretical link between elastic properties and vibration in the FE model approach.

Thus, in order to characterise a material in a candidate structure, numerical FE simulations can be used instead to minimize the error between estimated and experimental frequencies (or other modal parameters), and to fit the numerical model parameters, which would be the elastic properties of the candidate composite structure [Sol et al., 1997, Gibson, 2000]. Moreover, in the frame of structural monitoring, the mixed numerical-experimental identification provides useful feedback information about the state of elastic properties. One of these identification algorithms is detailed in subsection 2.3.2.

### 1.2.6 Optimal sensor placement

Another element of a SHM system is the transducer placement strategy, which is a requirement to ensure that all the necessary information is correctly extracted using as less transducers as possible. In the frame of optimal sensor placement (OSP), some

methods are available in scientific literature: the close-loop method [Güney and Es- kinat, 2008], the balanced reduced models method [Nestorović and Trajkov, 2013], the driving-point residue method [Worden and Burrows, 2001], the variance method [Meo and Zumpano, 2005], the kinetic energy method [Heo et al., 1997] and many oth- ers. However, none of them is directly applicable to the case of strain sensor networks. A simple and quick adaptation can nonetheless be considered for the method of the effective independence (EI) method [Li et al., 2007], which is based on the notion of "modal" energy of the vibrational system, although the formulation assumes the measurement of the linear displacements as starting point. The mathematical formu- lation to represent the transition between "displacement modes" and "strain modes", which are shown to be valid mode shapes [Yam et al., 1996], is based on the proposal by Foss [Foss and Haugse, 1995] and detailed further in chapter 6.

From the experimental point of view, it is important then to verify experimentally that PVDF patch transducers, with the proper manufacturing, handling and integration, are capable to provide exploitable electric signals and optimally extract reliable fea- ture information about the structure and thereby about the state of the constitutive properties of a composite panel. The transducer network should be capable of carry- ing out a signal acquisition (working as a sensor) as well as of providing enough modal excitation in case the external natural excitation is not sufficient over the analysed fre- quency band (working as an actuator).

The OSP problem remains however an open issue. Some of the other methods men- tioned above would be eventually applicable to the case of composite structures and strain sensors/actuators with the proper mathematical adaptations. This aspect of the SHM method constitutes a potential source of improvement.

### 1.3 Objectives and thesis structure

Considering the motivation and the elements introduced in the above paragraphs concerning SHM applied to composite structures, the main objective of this thesis is:

To develop a novel SHM system to be applied on full-scale composite struc- tures, primarily destined to aerospace applications, in order to monitor in real-time (or nearly real-time) the health of the structure and detect dis- tributed ageing-induced damage, using a piezo transducer network and a robust, non-destructive, fast and reliable feature extraction testing tech- nique.

The answer to the problem raised by this statement is not simple, and is constituted by several simpler questions that can be solved separately, in order to achieve the global

objective. Some modular objectives can be fixed then:

1. Ageing model: given a defined composite material (or candidates composites), design an appropriate ageing protocol and validate it experimentally, in order to establish a first ageing model to estimate the ageing rate in further experiments. The ageing protocol is supposed to be accelerated, but its effects should simulate those obtained by natural weathering. This objective implies implicitly the survivability of the integrated transducer network. In order to systematically characterize the ageing, several environmental factors (and their interactions) need to be taken into account.
2. Transducer network: given a geometry and material orientation, be able to provide an optimal solution for spatial placement of the components of a PVDF transducer network, which provides enough information about the structural health. If needed, the actuation capacity of the transducers should also be exploited to excite the structure.
3. Feature extraction: to extract modal information using the signals provided by the transducer network, and based on the link between elasticity and modal parameters in a solid structure, be able to identify the current elastic properties. It is required that the method be robust (work in a wide range of cases and to deal with low signal-to-noise ratios), fast (depending on the application, collect data in a few seconds/minutes) and reliable (give accurate information even in the case of singular hardware failure), which means that the accuracy of the extraction can deal with unforeseeable events, from simple perturbations to catastrophic events on single components.
4. Global solution: using the conclusions to the aforementioned objectives, design a global monitoring system and validate it on a prototype.

Similarly, this thesis report follows a modular structure, each chapter referring to an elementary topic, the conclusions of which constitute an element of the whole monitoring system. A preliminary chapter (chapter 2) introduces the main materials and methods considered as experimental objects and subjects in this thesis. Further, several topics are explored (as shown in figure 1.2) concerning the objectives mentioned above: ageing protocols (chapter 3), ageing characterization (chapter 4), transducers survivability (chapter 5), transducer network design and optimization (chapter 6) and feature extraction (chapter 7). Finally, the results are combined and assembled in a global method, which is applied and validated on a prototype demonstrator in chapter 8.

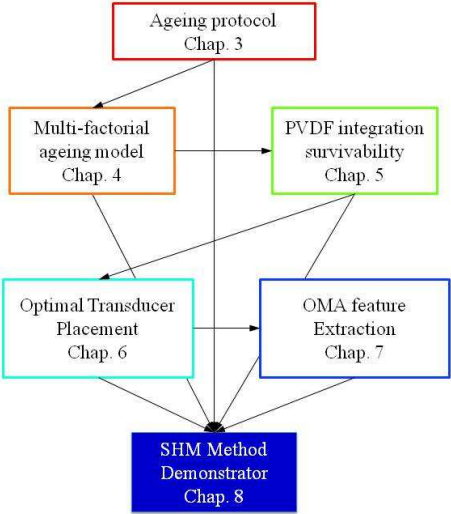


Figure 1.2 – Flowchart showing the structure of this thesis and the relationship between chapters.

# 2 Materials and methods

## 2.1 Introduction

As stated in the previous chapter, the research contained in this thesis is focused on the development and validation of a SHM tool that can be applied to composite structures, emphasising on aeronautical/aerospace applications. The monitoring has to combine several points: an ageing model, a non-destructive feature extraction method and a transducer network.

In summary, this SHM method's goal is to propose a monitoring tool that evaluates the ageing state of full-scale composite structures to weathering agents. The materials and methods listed below in this chapter contribute to the fulfilment of the thesis objectives.

## 2.2 Materials

### 2.2.1 Carbon Fibre Reinforced Plastic (CFRP)

Since CFRP is the most used composite material in the aeronautical industry, it has been decided to take them as primary study subject. More specifically, all the manufactured samples are made of Carbon-PrePreg PR-UD CST 125/300 FT109, a structural material supplied by Suter-Kunststoffe© AG (Switzerland). It is originally under scroll form of unidirectional (UD) carbon fibre tissue (Torayca©T700S carbon fibre), pre-impregnated in partially hardened epoxy polymer (PREDO©FT109) with an areal weight of 125 [g/m<sup>2</sup>] (60% of fibre volume fraction). The nominal after-curing elastic properties of this material are given in table 2.1.

A summary containing the main features (mass and dimensions) of each series of specimens is shown in table 2.2. Each series was issued from rectangular plates and was scheduled to be tested following the ageing protocols described in chapters 3

## Chapter 2. Materials and methods

and 5. The last three specimens, K, L and M demonstrators, had special design features since their purpose is to demonstrate the feasibility of the monitoring on more complex structures, and are described in chapter 8. For these three demonstrators, the equivalent width is computed so the demonstrator has the same volume as a rectangular plate with the same thickness and length.

The manufacturing process for the samples was a basic curing warm up under vacuum (0.02 [bar]). The surrounding pressure inside the autoclave and around the vacuum bag was 3 [bar] in all cases. The moulds were made of aluminium, and a demoulding agent (commercial demoulding wax) was used. The manufacturing parameters such as the curing temperature, the curing duration (14h in most of cases, 20h in a few), the estimated degree of hardening (>98% in all cases), the estimated glass transition starting temperature (between 85 [°C] and 95 [°C]) and the layup configuration (see table 2.3).

The layup configuration is in most cases UD, with the carbon fibres in the longitudinal direction, as illustrated in figure 2.1. The dimensions and nominal masses of the plates were measured using an electronic Vernier and Mettler-Toledo© weigh balances respectively (a 0.01 [g] resolution for the XS105 DualRange, a 0.1 or 1 [g] resolution for the PB8000, see table 2.2).

The advantage of a UD configuration is the macroscopic separation between the elastic properties dominated by the carbon fibres and by the epoxy resin. From reports in the current literature [Mouzakis et al., 2008, Fox et al., 2004, Dao et al., 2007, Tian and Hodgkin, 2010, Bondzic et al., 2006], the CFRP is expected to exhibit a heavy degradation in the resin component while carbon fibre remains relatively uncorrupted. The fibre/resin interface is also expected to suffer damaging.

As it will be shown further in chapters 4 and 5, only some of the global elastic properties measured fade clearly in a greater amount than others.

Table 2.1 – Nominal elastic properties of the PR-UD CST 125/300 FT109 PrePreg after layup and curing (1: longitudinal direction, 2: transverse direction, 3: normal direction). Over 63 measurements,  $\mu$  is average value and  $\sigma$  is the corresponding standard deviation.

	Young's modulus			Poisson's ratio			Shear modulus		
	[GPa]			[-]			[GPa]		
	$E_1$	$E_2$	$E_3(*)$	$\nu_{12}(*)$	$\nu_{13}(*)$	$\nu_{23}(*)$	$G_{12}$	$G_{13}(*)$	$G_{23}(*)$
$\mu$	96.00	7.67	8.70	0.38	0.3	0.03	3.60	3.59	2.24
$\sigma$	0.067	0.013	(-)	(-)	(-)	(-)	0.021	(-)	(-)

(\*) Nominal values as supplied in the supplier's data sheet.



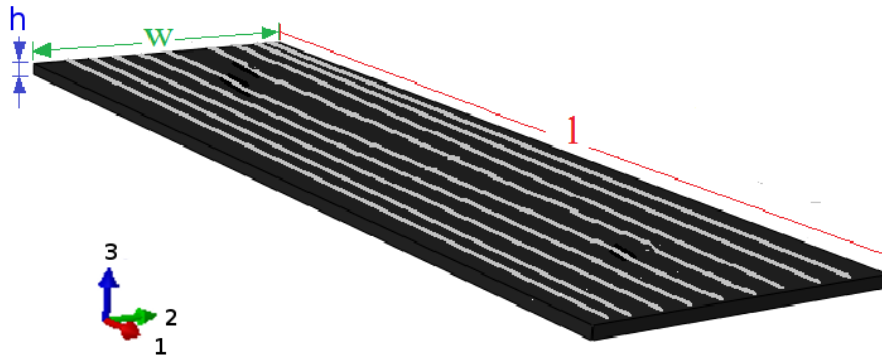


Figure 2.1 – Fibre orientation: 1 = longitudinal direction (length  $l$ ), 2 = transverse direction (width  $w$ ), 3 = normal direction (thickness  $h$ ). Carbon fibres are oriented along 1 in UD.

Table 2.2 – Specimen dimensions and average initial masses, as experimentally measured for each series.

Series	Length [mm]	Width [mm]	Av. thickness [mm]	Av. mass [g]
AaI-II-III-IV-V-VI	300	39.0	4.0	68.10 (*)
BbI-II-III-IV-V-VI	300	38.5	4.0	64.00 (*)
CI-II-III-IV-V	300	40.0	4.5	76.43 (*)
DI-II-III-IV-V-VI	150	99.0	4.0	83.49 (*)
EI-II	300	98.5	4.4	188.5 (**)
FI-II	300	81.6	4.0	134.1 (**)
GI-II-III	300	92.0	3.7	153.5 (**)
HI-II-III	300	95.4	4.2	179.0 (**)
JI-II-III	300	98.2	4.3	181.3 (**)
K	580	332 (****)	2.9	782 (***)
L	580	330 (****)	3.0	810 (***)
M	580	330 (****)	3.0	811 (***)

(\*) Mettler-Toledo®Balance,  $\pm 0.01$  [g] precision.

(\*\*) Mettler-Toledo®Balance,  $\pm 0.1$  [g] precision.

(\*\*\*) Mettler-Toledo®Balance,  $\pm 1$  [g] precision.

(\*\*\*\*) Equivalent width of the specimen.

### 2.2.2 PVDF film transducers

Before discovering its piezoelectric properties, PVDF was used almost exclusively as a protection paint for metallic structures thanks to its remarkable color retention prop-

## Chapter 2. Materials and methods

Table 2.3 – Curing protocol parameters, estimated degrees of curing (based on the supplier’s datasheet), estimated starting point of the glass transition zone and lay-up configuration. The autoclave pressure was set to 3 [bar] in all cases .

Series	Curing protocol (temperature /time)	Hardening (%)	Start. $T_{glass}$	Lay-up
Aa	70[°C]/10[h] + 80[°C]/8[h]	98	85[°C]	CP : [0°/90°/90°/0°] <sub>6s</sub>
Bb	70[°C]/10[h] + 80[°C]/8[h]	98	85[°C]	UD : [0°] <sub>24</sub>
C	70[°C]/10[h] + 80[°C]/8[h]	98	85[°C]	CP : [0°/90°/90°/0°] <sub>7s</sub>
D	85[°C]/10[h] + 90[°C]/4[h]	99	95[°C]	UD : [0°] <sub>24</sub>
E	70[°C]/10[h] + 85[°C]/10[h]	98	90[°C]	UD : [0°] <sub>28</sub>
F	70[°C]/10[h] + 85[°C]/10[h]	98	90[°C]	UD : [0°] <sub>24</sub>
G	85[°C]/10[h] + 90[°C]/4[h]	99	95[°C]	UD : [0°] <sub>22</sub>
H	85[°C]/10[h] + 90[°C]/4[h]	99	95[°C]	UD : [0°] <sub>28</sub>
J	85[°C]/10[h] + 90[°C]/4[h]	99	95[°C]	UD : [0°] <sub>28</sub>
K	85[°C]/10[h] + 90[°C]/4[h]	99	95[°C]	UD : [0°] <sub>20</sub>
L	85[°C]/10[h] + 90[°C]/4[h]	99	95[°C]	UD : [0°] <sub>20</sub>
M	85[°C]/10[h] + 90[°C]/4[h]	99	95[°C]	UD : [0°] <sub>20</sub>

erties. PVDF piezoelectric properties were measured for the first time in the early seventies, and it exhibited almost 10 times larger piezoelectric coefficients than any other polymer. Since then, industrial processes to better polymerise PVDF have increased the electricity-related properties, so PVDF film transducers are able to be used in structural applications not only as gauge sensors, but as actuators as well, as it will be shown in chapter 7 for light structures.

The piezoelectric materials linear constitutive law is expressed by a combination of two equations (so-called coupled equations):

$$\mathbf{s} = \mathbf{S}^E \boldsymbol{\sigma} + \mathbf{d}^T \mathbf{e} \quad (2.1)$$

$$\mathbf{d}_e = \mathbf{d} \boldsymbol{\sigma} + \boldsymbol{\epsilon} \mathbf{e} \quad (2.2)$$

where  $\mathbf{e}$  and  $\boldsymbol{\sigma}$  denote the electrical and stress field respectively,  $\mathbf{s}$  denotes the strain and  $\mathbf{d}_e$  denotes the electrical charge density inside the piezoelectric patch. Those variables are connected by constitutive constant matrices:  $\mathbf{d}$  is the matrix for the direct piezoelectric effect and  $\mathbf{d}^T$  is the matrix for the converse piezoelectric effect,  $\mathbf{S}^E$  denotes the compliance matrix (which is somehow the inverse of the stiffness matrix) and  $\boldsymbol{\epsilon}$  is the electric permittivity. In general, many elements inside these matrices are zero, and thus piezoelectric behaviour can actually be explained by a few constants. For example, in the case of piezoelectric patches, such as the PVDF transducers, the

matrix of piezoelectric effects can be written as:

$$[\mathbf{d}] = \begin{bmatrix} 0 & 0 & d_{31} \\ 0 & 0 & d_{32} \\ 0 & 0 & d_{33} \\ 0 & d_{24} & 0 \\ d_{15} & 0 & 0 \\ 0 & 0 & 0 \end{bmatrix} \quad (2.3)$$

The PVDF film transducers mentioned in this thesis come almost exclusively from the same commercial supplier, Measurement Specialties©. The most relevant properties of their PVDF are summarized in table 2.4. In table 2.5, several observations can be pointed out:

1. The piezoelectric effects  $d_{31}$  and  $d_{33}$  (see table 2.4) are indeed unusually high for a polymer material (around 0.1 [pC/N] for other regular polymers). These coefficients reflect the proportionality between the electrical field applied in direction 3 (normal to plane), and the corresponding strain deformations, in directions 1 and 3. The convention in this thesis is that one dominant direction (length) is defined as direction 1.
2. Unfortunately, it is a relatively weak electromechanical transmitter when compared to ceramics due to its low Young's modulus (as compared to structural materials as, in this case, CFRP) and its low acoustic impedance, particularly in static and in low frequency applications. However, as it will be shown in chapter 7, PVDF works well as an actuator at high frequencies.
3. From the design point of view, PVDF can be manufactured into unusual designs thanks to its high mechanical compliance. It can be easily shaped and embedded into structures or glued with commercial adhesives. The transducers can be either fully integrated on the surface or inside the composite plate between two layers, as shown in figure 2.3. This is one major advantage over not only piezoceramics (which are usually mechanically fragile and heavy), but also over non integrable sensors such as accelerometers or interferometers.
4. The Curie temperature is around 145 [°C] as reported from several authors [Wegener et al., 2009, Lovinger et al., 1986, Chen et al., 2007]. This limit guarantees resistance of the piezoelectric properties to high temperatures as long as it is for short periods of time. As it will be shown, PVDF transducers remain operational after being exposed to temperature cycles up to 135 [°C].
5. PVDF shows a great resistance to moisture diffusion (less than 0.02% of saturation concentration). This makes PVDF a very good candidate in weathering monitoring applications.

6. PVDF low density is another strong point. It makes this type of light weight sensors less intrusive when it comes to dynamic monitoring methods, as the ones suggested in this thesis.

Many other reasons evoked and quoted in the literature support and justify the choice of PVDF as a technically suitable candidate for the dynamic sensing of composite structures. Furthermore, from the economic point of view, PVDF transducers represent a real breakthrough because of their low cost. Along with its mechanical compliance, it represents one of the reasons to expect that PVDF sensors can be massively integrated in composite air frames in order to constitute transducer neural networks, that would be capable of sensing and working on the structure, in a similar way as neurones do in the human body. It will be demonstrated in chapter 5 that PVDF transducers are able to survive the ageing process without seeing their dynamic measurement capabilities affected [Guzman et al., 2013].

A recurrent issue that should be taken into account is the sensibility to electromagnetic interference (EMI), expressed usually as a parasite electromagnetic resonance peak at the powerline distribution frequency, which is 50 [Hz] in Switzerland. As advised by the supplier [MSI,1999], special precaution needs to be taken in order to reject this intruder signal, and this is why the use of co-axial cables is required. In practice, this solution demonstrates to be effective, although in some case an additional analogical or digital filter is advised.

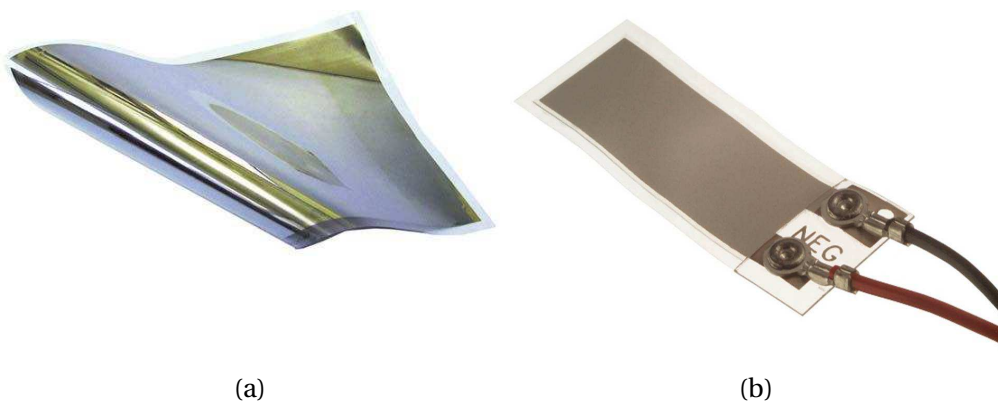


Figure 2.2 – PVDF products as supplied by Measurement Specialties: (a) PVDF film sheet (b) DT series PVDF sensors.

### 2.2.3 Weiss Technik 180/40 Climatic chamber

The choice of a test chamber has been based on considerations that are carefully detailed in chapter 3. At first, a domestic solution for the device was being considered among the feasible solutions, taking example from other reports, as for example the

## 2.2. Materials

Table 2.4 – Physical properties of the PVDF film as provided by Measurement Specialties [MSI,1999] and from literature [Wegener et al., 2009, Lovinger et al., 1986, Chen et al., 2007].

Property	Unit		From supplier's datasheet	Measured
Thickness	[ $\mu\text{m}$ ]	$t$	52 or 28	-
Young's modulus	[GPa]	$E$	2 to 4	3.8
Piezo Strain Constants	[pC/N]	$d_{31}$	23	23.5
		$d_{33}$	-33	-
Moisture absorption	[%]	$M_s$	<0.02	-
Frequency range	[Hz]	$f$	$10^{-3}$ to $10^9$	-
Operating temperature range	[ $^{\circ}\text{C}$ ]	$T$	-40 to +100	-
Curie temperature	[ $^{\circ}\text{C}$ ]		+145	>+135
Operating voltage	[V]		750	>500

Table 2.5 – Physical properties of the PVDF film, as provided by the supplier's datasheet.

Property	Units	PVDF film	PZT	BaTiO <sub>3</sub>
Density	[ $\text{kg}/\text{m}^3$ ]	1780	7500	5700
Relative Permittivity	$\epsilon/\epsilon_0$	12	1200	1700
Piezo charge constants $d_{31}$	[pC/N]	23	110	78
	[pC/N]	-33	-290	-160
$d_{33}$	[pC/N]	-33	-290	-160
Acoustic impedance	[ $\text{kg}/\text{m}^2 \text{ s}$ ]	2.7	30	30

in-home built hardware described by [Mouzakis et al., 2008]. However, it was ultimately decided that a commercial solution would be more appropriate because of the necessary know-how and the accuracy needed to follow the temperature, relative humidity and UV radiation intensity setpoints required by the ageing protocol design.

The Weiss Technik test chambers of the WK series allow reproducing different climates to be applied in various industrial sectors, ranging from basic testing to quality control. Regardless of the shape and nature of the specimens, high temperatures can be achieved thanks to the climate conditioning of the test space. According to the supplier's description brochure, "a wide range of standard test space volumes is available for a great variety of applications" [Weiss Technik GmbH, 2011]. An important aspect is the stated compliance with all relevant testing standards such as DIN, ISO, MIL, IEC, DEF, but especially ASTM. The digital measuring and control system with 32-bit processor developed by Weiss Technik offers programming possibilities for operator-defined climate profiles, as it is required by in this case.

An airstream that is conditioned exactly to the entered setpoint values flows continuously through the chamber. Plates on the floor and ceiling guarantee an optimum

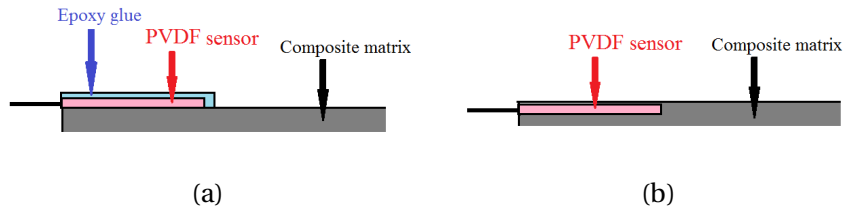


Figure 2.3 – Schemes of sensor mounting:(a) glued PVDF sensor and (b) embedded PVDF sensor.

distribution of the air and temperature throughout the test space. The core test chamber comes with an optimized airflow propelled by two fans for circulating the air. The components for air conditioning are located in the rear compartment. A large axial fan with external drive motor draws the air out of the test space. The air then flows through a finned heat exchanger through which it can be cooled down and/or drought. Specially designed heat exchangers prevent undesired condensation from forming on the test space's walls and on the specimens, ensuring maximum temperature and humidity constancy (in time).

For high temperature applications, an electrical heater is installed in front of the heat exchanger. The air stream then passes over a water bath, integrated heating and cooling elements ensure that the water is tempered quickly and exactly. The humidity of the test space air adapts according to the water temperature. A climate system enables a highly accurate relative humidity control even with a heat load. The humidity is measured psychrometrically by two resistance thermometers. The dry and wet bulbs are located next to each other in the airstream. The wick of the wet bulb sensor is automatically wetted [Weiss Technik GmbH, 2011]. The climate diagrams illustrating the technical limits of the chamber are shown in figure 2.4.

The external housing is made of corrosion-resistant steel, while the test space is walled by a single-block, deep drawn, stainless steel metal sheet. The chamber is equipped with 2 standard port holes (50[mm] and 125 [mm] diameter) that are located on the left and right side of the test chamber, and can be used for inserting measuring and control cables, other supply connections or additional equipment (like thermocouples). Threshold temperature security systems are also included to protect the specimens and the chamber.

A photo is shown in figure 2.5. The most relevant technical features are summarised in table 2.6. Finally, an electric lamp can be connected to a ceiling socket. The chosen model was an OSRAM® Ultra Vitalux© 300 [W] solar lamp, which recreates the full-solar spectrum in a sunny day at sea level. Only a very low proportion is however composed of UV-A radiation [ $\sim 1\%$ ], which has been reported in literature to be the most harmful to CFRP [Mouzakis et al., 2008, White, 2006]. The total radiation inten-

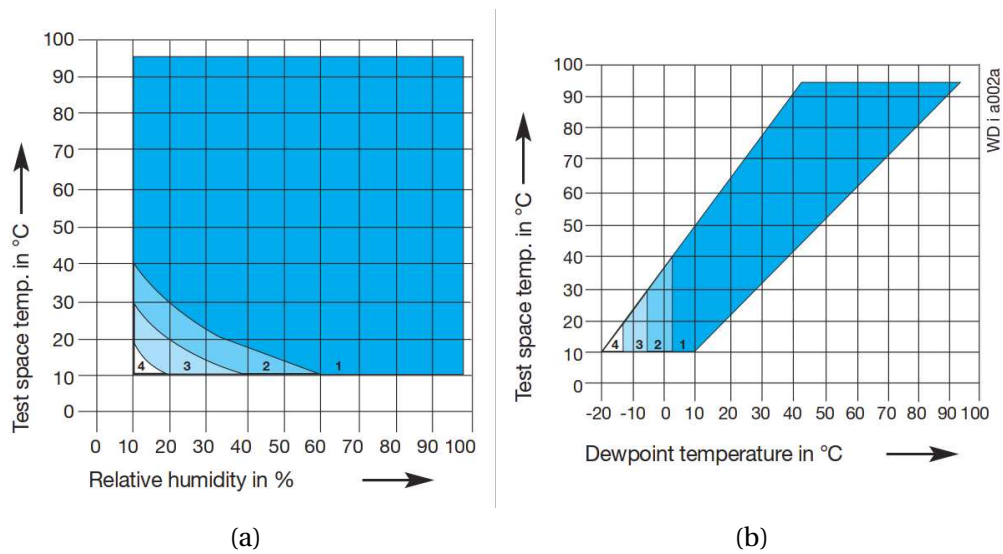


Figure 2.4 – Relative humidity control charts for the WK180/40 test chamber (photo courtesy of Weiss Technik GmbH ©).

sity inside the test space is  $\sim 300$  [W/m<sup>2</sup>].

Table 2.6 – Technical features of the Weiss Technik WK180/40 climatic chamber.

Test space volume	[l]		190
Test space dimensions	[mm]	Height	750
	[mm]	Width	580
	[mm]	Depth	450
Maximum weight	[kg]		425
Maximum temperature	[°C]		+180
Minimum temperature	[°C]		-45
Average heating rate	[°C/min]		4.7
Average cooling rate	[°C/min]		4.0
Max. temperature deviation	[°C]	in time	$\pm 0.5$
	[°C]	spatial	$\pm 2.0$
Humidity range	[%]		10 to 98
Temperature range with humidity	[°C]		+5 to +95
Humidity deviation	[%]	in time	$\pm 3$

## 2.2.4 Excitation/Acquisition hardware

### HP dynamic analyzer

Another key instrument in the measurement sequence is the Hewlett-Packard 35670A Dynamic Signal Analyzer©, which admits up to 4 signal channels. This is the main device used to acquire signals when carrying out impact hammer-actuated EMA on the



Figure 2.5 – External view of the WK180/40 test chamber.

specimens. The information extracted was usually an FRF, corresponding to a specific output/input signal ratio. Sensors included accelerometers and eventually other piezoelectric sensors.

The signal processing functions include fast Fourier transform (FFT) and inverse fast Fourier transform (IFFT), different displays for FRFs, and the possibility of carrying out curve-fitting using the single degree-of-freedom (SDoF) hypothesis for modal extraction. This way, the HP35670A is a powerful tool if quick EMA is needed. During the experiments, channel 1 (far left input) has served as the reference channel, with the impact hammer plugged in. The other three channels are available for the output signals coming from accelerometers (in some cases from PVDF patches).

For a EMA, some basic settings need to be introduced for a correct acquisition:

- The acquisition mode is FFT Analysis.
- The frequency range depends on the choice of the user, and therefore on the subject specimen. The chosen frequency ranges are summarized in table 2.7. Only frequency spans of 200, 400, 800, 1600, 3200,... [Hz] are possible.





Figure 2.6 – Front view of the HP35670A Dynamic Signal Analyzer (photo courtesy of Hewlett-Packard©).

- Channel 1 (hammer) is conditioned by a rectangular window (fixed at 10 [ms]) and the other channels (2,3,4) by an exponential window. The decaying time constants are summarized in table 2.7. The goal of introducing this exponential window in the signal processing, is to eliminate residual vibrations at the end of the acquisition time, in order to avoid the "leakage" effect, which can be observed by the appearance of small side lobes around resonance peaks in the FRFs.
- Finally, the number of spectral lines is generally chosen to have enough spectral resolution. The selected values are shown in table 2.7 as well. The acquisition duration is then automatically determined by the HP35670A.

Table 2.7 – Nominal settings selected for the HP35670A.

Series	Lower frequency	Upper frequency	Acquisition duration [s]	Nb. spectral lines	Spectral resolution [Hz]	Exp. time constant [s]
C-J	0	3200	0.5	1600	2	0.5
K-M	0	800	1	800	1	1

### Data acquisition boards

Data acquisition hardware includes National Instruments acquisition boards PCI 6229, PCI-MIO-16XE and BNC2090 rack-mounted BNC terminal block (up to 16 input channels and 2 output channels, -10 [V] to +10[V]), working with NI-DAQmx 8.5, 8.8 or 9.1 versions (see figure 2.7). Any of them can work as a data acquisition device, but only the BNC2090 can generate signals and send them simultaneously.

An example of the test bench setup is depicted in figure 2.8. To simulate free-free boundary conditions, the specimen is suspended on a rack with a thin plastic thread.

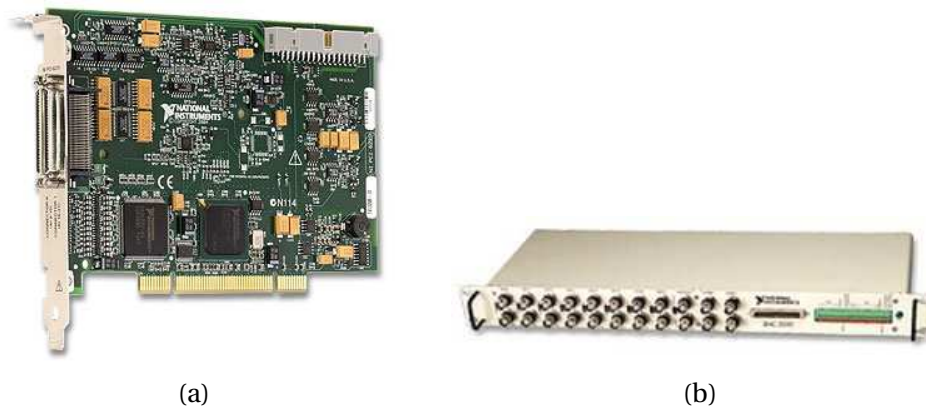


Figure 2.7 – NI acquisition hardware: (a) PCI6229 acquisition board and (b) PCI-MIO-16XE with BNC2090 rack-mounted terminal block (photos courtesy of National Instruments©).

The excitation can be done using a fan, loud-speakers or eventually the integrated piezoelectric patches.

### 2.2.5 Additional material

#### Accelerometers and amplifiers

Brüel&Kjaer charge accelerometers are used as reference piezoelectric sensors for all dynamic testing in this thesis of two types: 4517C and 4374 (see figure 2.9). Their electric and mechanical features are summarized in table 2.8. In average, the 4517C model has a slightly higher sensitivity. The masses are extremely low compared to the mass of the samples (less than 0.8 % ratio in all cases) and their influence on the dynamic behaviour of the sample is negligible. A short analysis is commented in appendix A.

Table 2.8 – B&K accelerometers operating features.

Type	Mass [g]	Sensitivity [pC/g]	Operation freq. [Hz]
4517C	0.6	1.7±0.1	up to 10k
4374	0.65	1.5±0.1	up to 26k

The accelerometers and PVDF transducers signal conditioning is carried out by conditioning amplifiers. The main device for this task is the multi-channel conditioning amplifier Brüel&Kjaer Nexus 2692-0S4 with four input channels (see figure 2.10). In some cases, when more than 4-channels were needed to be amplified, auxiliary conditioning amplifiers of the 2635 type were used. For the aforementioned accelerometers, the used gain is 3.16 [V/m s<sup>-2</sup>]. The resulting signal after an impact excitation gives around ±10 [Vpk] signals, and 7 [Vrms] after a steady excitation with a fan, which is

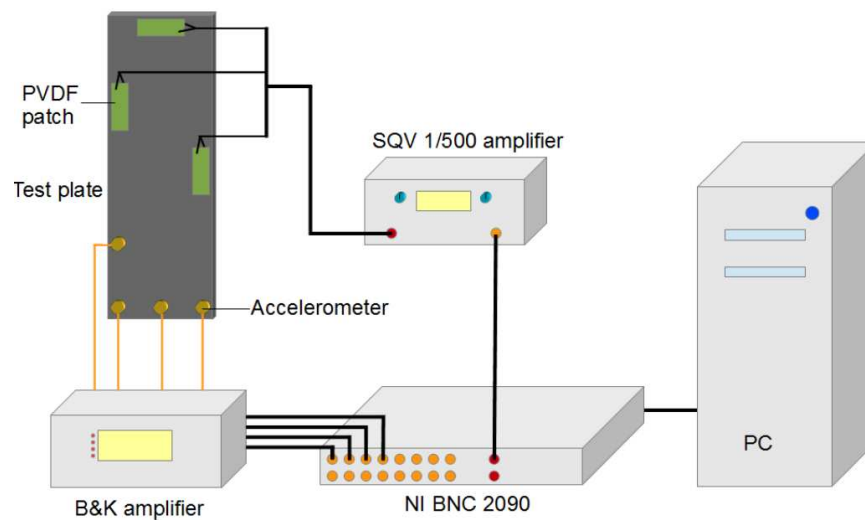


Figure 2.8 – Example of an experimental setup including the actuation and the sensing data flows. PVDF provide the excitation source while accelerometers provide the output signal.

described below.

Concerning the electric signal received from the PVDF sensors, it is necessary to fix an "equivalent sensitivity" to calibrate the conditioning amplifiers. In order to do so, an accelerometer and an integrated PVDF patch are used simultaneously, using the same amplification gain. Both signals are compared, and the sensitivity of the PVDF channel is adjusted so that the RMS voltage is similar for both. This process is repeated for each integrated sensor before the ageing process takes place. The calibration sensor is a 4517C-type accelerometer.

The calibrations obtained for the integrated PVDF sensors (mean  $\pm$  standard deviation for all the patches in a given series) after integration are summarized in table 2.9.

These conditioning amplifiers include frequency low-pass and high-pass filters, the usefulness of which is to reduce the influence for unnecessary parasite signal spectra outside the working frequency band. These cut-off frequencies were selected and kept constant for all the composite plate samples (C- to J-series) and the three demonstrators (K to M), and are summarized in table 2.10.

Finally, the amplification circuit takes the ground as reference, in order to avoid electrostatic parasite charges.



Figure 2.9 – B&K tool box for data acquisition: charge accelerometers (a) 4517C and (b) 4374 (photos courtesy of Brüel&Kjaer).

### **Polytec interferometer**

A Polytec OFV055 interferometer (see figure 2.11) was used as support tool to perform very accurate EMA. This is particularly useful in the case of structures with high spectral density. This is why the Polytec has been mainly used in the case of the three demonstrators, in order to compare and make sure the match between the simulated modes and the measured modes (by OMA or EMA).

The Polytec OFV055 uses the Doppler-effect and the interferometry principles for the measurement of velocity. More information can be consulted in [Waldbronn, 2014]. This specific model has three different acquisition modes, although the most interesting is the scanning mode. Indeed, the laser beam scans a rectangular region on the sample where the uniformly distributed output locations are covered with reflecting tape. The result of the scan is a set of FRFs which can be processed in order to obtain directly the natural frequencies and the corresponding vibration modes.

### **Impact hammer**

An impact hammer is a device designed to provide an excitation signal close to a Dirac delta pulse. In signal processing theory, this pulse of infinitely high force applied to a structure during an infinitely short time has the ability to excite uniformly vibrations at all the frequencies from zero to infinity. In the real case, the impact hammer has a limited excitation frequency range.

The maximum excitation frequency depends essentially on the contact between the

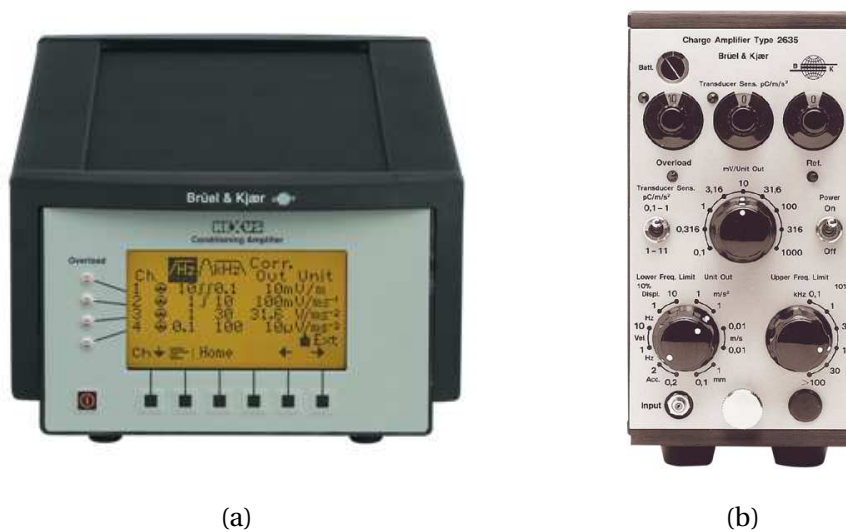


Figure 2.10 – B&K tool box for data acquisition: charge amplifiers (a) Nexus 2692 and (b) 2635 (photos courtesy of Brüel&Kjær ©).

Table 2.9 – Calibrated equivalent sensitivities for PVDF transducers. The calibration is carried out with a 4517C-type accelerometer as reference.

Series	Sensitivity [pC/g]	
	Accelerometer	PVDF patch
C	1.814	4.8 ± 0.5
D	1.814	4.2 ± 0.8
E	1.814	3.9 ± 0.6
F	1.814	4.7 ± 0.7
G	1.814	4.6 ± 0.8
H	1.814	3.8 ± 1.2
J	1.814	4.4 ± 1.0
K	1.814	3.2 ± 1.9
L	1.814	3.2 ± 1.7
M	1.814	3.1 ± 2.1

Table 2.10 – Selected cut-off frequencies for signal acquisition, for all sample series.

Series	High-pass cut-off frequency [Hz]	Low-pass cut-off frequency [kHz]
C-J	10	3
K-M	1	1

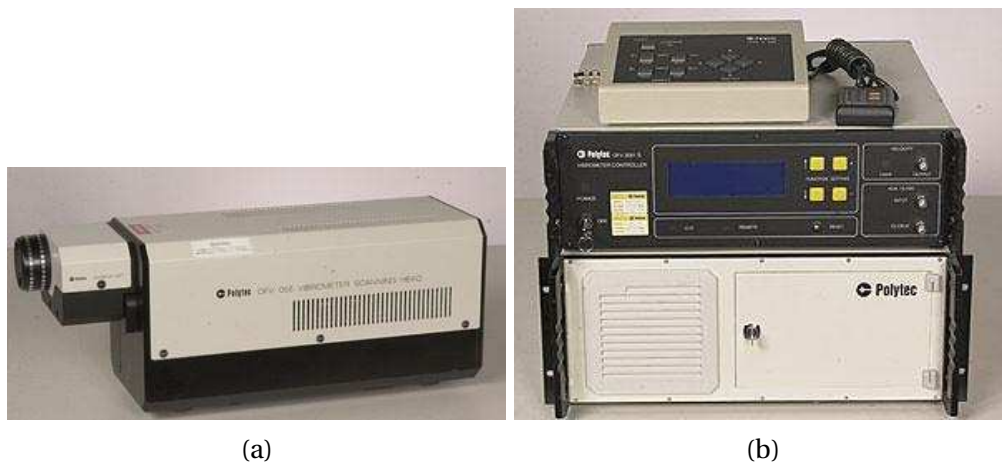


Figure 2.11 – Polytec acquisition tool: (a) laser beam generator and (b) controller (photos courtesy of Polytec©).

hammer's tip and the structure. A trade-off is then imposed by the hardware limitations:

- A soft tip produces a long shock: fewer frequencies can be excited but a better excitation signal is sampled. In this case, the corresponding discrete Fourier transforms are less aliased and give a more accurate excitation spectrum.
- A hard tip produces a short shock (closer to a Dirac delta function excitation signal): higher frequencies can be excited but the excitation signal is poorly sampled, usually leading to a truncated discrete impulsion and lesser quality excitation spectrum.

In conclusion, an impact should be short enough to excite as much frequencies as possible but long enough to be correctly sampled. For the CFRP specimens in this thesis, an aluminium tip (hard) showed the most suitable features in terms of excitation and quality signal. The used impact hammer is shown in figure 2.12 (a). Its a 8206-002 type impact hammer, with a 2.3 [mV/N] sensitivity and a maximum application force of 2200 [N]. It is important to point out that the hammer is an ICP-type transducer (no conditioning or charge amplifier).

### Loud-speakers

Loud-speakers are used to generate the excitation signals in the frame of OMA, but also EMA using the Polytec interferometer. The excitation comes from the air pressures waves generated by the vibration of membranes.

- For OMA, the loud-speakers are used to produce a pseudo-random excitation signal in order to comply with the randomness hypothesis, as stated in the theory men-

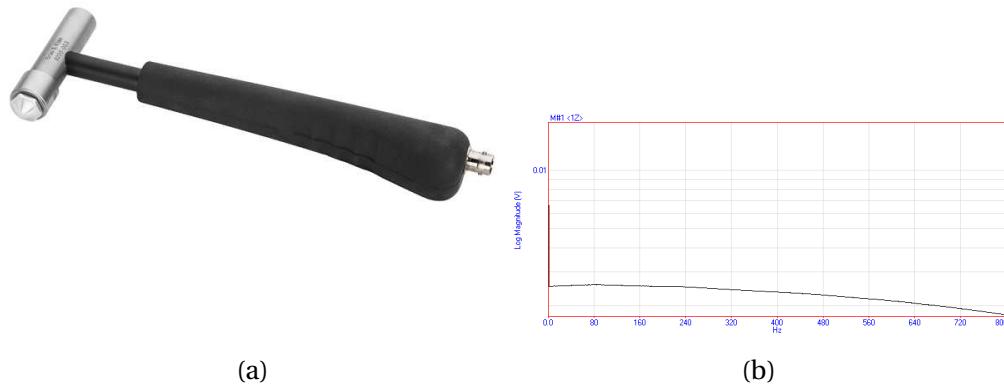


Figure 2.12 – (a) B&K excitation impact hammer (mainly used for EMA) (photo courtesy of Brüel&Kjaer ©), (b) Typical impact hammer excitation spectrum.

tioned in chapter 7.

- For EMA, the loud-speakers represent a more accurate alternative for excitation than a impact hammer, since they can be controlled by a PC. This is why they are used simultaneously with the Polytec interferometer.

Two types of loud-speakers were used, the features of which are summarized in table 2.11 (see figure 2.13). The choice of the model is motivated by the excitation ranges they can provide: the TS-1750 was used to excite the high frequencies and TS-W253F the low ones.

Table 2.11 – Pioneer loud-speakers features.

Type	Nominal power [W]	Impedance [ $\Omega$ ]	Frequency range [Hz]	Diameter [cm]
TS-1750	50	4	36-31000	17
TS-W253F	140	4	2-2500	25

### Standing Fan

A standing fan provides a regular airflow which produces some pressure waves when obstacles are found. The idea of using a standing fan is to take advantage of the airflow to excite the structure, in an attempt to emulate wind that would excite an aircraft, a windmill or a bridge.

In the frame of OMA testing, it can be assumed that a fan is a source of random excitation. The randomness hypothesis does not need to be strictly respected on the whole

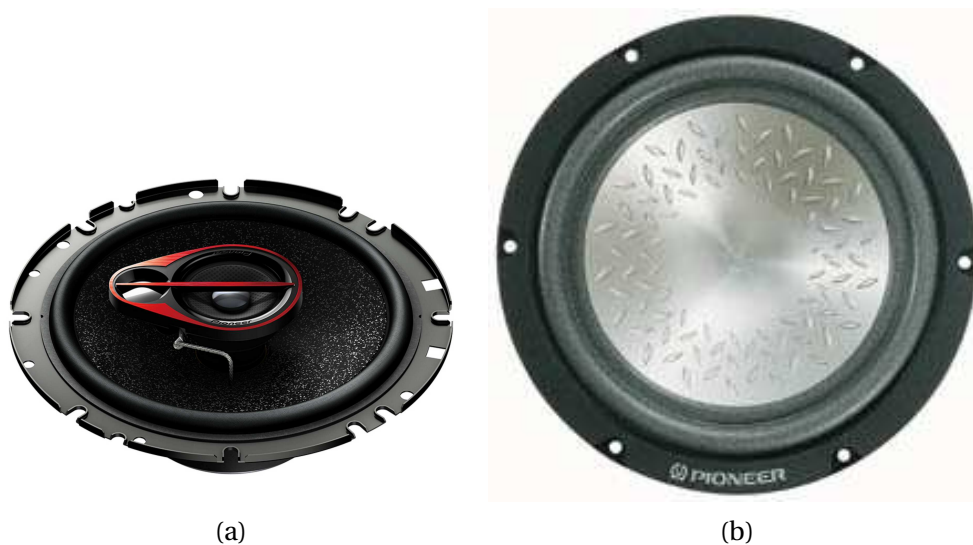


Figure 2.13 – Pioneer loud-speakers: (a) TS-1750 and (b) TS-W253F (photos courtesy of Pioneer ©).

frequency range as demonstrated in chapter 7. As it is demonstrated in the same chapter, the use of a standing fan is validated from the spectral point of view.

The standing fan used for the excitation of samples is a Tristar VE 5948 (see figure 2.14) with the following features:

- Nominal power: 50[W].
- Maximal speed: 1300[rpm].
- Diameter: 40[cm].
- Three blades.
- Distance to sample: 60[cm] to 1[m].

In order to validate its use, its spectral signature is compared with the one from a loud-speaker emitting a white noise signal. As a reference, the spectrum of the surrounding natural noise is also measured.

### Signal generator HP 33120A

The HP33120A (see figure 2.15) is a versatile waveform generator which can be used stand-alone or commanded by a PC. In the frame of this thesis, it is used mainly for generating pseudo-random excitations and white noise. The main receivers are the loud-speakers in the frame of EMA using the Polytec interferometer or the PVDF patches when used as actuators. A power amplifier is usually needed to amplify the signal before transmitting it: a Harman Kardon amplifier in the case of loud-speakers, and a Piezomechanik SQV 1/500 amplifier (see figure 2.16) in the case of PVDF patches





Figure 2.14 – VE5948 standing fan (photo courtesy of Cdiscount (France)©).

(see below). Indeed, the maximum voltage it can provide is 20[V] peak-to-peak (28 [W] of maximum power), and for a efficient excitation this signal is often to weak.

### **Piezo amplifier SQV 1/500**

Piezomechanik's SQV 1/500 analog amplifier (see figure 2.16) is specially conceived to excite piezo-ceramic patches, such as PZT. However, it has been used to provide high electric voltage to excite PVDF sensors.

As the maximum voltage supported by the waveform generator is 20 [V], the analog



Figure 2.15 – HP33120A signal generator (photo courtesy of Hewlett-Packard©).



Figure 2.16 – Piezomechanik's SQV 1/500 piezo amplifier, capable to generate electric tension up to 500 [V] (photo courtesy of Piezomechanik©).

amplifier for the waveform is used. Indeed, since the PVDF has a limited block force capacity, it is necessary to compensate this by a very high excitation voltage, which can be supplied by the SQV. Via this amplifier, which provides a maximum voltage of 500 [V] (1000 [V] peak-to-peak), the signal is transferred from the first output channel to the three PVDF patches on the test plate, which are used simultaneously.

### Micro M30BX Earthworks

A M30BX Earthworks microphone (see figure 2.17) is used to measure the pressure waves from the loud-speakers and the standing fan, in order to validate the use of the latter as an excitation source. It is also used in the frame of interferometer-based EMA, in order to measure the excitation signal from the loud-speakers.



Figure 2.17 – Earthworks micro system: (a) M30BX microphone and (b) LAB1 preamp.

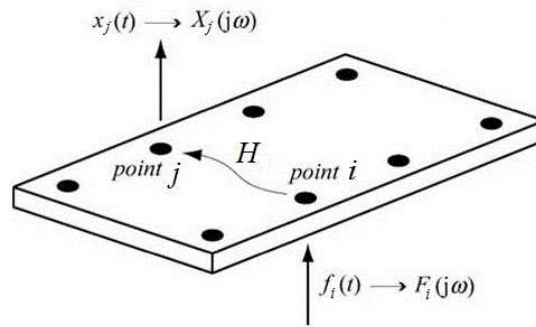


Figure 2.18 – Representation of excitation/response signals in modal analysis: the actuator excites the structure at input point  $i$  and the sensor measures the response at output point  $j$ .

## 2.3 Methods

### 2.3.1 Modal Analysis

#### Experimental Modal Analysis

EMA is a well-known, reliable, widely used modal analysis method in engineering. Only some principles are reminded in this section. The approach of classic EMA starts by the establishment of a non-parametric model using experimental time data: an excitation signal  $f(t)$  (called the input) and a structural response signal  $x(t)$  (called the output). The response signal carries inherently the necessary information about the structure's vibration behaviour, and so the modal parameters can be extracted from this. However, the practical aspects of this method require some attention since the brute signals need to be correctly handled before being exploitable.

Consider EMA applied to a structure, like the one in figure 2.18. This figure shows how the excitation of the structure at point  $i$  is perceived by a sensor located at point  $j$ . Both excitation and response are characterized by the direct measurement of a physical magnitude (displacement, velocity, acceleration, force, pressure, charge, etc.) using a transducer, which provides in turn a proportional electric signal, measured in [V]. In this thesis, EMA was carried out using an impact hammer/accelerometer combination for excitation/response acquisition. In a few cases, other combinations like impact hammer/PVDF patch or loud-speaker/interferometer were also used to carry out EMA, in general for technical or validation reasons. The practical aspects of data handling to be taken into account by the user are anyway the same for all.

Consider the example of the impact hammer/accelerometer input/output combination. The input signal  $f(t)$  is provided by the load cell at the tip of the impact hammer, and the output signal  $x(t)$  by the accelerometers. A flowchart showing the data han-

## Chapter 2. Materials and methods

---

ding is shown in figure 2.19:

1. First, the output signal  $x(t)$  is amplified and filtered: the signal amplification is needed in order to transform a high-impedance charge signal provided by the accelerometer to a low-impedance voltage electric signal; the filtering reduces the influence of resonant natural frequencies outside the analysed frequency range, improving the signal. The NEXUS conditioning amplifier combines both functions. The impact hammer is directly connected to the HP35670A since it is an ICP transducer (it provides voltage as an output).
2. The two voltage signals are then sampled by the HP35670A, with the frequency settings described in table 2.7. The user fixes usually two of the three parameters: the number of spectral lines for the FFT transformation, the frequency band and the acquisition time, with the third automatically computed. The windowing is a mathematical operation aiming to avoid the spectral leakage [Harris, 1978], forcing the time signals to be close to zero at the end of the measurement. In the case on the impact hammer, a simple rectangular window suffice (since the impact is short anyway). On the other hand, the response signal needs to be slowly decreased, and this is why an exponential window is preferred. The FFT is carried out on the signals once this parameters are set.
3. Finally, the FRF  $H_{ij}(j\omega)$  spectrum is obtained by the one-by-one division of the discrete spectra  $X_j(j\omega)$  and  $F_i(j\omega)$ .

The parameters for an impact hammer/accelerometer EMA are summarized in table 2.12.

Table 2.12 – Settings for an impact hammer/accelerometer installation for performing EMA, as performed of the CFRP specimens.

Settings	Input $f(t)$	Output $x(t)$
<i>Conditioning amplifier</i>		
Sensitivity	-	1.5 - 1.7 [pC/g]
High-pass filter cutoff	-	0.1 - 1 [Hz]
Low-pass filter cutoff	-	3000 [Hz] (plates)
Low-pass filter cutoff	-	1000 [Hz] (demonstrators)
<i>Dynamic Analyzer</i>		
Signal level	$\approx 2$ [V]	10 [V] - 20 [V]
Frequency band		800-3200 [Hz]
Number of spectral lines		800-1600
Acquisition time		0.5 - 1 [s]
Windowing	Rectangular, 6-10 [ms]	Exponential, 0.5 - 2 [s]

A non-parametric experimental model is thus obtained directly, as expressed in equa-

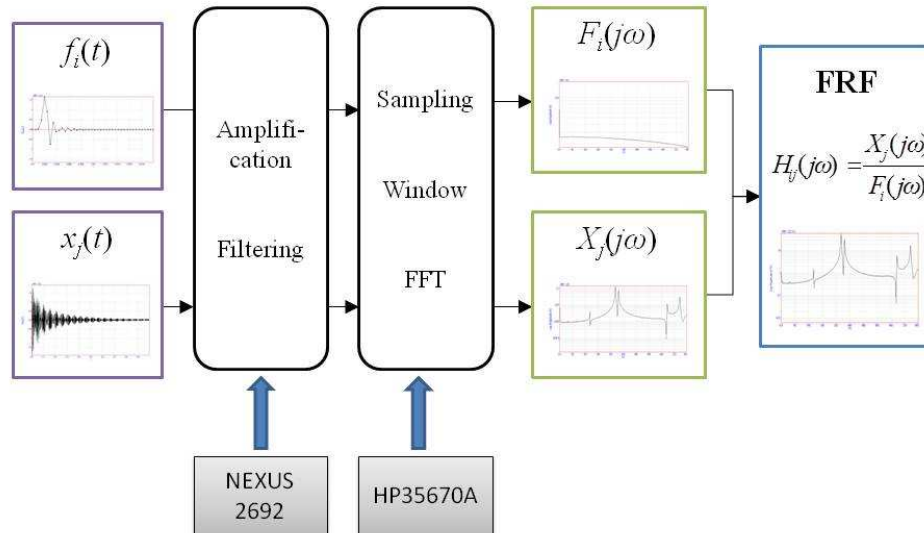


Figure 2.19 – Data handling scheme in EMA.

tion (2.4):

$$FRF = H_{ij}(j\omega) \quad (2.4)$$

where  $\omega$  is the excitation frequency (in [rad/s]). It can be seen in figure 2.19 that the FRF function plot shows local resonance peaks. Under single degree-of-freedom (SDoF) hypothesis, the  $k^{th}$  resonance peak can be assimilated to an elementary oscillator, the parametrized model of which can be expressed as:

$$H_{ij}(j\omega) \approx_{\omega \rightarrow \omega_k} \frac{\phi_i^k \phi_j^k}{(j\omega)^2 + 2\eta_k \omega_k (j\omega) + \omega_k^2} \quad (2.5)$$

where  $\phi^k$  is the  $k^{th}$  modal vector,  $\omega_k$  is the  $k^{th}$  natural frequency (in [rad/s]) and  $\eta_k$  is the  $k^{th}$  modal damping factor, all corresponding to the  $k^{th}$  mode. The superposition

principle allows building the complete parametrized FRF function as:

$$H_{ij}(j\omega) = \sum_{k=1}^n \frac{\phi_i^k \phi_j^k}{(j\omega)^2 + 2\eta_k \omega_k(j\omega) + \omega_k^2} \quad (2.6)$$

where  $n$  in this case is the number of vibrational modes taken into account. The global vibration behaviour of the structure can be perceived as the linear combination of independent, single mass, fundamental oscillators. From the structural identification point of view, the most important value is  $\omega_k$ , given the fundamental relationship between the elastic properties and the natural frequencies.

Commercial software, such as ME-Scope VES®, carry out the data treatment of multiple FRFs simultaneously. ME-Scope is a modal analysis program developed by Vibrant Technology Inc (Scotts Valley, CA, USA), which focuses in modal extraction by EMA. It allows obtaining parametric models using a least square method applied to the FRF and time-domain counterpart, respectively. The extraction methods in ME-Scope VES are based on the theory developed originally by [Richardson and Formenti, 1982] and improved on the following years.

Insisting on the case of the impact hammer/accelerometer EMA, the modal model of a structure needs then the creation of an "experimental mesh", as shown in figure 2.18, *ie* a mesh of points to be used as supports for defining the input-output locations and later the mode shapes. With exception of the C-series, all the samples and demonstrators were modelled using a 15-point mesh ( $5 \times 3$ ). Given its geometry, the C-series samples were given only a 10 point mesh ( $5 \times 2$ ). FRF spectra were obtained by hitting each one of the points. Depending on the number of sensors, the number of available FRFs at the end of the measure would be 15, 30 or 45, depending on the number of sensors. The extraction of the natural frequencies in ME-Scope was then later carried out by averaging all the available FRFs. Sometimes, in order to estimate some statistical parameters like the standard deviation, these FRFs could be split in groups, and the averaging with ME-Scope would happen inside the group. This method in particular showed to be very accurate and less vulnerable to random errors (always less than 1% percent on natural frequency extraction).

The acquisition aspects mentioned here are similar for other hardware combinations, notably in the case of loud-speaker/interferometer EMA.

### Operational Modal Analysis

The principles behind OMA (also called Output-only Modal Analysis) are detailed in chapter 7. Basically, the main difference with respect to EMA is the absence of a measured excitation signal. In this case, FRFs cannot be properly identified. However, it can be demonstrated that all the necessary information can be extracted from input signals, as long as the non-correlation hypothesis (noise) about the nature of the input excitation signal is assumed and verified in practice. OMA has its origins in civil engineering, where the dynamic behaviour of very large structures needs to be investigated. In these cases, an artificial excitation is difficult and often impossible. Since then, the OMA techniques have evolved in order to apply it to a broader range of fields, especially in mechanical engineering.

It is important to mention that, as in the case of EMA, there is not a unique OMA technique. Two family of methods can be distinguished:

1. Time-domain methods: typically OMA methods of this family try to fit a mathematical model directly from (discrete) temporal data.
2. Frequency-domain methods: this family of OMA methods uses heavily the concept of Fourier transform (in particular the discrete variant) and the power spectral density (PSD) matrices to obtain the desired information. The advantage of this kind of methods is the possibility to obtain directly the desired qualities, namely the natural frequencies and the vibration mode shapes. The Frequency Domain Decomposition (FDD) and its subsequent improvements will be described in further chapters.

There is an obvious advantage of OMA over EMA from the operational point of view, since only input signals are necessary: less energy and equipment are needed, which makes it ideal for SHM.

#### **2.3.2 Numerical-experimental identification of elastic properties from natural frequencies and vibration modes**

The mixed numerical-experimental identification algorithm is based on the method proposed by [Cugnoni et al., 2007], and is also a cornerstone in the ageing monitoring method.

The relationship between rigidity and natural frequencies is a consequence of the wave equation and the Hooke's law. Indeed, linear elasticity is adopted as the constitutive law in this thesis, since the ageing evaluation is based on the tracking of elastic properties and vibration occurs in the frame of small displacements. As shown in figure 2.20, the algorithm uses a finite element model of the structure as a base to

propose an objective function.

### FE model

As a general description, the identification algorithm uses an FE model with structured meshes (in general, although in some cases other mesh generation methods are more suitable) with 20-node solid hexahedral elements were used. All the simulations were run exclusively using the ABAQUS FE software.

The rigidity and inertia matrices are based on quadratic polynomials, using the reduced integration technique to obtain the former. In the case of both UD and CP rectangular plates (C- to J-series) are modeled by assuming an equivalent homogeneous orthotropic elasticity model. The remaining parameters have been assumed as constant and as indicated in table 2.1. The FE of the plates included one C3D20R element (in ABAQUS language, this is a 20-node solid element with reduced integration) across the thickness. The boundary conditions were fully-free, and the Lanczos solver was used.

### Objective function

In the first version, used in most cases in this thesis, only the natural frequencies are used to constitute the objective function:

$$\epsilon = |\epsilon_f| \quad (2.7)$$

where  $\epsilon_f$  is the frequency error vector the components of which are given by:

$$\epsilon_{f,i} = \frac{f_{i,FE} - f_{i,Exp}}{f_{i,Exp}} \quad (2.8)$$

This approach is simple and allows fast calculations. However, the numerical/experimental pairing between frequencies assumes no order swapping due to ageing. This hypothesis is realistic and appropriate in cases like the rectangular plates described above, mainly because of the clear spectral separation between resonance peaks. In full scale structures, this is not usually the case, since the spectral separation can eventually be of some [Hz]. In this case, a more exhaustive identification criterion and a more elaborate objective function are necessary, and this will be described further in subsection 8.3.5.



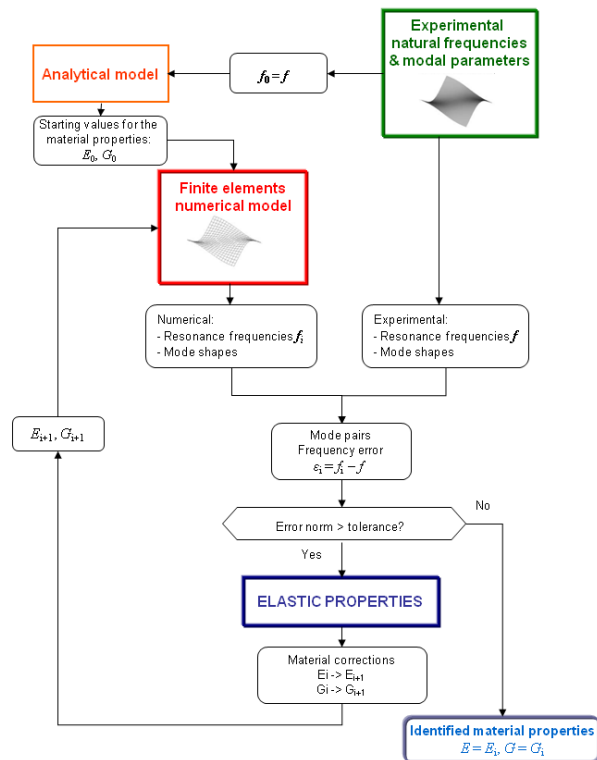


Figure 2.20 – Flow chart representing the mixed-numerical identification algorithm based on the comparison between simulated and measured natural frequencies.

It is important to point out that the presence of accelerometers and piezoelectric sensors has been simulated as well, their mass being added to the FE model as a punctual mass. However, the influence in the dynamic modelling is negligible at the studied frequencies (see appendix A).

### 2.3.3 Sensitivity analysis and propagation of uncertainty

In a multivariate mathematical model, the notion of sensitivity can be defined by the "amount of influence" that the independent variables have on the dependent ones. Around a certain state point, this is usually defined and expressed as a quotient between the (small) variation of the independent variable and the consequent variation in the dependent one.

For example, the value of the natural vibration frequencies in a composite structure depend on the stiffness. Depending on the vibration mode, a given natural frequency can be more influenced by a given elastic modulus than the others. This sensitivity

parameter is mathematically defined as:

$$S_{f,E} = \frac{\Delta_E f / f}{\Delta E / E} \approx \frac{\partial f}{\partial E} \frac{E}{f} \quad (2.9)$$

where  $f$  denotes a particular natural frequency and  $E$  an elastic modulus, and  $\Delta_E$  is the variation of  $f$  due to  $E$ . The  $\Delta$ -variations are divided by the nominal values in order to get rid of dimensional ambiguity, proposing a non-dimensional sensitivity factor. For example, in the case of the analytical formulae in subsection 1.2.5, the sensitivity can be estimated as follows:

$$S_{f,E} \approx \frac{\partial f_{bend}}{\partial E} \frac{E}{f_{bend}} = 0.5 \quad (2.10)$$

for bending modes, and

$$S_{f,G} \approx \frac{\partial f_{tors}}{\partial G} \frac{G}{f_{tors}} = 0.5 \quad (2.11)$$

for torsional modes. Concerning composite layups, this estimation becomes a much more complex problem. An FE model can be useful in that case, since it is possible to compute multiple sensitivity quotients (for several frequencies) when slightly varying the elastic parameters of the model.

Consider the example of the manufactured UD plates of the D-series mentioned in section 2.2. These samples were modelled assuming a homogeneous orthotropic elasticity model. In figure 2.21, it can be seen that the basic vibration modes of the series samples depend essentially on two tensile moduli ( $E_1$  and  $E_2$ ) and one shear modulus ( $G_{12}$ ). The other six mechanical variables  $E_3$ ,  $\nu_{12}$ ,  $\nu_{13}$ ,  $\nu_{23}$ ,  $G_{13}$  and  $G_{23}$  have a limited and negligible influence in the determination of the vibration modes and natural frequencies. Thus, it is not necessary to include in the variable vector all of the nine independent engineering constants that determine the elastic behaviour of an orthotropic material, in the case of thin shells. Further in chapter 8, another sensitivity analysis concerning the demonstrators K, L and M is carried out for those specific cases.

There is a double purpose of the sensitivity analysis. On one hand, it allows the selection of the most influential elastic moduli on the dynamic behaviour of the composite samples. This is essential in order to reduce the number of necessary computations in the identification algorithm since instead of investigating all the elastic properties,

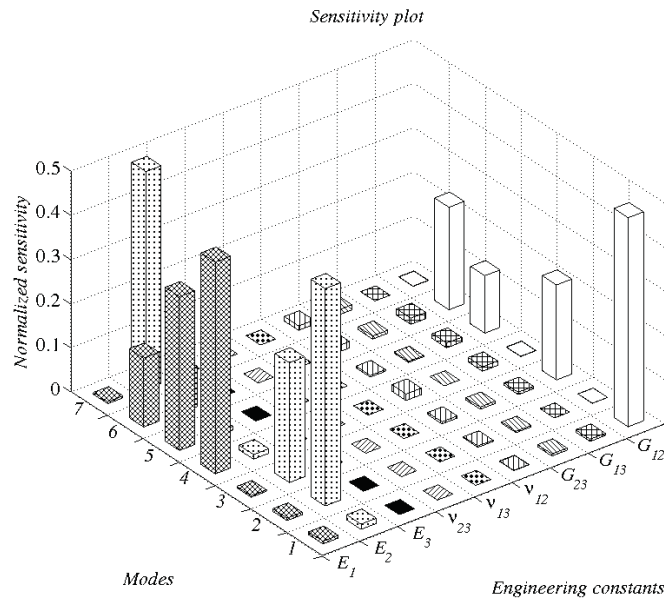


Figure 2.21 – Example of sensitivity analysis between engineering constants and natural frequencies for a D-series sample. The latter are mainly influenced by the longitudinal and transverse tensile moduli  $E_1$  and  $E_2$ , and the transverse shear modulus  $G_{12}$ .

only a reduced number (in the case of the plates three) of factors are considered.

The other application is the uncertainty propagation analysis. Indeed, the uncertainty in the experimental measurements of the frequencies is propagated, through the identification process, to the estimation of the elastic properties of the structure.

Again, the uncertainty can be somehow estimated on the standard basis. According to [Ku, 1966], the standard deviation of a dependent variable can be computed from the standard deviation of all its independent variables through the sensitivity factors  $S$ :

$$\sigma_E^2 = \sigma_{f_1}^2 S_{E,f_1}^2 + \dots + \sigma_{f_n}^2 S_{E,f_n}^2 \quad (2.12)$$

where  $E$  denotes the identified modulus,  $f_1, f_2, \dots, f_n$  denote the  $n$  considered frequencies. It is important to note that  $S_{E,f_i} = 1/S_{f_i,E}$ , since the sensitivity quotient can be inverted. This formulation is useful in the estimation of experimental uncertainty around the identified values of elastic properties and the corresponding statistical analysis of the ageing.



# 3 Weathering and accelerated ageing protocols for composite structures

## 3.1 Motivation and state-of-the-art

The creation of an ageing model is a key part for the success of the whole monitoring process. Indeed, the ageing characterization of a given material allows estimating beforehand its future evolution and decide if the structural safety is compromised. However, it is very important to fix some standards to the laboratory-scheduled ageing process for many fundamental reasons, in particular in order to link the accelerated, artificial process to "real-life", *in situ*, natural ageing (or weathering as it is called by some authors) of full-scale structures during their service lifetime.

As it was introduced in chapter 2, written documentation comparing accelerated ageing opposite to real ageing includes experimental results and analyses carried out by several authors in the last decade [Mouzakis et al., 2008, Fox et al., 2004, Dao et al., 2007, Tian and Hodgkin, 2010], of which a summary table has been established in table 3.1. In these papers, several ageing mechanisms have been reported: water diffusion, polymer molecules cross-linking/de-linking, alternate dilatation/contraction cycles, photo-oxidation, post-curing, residual stress, temperature gradients, and many others. There are several aspects of composite ageing that this bibliographic research of the current knowledge points out:

1. The cyclic nature of real ageing needs to be included, specified and quantified in the accelerated ageing protocol. Intuitively, cyclic accelerated ageing can be compared to high-cycle fatigue tests, that evaluate structural health based on the number of cycles necessary to break a sample under a given stress. As well as for fatigue, it is expected to establish a statistical mathematical model.
2. Concerning the weathering agents to be taken into account, most papers report effects coming from three main agents: (relatively) high temperatures, moisture and UV radiation, which composite airframes are commonly confronted to.
3. The working temperature range goes from room temperature up to 250 [° C] in

## **Chapter 3. Weathering and accelerated ageing protocols for composite structures**

---

some cases. It can be pointed out that the top temperatures are adapted to the subject material, more specifically to two characteristic temperatures: the start of the glass transition zone  $T_{glass}$  and the end of transition zone  $T_{rubber}$ , where the material exhibits a rubber-like behaviour. It has been suggested [Fox et al., 2004, Dao et al., 2007] that most of the ageing amount occurs between these two temperatures.

4. "Accelerated ageing" has effectively shown equivalent loss of macro-mechanical degradation when compared to "real ageing". For example, epoxy CFRP laboratory samples made of the same material as parts for a B737, showed similar ageing degradation after 3000 one-hour cycles of artificial ageing at high temperature, as did epoxy CFRP parts after 58000 h ( $\sim$  20000 cycles) of B737 operating service.
5. Relevant ASTM standards are frequently quoted concerning the experimental frame the sample should be tested in. Among these, can be mentioned notably: D4762, C581, D1151, D5229, G151 and G154.
6. The experimental conditions obviously depend on the technical limits of the research facilities.
7. Expected loss in mechanical properties (stiffness [Mouzakis et al., 2008], strength [Tian and Hodgkin, 2010, Fox et al., 2004]) ranges roughly between 10% and 15% at maximum degradation.

All of these points are taken into account in the final part of this chapter, when an accelerated ageing protocol for the future testing is designed.

### **3.2 Preliminary ageing protocols**

As it was stated in the introduction, the measure of the mass is an important proportionality factor between the stiffness and the natural vibration frequencies of a structure. This is why this can represent an important source of error if any eventual mass evolution is not taken into account during the monitoring. Since a relatively low change in the mechanical properties ( $\sim$  10%) is expected, it is then of prime interest to include the weighing in the ageing model. This also means that an absorption model is needed for the monitoring and identification of elastic properties from modal data.

Among the mentioned weathering agents to be considered in the accelerated ageing protocol, water absorption is expected to be the primary cause for mass change. Indeed, besides some potential volatile residual organic molecules from the curing process (which have a negligible mass, as it will be shown in chapter 4), air and water are the only massively present fluids in the experimental environment of the climatic chamber. Thus, in the case of humid protocols, the principal source of mass changes to be considered is by moisture absorption.

### 3.2. Preliminary ageing protocols

Table 3.1 – Summary of the selected papers addressing the artificial ageing problem and its pertinence with respect to real-time ageing in aerospace applications.

Aspect	GFRPC	Epoxy TGDDM/DDS BMS-8-212	Epoxy TGDDM/T-GAP/DICY M20/IM7
Articles mentioning the material	Mouzakis, Zoga, "Accelerated environmental ageing study of GFRPC"	Hodgkin, Tian, "Long-term ageing in a commercial aerospace composite sample: Chemical and physical changes"	Dao, Hodgkin, "Accelerated ageing vs realistic ageing in Aerospace applications"
Ageing mechanisms	Preconditioning: 50 %RH at 23°C. Conditioning: UVB, 4h cycles about (50%-98%) RH and (50°C-60°C) up to 1008h	Real: ~58000 h in flight Accelerated: 3000 h at average 120°C Accelerated : 7500 h at 70°C, 45%, 65%, 85% RH	Isothermal: at 70°C, 120°C, 170°C and 200°C, until 7500 h. Spiking: 45%, 65%, 85% RH at 70°C, spiking 90°C, 120°C and 160°C up to 7500 h
Tests performed	DMA, 3PB, SEM	DMA, FTIR	DMA, FTIR, Weight, DSC
Results summary	1. Stiffening of the material is the main ageing process. 2. Micro-cracking at surface. 3. Water absorption → mass increment/weakening.	1. Normal ageing mostly surface effects. 2. Accelerated ageing: $T_{glass}$ goes down at core, goes up at surface.	1. Greater chemical corrosion at high temperature. 2. Surface micro-cracking.
Glass transition temperature	100°C ± 40 °C [60°C, 140°C]; peak at 130°C	~190°C ± 70 °C [120°C, 260°C]; peak at 230°C	165°C ± 95 °C [60°C, 25°C]; peak at 160° C - 200°C
Aspect	Pure Polyester	CSIRO CBR 320/328	Matrimid CIBA GEIGY
Articles mentioning the material	Mouzakis, Zoga, "Accelerated environmental ageing study of GFRPC"	Fox, Lowe, "Investigation of failure in aged aerospace composites"	Fox, Lowe, "Investigation of failure in aged aerospace composites"
Ageing mechanisms	Preconditioning: 50 %RH at 23°C. Conditioning: UVB, 4h cycles about (50%-98%) RH and (50°C-60°C) up to 1008h	Isothermal: 204°C and 250°C, up to 30 weeks	Isothermal: 204°C and 250°C, up to 30 weeks
Tests performed	DMA, 3PB, SEM	DCB, FTIR, Raman spect	DCB, FTIR, Raman spect
Results summary	1. Stiffening of the material is the main ageing process. 2. Micro-cracking at surface. 3. Water absorption → mass increment/strengthening.	1. Rapid surface degradation. 2. Core degradation is more gradual. 3. Degradation path is different with the temperature.	1. Rapid surface degradation. 2. Core degradation is more gradual. 3. Degradation path is different with the temperature.
Glass transition temperature	~70°C ± 30 °C [40°C, 100°C] ~peak at 100°C	~225°C ± 25 °C [200°C, 250°C]	~225°C ± 25 °C [200°C, 250°C]

DMA = Dynamic mechanical analysis.  
3PB = 3-point bending.  
SEM = Scanning electron microscope.  
FTIR = Fourier transform infrared spectroscopy.  
DSC = Differential scanning calorimetry.  
DCB = Double cantilever beam.

## **Chapter 3. Weathering and accelerated ageing protocols for composite structures**

Water diffusion can be modelled using a few parameters, like the material's water diffusion coefficient and saturation mass, or the relative humidity  $RH$  of the ageing environment. The former are usually given in the supplier's data sheet, but can depend strongly on the curing process. In order to characterize correctly the used structural material and to avoid systematic experimental errors, it is advised to carry out preliminary tests. As it will be shown in chapter 4, this short characterization is useful and necessary.

### **3.2.1 Isothermal diffusion in CFRP**

As mentioned above, epoxy CFRP are increasingly being used in the aeronautics and aerospace industries. The subject material is the CFRP introduced in section 2.2, supplied by Suter-Kunststoffe© AG (Switzerland).

To simplify the material characterization process (at least as a first approach), beam-like plates (roughly  $300 \times 40 \times 4$  [mm<sup>3</sup>]) were manufactured. Two sets of plates were produced: cross-ply (CP) named Aa-series samples, and unidirectional (UD) named Bb-series samples. Both series were manufactured using exactly the same curing process: vacuum curing at 70 [°C]/10h, followed by curing at 80[°C]/8h.

Table 3.2 – Nominal geometric dimensions and initial mass of plates.

	Aa-series	Bb-series
Length [mm]	$300 \pm 1$	$300 \pm 1$
Width [mm]	$39.0 \pm 0.1$	$38.5 \pm 0.1$
Thickness [mm]	$4.0 \pm 0.1$	$4.0 \pm 0.1$
Initial mass [g]	$68.10 \pm 0.01$	$64.00 \pm 0.01$
Number of specimens	6	6
Groupe 1 (60 [°C])	2	2
Groupe 2 (80 [°C])	2	2
Groupe 3 (100 [°C])	2	2

As mentioned above, the first experimental campaign had the following characteristics:

- Isothermal exposition to three different temperatures (both Aa- and Bb- series are reorganized in three groups, see table 3.2).
- Total duration: 1000 hours ( $\sim 6$  weeks).
- Mass measurements at  $\sim 168$ -hours intervals (once per week).

The constitution of mixed groups of samples Aa and Bb is justified by the following hypothesis: the properties are uniform through the thickness. Even if this is not strictly true in the case of cross-ply plates (like Aa-series samples), the results showed in figure 3.1 show an agreement with the diffusion theory. With this protocol, it was expected to observe mainly a rapid rise of the mass due to water absorption. The reasons



for this type of ageing protocol are justified in the following section. The experimental results have been published in [Guzman et al., 2012] and are shown in figure 3.1. The Aa- and Bb- samples were subjected to ageing protocols in steady-state isothermal conditions with constant  $RH \approx 95\%$ , at 60 [°C], 80 [°C] and 100 [°C]. In these graphs,  $M(t)$  symbolizes the water concentration ratio, expressed in percent, as the quotient between the absorbed water mass and the initial mass of the sample. As expected, the absorption shows an exponentially asymptotic pattern. As it will be detailed in the section 3.2.2, the diffusion theory inside infinite thin plates, provides an accurate shape, proposes two diffusion parameters and justifies by the way this assumption. Furthermore, it can be pointed out that there is very little difference between diffusion in CP and UD lay-ups.

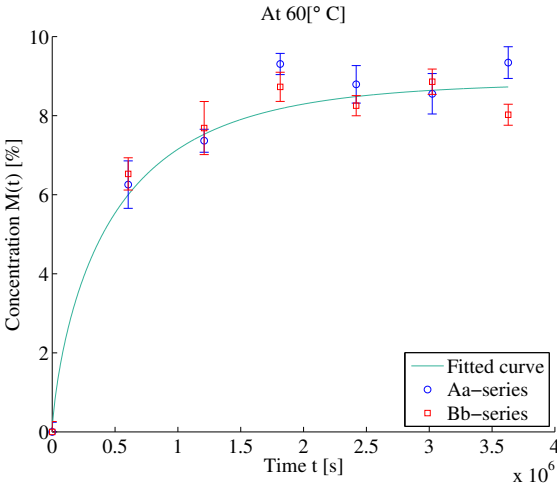
### 3.2.2 A model for water diffusion in isothermal conditions

Water absorption is possible only in the presence of some humidity in the surrounding atmosphere ( $RH \neq 0\%$ ). This can be attributed to evaporation of phenols (or other volatile components remaining unreacted from the curing process), but also due to evaporation of thermal oxidation and photo-oxidation products. Because of this double trend, it is legitimate to suppose that in the case of humid protocols, besides water absorption there is at the same time evaporation of some components. This apparent loss of mass due to the evaporation of these marginal phenols is much smaller than the gain, for equivalent "dry" protocols. Thus, to simplify the calculation, the following hypotheses are going to be adopted: the water absorption and the evaporation of phenols and oxides are independent from each other (no chemical influence between inbound/outbound species), and the surface moisture evaporation of phenols is neglected.

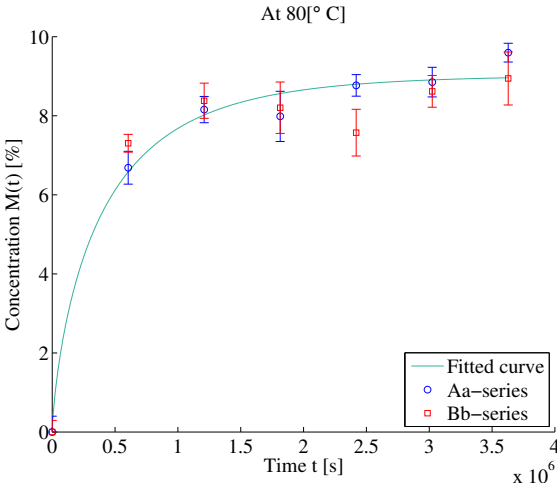
Concerning the water absorption, a simple mathematical reasoning can be adopted in order to estimate the water concentration absorbed by a sample when subjected to accelerated ageing conditions. This amount is generally not equal for periodic or isothermal conditions. The mathematical approach to model the water absorption comes from Fick's law of diffusion in combination with the mass conservation principle, as expressed in the following equation

$$\frac{\partial c}{\partial t} = \frac{\partial}{\partial x} \left( D \frac{\partial c}{\partial x} \right) \quad (3.1)$$

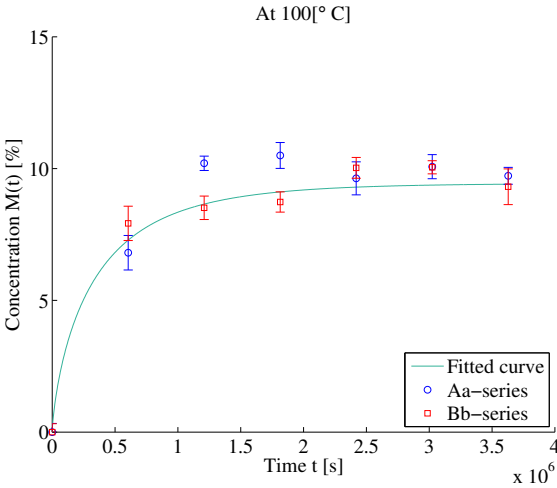
where  $c$  is the volume concentration,  $D$  represents the diffusion coefficient (sometimes called diffusivity),  $t$  is the time coordinate and  $x$  is the space coordinate along the thickness.



(a)



(b)



(c)

Figure 3.1 – Experimental results of sample weighing, for isothermal exposure at (a) 60 [°C], (b) 80 [°C] and (c) 100 [°C].

### 3.2. Preliminary ageing protocols

Under the hypothesis of absence of swelling, the volume concentration  $c$  (no units) is proportional to the water mass concentration ratio  $M$  (no units). This case can be assimilated to an infinite plate with thickness  $h$  with two exposed boundary conditions (since  $l \gg h$  and  $w \gg h$ ). The solution of equation (3.1) in such conditions is obtained by application of the Fourier's series theory, giving the following result

$$\frac{M(t)}{M_s} = 1 - \frac{8}{\pi^2} \sum_{k=0}^{\infty} \frac{1}{(2k+1)^2} \exp\left(-\frac{(2k+1)^2 \pi^2 D t}{h^2}\right) \quad (3.2)$$

where  $M_s$  is the saturation mass concentration. However, this expression is complicated, and a simpler function can be used to approximate it

$$\frac{M(t)}{M_s} \approx 1 - \exp\left(-1.31 \left(\frac{\pi^2 D t}{h^2}\right)^{0.75}\right) = 1 - \exp\left(-1.31 \left(\frac{t}{\tau}\right)^{0.75}\right) = \Theta\left(\frac{t}{\tau}\right) \quad (3.3)$$

where  $\tau = h^2/(\pi^2 D)$  is a time constant for this specific exponential growth and  $\Theta$  symbolises a function. It is assumed that diffusivity depends on temperature following an Arrhenius-type law:

$$D = D_0 e^{-\frac{E_D}{RT}} \quad (3.4)$$

$$\ln(D) = \ln(D_0) - \frac{E_D}{RT} \quad (3.5)$$

where  $D_0$  is the diffusion coefficient when  $T \rightarrow \infty$ ,  $E_D$  is the diffusion activation energy and  $R$  is the universal gas constant. Similarly, the saturation mass  $M_s$  depends exponentially on the inverse of the temperature by the equation (3.6)

$$M_s = M_{s0} e^{-\frac{E_S}{RT}} \quad (3.6)$$

$$\ln(M_s) = \ln(M_{s0}) - \frac{E_S}{RT} \quad (3.7)$$

where  $M_{s0}$  is the saturation mass when  $T \rightarrow \infty$  and  $E_S$  is the corresponding diffusion activation energy. Concerning the influence of the relative humidity  $RH$  on the saturation mass, it has been proposed by some authors [Weitsman, 2012, Crank, 1989, Lin and Chen, 2005] that a power law model can be used to determine the relation

## Chapter 3. Weathering and accelerated ageing protocols for composite structures

between both

$$M_s = M_{s_{max}}(RH)^\zeta \quad (3.8)$$

where  $\zeta$  is an exponent depending on the temperature and the absorbing composite and  $M_{s_{max}}$  is the maximum saturation mass possible. After [Weitsman, 2012], in the case of an epoxy matrix, this value of  $\zeta$  is 1 in the current temperature range, so this hypothesis is adopted in this thesis.

The thermodynamic constants  $D_0$ ,  $E_D$ ,  $E_S$ ,  $M_{s0}$  defined in equations (3.4), (3.5), (3.6) and (3.7) can be estimated experimentally by a regression, if datasets of measured  $(T, M_s)$  and  $(T, D)$  are available (see figure 3.2). This regression becomes linear (and more accurate) if  $(1/T, \ln M_s)$  and  $(1/T, \ln D)$  are considered instead.

The experimental data obtained in subsection 3.2.1 can provide three  $(T, M_s)$  and  $(T, D)$  pairs, corresponding to the isothermal ageing protocols at 60 [°C], 80 [°C] and 100 [°C]. Indeed, using a non-linear least square algorithm (a negative exponential model as in equation (3.3)), the corresponding  $D$  and  $M_s$  can be estimated at each temperature. These estimations can be consulted in table 3.3.

From this, and supported by information in literature [Crank, 1989, Lin and Chen, 2005], the associated diffusion activation energy  $E_D = 9.067$  [kJ/mol], and the saturation enthalpy  $E_S = 1.68$  [kJ/mol] can be deduced in a range of temperature between 5[°C] and 135[°C]. With these two linear models, it is possible to estimate quite accurately the diffusion and the saturation mass in isothermal conditions.

Table 3.3 – Computed diffusion coefficients in preliminary tests with test series A and B.

Temperature		Diffusion	Saturation mass
$T$ [°C]	$T$ [K]	$D$ [mm <sup>2</sup> /s]	$M_s$ [%]
60	333	2.21e-7	8.84
80	353	2.67e-7	9.02
100	373	3.14e-7	9.44

The results of this preliminary isothermal ageing will be used extensively in chapter 4, in particular in section 4.4. Indeed, "equivalent" cyclic diffusion parameters will be defined, in order to quantify the water diffusion as functions of the number of cycles instead of time.

### 3.3 Design of the accelerated ageing protocols

As stated in the introduction and in section 3.1, in order to reveal any changes in stiffness due to exposition to relatively aggressive ageing factors, a multi-stage exper-

### 3.3. Design of the accelerated ageing protocols

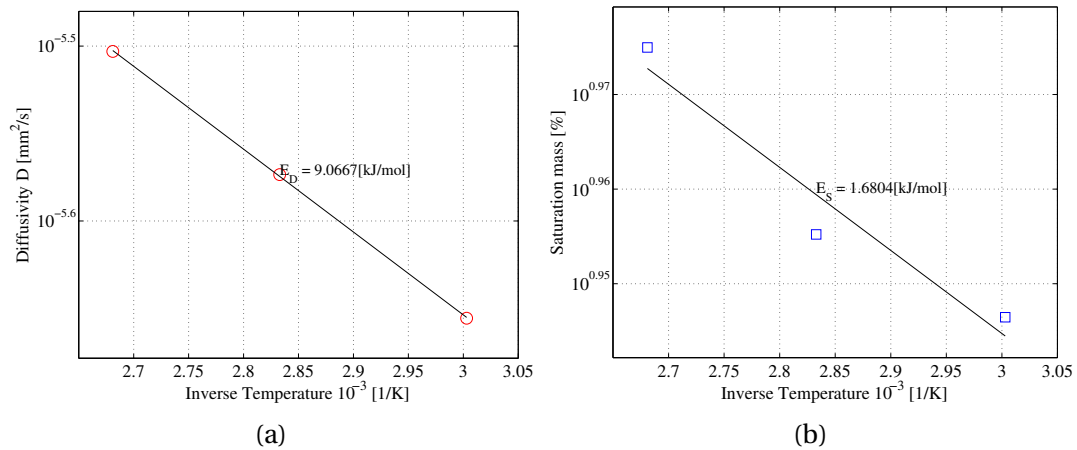


Figure 3.2 – Graphs of linear regressions ( $1/T, \ln M_s$ ) and ( $1/T, \ln D$ ) as in equations (3.5) and (3.7) for measured values of Aa- and Bb-series. The slopes give respectively the values of  $E_D$  and  $E_S$ .

imental campaign should take place.

Taking into consideration the points in section 3.1, it has been decided that the ageing factors have to include temperature, relative humidity and ultraviolet (UV) radiation, as they are frequently met by full-scale CFRP aeronautical structures during a life cycle. The ageing protocols were inspired from past works previously mentioned [Mouzakis et al., 2008, Dao et al., 2007, Fox et al., 2004, Bondzic et al., 2006]. The following ASTM standards were taken into account for the experimentation guidelines: D4762 for cyclic ageing protocols, C581, D1151 and D5229 for the combined hygro-thermal testing, and G151 and G154 for UV radiation testing.

The chosen ageing factors, whether these are alone or combined, have several effects on polymer-based parts inside long-time operating aircraft and rotorcraft. In summary, a proposed ageing protocol should integrate the following characteristics:

1. Cyclic conditions are more likely to induce damage at molecular and macroscopic levels than isothermal conditions. Dilatation/contraction cycles induce thermo-mechanical fatigue, probably leading to matrix cracking and fibre pull-out (this has not been verified explicitly since the surveillance method is supposed to be macroscopic, global and non-destructive). Moreover, this is far closer to reality since aerospace components are constantly exposed to cyclic environments (ground/air, daytime/night-time state).
2. Temperature peaks are usually fixed slightly above the starting point of the glass transition zone, which is usually measured by some material tests such as the dynamic mechanical analysis (DMA) or the Fourier transform infra-red spectroscopy (FTIR). In the experiments run for this thesis, this range of tempera-

## Chapter 3. Weathering and accelerated ageing protocols for composite structures

tures was estimated from the supplier's data sheet and after the corresponding curing process (the theoretical curing rate is in all cases superior to 99%). Physically, dilatation, vitreous transition and thermal oxidation are likely to occur at elevated temperature.

3. Highly humid environments can contribute to composite ageing as well, facilitating fibre debonding, delamination, embrittlement, polymer chemical weakening, inner stressing, etc. The mass absorption is to be verified by weighing periodically the total mass of the samples, in order to evaluate the diffusion coefficient.
4. High UV radiation is generally more specific to structures continuously dwelling at high altitudes, leading to photo-oxidation and polymer chain dissociation, among others.

Thus, it has been decided that the specimens would be subjected to cyclic environments, with the following factors controlled: the surrounding temperature ( $T$ ), the relative humidity ( $RH$ ) and the intensity of an A-class ultraviolet radiation ( $UV$ ) lamp on one face of the plate samples. Due to technical reasons, humidity takes longer to be controlled, and cycles are longer for the humid protocols. The scheduled campaigns and the series, with the respective codes and samples included, the protocol parameters and the durations are summarized in table 3.4. Hardware included the Weiss Technik®WK180/40 climatic chamber, with the required control and data acquisition software.

### 3.3.1 Justification of a factorial experiment

As stated in the introduction and in chapter 2, the survey of elastic properties is justified as a mean to evaluate the health status of a structure. From a mathematical perspective, ageing can be viewed as the relative degradation of these constitutive properties, which would be a function of a non-dimensional time unit. Thus, this time unit can be the number of ageing cycles, and the degradation of the elastic properties is measured by the changes of the current values with respect to their initial values. An ageing model could globally be expressed as

$$y = \frac{Y}{Y_0} = f(g(T, RH, UV); n) \quad (3.9)$$

where  $y$  is the measured degradation, which is a composed function  $f$ , which in turn depends of a set of ageing parameters  $T, RH, UV$  and on the number of cycles  $n$ .  $Y$  and  $Y_0$  denote respectively the current and the initial value (in absolute units) of the target elastic property. For example, the longitudinal Young's modulus is denoted  $E_1$ ,

### 3.3. Design of the accelerated ageing protocols

its initial value  $E_{10}$  and the relative degradation  $\epsilon_1 = \frac{E_1}{E_{10}}$ . The function  $g$  depends then exclusively on the experimentation conditions. The most simple approach to define this function is suggested by the Design of Experiments (DoE) theory. A  $2^3$  factorial (or full-factorial) experiment making vary this three parameters allows establishing a prediction model. This is the reason of the 8 different manufactured series introduced in chapter 2. Each series is subjected to one of eight possible combinations of parameters.

In order to set up such a mathematical model, it is suggested to normalize the ageing parameters. For a real factor  $u$  (that can be either  $T$ ,  $RH$  or  $UV$ ), the corresponding normalized factor  $x$  is given by

$$x = \frac{u - u_{min}}{u_{max} - u_{min}} \quad (3.10)$$

where  $u_{min}$  and  $u_{max}$  are respectively the minimum and maximum value adopted by  $u$ . Thus, the value of  $x$  is always between 0 and 1, inclusively. The results of the normalization are given in table 4.1. The normalized temperature is given by  $x_1$ , the normalized relative humidity is given by  $x_2$  and the normalized UV radiation is given by  $x_3$ . To complete the overview of the whole set of ageing protocols, the number of cycles and the time parameters: the low temperature period  $\Delta t_-$  ("cold phase"), the high temperature period  $\Delta t_+$  ("hot phase") and the total cycle period  $\Delta t$  are given (then  $\Delta t = \Delta t_- + \Delta t_+$ ). The experimental plan and the factorial points corresponding to each series are summarized in table 3.4 and in figure 3.3. It is advised by [Box et al., 2005] to verify that the "volume" of the  $2^3$ -factorial solid (in this case not a cube exactly, but a trapezoidal prism) is not close to zero. The volume would represent the Jacobian of the linear system which the linear regression is based on.

Concerning the question about which temperature, relative humidity and UV radiation intensity are going to serve as the "real factors"  $u$ , different choices are possible. The selection is based mainly on technical and practical reasons, and the following cases can be discussed:

- $T = u_1$ : Temperature will oscillate between two values, while the amplitude of the oscillation remains constant. In the low temperature cycle ( $x_1 = 0$ ), temperature is set to oscillate in the [5°C,95°C] interval, while in the high temperature cycle ( $x_1 = 1$ ), this interval is [45°C,135°C]. It can be noticed that 95[°C] corresponds to the estimated starting point of the glass transition zone of the composite, while 135[°C] is the estimated middle point. These estimations are decided in agreement to the supplier's data sheet.
- $RH = u_2$ : Relative humidity is kept at zero (completely dry air) when  $x_2 = 0$ , and

### Chapter 3. Weathering and accelerated ageing protocols for composite structures

it oscillates between 0% and 95% when  $x_2 = 1$ . In the second case,  $RH$  and  $T$  are alternated, *ie* when  $RH = 0\%$ ,  $T$  is at its top temperature (95[°] or 135[°C] depending on the protocol) and when  $RH = 95\%$ ,  $T$  is at its bottom temperature (5[°] or 45[°C]). Exception is made for two series: EF1 and EF2 (table 3.4), since the UV lamp does not work properly above a surrounding temperature of 70 [°C] and a relative humidity of 70 %.

- $UV = u_3$ : The radiation intensity profile is similar to the  $RH$  one. For technical reasons, the working period of the UV lamp is restricted to the period of low temperatures ( $T < 70[°C]$ ) and low relative humidities ( $RH < 70\%$ ).

All these points considered, the general pattern of the control setpoints is graphically represented in figure 3.4. This profile can be programmed in the climatic chamber controller.

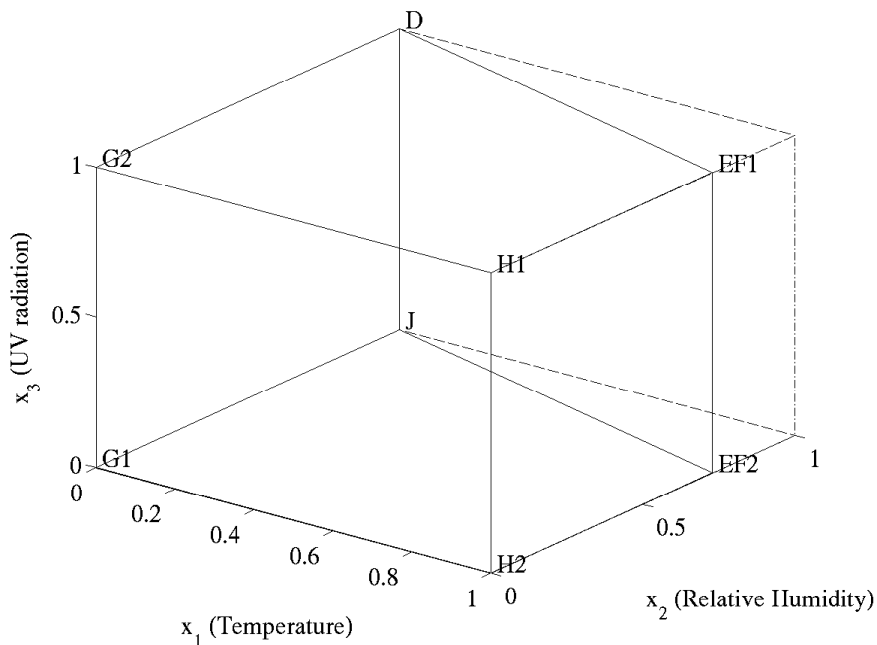


Figure 3.3 – Graphic representation of the factorial experiment in the 3D cartesian space, showing the position of the individual subject series.

#### 3.3.2 Justification of dwelling times

As discussed in chapter 2, the experimental data is periodically measured by means of EMA and OMA: the natural frequencies of the samples are measured, which in turn, by the numerical-experimental identification method, give the elastic properties  $Y$ . The variable  $y = \frac{Y}{Y_0}$  is the relative degradation,  $Y$  is the degraded elastic property and  $Y_0$  is the non-degraded, pre-ageing, initial elastic property. The detailed results and the establishment of the mathematical model proposed initially in equation (3.9) are



### 3.3. Design of the accelerated ageing protocols

Table 3.4 – Summary of ageing protocol parameters for all the series: nominal values ( $T$ ,  $RH$  and  $UV$ ), normalized values ( $x_1$ ,  $x_2$  and  $x_3$ ), the number of cycles  $N_{cyc}$ , the time period  $\Delta t = \Delta t_+ + \Delta t_-$  and the number of measurements  $q$ .

Series	Samples	Temperature			Relative humidity			UV radiation			$N_{cyc}$	$\Delta t$ [min]	$q$	$\frac{\Delta t_-}{\Delta t_+}$ (*)
		$T$ [°C]		$x_1$	$RH$ [%]		$x_2$	$UV$ [W/m <sup>2</sup> ]		$x_3$				
		Min	Max		Min	Max		Min	Max					
D	DI-DVI	5	95	0	0	95	1	0	300	1	800	90	8	2:1
EF1	EI, FI	45	135	1	0	70	0.73	0	300	1	900	90	9	1:1
EF2	EII, FII	45	135	1	0	70	0.73	0	0	0	900	90	9	1:1
G1	GI, GIII	5	95	0	0	0	0	0	0	0	1100	60	12	1:1
G2	GII	5	95	0	0	0	0	0	300	1	1000	60	11	1:1
H1	HI, HIII	45	135	1	0	0	0	0	300	1	1100	60	12	1:1
H2	HII	45	135	1	0	0	0	0	0	0	1100	60	10	1:1
J	JI-JIII	5	95	0	0	95	1	0	0	0	800	90	8	1:1

(\*)  $\Delta t_+$  is the part of the cycle at high temperature and  $\Delta t_-$  is the part at low temperature.

deeply explored and analysed in the next chapter.

After an estimation based on data provided by the supplier of the WK climatic chamber and in the literature, the thermal equilibrium due to convective transfer inside the climate chamber is reached after between 15-20 [min] (this is the time it takes to increase the temperature by 90 [°C] at a heat rate of 4.7 [°C/min]) in the range of temperature 25 [°C]-125[°C]. On the other hand, RH setpoints can be reached much faster, although a true stability is not generally reached until the temperature itself is stable.

Concerning the equilibrium inside the composite samples, the time needed depends on the thermal and the water diffusion coefficients from CFRP PrePreg supplier's data sheet. For example, the thermal equilibrium inside a  $\sim 4$ [mm]-thick specimen is estimated to take 15 [min]. On the other hand, the moisture saturation inside the same  $\sim 4$ [mm]-thick plate samples is not reached in one cycle. This is expected, after inspection of the tests carried out prior to the cyclic ageing tests (as detailed in subsection 3.2.2). However, the water concentration is accumulative, since most of the water absorbed in each cycle remains inside the structure during the “dry phase” of the cycle. At the end of the protocol, there is a significant amount of water inside the bulk body of the sample (as shown in section 4.4). Concerning the penetration of UV radiation, the same problem can be observed. After the information available in the literature, the equilibrium of radiant heat on plates by UV radiation (340 [nm] wavelength, 0.35 [W/m<sup>2</sup>/nm] intensity, as recommended by the G155 ASTM standard, corresponding to a direct sunlight beam at sea level and 0° latitude) is estimated to take about 20 [min]. This time period is less than any of the periodic exposure times faced in the protocols (the shortest is 1800 [s] = 30 [min]). To summarize:

- The total dwelling time to reach the thermal equilibrium in the middle of the sample is around 30 [min] after the start of the temperature change.
- Radiative equilibrium is reached after 20 [min]. This does not constitute then a design limitation factor.
- Moisture equilibrium is not reached in one cycle inside the sample, and is only fairly

### **Chapter 3. Weathering and accelerated ageing protocols for composite structures**

stabilized in the chamber after the 30[min] (this 30 [min] correspond to the heating/cooling phase). For humid protocols, it was decided to add a supplement of 15 [min] to the "wet phase", in order to make sure the sample dwells during this time to a nearly stabilized RH (which makes a total of 45 [min]).

- The search of the equilibrium point takes place twice in a cycle (one when heating up and one when cooling down). Thus, 60 [min] is fixed as the total cyclic period for the protocols with no moisture, and 90 [min] for the protocols with programmed moisture absorption.

In chapter 8, the ageing protocols are similar to those described in this chapter, which are applied on the demonstrators. The objective is to validate the development of the ageing model.

### 3.3. Design of the accelerated ageing protocols

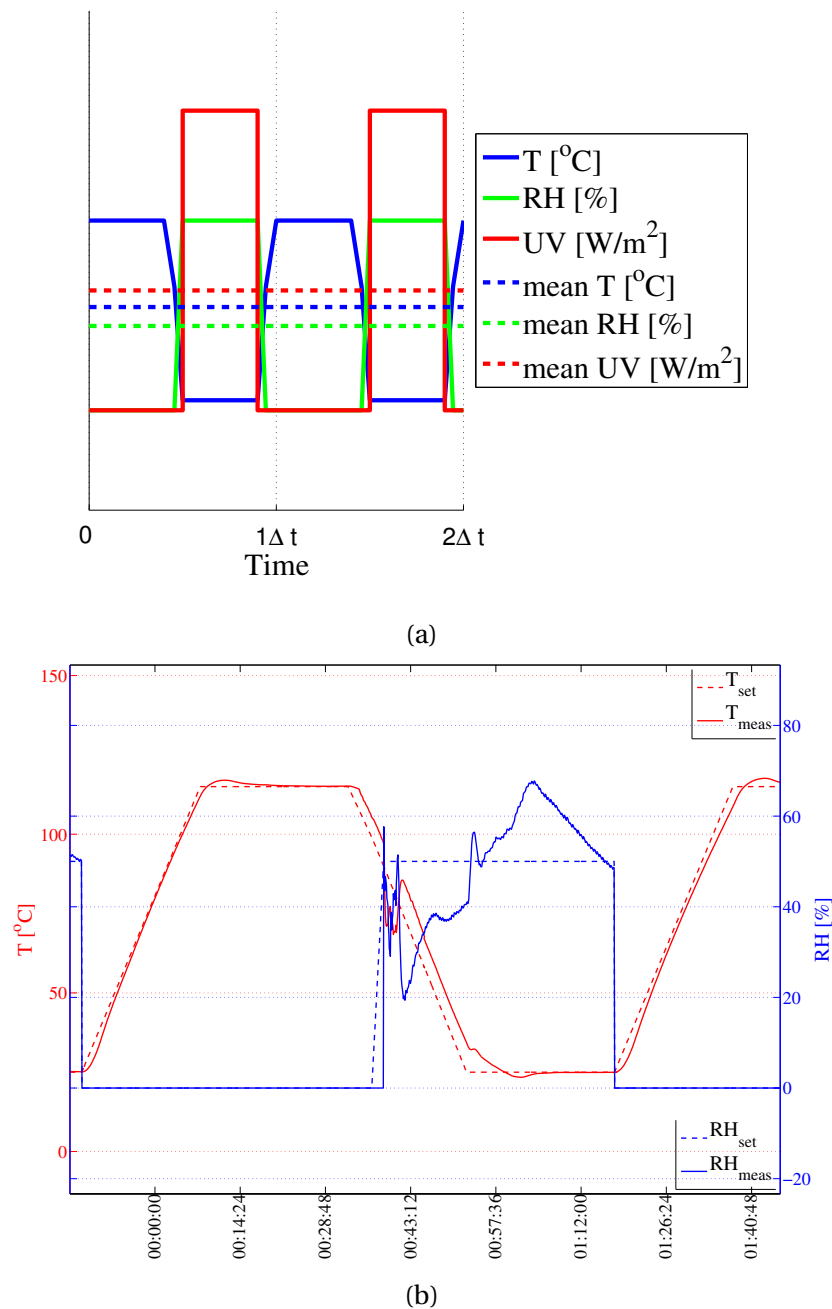


Figure 3.4 – (a) General form of an ageing protocol plot of set points: the temperature  $T$  (in blue), the relative humidity  $RH$  (in green) and UV radiation intensity  $UV$  (in red). The mean values are in dashed line. Temperature and relative humidity profiles exhibit finite slopes in the transient phases, while UV radiation can be turned on/off instantaneously. (b) Example of actual measurements (full lines) compared to the set points (dashed lines), for an ageing protocol with  $x_1 = 0.5$ ,  $x_2 = 0.53$  and  $x_3 = 0$ .



# Multi-factorial model for CFRP ageing

## 4.1 Ageing protocols and experimental campaign

The details of the ageing protocol design were detailed and discussed in chapter 3. The subject specimens in this chapter were then submitted to cyclic environments, with the following factors controlled: the surrounding temperature ( $T$ ), the relative humidity ( $RH$ ) and the intensity of an A-class ultraviolet radiation ( $UV$ ) lamp on one face of the plate samples. The cycles are longer for the humid protocols due to technical reasons. The scheduled campaigns and the series, with the respective codes and samples included, the protocol parameters and the durations are summarized in table 3.4. Hardware includes the Weiss Technik®WK180/40 climatic chamber, with the required control and data acquisition software. As a reminder, the normalized variable  $x$  for a real variable  $u$  (that can be either  $T$ ,  $RH$  or  $UV$ ) is given by:

$$x = \frac{u - u_{min}}{u_{max} - u_{min}} \quad (4.1)$$

where  $u_{min}$  and  $u_{max}$  are respectively the minimum and maximum value adopted by  $u$ .

The experiments were carried out as follows:

1. After a sensitivity analysis, the number of monitored natural frequencies is fixed, which are the 8 lowest in the case of the series E to J (D only had 7 frequencies monitored).
2. Before ageing, the elastic moduli are estimated *via* EMA (with impact hammer, under free-free boundary conditions) and numerical-experimental identification. This is defined as the initial state ( $Y = Y_0$ ).

## Chapter 4. Multi-factorial model for CFRP ageing

3. The samples are introduced into the climatic chamber afterwards for ageing. The same elastic moduli identification process is repeated at regular intervals (after 100 or 112 cycles depending on the protocol). At the end of the ageing process, between 8 and 12 "rounds" (depending on the groupe) of experimental tests have taken place.
4. The sensors providing the electric signal are accelerometers and PVDF patches (if the patches are integrated on the sample). The electric signals are subjected to FFT and modal extraction, through ME-Scope VES, to obtain the modal parameters. The polynomial method for curve fitting was used.
5. The sensors are located following a "naive" placement strategy (see chapter 6). Accelerometers are placed in the corners (where displacement is maximum) and PVDF patches close to the middle points of the borders (where strain is maximum).
6. For each series and at each round, a mean and a standard value for each elastic moduli estimation are obtained. From this point of view, elastic moduli are assumed to follow a normal distribution.
7. The experimental tests are carried out at room temperature (25 [°C]). The samples are weighed using a Mettler-Toledo weighing scale. All the out-of-the-chamber testing takes between 20 and 30 minutes.

The experimental parameters (number of cycles, monitored natural frequencies, testing intervals) are shown in table 4.1.

Table 4.1 – Normalized ageing parameters  $x_1$ ,  $x_2$  and  $x_3$  and time parameters for all the series.

Group	$T$	$RH$	$UV$	Cycle period $\Delta t$ [min]	$N_{cyc}$	Measurement Intervals	Monitored Nat. Freq.
	$x_1$	$x_2$	$x_3$				
D	0	1	1	90	800	112 (*)	7
EF1	1	0.73	1	90	900	112 (**)	8
EF2	1	0.73	0	90	900	112 (**)	8
G1	0	0	0	60	1100	100	8
G2	0	0	1	60	1000	100	8
H1	1	0	1	60	1100	100	8
H2	1	0	0	60	1100	100(***)	8
J	0	1	0	90	800	112(*)	8

(\*) Last measurement at 800 cycles instead of 784.  
(\*\*) Last measurement at 900 cycles instead of 896.  
(\*\*\*) Two datasets were lost.

## 4.2 Introduction to the experimental results

This section synthesizes the main results of the experimental campaign. For the sake of uniformity and clarity, the changes in the constitutive properties of the samples are tracked with respect to their initial value. These relative magnitudes are defined in relative values, as in equation (4.2). For each sample, the denominator is the initial value, prior to the start of the ageing process. This way, the ageing curves start from the same point and reflect the relative variation.

$$\mu = \frac{m}{m_0}; \epsilon_1 = \frac{E_1}{E_{10}}; \epsilon_2 = \frac{E_2}{E_{20}}; \gamma_{12} = \frac{G_{12}}{G_{120}} \quad (4.2)$$

A condensed version of table 3.4 is shown in table 4.1.

The mathematical pattern of a model proposed as a solution for ageing characterization in the introduction chapter can be hinted by visual inspection of the pre-modelling evolution curves in figure 4.1. The asymptotically exponential increase or decrease are inspired from ageing behaviour reported in previous works on composite testing [Carraher, 2010, Brinson and Brinson, 2008], specially in the aerospace field [Tong et al., 1996]. A deeper analysis from a statistical point of view shows a correlation between the absorbed moisture mass and the loss of stiffness (see subsection 4.5). This statement leads to the replacement of the number of cycles by the water concentration as the time variable in the mathematical model previously suggested. As it will be explained later in this chapter, the usefulness of this reasoning becomes evident: it allows to generalize the model to mechanical parts with more complex shapes, and contributes to the future research on CFRP with an early estimation of the extent of their ageing using only some basic information about the material constitutive properties and diffusion coefficients. In the general case, the increase of the total mass seems regular and few scattered (figure 4.1). It is nevertheless difficult to determine how this additional mass is distributed across the thickness, and is thus assumed uniform.

In a UD configuration, the influence of the polymer matrix and the fibres on the elastic properties are partially decoupled. In our case, among the identified properties, the longitudinal tensile modulus  $E_1$  is mostly associated to the carbon fibres, while  $E_2$  and  $G_{12}$  are related to the epoxy matrix. Two opposite trends could be observed.

First, the longitudinal tensile modulus  $E_1$  increases over the weeks, as shown in figure 4.1. The value of  $\epsilon_1$  exhibits a clear trend in the first two weeks, followed by a much more irregular variation around a steady value. Globally, a slight increase was observed in the tensile modulus  $\epsilon_1$  in the longitudinal direction of the plate, at least during the first phase of the ageing process, although not statistically representative

## Chapter 4. Multi-factorial model for CFRP ageing

(error bars represent the standard deviation). On the other hand, an opposite evolution of  $\epsilon_2$  and  $\gamma_{12}$  can be observed in the examples featured in figure 4.1, and shows a decrease of stiffness. However, the extent of the loss depends on the ageing protocol parameters. It can be observed that percentage of loss is about 4% for the D-, 8% for the EF1-, 10% for the EF2-, and 8% for the H1-series at the end of the ageing process. In all cases, the loss of transverse bending and shear stiffness is much more significant than the scattering (as shown by the error bars), which let us suppose that the epoxy matrix properties are mostly affected.

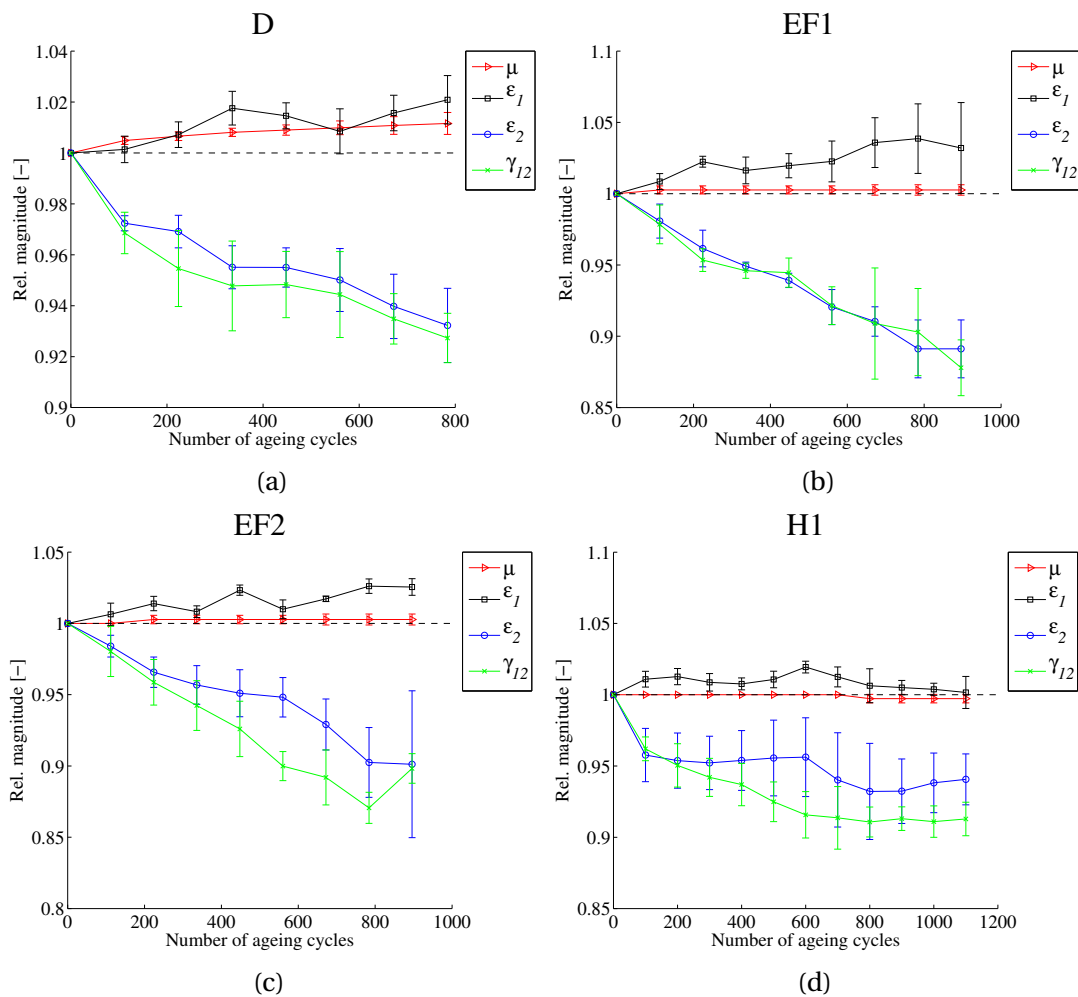


Figure 4.1 – Example of evolution of relative mass  $\mu$ , Young's moduli  $\epsilon_1$ ,  $\epsilon_2$  and shear modulus  $\gamma_{12}$  for (a) D-, (b) EF1-, (c) EF2- and (d) H1-series.



## 4.3 Multi-factorial statistical model

### 4.3.1 Mathematical model inspired from the Prony series

It is natural at this point to quantify the effects of the different ageing agents, whether those are alone or combined, by establishing a multi-factor mathematical model. At first sight, the trend curves shown in figure 4.1 exhibit an exponential behaviour over the time (represented by the number of cycles  $n$ ). On the other hand, the extent and the rate of the ageing depend on the temperature, the relative humidity and the UV radiation intensity. All these arguments taken into account, a mathematical model following the pattern of a Prony series has been established. The mathematical expression is given by the following equation, in which a linear interaction of the parameters is assumed:

$$\begin{aligned}
 y = \frac{Y}{Y_0} &= 1 + \sum_i a_i \phi_i(x_1, x_2, x_3) (1 - e^{-n/10^{b_i}}) & (4.3) \\
 \phi_0 &= (1 - x_1)(1 - x_2)(1 - x_3) \\
 \phi_1 &= x_1(1 - x_2)(1 - x_3) \\
 \phi_2 &= (1 - x_1)x_2(1 - x_3) \\
 \phi_3 &= (1 - x_1)(1 - x_2)x_3 \\
 \phi_{12} &= x_1x_2(1 - x_3) \\
 \phi_{13} &= x_1(1 - x_2)x_3 \\
 \phi_{23} &= (1 - x_1)x_2x_3 \\
 \phi_{123} &= x_1x_2x_3
 \end{aligned}$$

In equation (4.3), each "basis" function  $\phi_i(x_1, x_2, x_3)$  represents a series of samples under a given set of environmental conditions  $x_1$ ,  $x_2$  and  $x_3$  (see table 4.1),  $Y$  represents either  $m$ ,  $E_1$ ,  $E_2$  or  $G_{12}$ , and  $y$  represents  $\mu$ ,  $\epsilon_1$ ,  $\epsilon_2$  or  $\gamma_{12}$ . Physically, the identified constant coefficients  $a_i$  are the final asymptotic values of the loss/gain, and  $10^{b_i}$  are the corresponding time constants (in number of cycles). In other words, this expression is basically a mathematical model expressing an exponential decay (or rise) of the constitutive properties of the samples subjected to an accelerated ageing protocol.

Given the strong non-linearity of the model, the result of the identification process can be sensitive to the initial estimations. The Levenberg-Marquardt least-square optimization algorithm was used to find the best fitting parameters. To validate the robustness of the regression, random initial conditions (the assumed initial values for

## Chapter 4. Multi-factorial model for CFRP ageing

constants  $a_i$  and  $b_i$ ) were selected on a basis of multiple Monte Carlo simulations, in order to find a global minimum for the least-square fitting error. The boundaries of the space of possible solutions are detailed in table 4.2. Twenty-five points, randomly determined using a uniform distribution were used as initial conditions. The convergence zone for the  $a_i$  coefficients was very variable and depended on the analysed  $y$ ; on the contrary  $b_i$  coefficients converged almost systematically (with a few exceptions) to values around 3.

Table 4.2 – Domain of initial conditions for the Monte Carlo simulations: 25 points in the  $(a_i, b_i)$  plane are randomly selected in order to check that the convergence of the optimization algorithm is independent from the initial conditions.

Coefficients	Lower bound.	Upper bound.	Convergence to
$a_0, a_1, a_2, \dots, a_{123}$	-1	1	$a_i < 0$ for $\epsilon_2$ and $\gamma_{12}$ variable for $\mu$ and $\epsilon_1$
$b_0, b_1, b_2, \dots, b_{123}$	0	10	$\approx 3$

The global results are shown in figure 4.2, with the corresponding residuals and coefficients of determination  $R^2$ . As it can be seen, the fitting quality is very high for  $\mu$ ,  $\epsilon_2$  and  $\gamma_{12}$ , while it is considerably lower in the case of  $\epsilon_1$ . As it is shown in the following sections,  $\epsilon_1$  (which represents the stiffness along the carbon fibres direction) shows a behaviour that cannot be considered statistically interpreted.

An overview of the bar diagrams shown in figure 4.2 shows the clear dominance of some factors with respect to other. In particular:

- The mass absorption is clearly dominated by the relative humidity (high values for  $a_2, a_{12}, a_{23}$  and  $a_{123}$ , with 2 representing the RH factor). The influence on the mass by other factors is negligible. It should be noted as well the importance of the interaction factors  $a_{12}, a_{23}$  and  $a_{123}$ , which could be interpreted as the synergistic effect of the ageing factors.
- Concerning the fibre-dominated relative Young's modulus  $\epsilon_1$ , the dominance of the constant term  $a_0$  on the degradation shows that there is not a clear influence of the ageing factors. Coefficient  $a_0$  is moreover coupled with an unusually high time constant  $b_0 = 5$ , which can be interpreted as a very low "constant degradation" intervening after around 100000 ageing cycles, independently from the weathering factors. However, the low correlation in the dataset (given by the determination coefficient  $R^2$ ) does not allow concluding that this ageing model is representative of  $\epsilon_1$ 's degradation. This statement is further supported by the results in section 4.3.2.
- $\epsilon_2$  and  $\gamma_{12}$  show similar models, for which all the ageing factors (and more importantly their interactions) play an important part in material degradation.

### 4.3. Multi-factorial statistical model

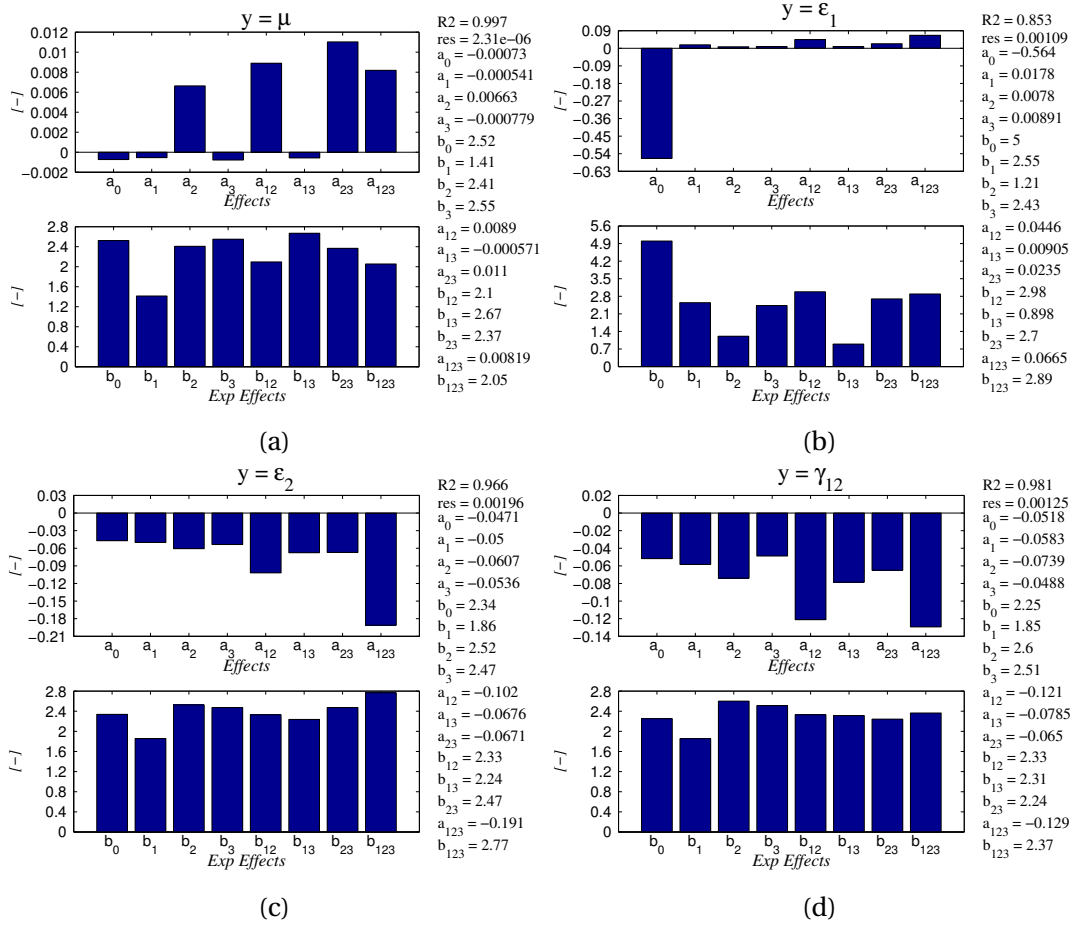


Figure 4.2 – Bar diagrams for identified model coefficients  $a_i$  for relative (a) mass  $\mu$ , (b) Young's modulus  $\epsilon_1$ , (c) Young's modulus  $\epsilon_2$  and (d) shear modulus  $\gamma_{12}$ .

#### 4.3.2 Validation of the exponential pattern

The validation of a model can be carried out either by graphical and analytical means. For the former, a simple way to do so is by establishing a scatter plot displaying a graphic comparison between the estimated curve and the experimental results of aged samples as shown in figures 4.3 and 4.4. Visually, it can be observed that the experimental results are globally well predicted by the model, especially concerning the ageing of the polymer matrix (tensile modulus  $\epsilon_2$  and shear transverse modulus  $\gamma_{12}$ ).

For the analytical validation, a lack-of-fit test is also performed on the global data, in order to show analytically the goodness-of-fit of the mathematical model. The total fitting error and its components are defined by equation (4.4)

$$\sum_i \sum_j (y_{ij} - \hat{y}_i)^2 = \sum_i \sum_j (y_{ij} - \bar{y}_i)^2 + \sum_i \xi_i (\bar{y}_i - \hat{y}_i)^2 \quad (4.4)$$

## Chapter 4. Multi-factorial model for CFRP ageing

---

$$S_{tot} = SS_{pe} + SS_{lof}$$

where  $y_{ij}$  is the  $i^{th}$  measurement of the  $j^{th}$  sample (in this case the measured value  $y$  is either  $\mu$ ,  $\epsilon_1$ ,  $\epsilon_2$  or  $\gamma_{12}$ ),  $\bar{y}_i$  is the average over all the samples after 100*i* cycles,  $\hat{y}_i$  is the prediction for  $y$  after 100*i* cycles, and  $\xi_i$  is the weighing coefficient which is equal to the number of samples in the series (then  $j = 1, \dots, \xi_i$ ).  $SS_{tot}$  is the total sum of squares of the error between the estimated and the measured values,  $SS_{pe}$  is the sum of squares due to the pure measurement error and  $SS_{lof}$  is the sum of squares of the error due to the "lack-of-fit" of the model, this is the inaccuracy from the "mathematical" model and the real "physical" model, without the effect of random measurement scatter. This sum-of-squares method to evaluate the lack-of-fit was intended to be used on linear models. It has been however demonstrated that this formulation can also be applied on exponential models [O'Brien et al., 2009].

If the lack-of-fit and the purely experimental errors are independent, the Fischer's quotient  $F$  defined by equation (4.5)

$$F = \frac{SS_{lof}/\nu_1}{SS_{pe}/\nu_2} \quad (4.5)$$

follows a Fischer distribution  $F(\nu_1, \nu_2)$  with  $\nu_1 = Q - p = 79 - 16 = 63$  and  $\nu_2 = N - Q = 193 - 79 = 114$  respectively as degrees of freedom. Here,  $N$  denotes the total number of measurements in the dataset,  $p$  is the order of the model (the total number of degrees of freedom for the error is  $N - p = 177$ ) and  $Q$  is the total number of averages. A hypothesis test is suggested:

$$\begin{cases} H_0 & : \lambda = 0 & (\text{ie the new data fit into the model}) \\ H_1 & : \lambda \neq 0 & (\text{ie the new data do not fit into the model}) \end{cases} \quad (4.6)$$

where  $\lambda$  is defined as the lack-of-fit. With a probability level of 95% ( $\alpha = 0.05$  is the probability of a false positive, *ie* the probability to reject the null hypothesis while this is true), the critical value is  $F_{crit} = F_{0.05}(63, 114) = 1.43$ . Below this value, the null hypothesis  $H_0$  is accepted. Else, the alternative hypothesis  $H_1$  is accepted. It can be seen in table 4.3 that  $H_0$  is accepted in all cases, except for  $\epsilon_1$ . In statistical terms, this demonstrates that the data scattering is dominated by the random measurement error rather than the lack-of-fit of the model in the cases of  $\epsilon_2$ ,  $\gamma_{12}$  and  $\mu$ . Along with the remarkably high values for the coefficient of determination, it can thus be concluded that the models are accurate enough to represent the ageing of an epoxy CFRP, in the frame of the previously determined temperature, RH and UV radiation intensity intervals.

### 4.3. Multi-factorial statistical model

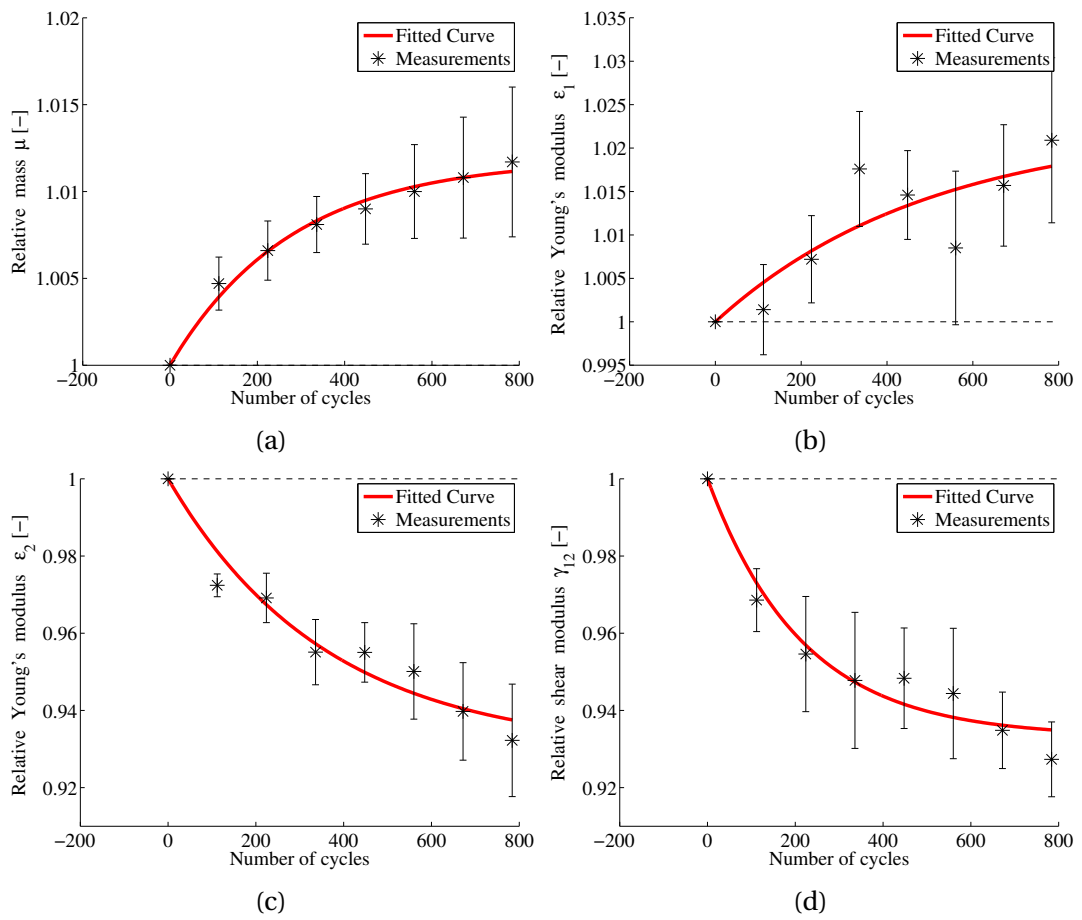


Figure 4.3 – Scatter plot for measurements of D-series samples (D: low  $T$ , high  $RH$  and  $UV$  on).

**Chapter 4. Multi-factorial model for CFRP ageing**

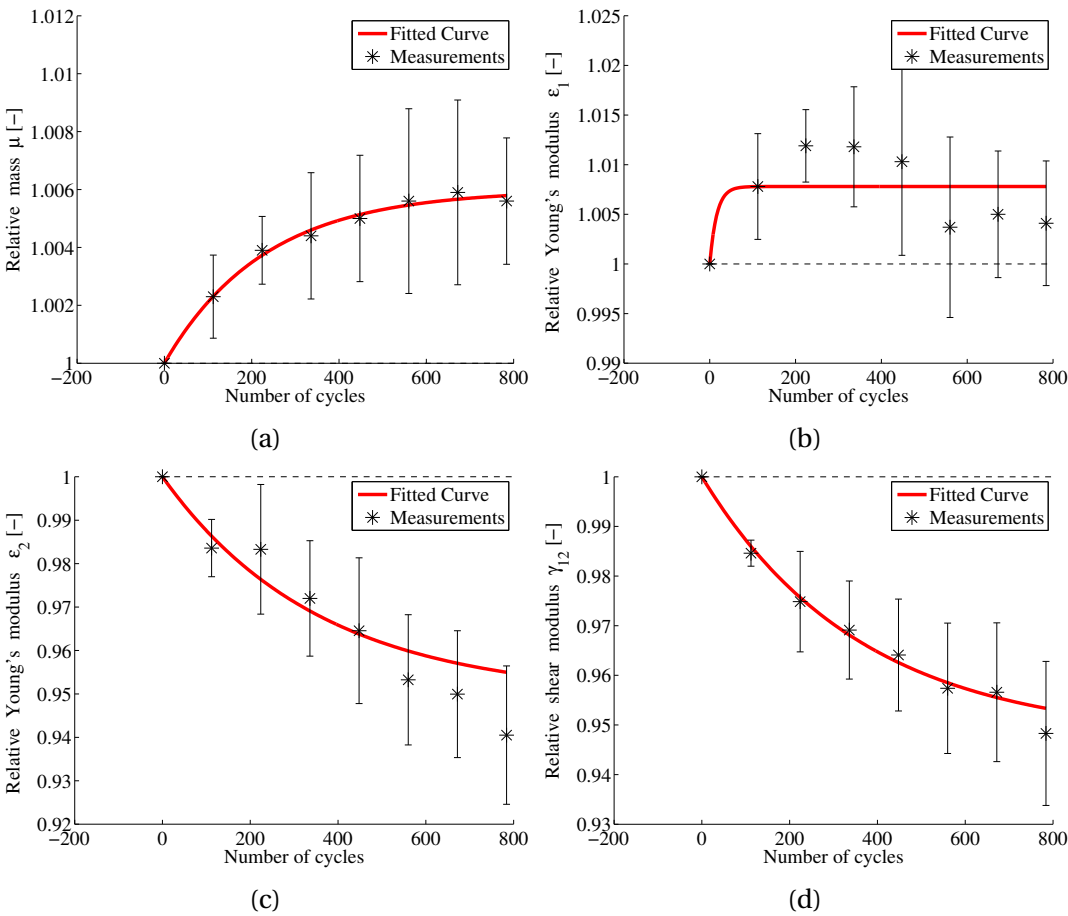


Figure 4.4 – Scatter plot for measurements of J-series samples (J: low  $T$ , high  $RH$  and  $UV$  off).

#### 4.4. Equivalent moisture absorption in cyclic ageing protocols

Table 4.3 – Lack-of-fit test, along with the coefficient of determination  $R^2$ , for a total of  $N = 193$  measurements ( $Q = 79$  averaged), and a  $p = 16$  DoF model. To accept the null hypothesis,  $F \leq F_{crit} = 1.43$ .

Model	Mass	Elastic moduli			
		$\mu$	$\epsilon_1$	$\epsilon_2$	$\gamma_{12}$
Coeff. of determination $R^2$		0.998	0.845	0.966	0.978
Sum of squares (SS)	DF				
Total SS	177	0.000464	0.0186	0.0372	0.126
Pure-error SS	114	0.000452	0.0090	0.0328	0.123
Lack-of-fit SS	63	0.000012	0.0096	0.0044	0.0035
$\lambda$		0.0469	1.936	0.240	0.051
Decision		$H_0$	$H_1$	$H_0$	$H_0$

#### 4.3.3 Interpretation of the validation

The first statement after inspecting figure 4.1 is that there is a temporal evolution of the elastic properties and the mass of the samples, which along with their dimensions determine their dynamic behaviour. Although the trend seems to initially be evolution at a constant rate, it is clear that over a long-term exposure to weather conditions, there is a limit for the degradation of properties. As stated in section 4.2, the exhibited trend of  $\epsilon_1$  is not very clear, since it seems to slightly increase. On the contrary,  $\mu$  shows a clear increase, and  $\epsilon_2$  and  $\gamma_{12}$  show a clear decrease.

Physically,  $\epsilon_1$  is associated to the stiffness of the carbon fibres in a UD composite. However, the carbon fibres are rather chemically and thermally inertial, thus the observed increase of  $\epsilon_1$  would not be due to a change in the inner structure of the carbon, but rather due to a post-curing effect, which has been reported in other cases in the relevant literature [Akay, 1990]. The changes in  $\epsilon_2$  and  $\gamma_{12}$  are less surprising since they were expected, after the overview of the state-of-the-art in accelerated ageing of polymer composites. The loss of stiffness by the polymer matrix is a combination of several phenomena detailed in the literature, in particular due to polymer chain de-linking, photo-oxidation, water corrosion, etc.

From the observations made on the scatter plots, the determination coefficient  $R^2$  and the corresponding Fischer quotients  $F$  in the previous section, it is safe to state that the evolution of  $\mu$ ,  $\epsilon_2$  and  $\gamma_{12}$  can be explained by such a mathematical model. On the other hand, the model for  $\epsilon_1$  is not an accurate predictor.

#### 4.4 Equivalent moisture absorption in cyclic ageing protocols

In the previous section, mathematical models based on statistical regression of experimental data have been developed. Unfortunately, they remain uninteresting from

the experimental repeatability point of view, since they can not be directly applied to more general cases with other geometries, given that a particular geometry plays a determining role in several of the ageing mechanisms, such as moisture absorption, heat diffusion, penetration depth of UV radiation, etc.

In order to remove this dependency on geometry, a first step is to establish a link between theory and experiments in the moisture absorption. The main interest of doing so is the determination of "equivalent" constants of diffusivity and saturation mass, determined for cyclic conditions instead of constant conditions in temperature and relative humidity.

### 4.4.1 Diffusion for periodic ageing protocols

The behaviour under periodic protocols is different from those described in the previous section, since there is a constant charge/discharge cycle going on continuously. Despite this, the base hypothesis is that the amount of absorbed water oscillates around a local moving mean value, that is a fraction of the saturation mass  $M_s$ . As a reminder, the simplified isothermal diffusion mathematical model is given by equation (3.3). For the absorption (charge), we have

$$\frac{M'_1}{M_s} = \Theta\left(\frac{\Delta t_-}{\tau_-}\right) \quad (4.7)$$

where subscript 1 stands for first cycle. For the first desorption (discharge)

$$\frac{M_1}{M'_1} = 1 - \Theta\left(\frac{\Delta t_+}{\tau_+}\right) \quad (4.8)$$

where  $\tau_- = h^2/(\pi^2 D_-)$  and  $\tau_+ = h^2/(\pi^2 D_+)$ ,  $\Delta t_-$  and  $\Delta t_+$  are the corresponding durations of the low temperature and the high temperature part of the cycle (including the transient state), and  $D_-$  and  $D_+$  are the corresponding diffusion coefficients. Combining equations (4.7) and (4.8) gives

$$\frac{M_1}{M_s} = \left[1 - \Theta\left(\frac{\Delta t_+}{\tau_+}\right)\right] \Theta\left(\frac{\Delta t_-}{\tau_-}\right) \quad (4.9)$$



#### 4.4. Equivalent moisture absorption in cyclic ageing protocols

---

For the  $n^{\text{th}}$  charge, we have

$$\frac{M'_n}{M_s} = \Theta \left( \frac{\Delta t_- + \delta t_n}{\tau_-} \right) \quad (4.10)$$

where  $\delta t_n$  is the time it would take to have a concentration of  $M_{n-1}$  in isothermal conditions, and it is defined by equation (4.11):

$$\frac{\delta t_n}{\tau_-} = \Theta^{-1} \left( \frac{M_{n-1}}{M_s} \right) \quad (4.11)$$

where  $\Theta^{-1}$  is the inverse function of  $\Theta$  and  $M_{n-1}$  is the mass left after the  $(n-1)^{\text{th}}$  discharge. The physical meaning of  $\delta t_n$  is shown in figure 4.5. The corresponding discharge is given by:

$$\frac{M_n}{M'_n} = 1 - \Theta \left( \frac{\Delta t_+}{\tau_+} \right) \quad (4.12)$$

A mathematical sequence can then be defined to determine the absorbed mass after the  $n^{\text{th}}$  cycle:

$$\frac{M_n}{M_s} = \left[ 1 - \Theta \left( \frac{\Delta t_+}{\tau_+} \right) \right] \Theta \left( \frac{\Delta t_- + \delta t_n}{\tau_-} \right) \quad (4.13)$$

$$\frac{M_n}{M_s} = f \left( \frac{M_{n-1}}{M_s} \right) = \left[ 1 - \Theta \left( \frac{\Delta t_+}{\tau_+} \right) \right] \Theta \left( \frac{\Delta t_-}{\tau_-} + \Theta^{-1} \left( \frac{M_{n-1}}{M_s} \right) \right) \quad (4.14)$$

where  $f$  denotes a recurrence relation, where the mass concentration  $M$  can be determined recursively after the  $n^{\text{th}}$  cycle as a function of the concentration after the  $(n-1)^{\text{th}}$  cycle. In the graph shown in figure 4.5, the amplitude of the oscillation is exaggerated in order to show the concentrations and time variables. For the ageing protocols mentioned in this chapter, the discharge phase was much slower than the absorption phase.

From the expression in equation (4.14), it can be deduced that the absorbed moisture mass depends essentially on the ratios  $\Delta t_+/\tau_+$  and  $\Delta t_-/\tau_-$ . The final value  $\lim_{n \rightarrow \infty} M_n = M_\infty = M_{s,eq}$  (where  $eq$  stands for equivalent) of the mass absorption is given by the solution of  $x = f(x)$ . After using MATLAB to solve recursive equation (4.14), the results for the ageing protocols are summarized in table 4.4. The ratio  $M_{s,eq}/M_s$  is asymptotic ( $\approx 0.12$ ), representing the upper limit for the fraction of water absorbed at the end of a given periodic protocol, with respect to the mass at saturation  $M_s$  in isothermal conditions.

Concerning the results for humid protocols, it is interesting to see in table 4.4 that

independently from the exposure to UV radiation and thickness, the equivalent saturation concentrations  $M_{s,eq}$  are similar between the EF1-, EF2- and J-series. The equivalent saturation mass for D is on the other hand much higher. The difference comes mostly from the difference in the cyclic timing of the protocols, since the cycles in the D-series have a 2:1 ratio between  $\Delta t_-/\Delta t_+$  (instead of 1:1 for EF1-, EF2- and J-series).

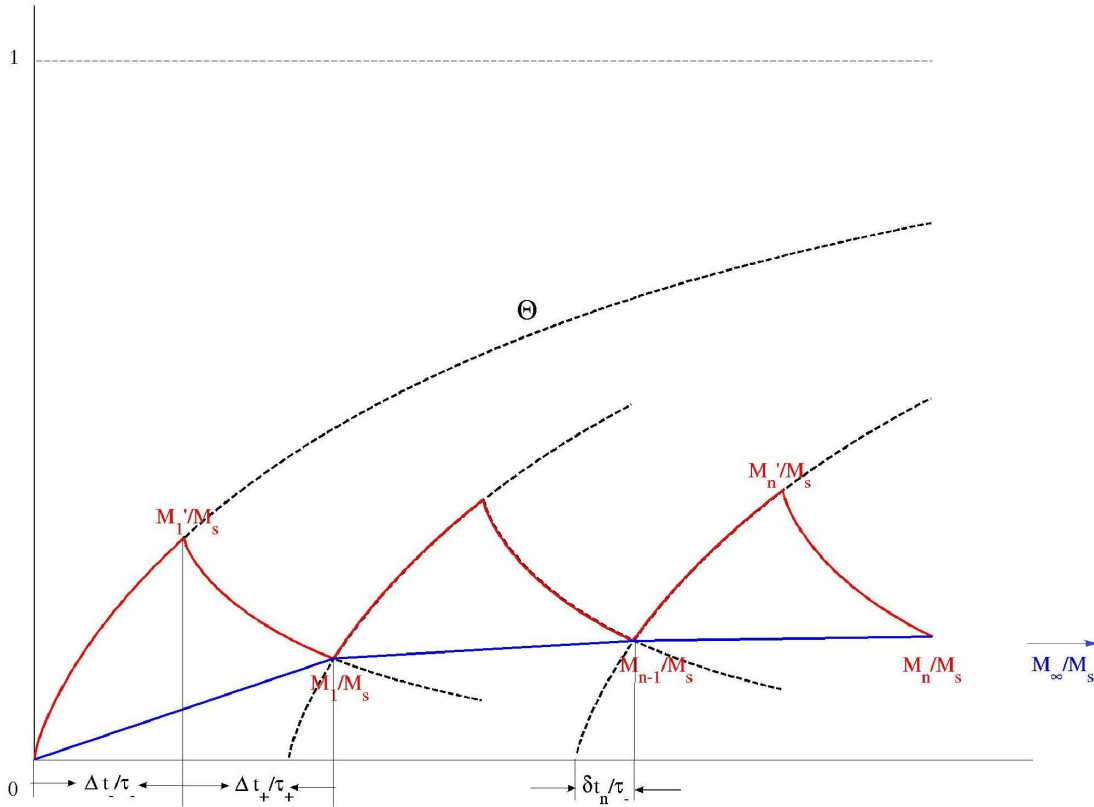


Figure 4.5 – Cyclic mass absorption. The variables are those described in equations (4.7) to (4.14) in subsection 4.4.1: the saturation mass in constant (isothermal) conditions is  $M_s$ , while  $M_\infty = M_{s,eq}$  is the equivalent saturation mass in cyclic conditions.

**4.4.2 Equivalent diffusivity and equivalent saturation mass**

The reasoning behind this mathematical development is to compare the results from both (theoretical and experimental) models for cyclic moisture absorption inside a structure, obtained from the experimental campaigns, using isothermal and periodic results, and more important, to see if the parametric model found in section 4.3 is able to predict accurately the experimental results.

The fitted mathematical model can be used to predict the saturation mass  $M_s$ , al-

#### 4.4. Equivalent moisture absorption in cyclic ageing protocols

though few can be known about the real physical diffusivity. To overcome this difficulty, it is useful to define an "equivalent" diffusivity  $D_{eq}$  for cyclic conditions.

In order to do so, let us consider the following approximation of the diffusion function  $\Theta(x) = 1 - e^{-1.311x^{0.75}} \approx 1 - e^{-1.3181x}$ , as it is shown in the graph of figure 4.6. This approximation has the same exponential form as the terms of the ageing mathematical model, as it is described in equation (4.3). A link between the theoretical diffusion and the statistical experimental model can then be established. For the  $i^{th}$  protocol, we have

$$1 - e^{-1.3181t/\tau_i} = 1 - e^{-n/10^{b_i}} \quad (4.15)$$

where  $t$  is the time (in [s]),  $n$  is the corresponding number of cycles,  $\tau_i$  is the diffusion time constant for the  $i^{th}$  protocol (defined in equation (3.3)) and  $10^{b_i}$  is the time constant in number of cycles of the  $i^{th}$  term in the mathematical model (4.3). For a single cycle,  $n = 1$  and  $t = \Delta t$ , so the following equation can easily be deduced:

$$\tau_i = 1.3181\Delta t \cdot 10^{b_i} \quad (4.16)$$

Time constant  $\tau$  has been defined in the context of isothermal water absorption by equation (3.3). Thus, in the case of cyclic absorption, the equivalent diffusivity  $D_{eq}$  for the  $i^{th}$  protocol can be defined as:

$$D_{eq_i} = \frac{h^2}{\pi^2\tau_i} \quad (4.17)$$

There are now at our disposal two ways to determine the value of  $D_{eq}$ : a theoretical value  $D_{eq,th}$  obtained from a non-linear curve fitting of the recursive absorption model described by equation (4.14), based on isothermal diffusion parameters and

Table 4.4 – Estimated mass increase for the four series subjected to humid protocols.  $M_{s,eq}$  is the equivalent saturation mass for the cyclic protocol and  $M_s$  the corresponding saturation mass under isothermal conditions.

Series	Cycles $N_{cyc}$	Temperature [K]		Time period [s]		Thickness [mm] $h$	Mass ratio $M_{s,eq}/M_s$	Equivalent sat. mass (cyclic) $M_{s,eq}$			Saturation mass (isothermal) $M_s$		
		$T_-$	$T_+$	$\Delta t_-$	$\Delta t_+$			$a$	$b$	$c$	$a$	$b$	$d$
D	800	278	368	3600	1800	4.04	0.135	0.0106	0.0100	0.0101	0.079	0.074	0.075
EF1	900	318	408	2700	2700	4.23	0.110	0.0059	0.0066	0.0060	0.054	0.060	0.055
EF2	900	318	408	2700	2700	4.02	0.112	0.0064	0.0067	0.0064	0.058	0.060	0.057
J	800	278	368	2700	2700	4.29	0.124	0.0063	0.0066	0.0061	0.051	0.054	0.049

<sup>a</sup> Predicted from the fitted model.

<sup>b</sup> Predicted from the theory.

<sup>c</sup> Mean residual mass, obtained by drying of the samples.

<sup>d</sup> Predicted from the experimental result.

## Chapter 4. Multi-factorial model for CFRP ageing

an experimental value  $D_{eq,exp}$  obtained from the cyclic experimental results:

$$D_{eq,exp} = \frac{h^2}{13.01\Delta t \cdot 10^{b_i}} \quad (4.18)$$

These values are compared for all four wet protocols in table 4.5.

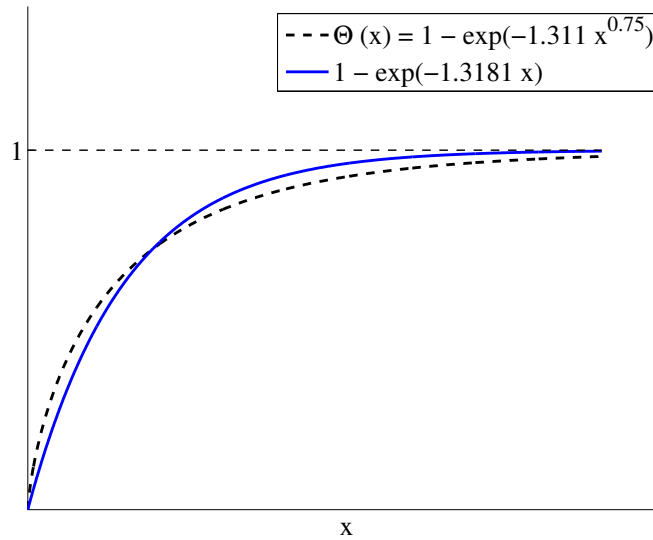


Figure 4.6 – Comparative plot show the closeness of the two exponential functions  $\Theta(x) = 1 - e^{-1.311x^{0.75}}$  and  $1 - e^{-1.3181x}$ .

Table 4.5 – Comparison between theoretical and experimental estimations of the equivalent diffusivity.

Series	Fitted model $D_{eq,exp}$ (cyclic test)	Theoretical $D_{eq,th}$ (from isothermal data)	Rel. Error %
D	1.27E-12	1.54E-12	21.5
EF1	4.45E-13	5.08E-13	14.2
EF2	4.61E-13	4.93E-13	7.1
J	4.44E-13	5.39E-13	21.5

All taken into account, the theoretical prediction of the saturation mass and diffusivity, and their experimentally determined counter-parts, are quite close. A fair prediction of the absorption rate can be done, starting only from theoretical considerations and isothermal diffusion data. However, it can be observed in table 4.5 that the experimental diffusion is systematically overestimated by the model.

The graphic representations of the predicted model (in black line), along the fitted model (red line) and the experimental results (blue dots and error bars) are shown

## 4.5. Relationship between moisture concentration and loss of stiffness

in figure 4.7. The plotted results show that the model given by equation (4.14), based on isothermal absorption data, is able to predict reasonably well the observed experimental cyclic response. The advantage of this "equivalent modelling" procedure is that the ageing problem can finally be seen freed from the influence of geometry, and then applicable to a much wider range of composite parts.

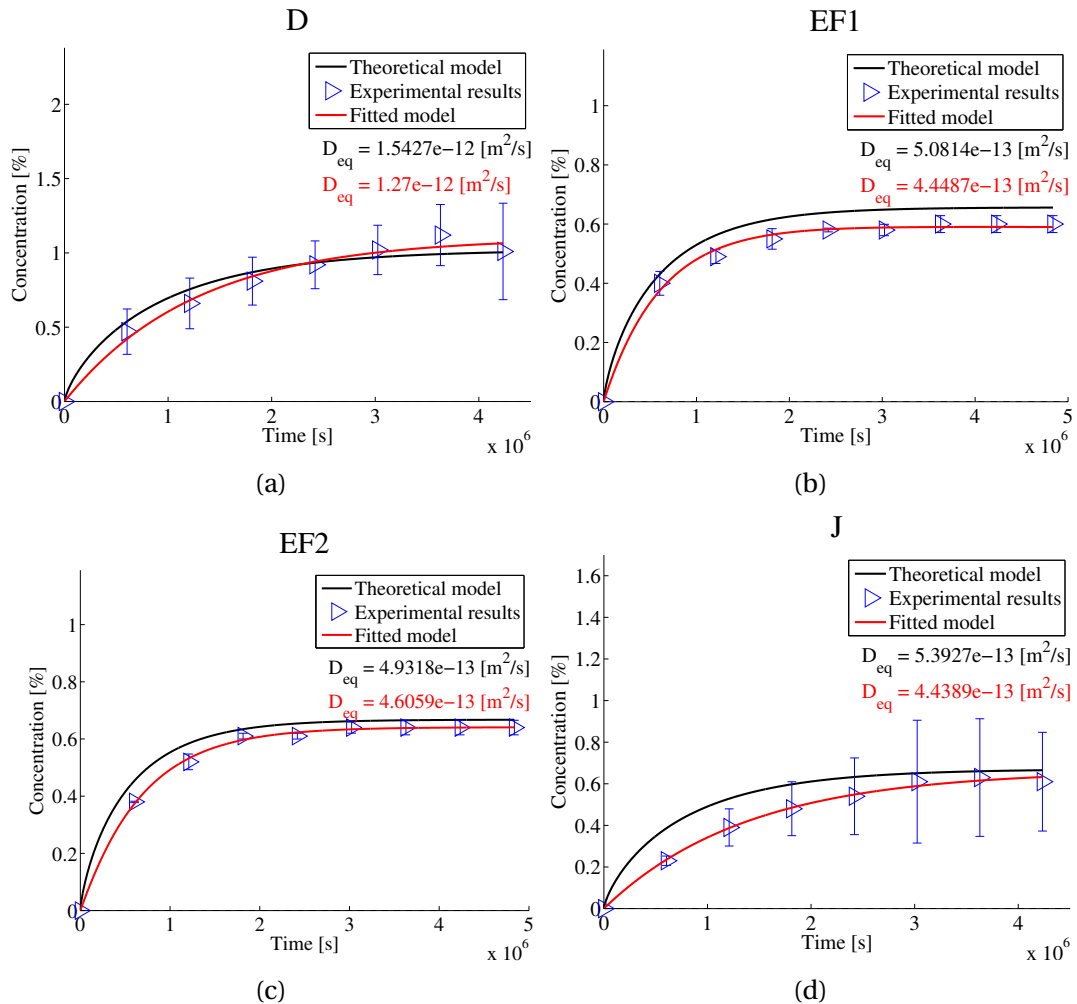


Figure 4.7 – Comparison between the theoretical and fitted models, for (a) D-, (b) EF1-, (c) EF2- and (d) J-samples.

## 4.5 Relationship between moisture concentration and loss of stiffness

### 4.5.1 Linear regression between mass and elastic properties

In figure 4.8, a certain pattern of correlation between the mass variation and the elastic properties can be observed. Depending on the relative humidity, the evolution of

the mass depends essentially on the existence/absence of moisture in the ageing environment. In the graphs, the specimens can be grouped to distinguish 4 categories, clearly differentiated by their respective ageing conditions: (D- and J-series) with 95% RH and low temperature, (EF1- and EF2-series) with 70% RH and high temperature, (G1- and G2-series) with 0 % RH and low temperature, and (H1- and H2-series) with 0 % RH and high temperature. The correlation seen in figure 4.8 highlights the inherent relationship between polymer ageing, water diffusion and loss of stiffness inside a resin matrix.

More particularly, it shows that the pattern of the stiffness evolution over the time is similar between ageing protocols that exhibit the same relative humidity, although the intensity of the loss grows deeper when UV radiation and high temperatures are applied. It can be deduced that two *a priori* independent variables are related: the water concentration and the elastic moduli. In figure 4.8 and table 4.6, linear regression models for the aforementioned groups (D-J, EF1-EF2, G1-G2, H1-H2) have been established, including the fitted straight lines and the corresponding Pearson correlation coefficients for each category.

#### 4.5.2 Correlation test

The corresponding Pearson's correlation coefficients  $\rho$  for each series is given in table 4.6. If the absolute value  $|\rho|$  is close to one, the linear regression is appropriate. A correlation criterion often mentioned in literature is  $|\rho| > 0.9$ . The Pearson's correlation coefficient between two statistics variables  $x$  and  $y$  is defined by the following formula

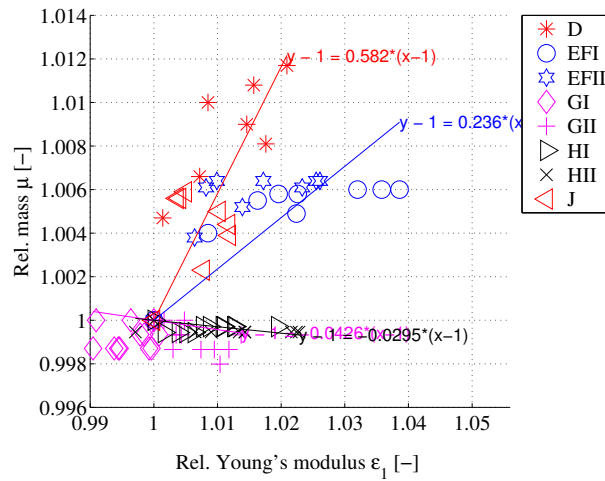
$$\rho = \frac{\sum_i (x_i - \bar{x})(y_i - \bar{y})}{\sqrt{\sum_i (x_i - \bar{x})^2 \sum_i (y_i - \bar{y})^2}}, \quad (4.19)$$

where  $\bar{x}$  and  $\bar{y}$  symbolize the respective mean values. In this case, let  $x$  and  $y$  be the water absorption mass rate  $\mu$  and the loss of stiffness rate  $(\epsilon_1, \epsilon_2, \gamma_{12})$ . A hypothesis test based on the value of a Student's t-distribution parameter  $\theta$  is carried out to find out if the correlation, for each series and each elastic variable, is statistically significant, and can be formulated as follows:

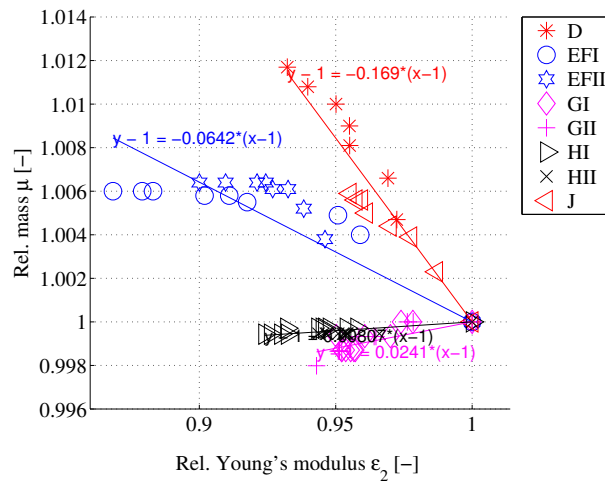
$$\begin{cases} H_0 & : \quad \rho = 0 & \text{(ie there is no correlation between variables.)} \\ H_1 & : \quad \rho \neq 0 & \text{(ie there is a correlation between variables.)} \end{cases} \quad (4.20)$$

The observed parameter is defined as  $\theta = \rho \sqrt{\frac{q-2}{1-\rho^2}}$ , following a Student's t-distribution, with  $q - 2$  DoF, where  $q$  is the number of observations per series. The null hypothesis

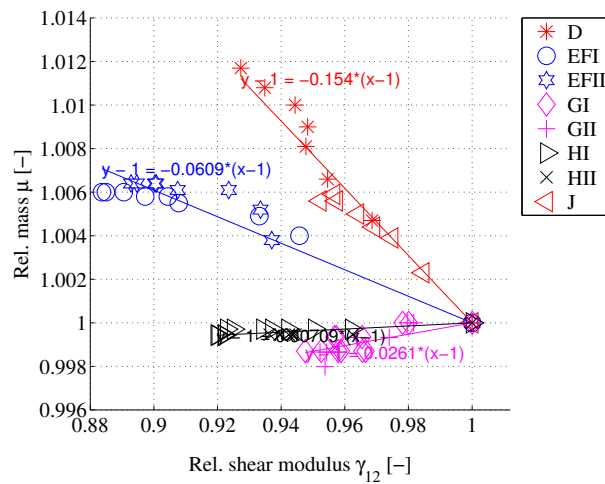
#### 4.5. Relationship between moisture concentration and loss of stiffness



(a)



(b)



(c)

Figure 4.8 – Correlation plots between the relative mass  $\mu$  and (a)  $\epsilon_1$ , (b)  $\epsilon_2$  and (c)  $\gamma_{12}$ .

## Chapter 4. Multi-factorial model for CFRP ageing

(no correlation) is accepted if  $|\theta| > \theta_{crit} = t_{\alpha/2}(q-2)$ . In table 4.6, assuming an  $\alpha = 5\%$  probability of type I error (false positive), it can be seen that the null hypothesis is constantly rejected for  $\epsilon_2$  and  $\gamma_{12}$ , while it is almost constantly accepted for  $\epsilon_1$ . This reinforces our past statements: the modelling of  $\epsilon_2$  and  $\gamma_{12}$  is appropriate, while  $\epsilon_1$ 's is statistically incorrect. To sum up, this shows that the ageing by water absorption and the decrease of stiffness inside the polymer matrix are correlated.

Since, by definition, the fitted straight lines (see figure 4.8) start always at (1,1), the regression formula takes invariably the form described in equation (4.21) or (4.22)

$$M = \mu - 1 = A_i(y_i - 1) \quad (4.21)$$

$$y_i = \frac{1}{A_i}(\mu - 1) + 1 = \frac{1}{A_i}M + 1 \quad (4.22)$$

where  $i = 1, 2, 3$ , namely  $y_i$  stands for either  $\epsilon_1, \epsilon_2$  or  $\gamma_{12}$  and  $A_i$  denotes the slope of the lines. Physically,  $A_i$  is the magnitude of the mass absorption effect on  $E_1, E_2$  or  $G_{12}$ .

Table 4.6 – Results of hypothesis testing on the correlation between  $\mu$  and the elastic properties. If  $H_0$  is accepted, there is no correlation, while if  $H_0$  is rejected, there is a correlation.

Series	Number of meas.	Pearson $\rho$			Student's t-distribution $\theta$			Student's crit. t-distribution $\alpha = 0.05$ $DoF = q_k - 2$	Decision		
		$\epsilon_1$	$\epsilon_2$	$\gamma_{12}$	$\epsilon_1$	$\epsilon_2$	$\gamma_{12}$		$\epsilon_1$	$\epsilon_2$	$\gamma_{12}$
D	8	-0.99	-0.99	-0.98	-17.2	-17.2	-12.1	2.31	$H_1$	$H_1$	$H_1$
J	8	-0.999	-0.99	-0.999	-54.7	-17.2	-54.7	2.31	$H_1$	$H_1$	$H_1$
EF1	9	-0.98	-0.91	-0.95	-13.0	-5.8	-8.0	2.26	$H_1$	$H_1$	$H_1$
EF2	9	-0.93	-0.77	-0.87	-6.7	-3.2	-4.7	2.26	$H_1$	$H_1$	$H_1$
G1	12	0.72	0.82	0.61	3.3	4.5	2.4	2.18	$H_1$	$H_1$	$H_1$
G2	11	0.96	0.91	0.88	10.3	6.6	5.6	2.20	$H_1$	$H_1$	$H_1$
H1	12	0.9	0.93	0.79	6.5	8.0	4.1	2.18	$H_1$	$H_1$	$H_1$
H2	10	0.52	0.89	0.38	1.7	5.5	2.4	2.23	$H_0$	$H_1$	$H_1$

### 4.5.3 A linear model for $A_i$

As it has been demonstrated in the previous section, there is a linear relationship between the mass absorption and the ageing of the polymer matrix, represented by a decay of  $\epsilon_2$  and  $\gamma_{12}$ . Since the time variable is implicitly included in  $\mu = \frac{m}{m_0}$ , the proportionality coefficient  $A_i$  should depend on the weathering conditions  $x_1$  (temperature),  $x_2$  (relative humidity) and  $x_3$  (UV radiation). Thus, a linear model for  $A_i$  is



## 4.5. Relationship between moisture concentration and loss of stiffness

suggested in the following equation

$$A(x_1, x_2, x_3) = \alpha_0 + \alpha_1 x_1 + \alpha_2 x_2 + \alpha_3 x_3 + \alpha_{12} x_1 x_2 + \alpha_{13} x_1 x_3 + \alpha_{23} x_2 x_3 \quad (4.23)$$

where  $A(x_1, x_2, x_3)$  represents any of the coefficients  $A_i$  in equation (4.21) or (4.22).

The coefficients  $A_i$  identified by linear regression are summarized in table 4.7, along with the corresponding Pearson's  $\rho$ , computed in subsection 4.5.2. Under the hypothesis that the coefficients of the linear regression follow a normal law, an analysis of variance (ANOVA) can be then carried out, in order to check the significance of the different factors in the ageing of the composite. This multi-factorial analysis of variance (ANOVA) can be performed as described by [Box et al., 2005] and [Montgomery, 2009]. In the context of ANOVA, as it can be seen in tables 4.8 and 4.9, the null hypothesis (the factor is statistically significant) is accepted for  $\alpha_0, \alpha_1$  and  $\alpha_2$  for both cases, and also  $\alpha_{12}$  in the case of  $\gamma_{12}$ . Physically, this can be interpreted as follows:

1. Since  $\alpha_0 \neq 0$ , there is a natural ageing in "normal conditions" (no humidity nor UV radiation, temperature is cyclic but always under the glass transition threshold).
2. The polymer matrix is sensitive to temperature ( $\alpha_1$ ) and humidity ( $\alpha_2$ ), and eventually a combination of both ( $\alpha_{12}$ ) for what concerns  $\gamma_{12}$ .
3. The part of UV radiation is close to negligible, at least with the intensity of the lamps used in the ageing processes analysed in this chapter.

Table 4.7 – Summary table of data  $y_i = A_i(x_1, x_2, x_3)$  used to set up a linear model with interactions, along with the corresponding correlation coefficients  $\rho$ .

Series	$x_1$	$x_2$	$x_3$	$\epsilon_2$		$\gamma_{12}$	
				$A_2$	$\rho$	$A_3$	$\rho$
J	0	1	0	-0.138	-0.99	-0.133	-0.98
D	0	1	1	-0.185	-0.99	-0.164	-0.99
EF1	1	0.73	1	-0.056	-0.88	-0.057	-0.96
EF2	1	0.73	0	-0.077	-0.95	-0.065	-0.97
G1	0	0	0	0.023	0.82	0.024	0.77
G2	0	0	1	0.025	0.91	0.028	0.88
H1	1	0	1	0.007	0.88	0.006	0.81
H2	1	0	0	0.011	0.93	0.010	0.93

### 4.5.4 Conclusion about the correlation tests

Since ageing and water absorption are correlated, equations (4.21) and (4.22) show that the time (or the number of cycles) can be replaced by the water concentration as

## Chapter 4. Multi-factorial model for CFRP ageing

Table 4.8 – ANOVA for the linear model with interactions of  $y_2 = A_2(x_1, x_2, x_3)$ , corresponding to  $\epsilon_2$ .

$\epsilon_2$	Effects	$SS$	$DoF$	$MS$	$F$	$p$ -value	$p \leq 10\%$
$\alpha_0$	0.0305	0.0190	1	0.0190	31.06	0.51 %	Yes
$\alpha_1$	-0.0294	0.0031	1	0.0031	5.15	8.58 %	Yes
$\alpha_2$	-0.1754	0.0377	1	0.0377	61.69	0.14 %	Yes
$\alpha_3$	-0.0127	0.0001	1	0.0001	0.18	69.67 %	No
$\alpha_{12}$	0.0822	0.0023	1	0.0023	3.84	12.16 %	No
$\alpha_{13}$	0.0280	0.0005	1	0.0005	0.77	42.88 %	No
$\alpha_{23}$	-0.0200	0.0002	1	0.0002	0.25	64.20 %	No
Residual		0.0006	1	0.0006			
Total		0.0635	8				

Table 4.9 – ANOVA for the linear model with interactions of  $y_3 = A_3(x_1, x_2, x_3)$ , corresponding to  $\gamma_{12}$ .

$\gamma_{12}$	Effects	$SS$	$DoF$	$MS$	$F$	$p$ -value	$p \leq 10\%$
$\alpha_0$	0.0287	0.0154	1	0.0154	69.70	0.11 %	Yes
$\alpha_1$	-0.0252	0.0024	1	0.0024	10.65	3.10 %	Yes
$\alpha_2$	-0.1663	0.0330	1	0.0330	149.05	0.03 %	Yes
$\alpha_3$	-0.0049	0.0001	1	0.0001	0.28	62.72 %	No
$\alpha_{12}$	0.0804	0.0022	1	0.0022	10.15	3.33 %	Yes
$\alpha_{13}$	0.0132	0.0001	1	0.0001	0.54	50.35 %	No
$\alpha_{23}$	-0.0168	0.0001	1	0.0001	0.49	52.41 %	No
Residual		0.0002	1	0.0002			
Total		0.0535	8				

an ageing variable. The time variable is then implicitly included in the water diffusion model, which can be predicted theoretically from the models in subsection 4.4.2.

On the other hand, the  $A_i$  coefficients depend only on the material and environmental conditions of the ageing protocol (temperature  $T$  and relative humidity  $RH$ , UV radiation intensity  $UV$  showed to be less harmful) and can be estimated by the linear model in equation (4.23) with the parameter  $\alpha_i$  (ANOVA effects) in tables 4.8 and 4.9.

### 4.6 A prediction method for composite ageing

From a scientific point of view, the multi-factorial model presented in this chapter can prove to be useful in two ways:

- for characterization and design of experiments, *ie* for the experimenter to follow a similar method to characterize other composite materials using different combinations of fibre/resin,

- for prediction, using this ageing model to estimate the ageing of a CFRP composite structure with variable geometries, since the effect is known.

### For material characterization/design of experiments

Based on all that has been exposed in this chapter, a simple method for establishing a statistical ageing model for a given material is proposed:

1. By isothermal tests or from material supplier's datasheet, establish the diffusivity  $D$  and saturation moisture  $M_s$  Arrhenius' laws, as in equations (3.4) and (3.6).
2. Determine the parameters of the ageing protocol: time duration of the cycle ( $\Delta t_-, \Delta t_+, \Delta t$ ) and the corresponding temperature and relative humidity levels, in order to determine  $M_s, D_-$  and  $D_+$  by using the model described in section 4.4.1.
3. Build a water absorption model using the recursive equation (4.14), determining by least squares and equation(3.3) the equivalent diffusivity  $D_{eq}$  and equivalent saturation mass concentration  $M_{s,eq}$ .
4. Design and carry out an experimental campaign, using  $2^k$  sample series (where  $k$  is the number of factors to be considered; in this chapter,  $k = 3$ ).
5. The parameters  $\alpha$  of the simplified ageing model (4.23) for the elastic moduli of the composite can be then determined by a linear regression, while the pertinence of the model can be statistically assessed by an ANOVA.

### For prediction

If the ageing model for a material (CFRP or other) is available, the experimenter can use it to predict the ageing of the analysed structure:

1. Simulate the evolution of water concentration  $\mu$  using an analytical or numerical model that takes into account the geometry of the part, since the equivalent diffusion parameters ( $D_{eq}$  and  $M_{s,eq}$ ) are known.
2. Using linear models (4.22) and (4.23), determine the level of ageing for a given water concentration state.

## 4.7 Conclusions about the ageing model

Independently from the microscopic mechanisms of transformation, the hereby presented mathematical model, based on Prony series, proposed a characterization and prediction method for a set of simultaneous physical/chemical phenomena that intervene macroscopically on CFRP ageing. The parameters of that model, fitted on the basis of the non-linear least squares (NLLS) criterion, were determined from experimental results. However, the application of these results was restricted to samples with the same geometrical dimensions and proportions. Other state variables can eventually replace the time variable in this formulation, although keeping the same objective.

## Chapter 4. Multi-factorial model for CFRP ageing

---

Thus, the main contribution of this chapter is not only to suggest the form of a mathematical model, but also to set this model free from the specific dimensions of the physical samples that were experimented with. In order to do so, the first step was to study the link between the theoretical and the experimental results of water diffusion and mass absorption. Such analysis gave as a result "equivalent" diffusivity coefficients and saturation masses. The second step proved by statistical means that there is a correlation between the absorbed moisture and the ageing in cyclic conditions, that can be related to isothermal ageing properties. The water concentration works then as a "state" variable for a multifactor ageing model. In this case, the model gets free from the geometry of the specimen. In other words, based only on the constitutive properties of a composite material and the features of a cyclic ageing protocol, the ageing can be approximately predicted. Other state variables can eventually replace the time variable.

These models are going to be used in chapter 8 to predict the material ageing in a more complex demonstrator, using the same material and measurement techniques. This part of the work has been published [Guzmán et al., 2014].

# Survivability of integrated piezoelectric PVDF film transducers

## 5.1 PVDF transducers survivability tests

Part of the continuous monitoring method developed in this thesis is the ageing of the embedded piezoelectric transducers. Indeed, this fact is to be taken into account: integrated sensors will inevitably suffer the same constraints as the main structure, and transducer survivability must then be validated as well.

The goal of this chapter is to show experimental results proving that PVDF sensors, properly manufactured, handled and integrated to a composite structure, are capable to provide accurate information about the constitutive properties of the latter, even after exposure to accelerated ageing. As mentioned in chapters 2 and 4, the monitoring method is based on modal analysis and numerical-experimental identification. The validation is carried out by comparison between obtained data by PVDF patch sensors and by neutral non-aged sensors (accelerometers), even with the former going through a demanding long-term accelerated ageing process.

The accelerated ageing protocols for these tests were detailed in chapter 3. Among all the experimental series described there, four of the harshest environments were selected in order to analyse the ageing behaviour of the embedded PVDF sensors. The same ASTM standards (D4672, C581, D1151, D5229, G151 and G154) for polymer structures testing were applied to all four cases. In order to reveal any loss of sensitivity or measurement quality due to exposition to ageing factors, multi-stage experimental campaigns take place.

It was important to carry out experiments under these circumstances, since the main object of the whole method aims to the use of modal analysis with embedded sensor networks. On the contrary to static methods, dynamic methods are generally much better suited for implementation *in situ*. This is compatible with the purpose of SHM, since continuous and/or real-time monitoring is aimed. Modal parameters, in partic-

## Chapter 5. Survivability of integrated piezoelectric PVDF film transducers

ular natural frequencies, are extracted from the frequency response functions (FRF) in the case of experimental modal analysis. Moreover, this constitutes a base for future development, since SHM may require the use of output-only dynamic measurements in order to carry out an Operational Modal Analysis (OMA), much more adapted to *in situ* monitoring of full-scale aeronautical structures [Ewins, 2000]. The information provided by modal analysis is enough for the feature extraction, after what the inverse identification method allows deducing the mechanical properties of the materials. Based on the finite element (FE) method, this method takes into account more complex and non-linear interaction phenomena between several deformation modes [Farrar et al., 2001, Cugnoni et al., 2007] than analytical models. This family of identification methods is possible thanks to the currently available computing power of nowadays processors.

The selected ageing protocols were carried out on sample series C, D, E and F described in chapter 2, in a similar way as the protocols in chapter 4 (see table 5.1). It is important to point out the fact that the maximum temperature is under the Curie temperature of PVDF (around 145 [°C]). Even though the loss of piezoelectric properties is not necessarily expected, the objective is precisely to check that it does not affect the quality of dynamic measurements significantly. Processed and analysed data, used to validate statistically the survivability of PVDF transducers in this chapter, were obtained by means of EMA exclusively.

Data acquired from D-, EF1- and EF2-groups were used to set up the multi-factorial model established in chapter 4 as well. The details of experimental tests are mentioned in section 4.1. Concerning the samples of the C-series, the experiments were similarly carried out, with the following distinct parameters:

1. The number of cycles between rounds of experimental tests is 98 in this case, although the last test was carried out at 800 cycles instead of 784.
2. The lowest eight natural frequencies were monitored.
3. The only PVDF patch was located close to the middle. Since it had a reduced sensitivity in the transversal direction, some modes were more difficult to detect.

Table 5.1 – Summary of ageing protocol parameters for all the series: nominal values ( $T$ ,  $RH$  and  $UV$ ), the time period  $\Delta t$ , the number of cycles  $N_{cyc}$  and the number of rounds.

Group	Samples	Temperature		Relative humidity		UV radiation		$\Delta t$ [min]	$N_{cyc}$	$q$
		Min	Max	Min	Max	Min	Max			
C	CI-CV	5	95	0	95	0	0	120	800	9
D	DI-DVI	5	95	0	95	0	300	90	800	8
EF1	EI, FI	45	135	0	70	0	300	90	900	9
EF2	EII, FII	45	135	0	70	0	0	90	900	9

## 5.2. Interpretation and analysis of experimental results

Table 5.2 – Number of sensors used simultaneously for each plate.

Group	Sample	Accel.	Glued patch	Embedded patch
C	CI-II-III-IV-V	1	1	0
D	DI-III-IV-V-VI	1	0	1
EF1	EI, FI	1	0	2
EF2	EII, FII	1	0	2

### 5.1.1 PVDF film sensors and integration techniques

The PVDF sensors used in the experimental campaign are catalogued as DT1-028K, manufactured by Measurement Specialties© Inc (see subsection 2.2.2). The reference sensors were all Brüel&Kjaer© 's 4517C uniaxial accelerometers. The multi-channel conditioning amplifier B&K 2692-C was used to amplify the PVDF sensors and accelerometer signals in a frequency band of 0.1 [Hz] - 10 [kHz].

Two types of integration were adopted:

1. A PVDF sensor is considered glued if epoxy or other chemical glue was used to patch up the PVDF sensor on the surface after the curing process (figures 2.3(a) and 5.1(a)).
2. On the other hand, it is considered embedded if the integration took place during the layup process between two epoxy pre-impregnated (PrePreg) layers, before the curing process (figures 2.3(b) and 5.1(b)).

In general, both cases are referred to as integrated PVDF sensors. The number of PVDF sensors glued or embedded per plate is shown in table 5.2.

The weighing of the PVDF sensors, including the lead attachments (no cables), gives an average value of  $0.53 \pm 0.01$  [g], which is in the same order of magnitude as the accelerometers. The weight of the glue is much more important: an glued sensor adds in average 2 [g] of glue. This is why the weighing of the sample before ageing should be done **after** the sensor integration. For more details on the sensor influence, see appendix A.

## 5.2 Interpretation and analysis of experimental results

### 5.2.1 Visual inspection of the PVDF sensors

First of all, all the PVDF survived the chosen ageing protocols and they maintained their sensorial capability throughout the experimental campaigns. During the visual inspection, the samples did not exhibit particular problems threatening the acquisition of dynamic measurements. The dimensions were strictly measured and com-

pared, although no significant changes in length, width or thickness were noticed throughout time. The only noticeable change was a progressive browning of all the exposed surfaces, including the composite panel itself, as well as the layer of epoxy glue in the case of surface-attached PVDF sensors.

In the case of glued sensors, only a thin layer of epoxy resin (high temperature Araldite) glue was used at first to stick the PVDF sensor to the surface. The result is shown in figure 5.1(a). A problem found in some cases was the absence of any electric signal from the embedded sensors after the curing process. It is hypothesised this was due to the electric-conductive nature of carbon fibers that lead to the appearance of a short circuit between the electric attachments of the PVDF sensors. If the lead attachments are not electrically insulated, the contact with carbon fibres can establish a short circuit rendering any signal acquisition impossible. Thus, a layer of electric insulator (e.g. epoxy) should be applied to protect the electric attachments. Before embedding, cables should be protected as well, in order to avoid any metallic fatigue leading to fracture. In our case, shrink sheaths were used as reinforcement in addition to the electric cable insulator, which solved the problem.

### 5.2.2 Results interpretation

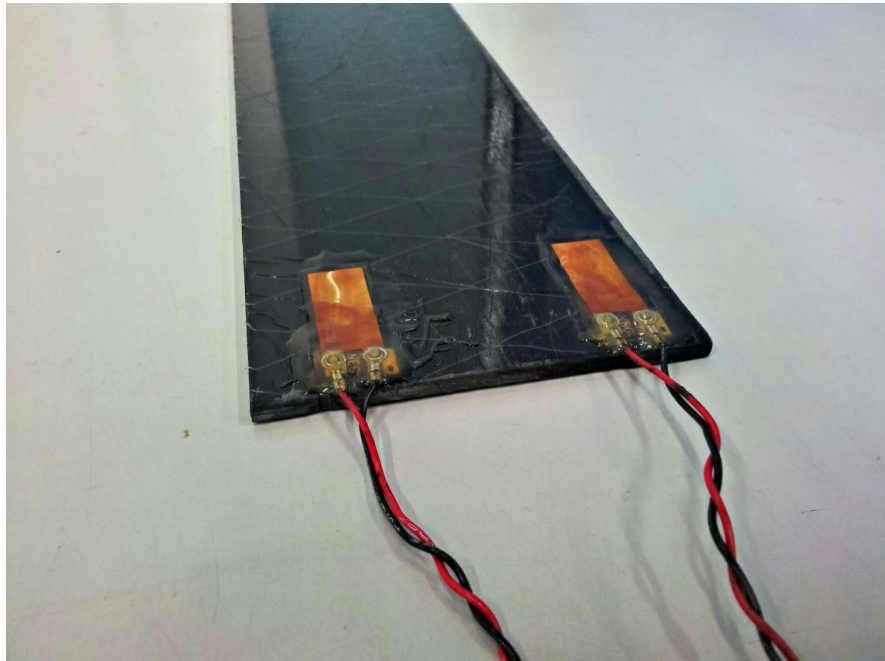
The relative mass and elastic moduli are noted similarly to the previous chapter:  $\mu = m/m_0$ ,  $\epsilon_1 = E_1/E_{10}$ ,  $\epsilon_2 = E_2/E_{20}$  and  $\gamma_{12} = G_{12}/G_{120}$ . The same observations concerning the evolution of water concentration and elastic moduli can be stated from the results shown in figures 5.2 and 5.3. These curves are constituted by the combined datasets coming from the integrated PVDF and the accelerometers.

1. In the general case, the increase of the total mass seems regular and not scattered, as shown in figure 5.2, and the shape of the graphs is approximately an exponentially increasing asymptotic curve. For example, the samples of the D-group absorb up to 0.3 %, while those of the EF1-group absorb 0.3%.
2.  $E_1$  changes irregularly over the weeks (figure 5.2) and exhibits a lot of scatter (up to 2 % of standard deviation). It is difficult to safely declare that there is a particular trend since the scattering shown by the results is quite significant.
3. The  $E_2$  and  $G_{12}$  plots exhibit a clear decrease of stiffness of the resin matrix-dominated elastic moduli. However, the extent of the loss depends on the ageing parameters. For example, the extent of the loss is 4% for the D-group, and 8% for the EF1-group after 5 weeks. In all cases, the decrease in relative stiffness is much more significant than the scattering (as shown by the error bars).

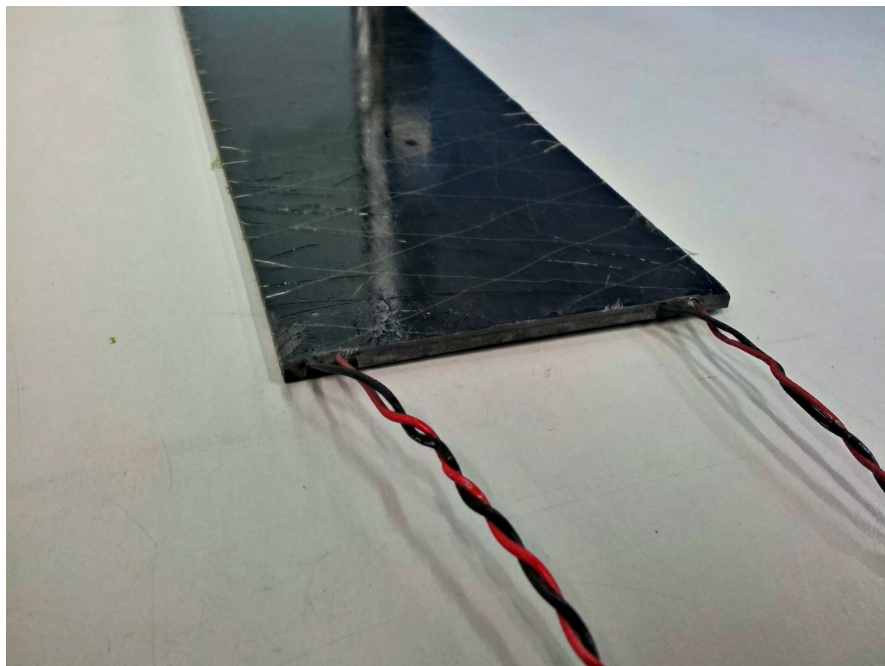


## 5.2. Interpretation and analysis of experimental results

---




(a)



(b)

Figure 5.1 – Examples of integrated PVDF sensors: (a) Correctly glued (and aged) PVDF sensors; (b) Correctly embedded PVDF sensors.

### 5.2.3 Measurement quality differences between PVDF film sensors and accelerometer

Qualitatively, measured FRFs by both accelerometer and PVDF sensors are very similar after the 900-cycle ageing process as it can be verified in figures 5.4 (a) and (b). 

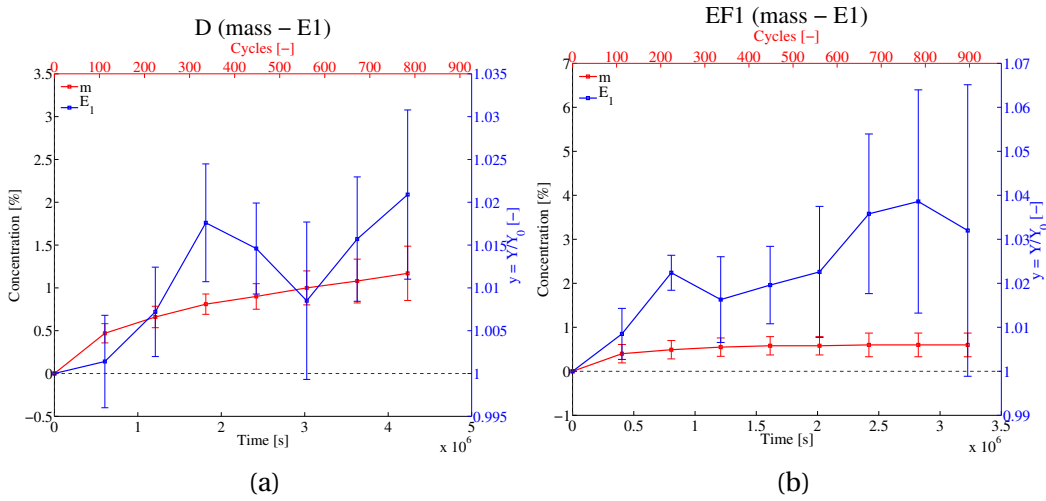


Figure 5.2 – Evolution of mass  $m$  and Young's modulus  $E_1$  in (a) D- and (b) EF1-groups. Error bars represent the standard deviation.

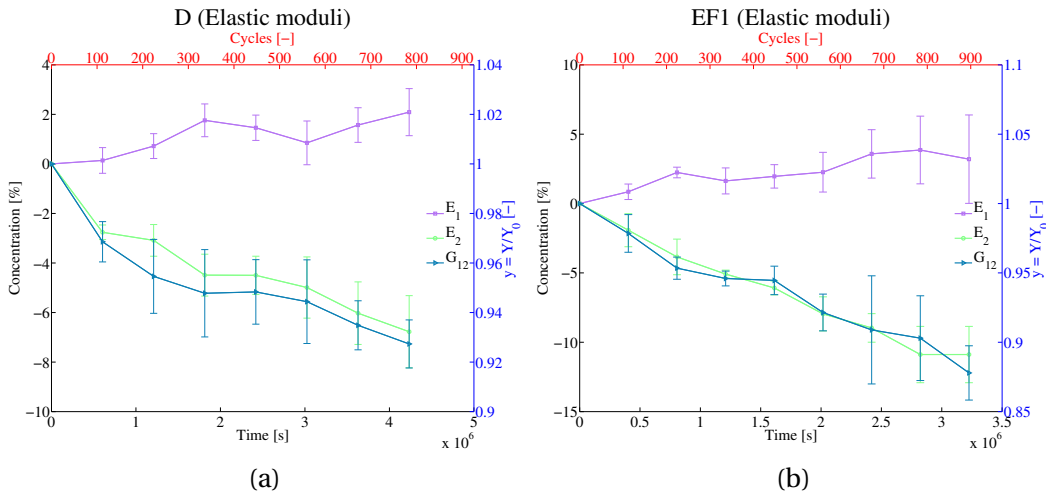


Figure 5.3 – Evolution of  $\epsilon_1$ ,  $\epsilon_2$  and  $\gamma_{12}$  in (a) D- and (b) EF1-group. Both series were subjected to UV radiation ageing.

figure 5.4(a), the two FRF match almost perfectly. In figure 5.4(b), the position of the peaks is the same, but the amplitude is different over the frequency band. Differences in the measured dynamic amplitude between the FRFs can be mainly attributed to the fact that accelerometers and PVDF measure to very different magnitudes (acceleration and strain), and are at very different locations on the sample. Anyhow, in both cases the positions of resonance peaks are observed by the accelerometer and the PVDF sensor independently of the nature of the measurement.

It is important to point out that in some cases, the pre-amplifier gain had to be adjusted to increase the signal-to-noise ratio, to compensate the fading signal some

## 5.2. Interpretation and analysis of experimental results

---

PVDF were object of. The compensation at the end of the ageing protocol could reach a factor of 100 in some cases. This fading could be attributed to the loss of piezoelectric sensitivity, specially since some of the protocols heat up the specimens close to the Curie temperature.

Since the necessary information about the position of the resonance peaks is not disturbed by changes in the signal amplification, this has no repercussions on the identification process, and the question of the piezoelectric sensitivity loss was not further investigated. An example comparison between the parameter estimations obtained with the accelerometer and the PVDF is shown in figures 5.4(c) and (d), for specimens EII and DIV. In the first case, there are differences in some points in estimations of both  $\epsilon_1$  and  $\gamma_{12}$ , although globally the measurements follow the same patterns. In the second case, the results are even more satisfying since the estimations match almost perfectly, just like the FRF shown in figure 5.4(b).

These results demonstrate that PVDF can perfectly keep measuring correctly the natural frequencies, even if they are subjected to accelerated (or natural) ageing conditions that affect their elastic properties.

### 5.2.4 Statistical data analysis: ANOVA

An Analysis of Variance (ANOVA) test remains a useful statistical tool to validate the equivalence of two stochastic variables, in this case the elastic properties as measured by the accelerometers and by PVDF sensors. The ANOVA was carried out to demonstrate the significance (or insignificance) of environmental factors on a PVDF sensor measurement quality, with respect to measurements coming from a non-aged reference sensor, in this case the accelerometers. A multi-factorial model, similar to the one detailed in chapter 4, could be established, which included as basic factors: (a) the maximum temperature of the cycle, (b) the UV radiation intensity, (c) the integration technique and (d) the number of cycles. The inclusion of the latter as a experimental factor can be exceptionally be justified in this occasion, since the only goal of this model is to compare statistically the measurements carried out with and without using the PVDF sensors.

The linear model with interactions is based on equation 5.1.

**Chapter 5. Survivability of integrated piezoelectric PVDF film transducers**

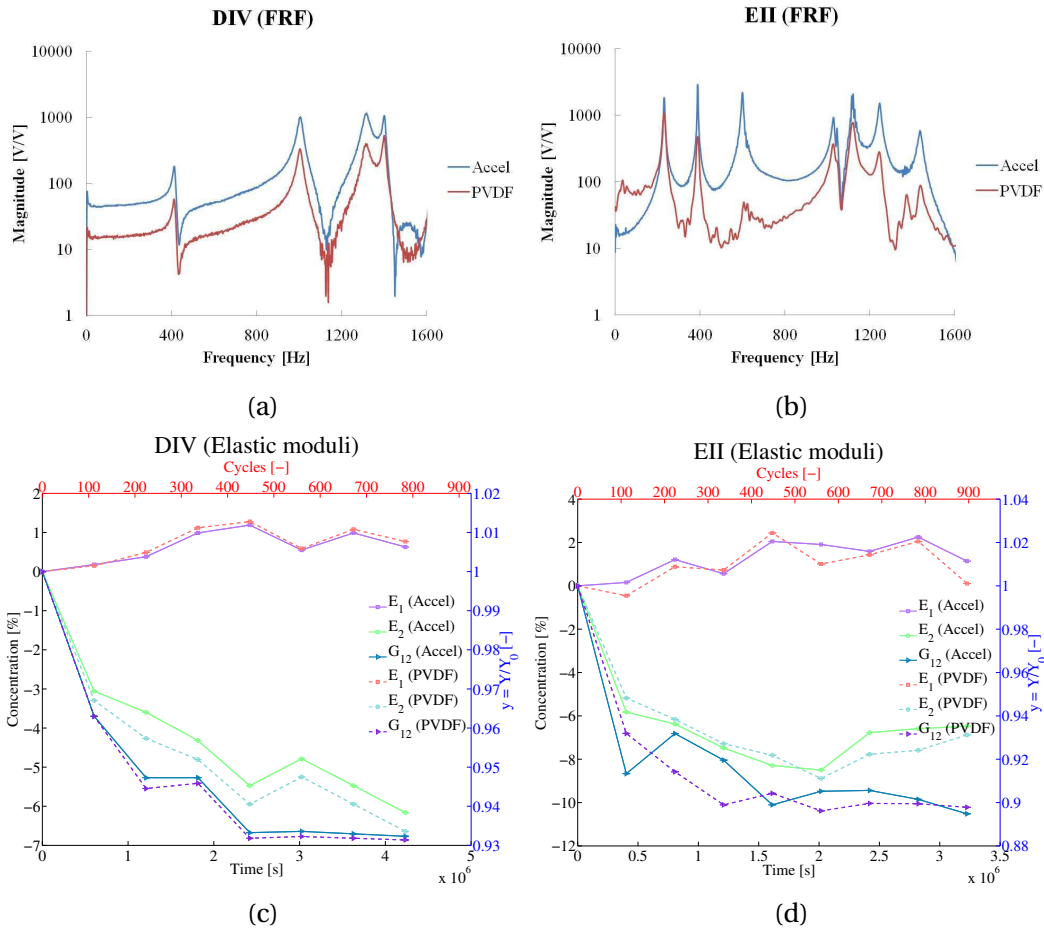


Figure 5.4 – (a) FRF as measured by the accelerometer and the PVDF sensor on DIV after a 300-cycle ageing period. (b) FRF as measured by the accelerometer and the PVDF sensor on EII after a 600-weeks ageing period. (c)  $[\epsilon_1; \epsilon_2; \gamma_{12}]$  vs. Time plot as estimated by the accelerometer and the PVDF sensor in DIV. (d)  $[\epsilon_1; \epsilon_2; \gamma_{12}]$  vs. Time plot as estimated by the accelerometer and the PVDF sensor in EII.

## 5.2. Interpretation and analysis of experimental results

Table 5.3 – Equivalence table between real and non-dimensional factor after application of equation (5.3).

Variable	$T [^{\circ} \text{C}]$		$RH [\%]$		$UV [\text{W}/\text{m}^2]$		Total cycles [-]	
	$x_1$		$x_2$		$x_3$		$x_4$	
	Low	High	Low	High	Low	High	Low	High
Absolute values	[5,95]	[45,135]	0	300	0	1	0	900
Normalized values	-1	+1	-1	+1	-1	+1	-1	+1

$$\begin{aligned}
 y^e &= a_0 + \sum_{i=1}^4 a_i x_i + \sum_{i=1}^4 \sum_{j=1}^4 a_{ij} x_i x_j + \sum_{i=1}^4 \sum_{j=1}^4 \sum_{k=1}^4 a_{ijk} x_i x_j x_k \\
 &+ a_{1234} x_1 x_2 x_3 x_4 = \mathbf{A} \cdot \mathbf{x} \\
 \mathbf{A} &= [A_0, A_1, A_2, \dots, A_{15}] = [a_0, a_1, a_2, a_3, \dots, a_{1234}] \\
 \mathbf{x} &= [1, x_1, x_2, x_3, \dots, x_1 x_2 x_3 x_4]
 \end{aligned} \tag{5.1}$$

The four independent variables  $x_1$ ,  $x_2$ ,  $x_3$  and  $x_4$  represent the normalized ageing factors (table 5.3). In this model, the relative variable  $y^e$  is defined as

$$y^e = (y)_{Accel} - (y)_{PVDF} \tag{5.2}$$

where the dependent variables  $y$  can be either  $\epsilon_1$ ,  $\epsilon_2$  and  $\gamma_{12}$ . Physically,  $y^e$  is defined as the difference between two estimations of the elastic moduli: one coming from non-aged accelerometers, and one from aged PVDF sensors.

The normalization formula is a bit different in this occasion from the one presented in chapter 4. Indeed, the normalization operation has been carried out by applying equation 5.3 to the absolute factors:

$$x = \frac{2(u - \bar{u})}{\Delta u}; \bar{u} = \frac{u_{max} + u_{min}}{2}; \Delta u = u_{max} - u_{min} \tag{5.3}$$

where  $u$  is the absolute value and  $x$  is the normalized value between -1 and +1 (no units). It must be noted that equations 3.10 and 5.3 are similar but not identical, since they lead to two different normalizations.

## Chapter 5. Survivability of integrated piezoelectric PVDF film transducers

Table 5.4 – ANOVA tables:  $SS$  = sum of squares,  $DoF$  = degrees of freedom,  $MS$  = mean square,  $F$  = Fischer's quotient,  $p$  = Fischer's probability function. For these results, the differences  $y^e$  where expressed as percentages.

$\epsilon_1$	$SS$	$DoF$	$MS$	$F$	$p$ -value	$1 - p$
Model	91.0	16	5.67	0.45	94.2 %	5.8 %
Residual	238.6	19	12.5			
Total	329.6	35				
$\epsilon_2$	$SS$	$DoF$	$MS$	$F$	$p$ -value	$1 - p$
Model	223.9	16	14.0	0.52	90.2 %	9.8 %
Residual	507.5	19	26.7			
Total	731.5	35				
$\gamma_{12}$	$SS$	$DoF$	$MS$	$p$ -value	$1 - p$	$1 - p$
Model	126.5	16	7.9	0.54	89.0 %	11.0 %
Residual	277.4	19	14.6			
Total	403.9	35				

The test of hypothesis corresponding to this ANOVA can be expressed as:

$$\begin{aligned}
 H_0 & : 0 = A_1 = \dots = \quad (\text{ie no diff. between PVDF sensors and accel.}) & (5.4) \\
 H_1 & : \exists A_i \neq 0 \quad (\text{ie significant diff. between PVDF sensors and accel.})
 \end{aligned}$$

In this test, the null hypothesis states that there is no significant statistical difference between elastic moduli as measured by the PVDF sensors and the accelerometers (the difference between the measurements are due only to random measurement error), while the alternative hypothesis states that there is at least one environmental factor affecting the measurement quality of the PVDF sensors. The results are summarized in table 5.4: the values of  $p$  correspond to the significance level of measurement randomness, and  $1 - p$  is the level of significance of a "systematic difference" between accelerometers and PVDF.

The null hypothesis can be proved with an acceptable level of significance. Indeed, but the most representative are the values of the  $p$ -value in the three cases detailed in table 5.4, 94%, 90% and 89%, corresponding to  $\epsilon_1$ ,  $\epsilon_2$  and  $\gamma_{12}$  respectively. The  $p$ -value represents the significance level of randomness in the obtained measurements, which is very high compared the level of significance of a "systematic" drift between PVDF sensors and accelerometers (5% for  $\epsilon_1$  and around 10 %  $\epsilon_2$  and  $\gamma_{12}$ ). Thus, this ANOVA test demonstrates that it is highly probable that the linear model with interactions has little or nothing to do with the differences between estimations of the elastic properties from both accelerometer and PVDF sensors, and that those are mostly due to measurement randomness.

### 5.2.5 Conclusions on survivability of integrated PVDF sensors

It has been demonstrated in this chapter that, in principle, PVDF film sensors are able to survive the integration process, as well as the natural ageing process within the limits stipulated in the previous sections, as long as they are properly handled and integrated. PVDF sensors provide reliable data about the state of the elastic properties of a composite material widely used in the aeronautical industry such as the carbon fibre/epoxy composite. This conclusion is based on comparisons strictly limited to dynamic measurements obtained from PVDF and standard non-aged accelerometers. The quality of the measurements is judged satisfying and sufficient for the primary purpose of using PVDF sensors in dynamic non-destructive structural monitoring process. Some recommendations in future investigation of the integration of PVDF sensors in aeronautical structures are however worth to be mentioned.

First, the survivability range of temperatures at which the sensors were tested (+5[°C] to +135[°C]) indicate the temperatures at which the PVDF sensors can be stored for short periods of time without suffering irreversible damage. This, combined to the safety storage range of temperatures given by the manufacturer (-50[°C] to +100[°C]) and the known Curie temperature (+145[°C]), allows a safe temperature range spanning from -50[°C] to +145[°C] for the use in cyclic ageing applications. Exception made of some spots (especially those close to the engines), this interval largely encompasses the range of temperatures found commonly in airframes, in all flight phases. However, it is advised that the dynamic testing should still be carried out only with PVDF inside the working temperatures given by the manufacturer, in this case between -5[°C] and +100[°C].

This work has been partially published in [Guzman et al., 2013].





# 6

## Establishment of a transducer network: placement strategy

### 6.1 Motivation

As stated in previous chapters, the full potential of modal analysis can be used only if an optimal placement of the sensor network is carried out.

The problem of the OSP has been studied widely in the literature. There are many possibilities concerning the choice of an objective function, and thus the optimization results can be very different from one method to the next.

1. Energy-based methods: the kinetic energy method (MKE) [Heo et al., 1997], the driving-point residue method [Worden and Burrows, 2001], effective independence (EI) method [Li et al., 2007], etc. These methods aim in general to maximize the energy transfer rates between the structure and the transducers.
2. Controllability/observability-based methods: the close-loop method [Güney and Eskinat, 2008], the balanced reduced models method [Nestorović and Trajkov, 2013], etc. Based mostly on space-state dynamic models of the structure, the look to guarantee the observability/controllability of the structural vibrations.
3. Stochastic methods: the noise-to-signal method [Kirkegaard and Brincker, 1994], the entropy method [Papadimitriou, 2004], the variance method (VM) [Meo and Zumpano, 2005], etc. These methods aim to minimize the effect of random variables in the signal acquisition.

From the methods mentioned above, the first family of methods is very commonly applied to structural engineering problems (civil or mechanical). Among these, the Effective Independence (EI) method was proposed by Kammer [Kammer, 1990]. Nowadays, this is one of the most reliable methods and used in aerospace applications. This method was selected to design the transducer network.

## 6.2 Effective Independence method for sensor placement

The formulation in this section is inspired from the one presented by [Li et al., 2007], but is adapted to work with strain mode shapes. The more complex is the shape of the candidate structure, the more sensors placed in strategic places are needed to ensure the observation of all lowest frequency modes. As a general rule, the minimum number of transducers needed to observe/control the vibrational behaviour of a structure depends on the sought modes and their shape. For the dynamic model of a given structure, OMA identifies the modal parameters: natural frequencies, damping factors and strain modes. In order to identify correctly the natural frequencies  $\omega_k$  of the  $k^{th}$  order and the corresponding modal vectors  $\phi_k$  (which are the solutions of the generalized eigenproblem in equation (1.4)), the sensors must be located in the right locations. The usefulness of a linear discrete model (for example an FE numerical model, or an experimental discrete model in the sense of EMA) to determine the couples  $(\omega_k, \phi_k)$  is evident, because an optimal placement can be determined before the manufacturing of the part (with the integrated transducers).

A simple but naive way to place the transducers in the structure is to check visually the distribution of the strain field for each deformation mode, after a dynamic simulation of the FE model, and the transducers are placed in the spots showing the maximal strain deformation afterwards. However, this technique becomes too complex and resource-consuming when more complex shapes are to be modelled. Smarter and more sophisticated techniques have been developed over the years, as reviewed by [Meo and Zumpano, 2005]. These techniques are either energy-based or data amount-based. Among the former, the effective independence (EI) technique was validated [Kammer and Tinker, 2004] for aerospace structures and compared to another similar, called the modal kinetic energy (MKE) method [Li et al., 2007]. The EI was used in this thesis to solve the OSP problem. An in-house software applying the mathematical principle behind EI was developed using MATLAB©.

An index vector  $\mathcal{K}$  is defined by

$$\mathcal{K} = \text{diag}(\Phi\Phi^+) \tag{6.1}$$

for the EI method. In these expressions,  $\Phi^+ = [\Phi^T\Phi]^{-1}\Phi^T$  denotes the pseudo-inverse matrix of matrix  $\Phi$  ( $\Phi^T$  denotes the transpose matrix), which contains the row-vectors corresponding to the total number  $m^e$  of eigenmodes  $\phi_k$  to be observed. In this con-

## 6.2. Effective Independence method for sensor placement

---

text,  $\Phi$  is given by

$$\Phi = [\phi_1 \dots \phi_k \dots \phi_{m^e}]^T \quad (6.2)$$

The  $diag()$  operator denotes the vector formed by the diagonal elements of a matrix. Let us consider a structure with  $r$  possible spots, and consequently  $r$  DoF in its modal representation, to which  $m$  sensors need to be integrated. After  $\mathcal{K}$  is evaluated, the element with the weakest energy (*ie* the lowest value of  $\mathcal{K}$ ) is tracked. The corresponding row is deleted from  $\Phi$  to form a reduced matrix  $\Phi_{(1)}$  (with a rank of  $r - 1$ ), which is used to evaluate the next iteration  $\mathcal{K}_1$  of the index vector, based on formula 6.1 for the EI technique. The procedure is sequentially repeated until the  $p^{th}$  iteration, where  $p = r - m$ :  $\mathcal{K}_p$  has in that case  $m$  elements, corresponding to the  $m$  optimal spots where the sensors should be placed.

As it has been demonstrated by [Li et al., 2007] that the EI technique has the advantage of "renormalizing" the index vector  $\mathcal{K}$  after each iteration. This is a fundamental point (and the main reason to have chosen the EI technique over the similar concurrent MKE method [Heo et al., 1997]), because this renormalization is compatible with the general case where the modal mass matrix  $M$  is not a multiple of the identity matrix  $I$ . Indeed in that case, the index vector becomes for the EI method

$$\mathcal{K} = diag(M^{1/2} \Phi [M^{1/2} \Phi]^T M^{1/2} \Phi)^{-1} [M^{1/2} \Phi]^T = diag(\Phi \Phi^+) \quad (6.3)$$

where  $M^{1/2}$  is the square root of the symmetric positive definite mass matrix  $M$ . It can be seen that  $\mathcal{K}$  remains independent of the mass matrix in this.

An inconvenient of this approach is found when  $r$  is large, *ie* there are too many DoF, a condition frequently observed when the analysed model is based on the FE formulation. A simplifying additional step is to turn to a triangular-orthogonal QR decomposition in order to speed up the computation. For each iteration, the (reduced) mode shape matrix  $\Phi_{(i)} = QR$  is decomposed, with the unitary orthogonal matrix  $Q_{[r \times p_i]}$  ( $p_i = r - i$ ) and the upper triangular matrix  $R_{[p_i \times p_i]}$ . By substituting  $QR$  in equation (6.1), the index vector becomes then:

$$\mathcal{K} = diag(QR [R^T Q^T QR]^{-1} R^T Q^T) = diag(QQ^T) \quad (6.4)$$

since  $\mathbf{Q}^T \mathbf{Q} = \mathbf{I}_{[p_i \times p_i]}$  and can be computed directly through the row norms  $|\bar{Q}_j|$  of matrix  $\mathbf{Q}$

$$\mathcal{K} = \text{diag}(\mathbf{Q}\mathbf{Q}^T) = [|\bar{Q}_1|^2, |\bar{Q}_2|^2, \dots, |\bar{Q}_r|^2]^T \quad (6.5)$$

This last definition in (6.5) for the EI index is between 4 to 5 times faster than the classic formulation in equation (6.1).

### 6.2.1 Note about optimization of PVDF transducers as actuators

Since the inverse energy transformation (electric to mechanical) is possible using the PVDF transducers, as shown in the literature [Giurgiutiu, 2008, Park et al., 2006], it is possible to introduce the actuation to the PVDF. The optimization problem for actuators shares the same mathematical base as the equivalent problem in sensing. This means that for a given configuration of the PVDF network, all the modes that can be discerned can also be excited, and this is due to the symmetric relationship between mechanical and electric displacement in the fundamental piezoelectric equations [Tichý et al., 2010]. If for example an EI-optimized PVDF network is considered, the transmission of the modal kinetic energy is optimized for the whole set of considered modes. Those can be sensed and excited at the same time.

## 6.3 Transformation to strain mode shapes

In modal analysis, the framework is generally based on the hypothesis that the displacement (or the acceleration) signals are the available output from the transducer network. The notions of modal orthogonality and linear independence may be lost if the modal analysis procedures are indiscriminately used replacing the displacement mode shapes by the strain shapes. In order to validate the latter instead, a theoretical derivation (for an FE model) was carried out by Yam *et al* [Yam et al., 1996], who showed that a strain mode is an energy equilibrium state as a displacement mode is, and therefore a modal parameter of the structure.

In an attempt to justify the use of strain mode shapes in the EI formulation, a transformation function between strain and displacement is suggested. This geometric transformation was detailed by [Foss and Haugse, 1995]: let us consider an FE model with  $r$  DoF (which can be equal to the number of elements) and  $m^e$  mode shapes. The modal strain matrix  $\mathbf{s}$  and displacement matrix  $\mathbf{d}$  can be expressed in modal coordinates  $\bar{q}$

### 6.3. Transformation to strain mode shapes

through the corresponding modal 3-order tensors  $\Phi_s$  and  $\Phi_d$ :

$$\mathbf{s}_{[6 \times r]} = \Phi_s [\mathbf{s}_{[6 \times r \times m^e]} \bar{q}_{[m^e]}] \quad (6.6)$$

$$\mathbf{d}_{[3 \times r]} = \Phi_d [\mathbf{d}_{[3 \times r \times m^e]} \bar{q}_{[m^e]}] \quad (6.7)$$

$\Phi_s$  and  $\Phi_d$  contain the 6 strain and respectively 3 displacement modal  $r \times m^e$  matrices. Since in general  $m^e \ll r$ , a least-square approach leads to the determination of the nodal coordinates:

$$\bar{q} = \Phi_s^+ \mathbf{s} = [\Phi_s^T \Phi_s]^{-1} \Phi_s^T \mathbf{s} \quad (6.8)$$

$$\mathbf{d} = \Phi_d \Phi_s^+ \mathbf{s} = \mathbf{T} \mathbf{s} \quad (6.9)$$

where  $T_{[3 \times 6]}$  is the displacement-strain transformation matrix (which is basically a coordinate transformation matrix). Theoretically, this linear transformation allows a direct safe-passage between modal strain analysis and modal displacement analysis. Indeed, let us consider a vibrational response of the candidate structure at the  $k^{th}$  frequency, at a given point, first expressed as a displacement:

$$\mathbf{d} = \phi_k^d e^{j\omega_k t} \quad (6.10)$$

and then as strain:

$$\mathbf{s} = \phi_k^s e^{j\omega_k t} \quad (6.11)$$

From these two equations and equation (6.9), it can be deduced that  $\phi_k^d = T \phi_k^s$ , and consequently  $\Phi_d = T \Phi_s$ . Experimentally, the results of modal reconstruction from strain and displacement data has been demonstrated to be equal [Ewins, 2000, Foss and Haugse, 1995, Yam et al., 1996] for flat specimens. Concerning the mathematical development in the previous section, a displacement sub-matrix of  $\Phi_d$  can be safely replaced by a strain sub-matrix of  $\Phi_s$  (both can be estimated using an FE simulated vibrational model).

To clarify the notation used in this section, let us consider the strain  $s_{11}$  in the longi-

tudinal direction. Its modal matrix, in the sense of the EI optimization algorithm, is noted:

$$\Phi_{s_{11}[r \times m^e]} = \Phi_{s,1[1 \times r \times m^e]} \quad (6.12)$$

As it can be seen,  $\Phi_{s_{11}}$  is 2-order tensor (in other words, an  $r \times m$  matrix), while  $\Phi_s$  is a 3-order tensor. Similarly,

$$\Phi_{s_{22}} = \Phi_{s,2} \quad (6.13)$$

$$\Phi_{s_{33}} = \Phi_{s,3} \quad (6.14)$$

$$\Phi_{s_{12}} = \Phi_{s,4} \quad (6.15)$$

$$\Phi_{s_{13}} = \Phi_{s,5} \quad (6.16)$$

$$\Phi_{s_{23}} = \Phi_{s,6} \quad (6.17)$$

Concerning the displacements, the notation is equivalent:

$$\Phi_{d_1} = \Phi_{d,1} \quad (6.18)$$

$$\Phi_{d_2} = \Phi_{d,2} \quad (6.19)$$

$$\Phi_{d_3} = \Phi_{d,3} \quad (6.20)$$

### 6.4 Example: transducer placement on rectangular composite plates

As an example, the EI method is applied to the case of UD-layup,  $300 \times 100 \times 4$  [mm<sup>3</sup>], rectangular composite plates, with nominal elastic properties as in table 2.1.

Two optimized configurations were considered in the manufacturing of the samples:

#### 6.4. Example: transducer placement on rectangular composite plates

1. A "naive" method, which uses the principle of overlapping modes to locate three locations where the whole set of 8 vibrational modes shows a deformation. Mathematically, the optimization vector can be approximated as  $\mathcal{S}$ , which is given by the following equation:

$$\mathcal{S} = \text{diag}(\Phi_{s_{11}} \Phi_{s_{11}}^T + \Phi_{s_{22}} \Phi_{s_{22}}^T) \quad (6.21)$$

where  $\mathcal{S}$  is a vector (similar to  $\mathcal{K}$ ), each component of which is the squared norm of the total strain on a given location in an FE model (an element for example).  $\Phi_{s_{11}}$  and  $\Phi_{s_{22}}$  are sub-matrices of the strain mode shape tensor  $\Phi_s$ . The three locations with the highest coefficients are taken into account. This approach is based on the Gram matrix theory and is not iterative. Graphically, the same three regions can be visually estimated by observing the vibration modes, as in figure 6.1. The inconvenience of this method is that orientation of the PVDF patches is not selected rigorously following the maximal strain directions, but rather intuitively. In this case, the PVDF patches were oriented "along the border" of the specimen. The version of the OSP for the accelerometers is,

$$\mathcal{S} = \text{diag}(\Phi_{d_3} \Phi_{d_3}^T) \quad (6.22)$$

where 3 denotes the normal direction.

2. A more sophisticated method, based on the EI method and its result in equation (6.5), where the three spots with the highest coefficients in  $\mathcal{K}$  are taken into account. The method is applied to both  $\Phi_s$  and  $\Phi_d$ . As for the naive case,  $\mathcal{K}$  will focus only on in-plane deformation, *ie* only the  $s_{11}$  and  $s_{22}$  components of  $s$  are taken into account. Mathematically,

$$\mathcal{K} = \text{diag}(\Phi_s \Phi_s^+) \quad (6.23)$$

where  $\Phi_s$  is given by:

$$\Phi_s = \begin{bmatrix} \Phi_{s_{11}} \\ \Phi_{s_{22}} \end{bmatrix} \quad (6.24)$$

In this case, the longitudinal and transverse directions are decoupled, *ie* the algorithm will search a optimal configuration by selecting columns of matrix  $\Phi_s$ . Depending on the final selection, the column will have to be included in either  $\Phi_{s_{11}}$  or  $\Phi_{s_{22}}$ , which is what is going to give it the preferred direction to the PVDF patch sensor. The version of the EI for the accelerometers is given by

$$\mathcal{K} = \text{diag}(\Phi_{d_3} \Phi_{d_3}^+) \quad (6.25)$$

where 3 denotes the normal direction.

On an initial approximation, the efficiency of the optimization methods can be theoretically evaluated by its ability to discern close vibration modes. For each optimal placement, the modal assurance criterion (MAC) is computed between each pair of modes, from the set of evaluated "reduced" FE mode shapes. These reduced modes can be represented as short vectors  $\phi_k$ , the components of which are only the "observable" components by the sensor network. This reduced mode shapes are often called operational deflection shapes (ODS) in modal analysis.

To illustrate this, a CFRP plate with the nominal geometry  $300 \times 100 \times 4$  [mm<sup>3</sup>] and nominal elastic properties in table 2.1 was modelled by FE. The model is discretised in  $\sim 2 \times 2 \times 2$  [mm<sup>3</sup>] size elements. Each element corresponds to a single DoF (ABAQUS computes the interpolated displacements and strains at the center of the element). The results of both optimization models are shown graphically in figures 6.2 and 6.3.

As it can be seen, three consecutive modes (4, 5 and 6) would eventually have some modal extraction issues with the naive  $S$ -based method, while these apparent issues are solved remarkably well with the EI  $\mathcal{K}$ -based method. Concerning a placement optimization based on displacement (or acceleration), both methods give indifferently as the optimal points the corners of the plate under free-free boundary conditions, as shown in figure 6.4. It should be noted that the MAC matrix for the accelerometers is more decoupled than the MAC matrix for PVDF sensors, which can be attributed to the non-orthogonality of strain mode shapes.

Concerning the practical aspects of sensor integration, it is important to point out two aspects. First, while the punctuality assumption is reasonable for charge accelerometers, the PVDF area is not negligible and by its size it will certainly cover more than one element. This problem was solved by matching the position of the PVDF sensor with the selected location. Second, the opposite problem appears if two or more (very) close elements are selected in the final optimization. In this case, it may be impractical or even impossible to place the PVDF very close to each other. This is why it is often preferable to used vibration models with a lower number of candidate locations: if an FE model is used for the optimization, it would be preferred to preselect a certain number of candidate locations uniformly distributed, with an average distance between them that is of the same order of magnitude than the strain sensors. In the case of the subject plates mentioned above, only 45 candidate locations ( $9 \times 5$ ) were considered.

Experimental validation of the optimization is detailed in chapter 7.



#### 6.4. Example: transducer placement on rectangular composite plates

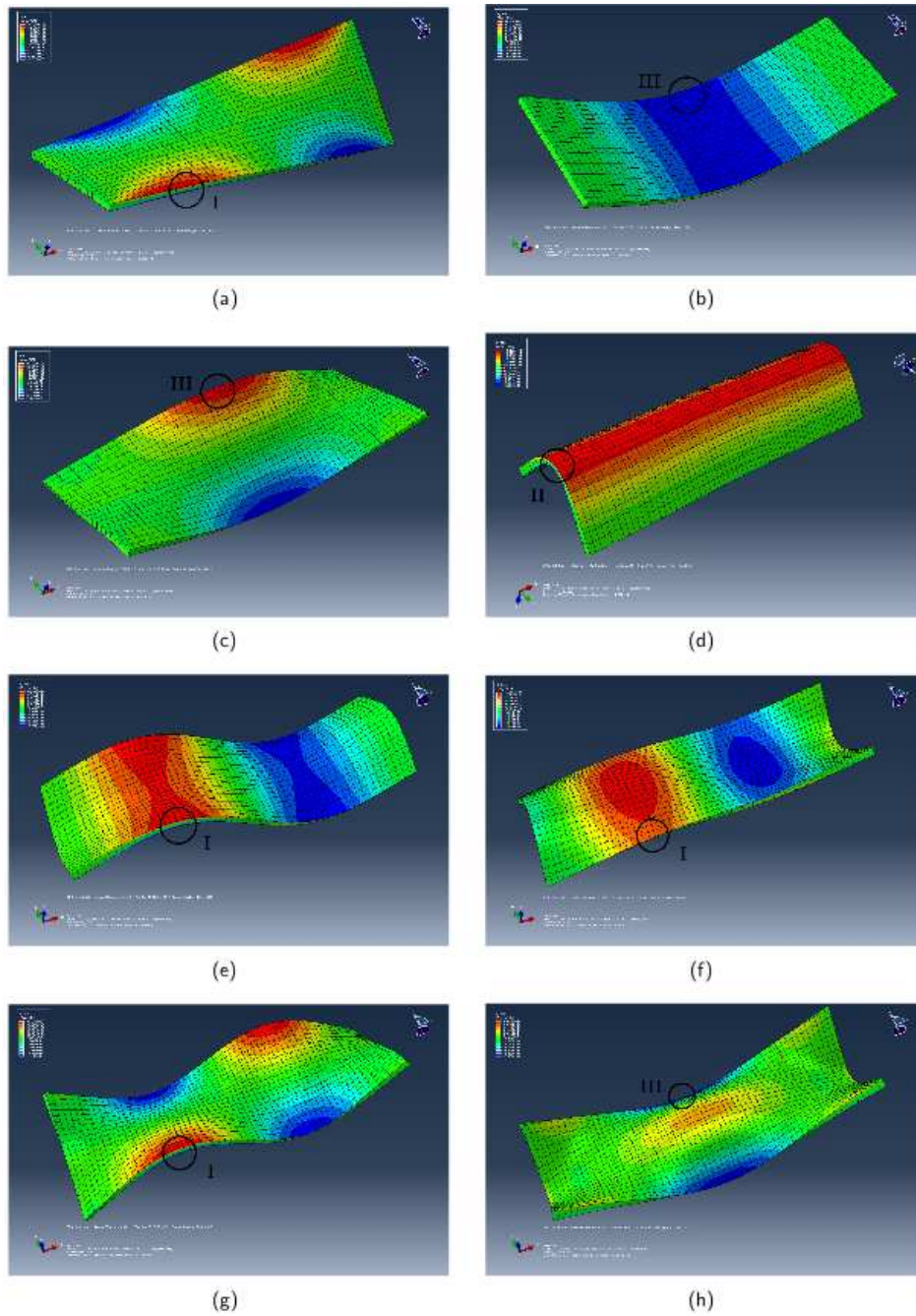


Figure 6.1 – Strain modes and strain levels for each of the 8 evaluated vibration modes. The regions with higher strain (in red) for each mode are superposed, and three of them are chosen.

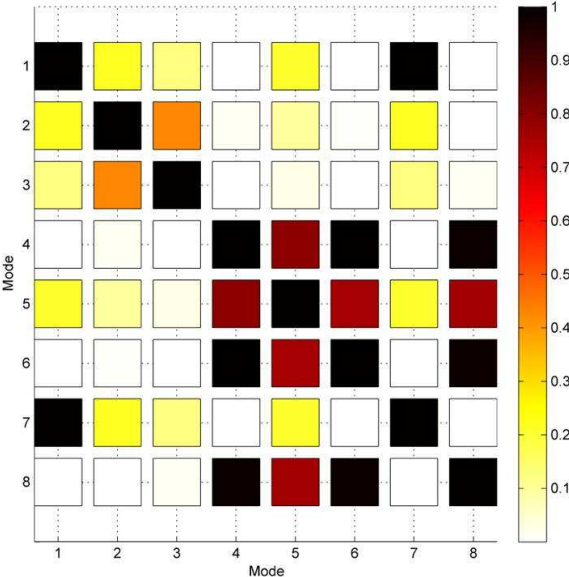
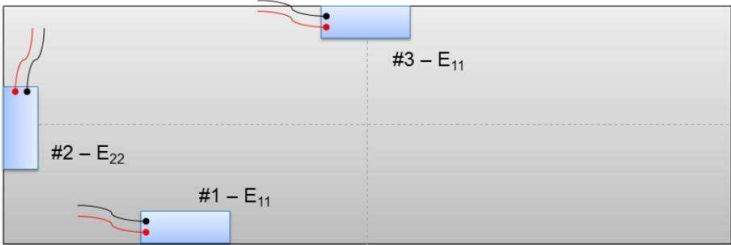


Figure 6.2 – Configuration 1: *S*-optimized placement, for 3 strain transducers.

## 6.4. Example: transducer placement on rectangular composite plates

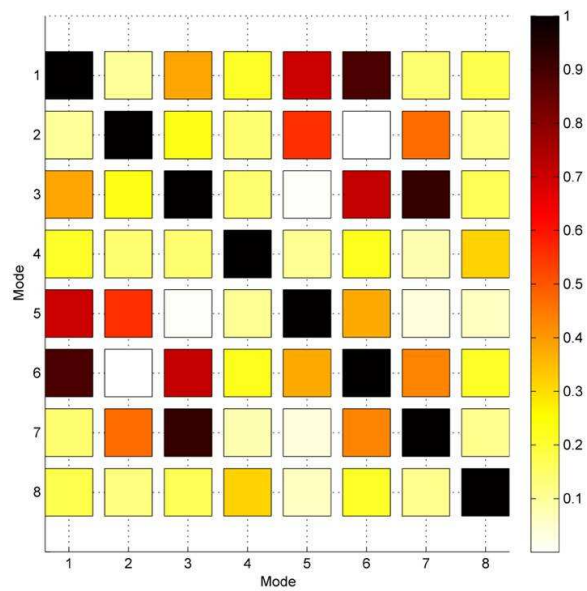
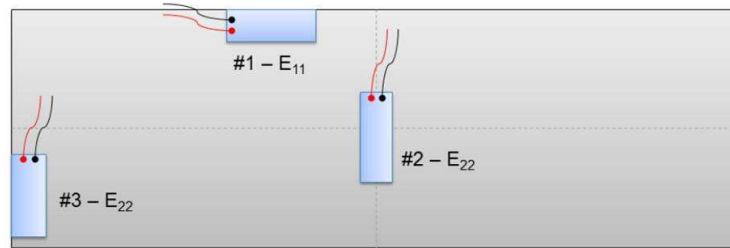


Figure 6.3 – Configuration 2:  $\mathcal{K}$ -optimized placement, for 3 strain transducers.

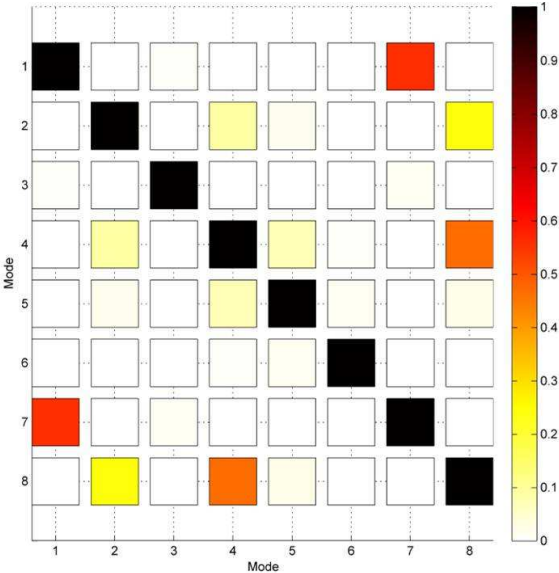


Figure 6.4 – Optimal placement of a 3-accelerometer network.

# 7

## Implementation of Operational Modal Analysis using strain transducers

### 7.1 Approach of the problem

The use of OMA based on information provided by a PVDF sensor network is one of the core topics of this thesis. In this chapter, several aspects and hypotheses mentioned in the previous chapters are tested. After a short review on the mathematical principle of the OMA algorithm used in this thesis, the results of an OMA modal extraction method are compared to those obtained using classic EMA.

Another approached aspect is the robustness of the method with respect to the quality of the excitation source. Since the theoretical formulation developed by OMA authors (see section 7.2) assumes a white noise excitation, it would be interesting to check how the method works out when this assumption is not strictly required any more. Furthermore, and this is one of the most interesting contributions of this work, the capacity to compensate a bad structural excitation by transducer actuation is demonstrated as well. This is a strong point to highlight, since it shows the worthiness of the method and opens to completely new possibilities for the future on modal analysis.

Additionally, the choice to include an optimal sensor strategy, as the one developed in chapter 6, in the design process becomes a critical step.

### 7.2 Operational Modal Analysis: a robust monitoring method

The first proposals of output-only modal analysis came as a response to needs in the civil engineering domain and the limitations of EMA. Indeed, EMA is a classic modal analysis method, of which the use is certainly limited to laboratory applications since careful measurement of the excitation signal is necessary to complete the analysis. Such a method is revealed to be difficult and often impossible to work out in most cases when full-scale structures are the study subject.

## Chapter 7. Implementation of Operational Modal Analysis using strain transducers

---

In an effort to solve this problem, several methods have been proposed over the years [Zhang and Brincker, 2005]. Basically, two kinds of approaches can be mentioned:

1. The time-domain approaches, which would be parametric auto-regressive models [Box and Pierce, 1970], like for example the Extended Ibrahim Time-Domain (EITD) method [Ibrahim, 1977], the Single-Station Time-Domain (SSTD) method [Zaghlool, 1980], etc. Among the non-parametric methods, can be mentioned the Stochastic Subspace Identification (SSI) [van Overschee and de Moor, 1996] and the Natural Excitation Technique (NExT) [James et al., 1992].
2. The frequency-domain based approaches include the Frequency Domain Decomposition (FDD) method, that has been suggested in the late 1990s and early 2000s [Brincker et al., 2000, Ventura and Horyna, 1997]. They are often preferred to time-domain methods because of their simplicity and speed [Zhang et al., 2010]. Considerable improvement has been achieved to increase the accuracy, passing by several peak-picking (PP) algorithm generations to estimate the natural frequencies and mode shapes. The Least-Square Complex Frequency-domain (LSCF) methods have a similar approach as FDD, although modal extraction in this case seems to be better adapted to FRFs than to PSDs [Peeters et al., 2004].

All of these approaches qualify as candidates for OMA. In the context of this thesis, the chosen OMA approach is based on FDD and its subsequent updates. It will be seen in the next paragraphs that, similarly to the experimental modal analysis (EMA) with the frequency response function (FRF), OMA uses the notion of power spectral density (PSD) to extract the modal parameters of a dynamic system.

### 7.2.1 Power spectral density (PSD) and singular value decomposition (SVD)

The fundamental difference of OMA with respect to EMA is the absence of knowledge about the excitation signal  $x(t)$ . For the transducer network, the integrated PVDF patches have been used to acquire multiple signals in order to set up a PSD matrix, which is necessary to the extraction of the structural resonance frequencies (and the corresponding mode shapes) of the specimen.

Let us consider the discrete Fourier transform  $X_d(\omega)$  of the signal  $x(t)$ , with a PSD defined as

$$G_{xx}(\omega_k) = \frac{(\Delta t)^2}{T} \left| \sum_{n=1}^N x_n e^{-i\omega_k n} \right|^2 = (\Delta t)^2 X_d(\omega_k) X_d^*(\omega_k) \quad (7.1)$$

where  $T = N\Delta t$  is the register time duration ( $N$  is the white noise register length

## 7.2. Operational Modal Analysis: a robust monitoring method

---

and the  $\Delta t$  is the sampling time) and  $\omega_k = 2\pi k/N$  denotes the  $k^{th}$  frequency line. The working hypothesis over  $x(t)$  is to assume it as white noise. As it will be seen, this requirement can be somehow be less strict if some conditions are gathered. By definition, white noise is statistically uncorrelated. This means that  $G_{xx}(\omega)$  is constant for the given frequency band.

Now let us consider multiple input signals. In this case, a function similar to PSD can be defined:

$$G_{x_i x_j}(\omega_k) = (\Delta t)^2 X_{d_i}(\omega_k) X_{d_j}^*(\omega_k) \quad (7.2)$$

$G_{x_i x_j}$  is a cross spectral density (CSD) function, for the input signals  $x_i(t)$  and  $x_j(t)$  (excitation signal at spots  $i$  and  $j$ ). If  $\mathbf{H}(\omega_k)$  is the matrix of EMA FRF, a similar PSD matrix for the output signals can be computed:

$$\mathbf{G}_{yy}(\omega_k) = \mathbf{H}^*(\omega_k) \mathbf{G}_{xx}(\omega_k) \mathbf{H}(\omega_k) \quad (7.3)$$

where  $y(t)$  is the measured output signal and  $\mathbf{G}_{yy}(\omega_k)$  is the corresponding output PSD,  $\mathbf{H}(\omega_k)$  is the FRF matrix, and  $\mathbf{G}_{xx}(\omega_k)$  is the PSD matrix of the input signals. The symbol \* stands for hermitian matrix. In the particular case of OMA,  $\mathbf{G}_{xx}(\omega_k) = \mathbf{D}$  becomes a diagonal matrix because of the nature of  $x(t)$  (white noise). The PSD matrix  $\mathbf{G}_{yy}$  carries all the necessary information about the modal parameters of the structure. The Single Value Decomposition (SVD) is a mathematical tool that can be applied to  $\mathbf{G}_{yy}$  in this case, given its symmetry:

$$\mathbf{G}_{yy}(\omega_k) = \mathbf{U}^*(\omega_k) \mathbf{S}_+(\omega_k) \mathbf{U}(\omega_k) \quad (7.4)$$

where  $\mathbf{S}_+$  is the diagonal matrix of singular values, and the orthogonal matrix  $\mathbf{U}$  contains the mode shapes. If done correctly, the SVD decomposition gives a diagonal matrix with the diagonal functions ordered in a decreasing order (see figure 7.1). As it can be stated visually, the natural frequencies are associated to the existence of "resonance" peaks, as for EMA.

Concerning the mode shapes, the question is to know which of the column vectors are those representing the physical mode shapes. According to [Rainieri and Fabbrocino, 2010], it can be demonstrated that, at the frequency line  $\omega_k$ , it is the first column of

## Chapter 7. Implementation of Operational Modal Analysis using strain transducers

---

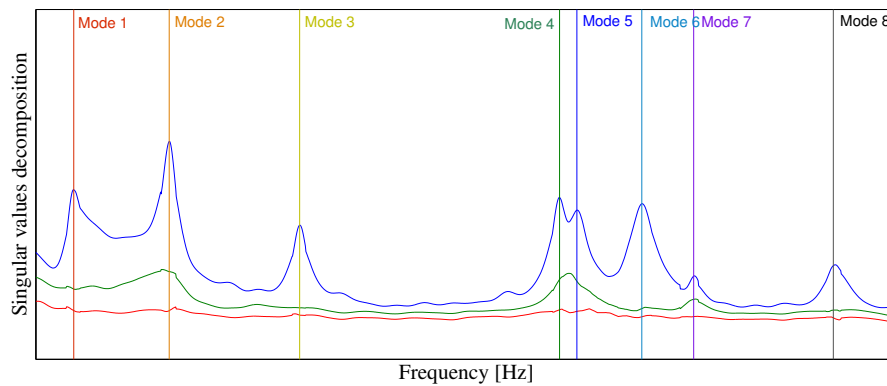


Figure 7.1 – Example of diagonal spectra from a  $S_+$  resulting of a SVD. The vertical lines are the values of the specimen's natural frequencies obtained by EMA.

$U(\omega_k)$  that contains most of the frequency domain information (column associated with the first singular value). This column vector will be denoted  $u_1(\omega_k)$  from now on. This statement could be hinted beforehand by visual inspection of figure 7.1, given that the first singular value shows most of the frequency domain information as well (the resonance peaks are clearer).

From the point of view of the modal domain, the singular values can be interpreted as scaling factors indicating the strength of the associated singular vectors, which are an estimation of the observed mode shapes. Thus, if two orthogonal modes are very close, the singular values will rank them in order of strength. This will be reflected in the frequency domain by the presence of resonance peak in the second singular value plot. This is one of the most interesting aspects of SVD: it allows discerning very close modes as long as they are orthogonal (or nearly orthogonal).

### 7.2.2 Modal Extraction: AutoMAC, the peak-picking algorithm and the influence zones

An accurate modal extraction requires the definition of the "influence zones" around resonance peaks.

Let us assume the SDoF hypothesis in this case. This hypothesis can be reasonably assumed since even in the event of very close modes, those are supposed to be separated by SVD. In the frequency band around a resonance peak, the influence of a single mode is much more important than the influence of the others. So, somehow this influence zone can be defined as the frequency band where the colinearity with the local mode shape remains above a relatively high value. However, this implies that the mode shape is known before hand, which is not necessarily the case since the goal



## 7.2. Operational Modal Analysis: a robust monitoring method

---

of modal extraction is exactly that: to find the natural frequencies, the modal damping and the mode shapes.

Consider a region in the SVD spectrum where there is a resonance peak. Let us assume that there are results available from an FE simulation, in particular a matrix of mode shapes  $\mathbf{U}_{FE}$ .

Mathematically, the modal assurance criterion (MAC) between the numerically simulated column vectors of  $\mathbf{U}_{FE}$ ,  $\mathbf{u}_{FE}(\omega_m)$ , and the experimentally obtained (by SVD)  $\mathbf{u}_1(\omega_m)$  lead to the definition of the "influence zone" ( $m$  denotes the estimated resonance frequency line), which in the sense of the single degree of freedom (SDOF) hypothesis can be defined by

$$MAC(\mathbf{u}_1, \mathbf{u}_{FE}) = \frac{\mathbf{u}_1^T \mathbf{u}_{FE}}{|\mathbf{u}_1| |\mathbf{u}_{FE}|} > MAC_{crit} \quad (7.5)$$

The threshold value  $MAC_{crit}$  is usually above 0.9 for fairly discernible modes, although it should be adopted higher if the modal density increases.

However, as long as a numerical-experimental identification is not pulled out, the FE model will most probably carry inaccuracies and therefore have a poor contribution to the modal extraction process. Moreover, if the numerical-experimental identification was necessary to calibrate the finite element model every time a change in the inner structures occurs (pertinently due to ageing or damage), the monitoring process would be time-consuming and the OMA would lose its purpose.

For the sake of simplicity, robustness and operational efficiency, OMA has to be as "self-sustaining" as possible, *ie* in absence of an accurate FE model or EMA model, or any other external support, OMA should be capable of estimating the modal parameters accurately by itself.

This problem has been mentioned and analysed by several authors in recent years [Farrar et al., 2001, Sohn et al., 2004], and proposed solutions are at the root of what is called the AutoMAC [aes et al., 2008, Rainieri and Fabbrocino, 2010] (see figure 7.3).

As implemented in this case, AutoMAC follows a statistical approach [aes et al., 2008, Rainieri and Fabbrocino, 2010], which is able to provide an estimation of the natural frequencies and mode shapes of the most recent state of a structure. It can be described by the following steps:

- A relatively long time signal (from 2-10 min depending on the structure and the excitation level) is first divided in shorter sub-signals. In order to avoid the "leakage" ef-

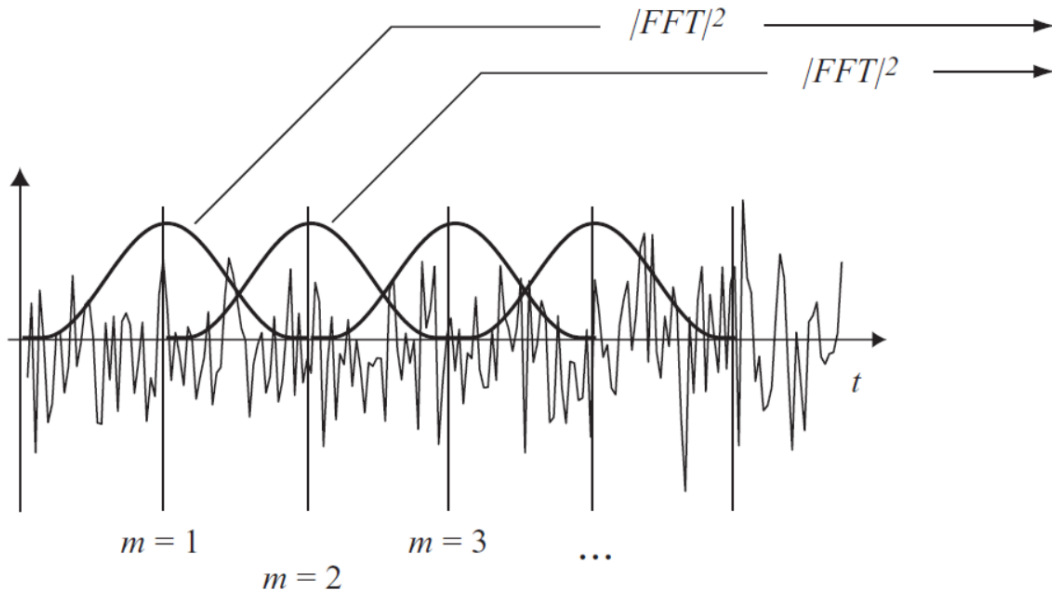


Figure 7.2 – Graphic representation of time signal division in sub-signals: local Hanning windows are applied to avoid the "leakage" effect.

fect of the Fourier transformation, a conditioning window is applied to every signal, as represented in figure 7.2. As an example, the Hanning windowing demonstrates suitable.

- Each sub-signal is subject to an FDD process as described in subsection 7.2.1. The matrix of singular vectors  $\mathbf{U}_n(\omega_k)$  is saved, where  $n$  is the number of the sub-signal.
- All the  $\mathbf{U}_n(\omega_k)$  vectors are paired to each other, and their respective MAC is computed. Out of all the possible combinations, the mean MAC ( $MAC_{mean}$ ) and the standard deviation of the MAC ( $MAC_{std}$ ) is computed.
- At the end of this algorithm, a mean value and a standard deviation are at disposal for each line of frequency  $i$ . The frequency bands where  $MAC_{mean}$  is high enough ( $>0.8$ ) and  $MAC_{std}$  is low enough ( $<0.2$ ) are judged as candidates for the "influence zones".

The parameters of this algorithm are the total number of sub-signals and the criteria on ( $MAC_{mean}, MAC_{std}$ ). While designing the monitoring process, it is necessary to think about having long enough time sub-signals (to have accurate SVDs) while having as many sub-signals as possible (to have a good statistical estimation). In reference [Rainieri and Fabbrocino, 2010], time signals have typically around 100000-200000 time samples, measured over  $\sim 1000$  [s]. The choice of the sampling rate will depend principally on the frequency bandwidth the user wants to monitor, which in turn depends essentially on the number of the vibration modes of interest. For example, if the upper limit of the frequency band is 2000 [Hz], the minimum sampling rate

## 7.2. Operational Modal Analysis: a robust monitoring method

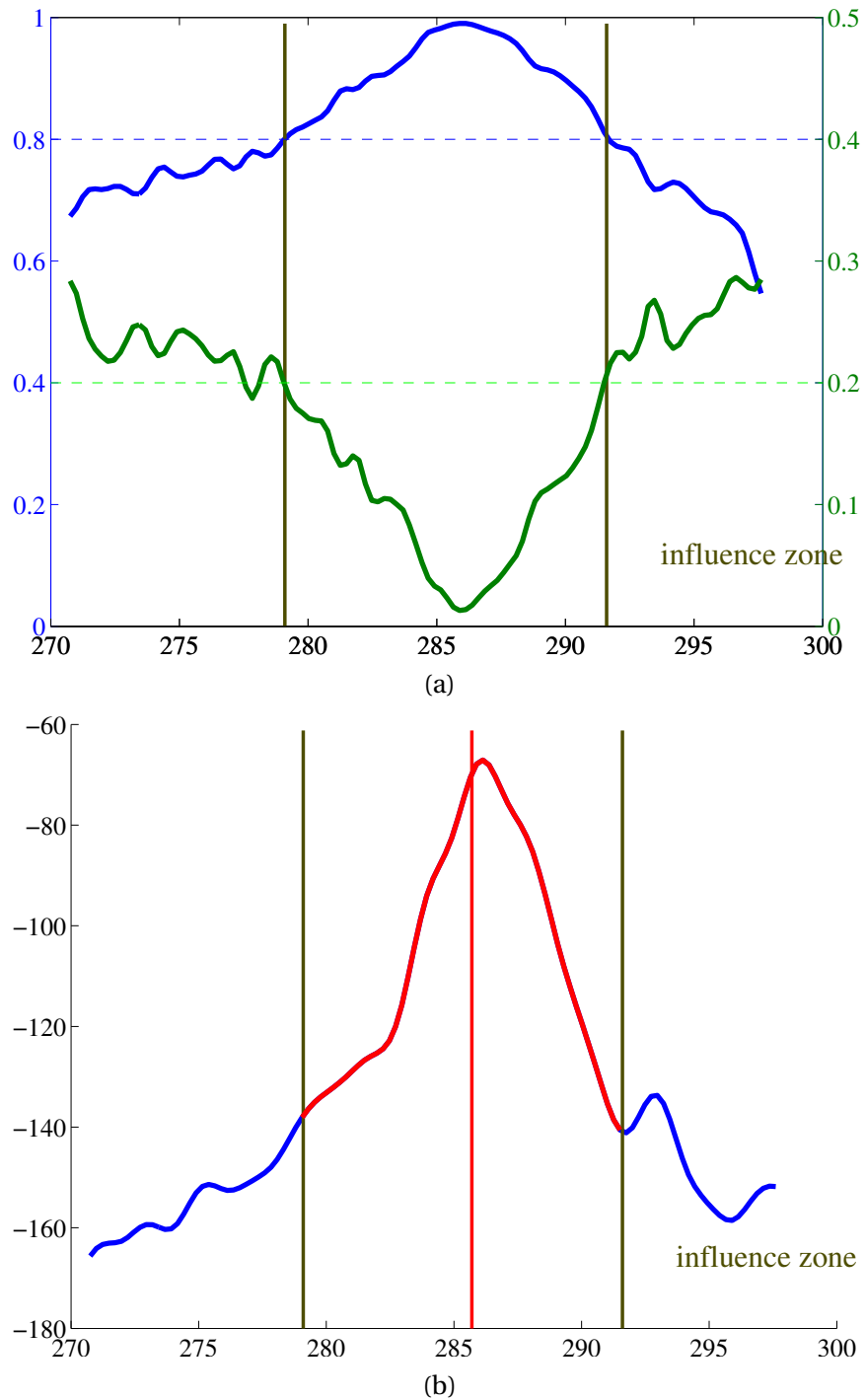


Figure 7.3 – Principle behind AutoMAC: (a) The influence zone is statistically determined as a continuous frequency interval where  $MAC_{mean}$  is high and  $MAC_{std}$  is low. (b) A resonance peak is isolated and the modal parameters identified, assuming the SDoF hypothesis (see subsection 7.2.3).

## Chapter 7. Implementation of Operational Modal Analysis using strain transducers

---

is given by the Nyquist theorem, *ie* 4000 [Hz].

Concerning the MAC criteria, they should be calibrated depending on the case. In this thesis, the calibration of these three statistical parameters is carried out at the "initialization step" (*ie* before the ageing). In this first step, the OMA signal is compared with an accurate initial estimation of the vibration model. This vibration model could be either a previously identified FE model or an EMA model. The minimum  $MAC_{mean}$  and the maximum  $MAC_{std}$  can be then fixed for the rest of the monitoring.

Since ageing changes are expected to be slow and gradual, the calibration of the statistical criteria does not need to be recalculated. For the next monitoring iterations, the previously identified modal parameters can be used as a more accurate initial estimations. Eventually, if two modes are spectrally close, the MAC criterion used to define the influence zone can be increased depending of the degree of separation. Moreover, if the resonance peaks are very close, a second resonance peak (corresponding to the second singular value) will appear.

The statistical nature of the "influence zone" delimitation aims to reduce the influence of random experimental error on the modal parameters estimation and carries some inherent advantages. Indeed, the signal-to-noise ratio happens often to be very low, as much in civil engineering as in aerospace applications. Additionally, the computational effort is reduced because of the reduced size of matrix  $G_{yy,r}$ ; the SVD is much faster to compute for a shorter time signal.

A few lines are necessary to speak about the possibility of having to face electromagnetic parasite spectra. As for all piezo-electric materials, PVDF is sensible to this phenomenon. The electromagnetic shielding described in chapter 2 would generally suffice to solve this problem, but sometimes the power transmitted by natural excitation is somehow still low. In those cases, numerical or analogical filters can be very useful.

### 7.2.3 Modal Extraction: FDD upgrades

Once the influence zones are delimited, the FDD modal extraction method is applied (combined with simple peak-picking algorithms). It is important to note that its application as described below assumes the SDoF hypothesis for each influence zone. As it will be seen later, the FDD approach shows a major advantage when multiple modes appear for one natural frequency, often found in symmetric structures.

The first peak-picking algorithm is almost trivial, since the maximum singular value of the influence zone is chosen as the natural frequency estimation. A more elaborated scheme comes with the second generation of FDD modal extraction algorithm. The Enhanced FDD (EFDD) redefines the influence zone delimited inside the SVD

## 7.2. Operational Modal Analysis: a robust monitoring method

---

spectrum. The new local PSD can be defined by the following formula:

$$G_{yy}^e(\omega_k) = \mathbf{u}(\omega_m) \mathbf{G}_{yy}(\omega_k) \mathbf{u}^*(\omega_m) \quad (7.6)$$

where  $\mathbf{u}(\omega_m)$  is the singular vector corresponding to the  $m^{\text{th}}$  natural frequency, and  $\omega_k$  is the  $k^{\text{th}}$  frequency line. It can be noted that this expression is close to the one of the first singular value  $S_{+,1}(\omega)$ , except that the enhanced PSD  $G_{yy}^e(\omega_k)$  depends on a fixed  $\mathbf{u}(\omega_m)$  and not on  $\mathbf{u}(\omega_k)$ . It should be pointed out that  $G_{yy}^e(\omega_k)$  is not written in bold letters since it is a scalar discrete function in this context.

$G_{yy}^e(\omega_k)$  can be assimilated to a SDoF frequency peak. In that case, applying an inverse FFT (IFFT) to  $G_{yy}^e(\omega_k)$  would give a decay signal or an impulse response function (IRF), *ie* the time response of an impulse excitation if this was a fundamental oscillator [Zhang et al., 2010]. Under this approximation, the common logarithm decrement technique can then be applied to compute natural frequency  $\omega_m$  (by the count of oscillations) and damping ratio  $\eta_m$  (by the estimation of the decrease rate).

A third generation of the FDD was proposed by [Zhang et al., 2010], called frequency-spatial domain decomposition (FSDD). It takes full advantage of the SDoF assumption inside a modal domain. It has been demonstrated that locally, the modal zone of influence can be expressed algebraically by:

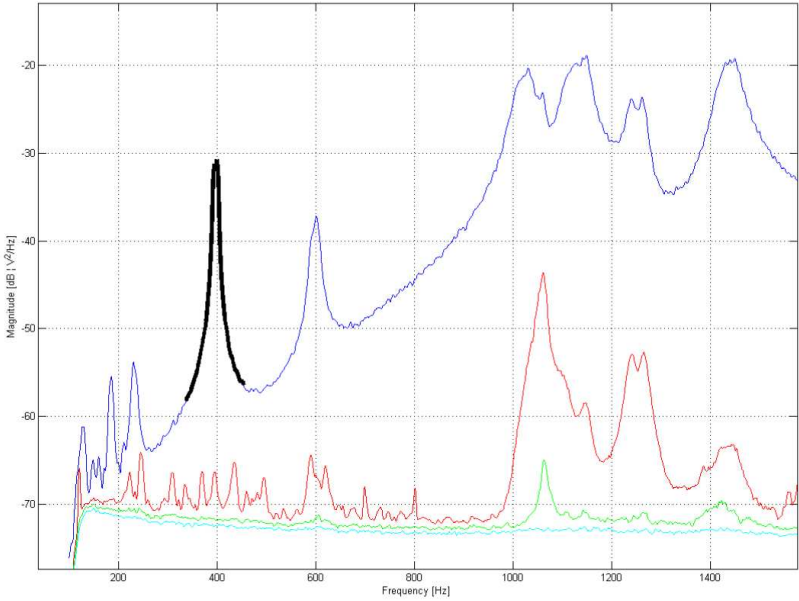
$$G_{yy}^e(\omega) = \mathbf{u}(\omega_m) \mathbf{G}_{yy}(\omega) \mathbf{u}^*(\omega_m) \approx_{\omega \rightarrow \omega_m} \mathcal{R} \left( \frac{2c_m}{\omega - \lambda_m} \right) = \frac{2c_m \eta_m}{\eta_m^2 + (\omega - \omega_m)^2} \quad (7.7)$$

where  $\lambda_m$  is the pole of the function and  $c_m$  is a proportionality coefficient. The pole  $\lambda_m$  contains the necessary modal information, given that  $\lambda_m = -\eta_m + j\omega_m$ . The determination of these three real constants ( $c_m, \eta_m, \omega_m$ ) is carried out by curve fitting. A simple estimation error is defined by the following formula:

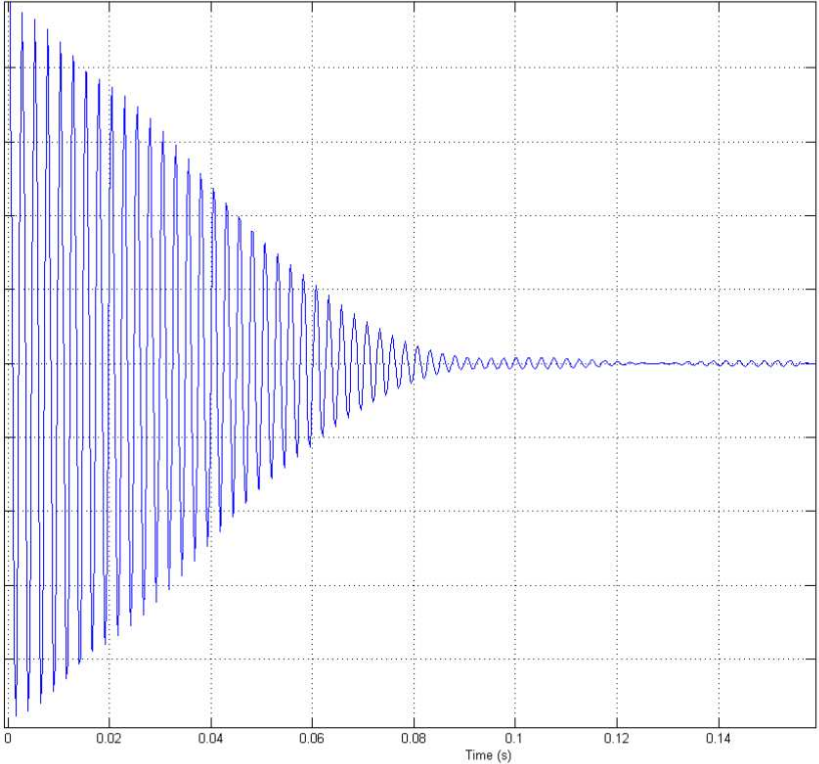
$$\begin{aligned} e(\omega_k) &= [G_{yy}^e(\omega_k) - \hat{G}_{yy}^e(\omega_k)](\eta_m^2 + (\omega_k - \omega_m)^2) \\ &= \eta_m^2 G_{yy}^e(\omega_k) + \omega_k^2 \hat{G}_{yy}^e(\omega_k) - 2\omega_k \omega_m \hat{G}_{yy}^e(\omega_k) + \omega_m^2 \hat{G}_{yy}^e(\omega_k) - 2c_m \eta_m \end{aligned} \quad (7.8)$$

As before,  $\eta_m$  is the damping ratio and  $\omega_m$  is the natural frequency. In the literature, the FSDD has shown an excellent performance in damping estimation when compared to

**Chapter 7. Implementation of Operational Modal Analysis using strain transducers**



(a)



(b)

Figure 7.4 – Application of EFDD to a SDoF peak: (a) local peak, (b) IFFT representing the IRF.

other frequency-domain (EFDD, pLSCF) and time-domain (NExT, SSI) methods. The use of the damping factor as a ageing monitoring feature leaves an open question for future work, although it should be approached cautiously since damping measurements exhibit in general more significant uncertainty than eigenfrequency measurements. From now on, the FSDD is the main approach adopted in the modal extraction of natural frequencies and mode shapes.

In the case of close frequency modes up to a 65% degree (*ie* 65% of the influence zone is estimated to be inside the influence zone of the other peak), the separation performance of FSDD has been evaluated satisfactory [Rainieri and Fabbrocino, 2011] if only one singular value is taken into account. In the case of coupled/multiple modes, the second (and eventually third, fourth, fifth,...) singular value is necessary to detect the presence of the second-order pole. This is one of the strengths of FDD: the SVD decomposition decouples automatically the mode spaces between them, as well as from the noise space. The rank of the singular value matrix  $S_+$  increases with the number of separate modes.

In order to test the performance of the FDD algorithm described in this chapter, a series of experimental tests were carried out, of which the results are reproduced in section 7.3. Each manufactured sample has a different configuration of integrated sensor network, based on the optimization process on chapter 6. The number of minimum sensing transducers was fixed to three, justified by a sensitivity analysis on the vibration modes in the 0-2000 [Hz] band. The optimization of the sensor placement was discussed in detail in chapter 6. This frequency band is judged to be wide enough to contain natural frequencies which allow the correct identification of as many mechanical properties as it is possible using the mixed numerical-experimental identification algorithm. For the selected samples  $\mathbb{A}$  to  $\mathbb{D}$ , the number of these modes is eight.

## 7.3 Experimental campaign

### 7.3.1 Placement strategy and specimens manufacturing

To carry out qualitative (visual inspection of SVD curves) and quantitative (error in the extracted natural frequencies) comparisons between standard (impact hammer, loud-speaker, accelerometers) and alternative (fan, PVDF transducers) hardware for modal analysis, progressive evaluation of the OMA method have been tested.

The subject specimens are four different rectangular UD CFRP plates with similar nominal dimensions as those used for the ageing modelling in the precedent chapters. Each specimen is manufactured in order to validate certain hypotheses such as the use of a standing fan and PVDF patches as actuators for OMA and the improvement of the placement strategy described in chapter 6:

## Chapter 7. Implementation of Operational Modal Analysis using strain transducers

---

1. Sample  $\mathbb{A}$  using an  $\mathcal{S}$ -optimized configuration.
2. Sample  $\mathbb{B}$  using a  $\mathcal{K}$ -optimized configuration (EI method).
3. Sample  $\mathbb{C}$  using two configurations: an  $\mathcal{S}$ -optimized one and a  $\mathcal{K}$ -optimized one. The main idea is to compare and experimentally confirm the advantage of the latter over the former in discerning close mode shapes.
4. Sample  $\mathbb{D}$  using a double  $\mathcal{K}$ -optimized network, for simultaneous actuation/sensing. The same configuration has been integrated on both faces.

The placements for all test specimens are shown in figure 7.5.

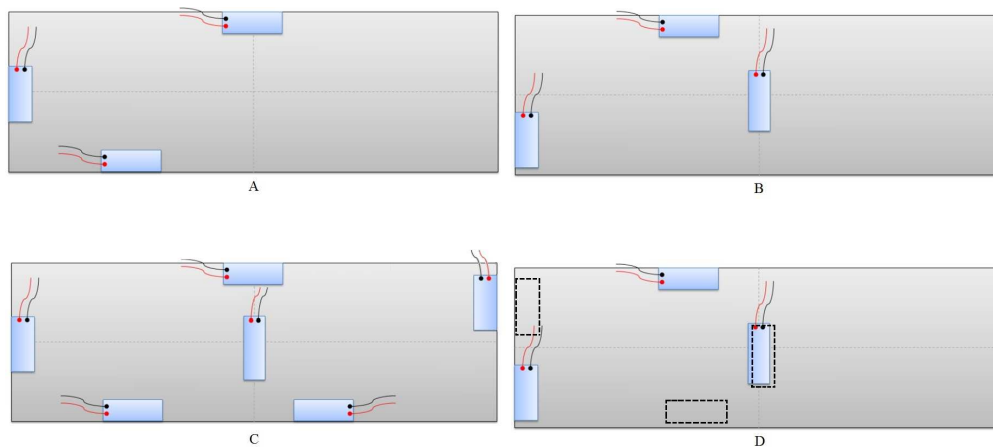


Figure 7.5 – Transducer placement on the surface of the manufactured samples (the dotted lines represent the PVDF patches on the no visible side of the plate).

### 7.3.2 Experimental planning

The specimens are subject to free-free boundary conditions.

The sequence of OMA experiments is summarized in table 7.1. Sample  $\mathbb{A}$  is used as a reference to test if OMA is well implemented. Except for the fan, the actuators are excited using a white noise generator (HP33120A). Sample  $\mathbb{B}$  is tested to check the validity of the use of strain sensors to carry out OMA. Sample  $\mathbb{C}$  is tested to compare the accuracy of a  $\mathcal{K}$ -optimized network with respect to a  $\mathcal{S}$ -optimized one. Finally, sample  $\mathbb{D}$  is used to show the usefulness of using PVDF transducers as actuators as well, as a complement for frequency ranges where the structure is not sufficiently excited naturally.

The electric signals from the sensors are acquired simultaneously by the PC, which is equipped by the PCI-MIO-16 card. Concerning the PVDF patches when used as actuators, they were excited simultaneously, used the same white noise generator and



the piezo amplifier SQV 1/500. Although this ignores the non-correlation hypothesis imposed to the input signals  $x(t)$  in the FDD formulation, this worked out surprisingly well. This reinforces the robustness qualities of this particular OMA method.

Table 7.1 – Test plan: EMA extracted natural frequencies are the reference, while OMA extracted natural frequencies are tested: IH = impact hammer, Sp = loud-speaker, Acc = accelerometer, PVDF = PVDF film transducers and Fan.

Sample	Test	Actuator/Sensor	Optimized configuration
A	EMA	IH/Acc	-
	OMA1	Sp/Acc	-
	OMA2	Fan/Acc	-
	OMA3	PVDF/Acc	$\mathcal{S}$ -optimized
B	EMA	IH/Acc	-
	OMA1	Sp/PVDF	$\mathcal{K}$ -optimized
	OMA2	Fan/PVDF	$\mathcal{K}$ -optimized
C	EMA	IH/Acc	-
	OMA1	Fan/PVDF	$\mathcal{K}$ -optimized
	OMA2	Fan/PVDF	$\mathcal{S}$ -optimized
D	EMA	IH/Acc	-
	OMA1	PVDF/PVDF	$\mathcal{K}$ -optimized
	OMA2	PVDF+Fan/PVDF	$\mathcal{K}$ -optimized

### 7.3.3 Validation of a standing fan as actuator

A fan produces an airflow that can emulate wind around an air foil, and it is possible that small vortex of turbulence can work a random sources for excitation. Even if intuitively such a flow can be considered as a random source, an experimental validation is necessary to justify this decision. Thus, a first approach is the direct measurement of the pressure wave field produced by a spinning fan when compared to known, controlled white noise source.

As stated in chapter 2, a microphone is used to measure the air pressure. The experimental settings are the following:

1. Both sources (TS-1750 loud-speaker and Tristar fan) are located at 60 [cm] of the M30BX microphone. They work at their nominal power.
2. A band-pass filter for frequencies inside the 0-2000 [Hz] band is implemented on the LAB1 preamp (40 [dB] of amplification). The sampling rate was fixed to 4000 [Hz].
3. The acquisition time is 20 [s] in both cases.
4. The corresponding PSD for each signal is then computed using an FFT.

## Chapter 7. Implementation of Operational Modal Analysis using strain transducers

---

The results are shown in figure 7.6: the graphs show both the time signals and the corresponding PSD. Several observations can be stated:

- The RMS voltage is comparable for both excitations, and far higher than the ambient noise level.
- The fan's PSD spectrum exhibits however a decreasing trend of the energy with the increasing frequencies: 0 dB at the lower frequencies, while around -90 dB at 2000 [Hz]. The white noise produced by the loud-speaker, as expected, remains almost constant around -50 dB. The ambient noise level is evaluated at -110 dB at the lower frequencies, and decreases to -150 dB at 2000 [Hz].

From this, the use of a fan can be validated for application at low frequencies (until 1000 [Hz]). The quality of the excitation for higher frequencies is still acceptable but the support of a complementary excitation source could be useful. This is where the PVDF actuators play an important role in the OMA acquisition process.

## 7.4 Results

### 7.4.1 EMA results and identification

The extracted frequencies using the FSDD method are summarized in table 7.2. Those values are used as references to compare the quality of OMA. To carry out EMA, an experimental mesh of 15 points uniformly distributed on the plate is used (see figure 7.7).

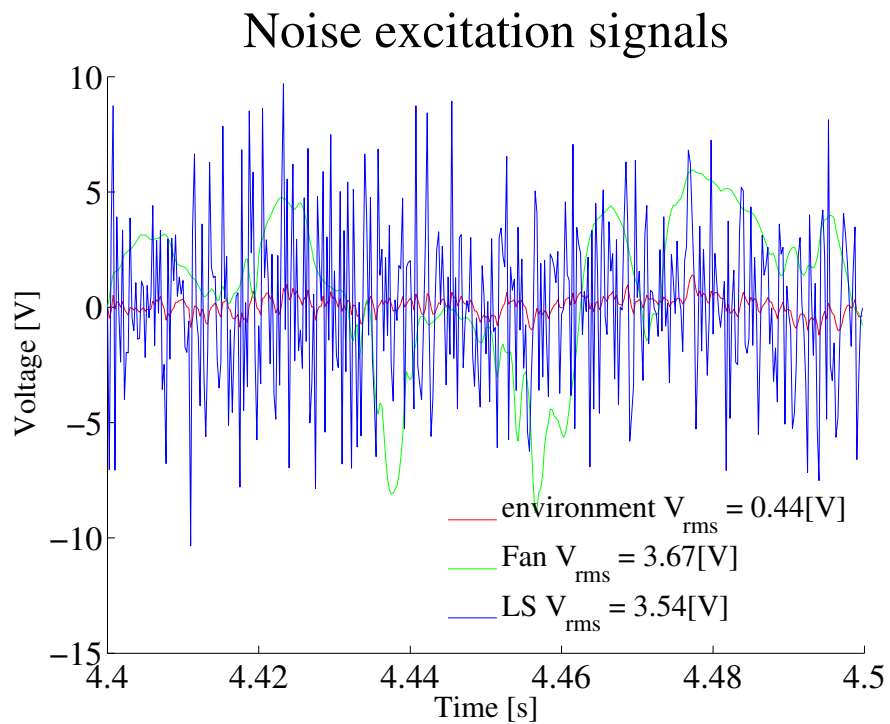
Table 7.2 – Natural frequencies (in [Hz]) identified by an EMA, using an impact hammer and an accelerometer. Several measurements were carried out on each sample, in order to reduce the scattering (less than 0.1% of standard deviation for each mode).

Sample	1	2	3	4	5	6	7	8
A	237.1	397	600.7	1030.2	1059.1	1147.4	1261.4	1448.8
B	270.1	447.2	683.4	1162	1199	1322	1414	1677
C	247.1	409.2	630.4	1072.6	1097.2	1176.5	1342	1500
D	295.1	433	680.4	1148.2	1192.4	1246.2	1445	1631.6

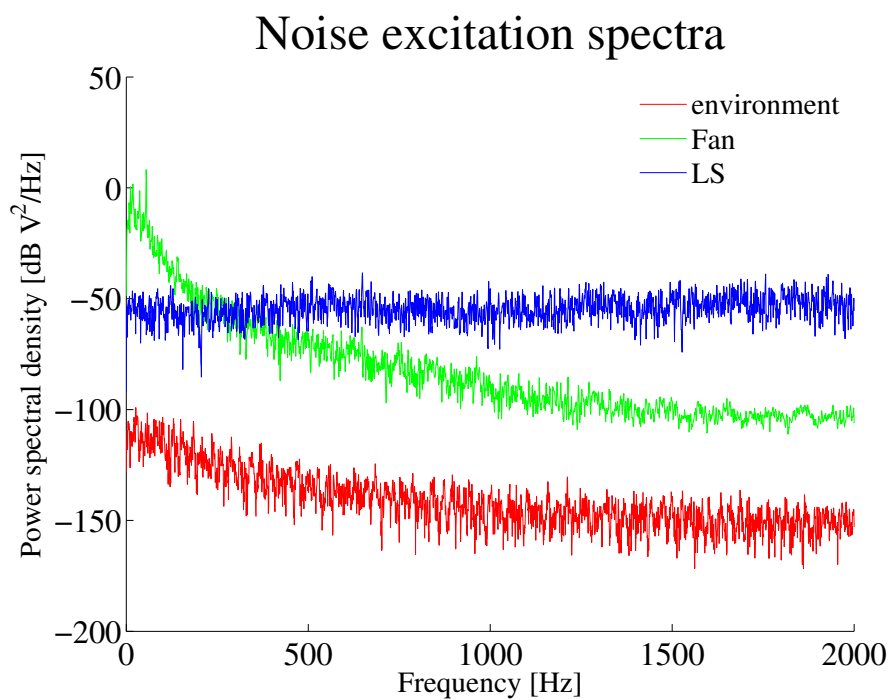
In the following subsections, a bias with respect to the EMA frequencies is defined as:

$$\bar{\epsilon} = \frac{1}{n^e} \sum_{i=1}^{n^e} \epsilon_i = \frac{1}{n^e} \sum_{i=1}^{n^e} \frac{f_{OMA,i} - f_{EMA,i}}{f_{EMA,i}} \quad (7.9)$$

where  $\epsilon_i = (f_{OMA,i} - f_{EMA,i})/f_{EMA,i}$ ,  $f_{OMA,i}$  and  $f_{EMA,i}$  are the  $i^{th}$  order extracted



(a)



(b)

Figure 7.6 – Random excitation signals coming from the Tristar fan and the TS-1750 loud-speaker, and compared to the environmental white noise: (a) time signals (zoomed in) and (b) PSD spectra.

## Chapter 7. Implementation of Operational Modal Analysis using strain transducers

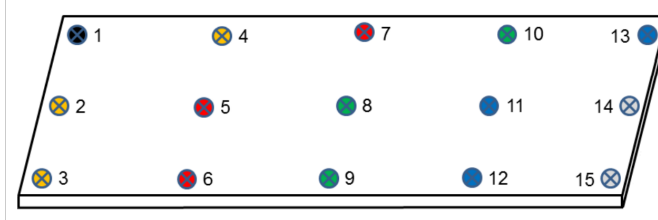


Figure 7.7 – Experimental mesh where the nodes are the location of the moving impact point. Accelerometers are located optimally as described in chapter 6.

natural frequencies after an OMA or an EMA, and  $n^e$  is the number of extracted modes. The normalization is justified by the increasing value of the frequencies and in order to weigh correctly the measurement scattering. In table 7.3, a hypothesis test is carried out, where the null hypothesis  $H_0$  is accepted if the bias is not statistically significant, and is rejected otherwise. The testing variable is defined by

$$t = \frac{|\bar{\epsilon}|}{\sigma_{\epsilon}/\sqrt{n^e}} \quad (7.10)$$

where  $\sigma_{\epsilon}$  is the estimated standard deviation of the bias, and  $n^e = 8$ . Under the null hypothesis,  $t$  follows a t-Student probability law  $T(\nu)$ , where  $\nu = n^e - 1$  is the number of degrees of freedom (DoF). The critical threshold  $t_{crit}$  is evaluated with a significance level of  $\alpha = 5\%$ , and the null hypothesis is accepted if  $t < t_{crit}$ . As it can be seen in the last column of table 7.3, the global results are satisfying since the null hypothesis is accepted in all cases. This means that there is no statistical difference between EMA/OMA. Moreover, excepting two cases, the standard deviation  $\sigma_{\epsilon}$  is lower than 1 %, which confirms a satisfying statistical coherence between the two methods.

Table 7.3 – Summary table of the extracted natural frequencies from EMA and OMA, with the corresponding errors, with  $\alpha = 5\%$  and  $\nu = 7$ .

Specimen	Test	$\bar{\epsilon}$ [%]	$\sigma_{\epsilon}$ [%]	$t = \frac{\bar{\epsilon}}{\sigma_{\epsilon}/\sqrt{n}}$	$t_{crit} = T_{\alpha}(\nu)$	Decision
A	OMA1	0.359	0.582	1.746	2.365	$H_0$
	OMA2	0.048	0.359	0.375	2.365	$H_0$
	OMA3	-0.632	1.512	1.183	2.365	$H_0$
B	OMA1	0.319	0.421	2.143	2.365	$H_0$
	OMA2	-0.357	0.464	2.180	2.365	$H_0$
C	OMA1	-0.402	0.721	1.575	2.365	$H_0$
	OMA2	-0.309	2.003	0.436	2.365	$H_0$
D	OMA1	0.305	0.781	1.103	2.365	$H_0$
	OMA2	0.214	0.451	1.340	2.365	$H_0$

The graphs in the following subsections represent the SVD spectra corresponding to

the OMA tests. For clarity, the original SVD have been slightly smoothed to show the position of the resonance peaks (this was carried out using the smooth function in MATLAB). The extracted natural frequencies by FSDD are highlighted along with the previously extracted natural frequencies by EMA.

#### **7.4.2 Reference case: Sp/Acc and Fan/Acc**

A reference example is set up in order to verify that the OMA algorithm implemented agrees with theory and the natural frequencies are correctly identified by the charge accelerometers and to validate the use of a Intertronic 40CM stand fan as a white noise excitation source. Three accelerometers were deployed as in figure 6.4. The fan has a 40 [cm]-diameter propeller, placed at 0.5 [m] in front of the specimen, turning at  $\approx 1000$  [rpm]. No 50 [Hz] electromagnetic harmonics are visible in the SVD spectra. The idea behind the use of a fan is the similarity of this reduced scale excitation source with the excitation of a plane in a turbulent airflow, a boat in a stream, or a race car on a track. According to what has been demonstrated in the previous section, the randomness of the air flow and the excitation bandwidth of the fan should be reasonably acceptable as a random pressure field.

Since the frequencies are more accurate for the fan than for the loud-speaker, its use can be validated. Moreover, the quality of the graphs in figure 7.8 shows that the OMA has been well implemented as all resonance frequencies could be determined with moderate standard deviations (less than 1% in all cases).

#### **7.4.3 PVDF as actuators: PVDF/Acc**

This constitutes the first series of OMA with PVDF patches as actuators, while three accelerometers were employed for sensing. As stated in the introduction, PVDF patches can theoretically excite the structure as strain actuators. As for the loud-speakers, a white noise generator was used to excite the PVDF transducers.

As it can be seen in figure 7.9, the PVDF patches work well as actuators, giving an accurate SVD plot. However, the modal extraction gives a standard deviation of about 1.51%, which is higher than the error given by the other accelerometer-sensed combinations. As it is investigated in the following sections, this is most probably due to the "naive" placement of the PVDF sensors, since the network is  $S$ -optimized rather than  $\mathcal{K}$ -optimized, and is then suboptimal for excitation.

**Chapter 7. Implementation of Operational Modal Analysis using strain transducers**

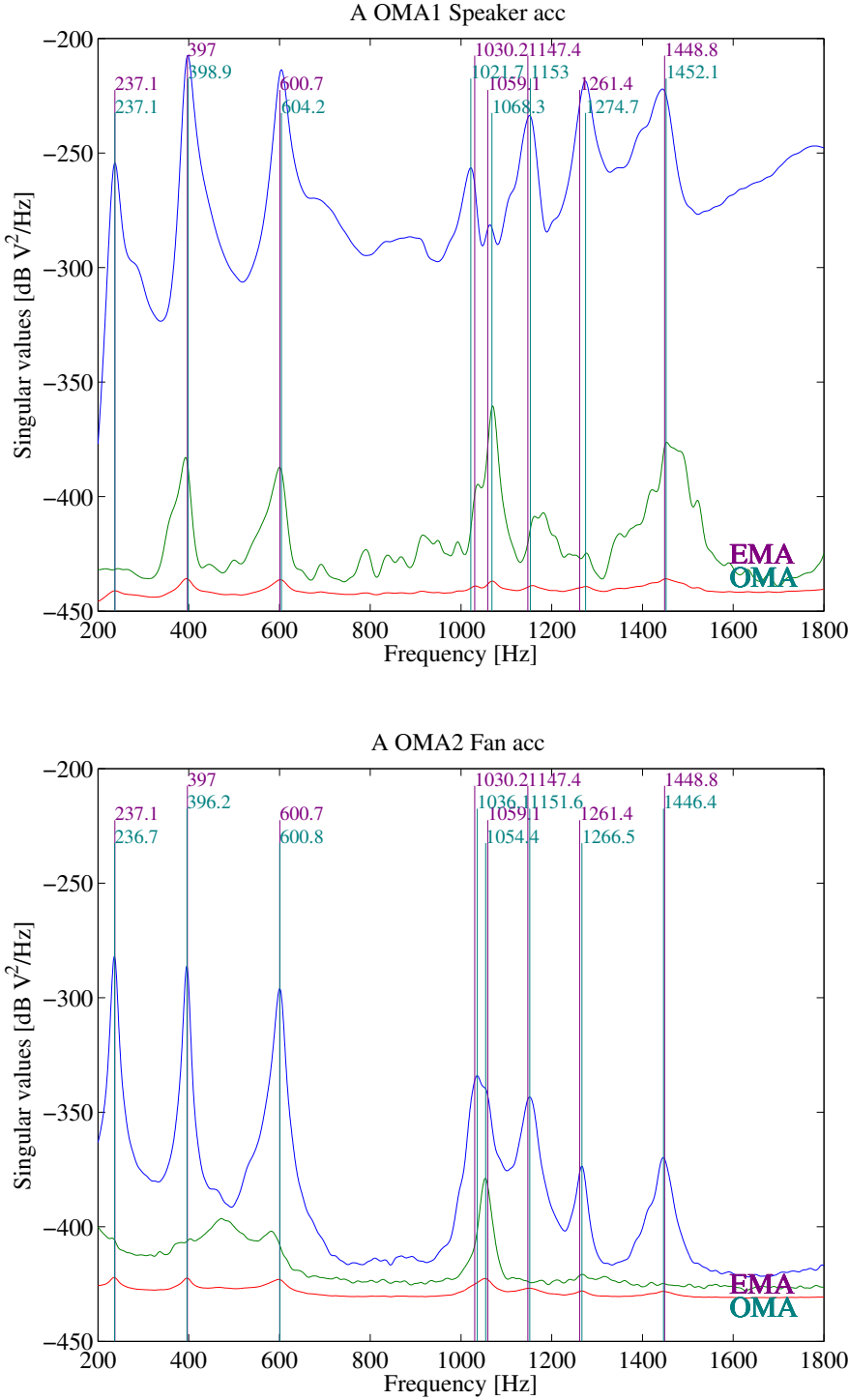


Figure 7.8 – SVD plot for Sp/Acc and Fan/Acc OMA combination.

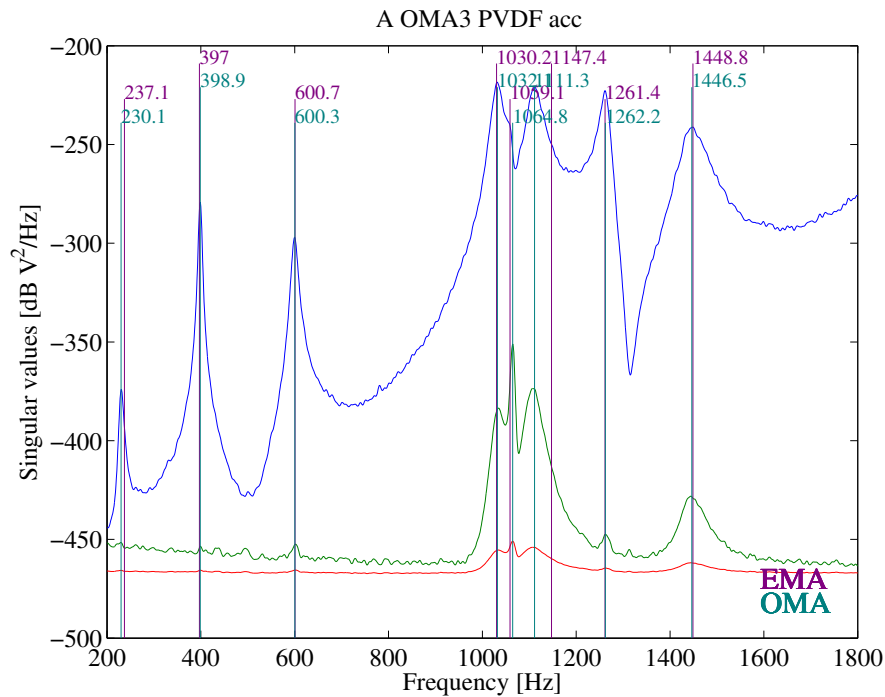


Figure 7.9 – SVD plot for PVDF/accelerometers OMA combinations.

#### 7.4.4 PVDF as sensors: Loud-speaker/PVDF and Fan/PVDF

The second sample uses the PVDF transducers as sensors, with the  $\mathcal{K}$ -optimized placement for 8 modes. As for sample  $\mathbb{A}$ , the center line of the fan and the loud-speaker were placed as close as possible in front of a corner in order to excite as many vibration modes as possible. The main idea is to show if the PVDF transducer network can measure signals leading to a modal extraction as accurate as with an accelerometer network, using the OMA method.

As it can be seen in table 7.3, the standard deviation of the bias is the same (about 0.45 %) for both excitations, and the same percentage as for the accelerometers networks (0.58% for Sp/Acc and 0.36% for Fan/Acc). Thus, optimally placed, PVDF transducers represent then an as accurate option as accelerometers (see figure 7.10).

#### 7.4.5 PVDF as sensors: Fan/PVDF in different configurations

The second feature to be explored is the comparison between the two optimization methods: based on the norm of strain modes or on the EI method. The  $\mathbb{C}$  OMA1 test is carried out with the PVDF network's  $\mathcal{K}$ -optimized configuration for sensing, while the  $\mathbb{C}$  OMA2 test uses the  $\mathcal{S}$ -optimized one for actuation. The idea is to check the differences between these two methods, using the exact same sample.

**Chapter 7. Implementation of Operational Modal Analysis using strain transducers**

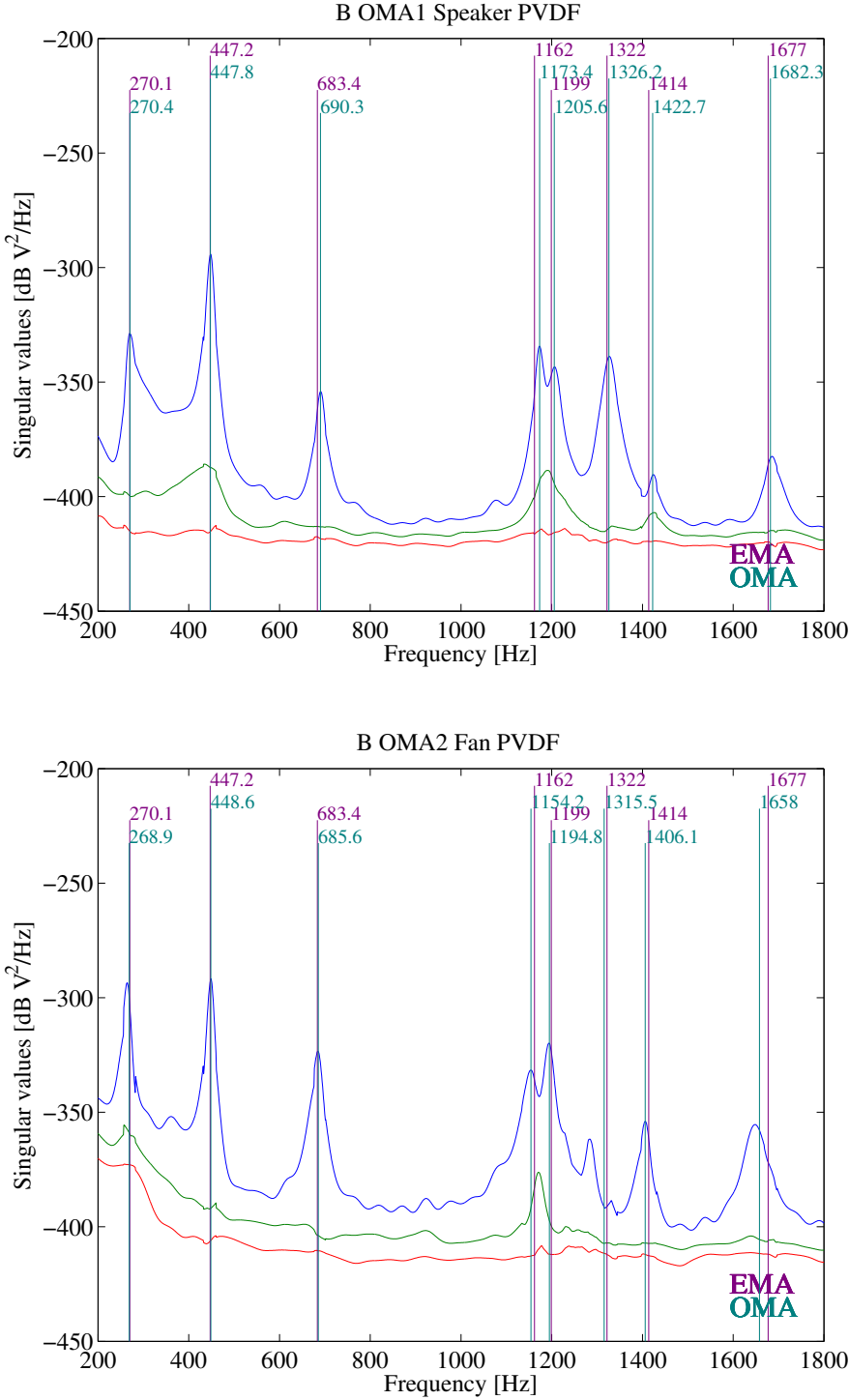


Figure 7.10 – SVD plot for Loud-speaker/PVDF and Fan/PVDF OMA combinations.



Visually (see figure 7.11), the quality of the SVD plots is the same. However, as it can be stated in table 7.3, the standard deviation is much higher, in the case of the  $\mathcal{S}$ -optimized network (around 2.0%), with respect to the natural frequencies extracted from EMA, than in the case of the  $\mathcal{K}$ -optimized one (around 0.72%), making conclusive the improvement provided by the EI method.

#### 7.4.6 PVDF as sensors/actuators: PVDF/PVDF

The experimentation with samples  $\mathbb{A}$ ,  $\mathbb{B}$  and  $\mathbb{C}$  have shown that PVDF actuation and sensing are possible. As final stage of experimentation, it is logic to try one last sample equipped only with PVDF sensors and actuators. The fourth sample, named  $\mathbb{D}$ , has two  $\mathcal{K}$ -optimized integrated networks of PVDF. As it can be seen in figure 7.12, the signal quality is satisfying.

The  $\mathbb{D}$  OMA1 test shows an error level of 0.78%, slightly higher than the aforementioned results. The second test,  $\mathbb{D}$  OMA 2, shows a supplementary test which combines PVDF transducers and fan excitation to achieve higher excitation in both lower and higher frequencies. The inspiration for this test is based on the possibility to use both natural and artificial actuators (as it would be possible in full-scale structures and *in situ* tests): the natural excitation would be the principal source of energy, but in absence of this, the PVDF complementary network would excite the structure to continue the OMA analysis. The final result shows a slight decrease of the error to 0.45%, for a PVDF excited band between 1000 [Hz] and 2000 [Hz].

#### 7.4.7 Discussion of the results

A summary of the standard deviation percentages is summarized in table 7.3 and ranked in decreasing order in figure 7.13.

The first statement about the scattering levels for the OMA tests involving the PVDF patches is the consistency around approximatively the same values, included in the interval between 0.42-0.78%, with two notable exceptions: the  $\mathbb{A}$  OMA3 test (PVD-F/Acc,  $\sigma_\epsilon = 1.5\%$ ) and the  $\mathbb{C}$  OMA2 test (Fan/PVDF,  $\sigma_\epsilon = 2.0\%$ ). These last two tests have in common the involvement of a  $\mathcal{S}$ -optimized PVDF network in actuation/sensing, which could be associated with a lower performance with respect to  $\mathcal{K}$ -optimized PVDF network.

Statistically, OMA and EMA can be considered statistically equivalent since the bias between both is proved insignificant. Concerning the usefulness of these measurements, the accuracy of the measured natural frequencies affects directly the accuracy of the material characterization, since these are related to the mechanical properties identification (by a factor of 2). Thus, the difference of the moduli estimation would

**Chapter 7. Implementation of Operational Modal Analysis using strain transducers**

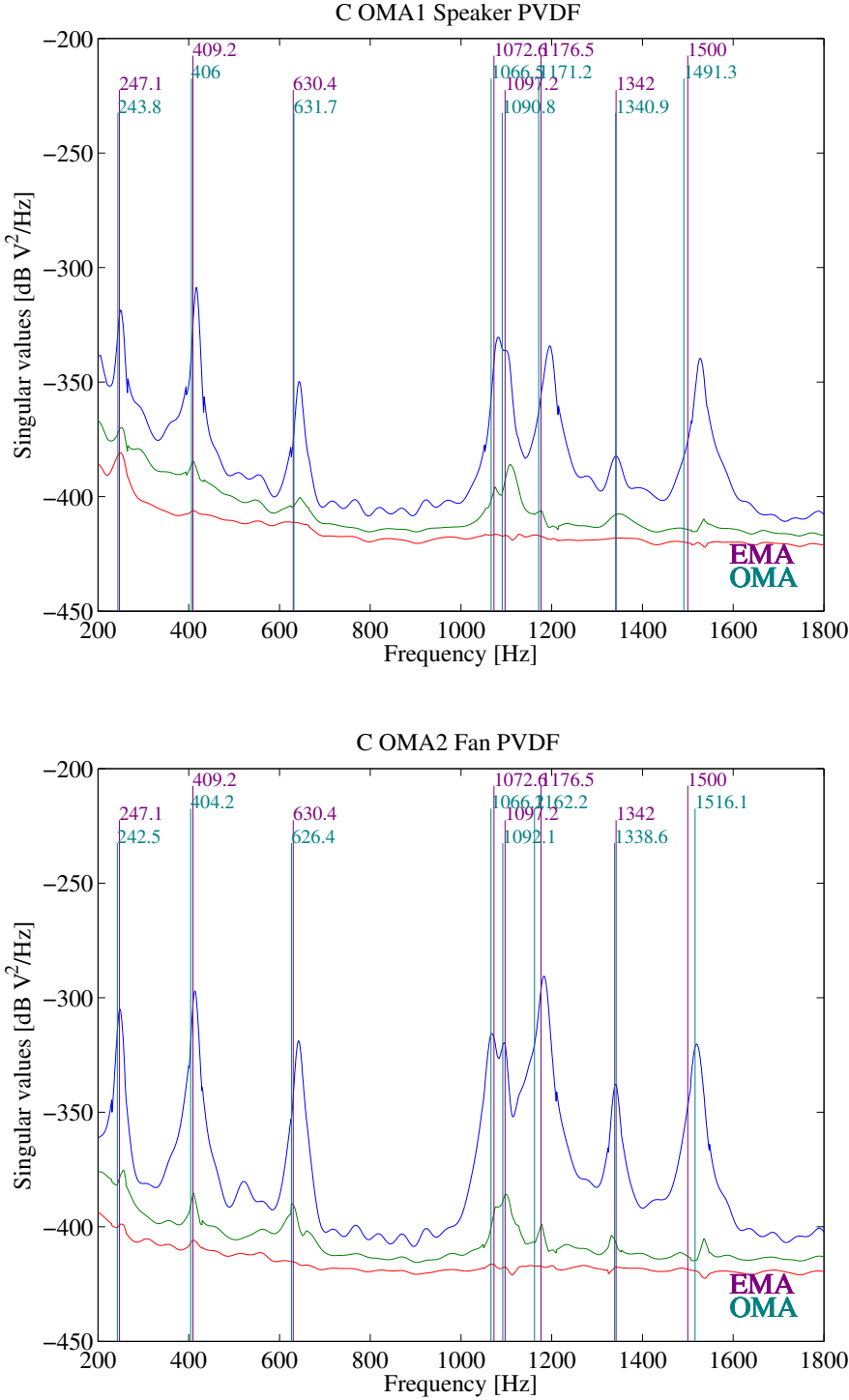


Figure 7.11 – SVD plot for the Fan/PVDF combination, test on two different configurations:  $\mathcal{S}$ -optimized and  $\mathcal{K}$ -optimized.

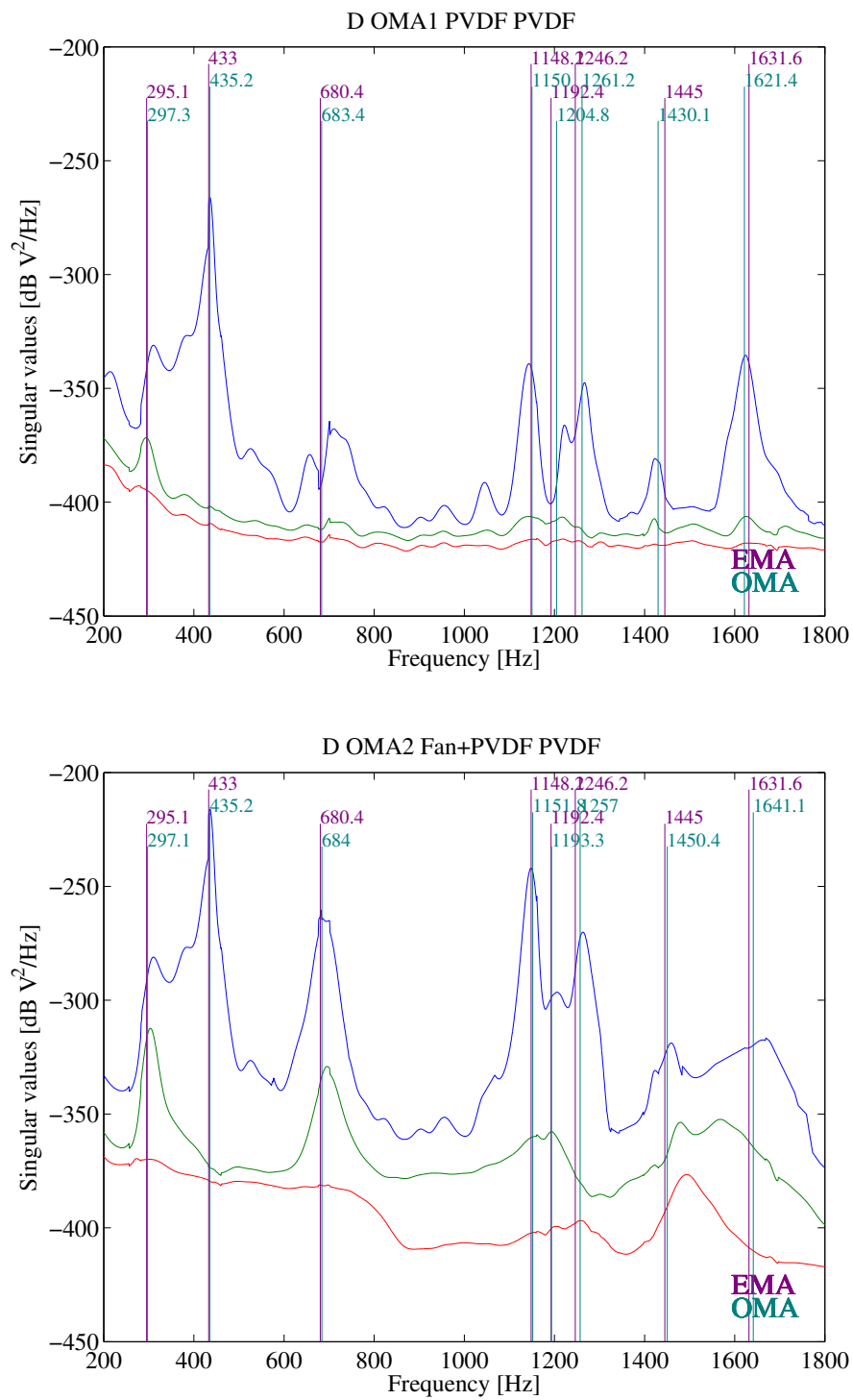


Figure 7.12 – SVD plot for the PVDF/PVDF and Fan+PVDF/PVDF OMA combinations, test with the  $\mathcal{K}$ -optimized network.

## Chapter 7. Implementation of Operational Modal Analysis using strain transducers

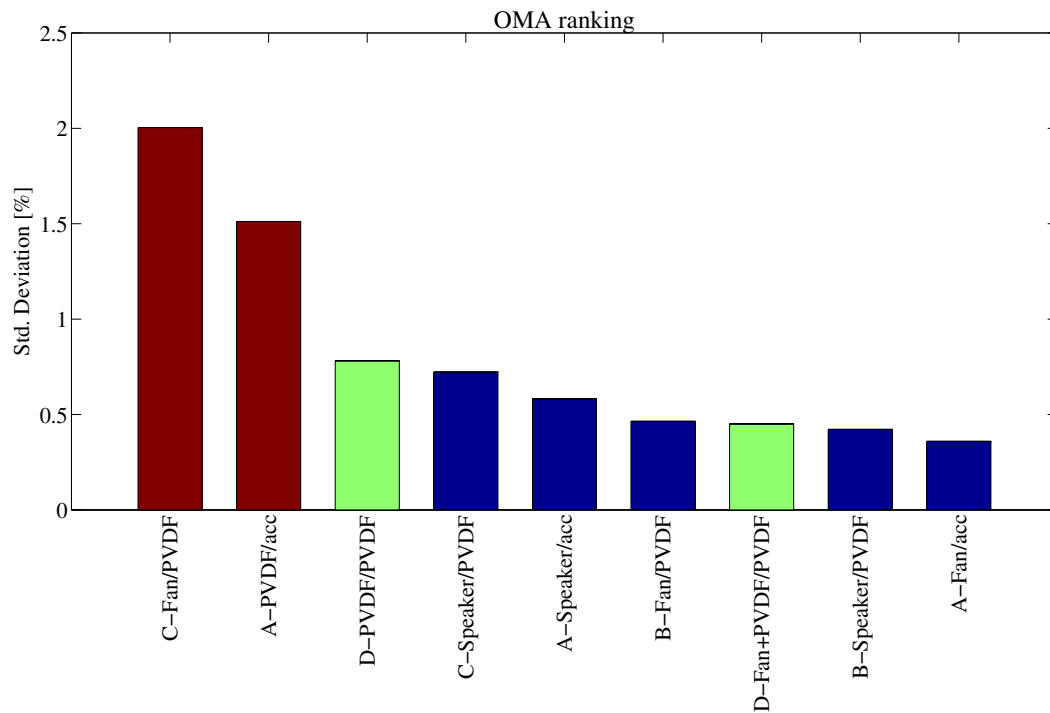


Figure 7.13 – OMA methods ranked by their performance, in terms of standard deviation with respect to the reference method (EMA). Red bars are the cases where  $S$ -optimized networks are involved for sensing or actuation, and green bars are the cases where  $K$ -optimized are involved for sensing and actuation. The latter show a better performance from this point of view.

be in the 0.21-0.39% interval. As an example, this would be very small, knowing that the natural ageing degradation of operational CFRP panels can reach a 10% loss of the local elastic properties. The efficiency of the technique suggested in this chapter is suitable for a SHM application.

### 7.5 Conclusions about OMA with PVDF

From the results stated in the previous section, several statements can be made. The placement strategy proposed by [Li et al., 2007], introducing the EI technique, improves significantly the accuracy of the natural frequencies extraction from OMA.

As actuators, the PVDF transducers show to be appropriate and suitable for SHM based on OMA, as long as they are optimally placed inside the composite structure. About the *a priori* concern about low stiffness and block force, PVDF film transducers were capable of producing enough force to bend correctly a CFRP sample and provide enough power for the sensors to acquire, an ability that increases with the frequency. As sensors, PVDF provide remarkably accurate results with respect to accelerometers,

confirming with this the results of previous chapters.

The eventual association of PVDF actuation with a natural excitation source (in this case represented by a fan) shows to be a powerful complementary tool to natural excitation, and is strongly suggested to be explored further and used in SHM applications using OMA. The results of this chapter have been submitted and are currently under review [Guzman et al., 2014].



# 8 Application of the SHM method: Section of a plane wing

## 8.1 Motivation

The development and validation of the tools proposed in the previous chapters were carried out with rectangular plate specimens as study subjects. This has been very useful given the simplicity of the geometry, which is somehow an advantage to prove the feasibility of the monitoring protocol and the ageing modelling, because of the inherent simplifications of working with two-dimensional samples.

However, from the operational point of view, composite lay-ups in the industry frequently show more complex shapes and larger geometrical dimensions. This leads to the increase of the modal mass and modal density in the spectral domain, and therefore the problem of modal extraction can be a source of inaccuracy. Other problems include: the increase of necessary computational means to perform numerical simulations, the design process of sensor networks, the problem of actuation when structures become larger, etc.

For all of these reasons, it was decided that the SHM tool would be tested on a three-dimensional demonstrator as a first step to the adaptation of the tool to "real-life" structures (in the technology readiness level scale, this would be the equivalent to pass from TRL4 to TRL5). This chapter is a description of the implementation and consequent results of the application of all the tools constituting the SHM system on three demonstrators named K, L and M.

The base demonstrator is an open NACA-profile skin (upper surface only), supported by three symmetric ribs made of CFRP, which are attached using high temperature epoxy resin glue. Two types of glue were used:

- Araldite©, which was already used for the sensor integration on plates, was used on demonstrator K.
- EPH573, provided by Suter-Kunststoffe.

## **8.2 Monitoring protocol**

The suggested protocol for monitoring a structure can be summarized as follows:

1. The specimen is designed with the assistance of computer aided engineering software, for building the corresponding FE model afterwards: an estimation from material's datasheet is used as a first approximation.
2. The FE model is used to simulate the vibrational behaviour of the structure, and allows designing an optimized sensor network, as shown in chapter 6.
3. Once the position of the sensors is determined, the manufacturing can start. The sensors are integrated on the structure. Eventual corrections (like local defects or special features) are added to the FE model.
4. Using an EMA technique, the first OMA is validated, and a reference modal state is acquired. Eventually, if the measured frequencies are very different from those predicted by the FE model, this one should be updated (by a numerical-experimental identification or by changing/updating the geometry).
5. The specimen is subjected to ageing.
6. During the ageing, several rounds of measurement take place in order to monitor the degradation process. For each iteration, the following features are to be extracted:
  - Modal parameters: natural frequencies (and mode shapes if possible), using the OMA method described in chapter 7.
  - Mass: in full-scale structures this may be impractical or even impossible. If the ageing conditions are known, an estimation could be computed from the diffusion model using the diffusion modelling method described in chapter 4.
7. After each iteration, the experimental data is used to identify the elastic moduli, which will be used as ageing indicators, using the procedure describe in chapter 2.
8. The user can decide on the base of this information if operating the structure is still safe enough, or how long the structure can still operate.

The demonstrators described in the following sections are monitored following these steps. In addition, but only for validation purposes, EMA is carried out at each round in order to validate the use of OMA in these three-dimensional structures. Also, the mathematical ageing model developed in chapter 4 is validated.



## 8.3 Design

### 8.3.1 NACA profile and structure choice

The NACA 2412 profile shown in figure 8.1 has been chosen given its frequent use in the aeronautical industry. The demonstrator is designed to be close to a full-scale structure, similar for example to the one represented in upper figure 8.2. It represents the internal structure of a common wing, featuring longitudinal (spars) and transversal (ribs) reinforcing parts. The demonstrator specimens include only the latter, in order to simplify the analysis and manufacturing. Thus, the demonstrators exhibit the following features:

1. The demonstrator is straight all along, with no dihedral angle nor sweep.
2. Only the upper skin is included.
3. No spars are included.
4. The ribs are symmetric. This is, the camber line is a horizontal straight line.
5. The ribs are located asymmetrically along the extrusion, at 3%, 75% and 97% of the length.

The limiting factor on the size is the size of the climatic chamber. The adopted dimensions are:

- Length: 580 [mm]
- Chord: 250 [mm]
- Thickness(average): 3 [mm], for both skin and ribs.

These dimensions are represented in figure 8.1.

### 8.3.2 Finite element model

The main difference with respect to the plates is the use of more adapted solid and shell elements. The adopted element types depend on the region, and they were chosen following the distribution shown in figure 8.3:

1. In the light blue zone, C3D20R (hexahedral) and C3D15 (triangular prism) elements make part of a unstructured mesh.
2. In the light gray zones, C3D20R elements make part of a unstructured mesh (extra-dos skin) or a structured mesh (ribs) .
3. In the green zones, only C3D15 elements.
4. In the red rib-skin interfaces, shell S4R elements to simulate the glue. It is important that these elements are given a thickness (in this case, 0.5 [mm]), in order

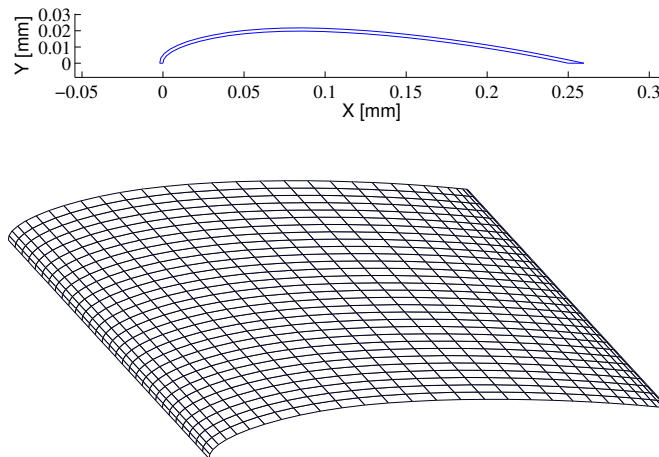


Figure 8.1 – NACA 2412 profile.

to include transverse shear in the formulation, as in the Reissner-Mindlin plate theory [Reddy, 1984].

5. The reduced integration is used to avoid locking, and hourglass control is included.
6. The simulation is run under fully free conditions.
7. In total, the FE mesh consist of 79379 nodes and 11427 elements, of which:
  - 10656 C3D20R ( $\approx 3$ [mm] sides, 1 element across the thickness),
  - 576 C3D15 and
  - 195 S4R.
8. In this case, the elements are in general more degenerated than in the plate case, but a preliminary analysis with ABAQUS shows no zero or negative volume elements.

The identified elastic properties using the numerical-experimental identification algorithm, before starting the ageing process, are shown in table 8.1. These values are slightly different from the nominal values given in table 2.1 for the plate samples, most probably due to the geometry imperfection. However, this does not constitute a real problem, since the ageing is always monitored with respect to the initial identified value.

An isotropic material model is adopted for the glue. Since no accurate information of the mechanical properties is provided by the manufacturer, it is assumed that the elastic moduli of the glue can be approximated by those dominated by the epoxy resin in the composite material, namely the transversal Young's and shear moduli. The advantage of this approach is that the ageing characterization will take into account the ageing of the glue as well.

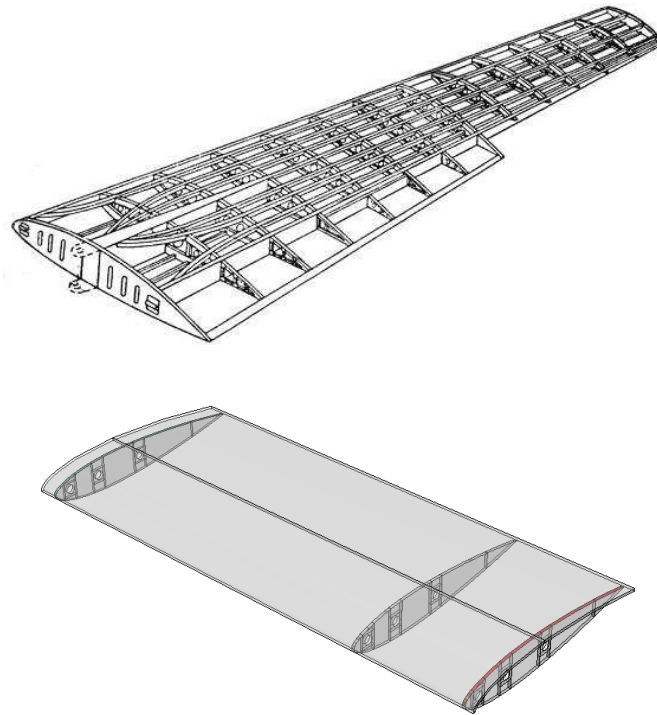


Figure 8.2 – Above: example of the internal structure of a wing (photo source: Wikimedia). Below: numerical model of the NACA 2412 profile demonstrator, with the ribs integrated to the upper skin.

The use of unstructured meshes and glue modelling were introduced after errors in the numerical-experimental identification were detected in preliminary simulations. This shows the importance of the accuracy of the FE model before the ageing monitoring starts. It is advised to run several simulations, in order to make sure of the robustness of the identification loop:

- Verify the FE model is correctly meshed: no aberrant elements, absence of hour-glass modes/membrane locking, correct number of natural frequencies computed.
- Verify the inverse method: verify that the convergence of the optimization is independent from the initial conditions, select correctly the sensitive elastic properties that can be identified by the algorithm, select an appropriate objective function.

The simulated vibration modes are shown in figure 8.4. It can be seen that they are similar to plate modes, since the ribs show little deformation. It can be deduced that the optimal place of the sensors is exclusively on the skin. The seven lowest-frequency vibration modes are considered.

## Chapter 8. Application of the SHM method: Section of a plane wing

Table 8.1 – Identified elastic properties before the ageing process. It can be noticed that the directions 2 and 3 have been interchanged. For further details, see subsection 8.3.6

Specimen	K	L	M	Estimation
$\rho$ [kg/m <sup>3</sup> ]	1402	1400	1400	Defined (*)
$E_1$ [GPa]	93.2	96.6	98.7	Identified
$E_2$ [GPa]	8.7	8.7	8.7	Estimated
$E_3$ [GPa]	7.51	7.40	7.36	Identified
$\nu_{12}$	0.3	0.3	0.3	Estimated
$\nu_{13}$	0.38	0.38	0.38	Estimated
$\nu_{23}$	0.03	0.03	0.03	Estimated
$G_{12}$ [GPa]	3.8	3.8	3.8	Estimated
$G_{13}$ [GPa]	3.86	3.63	3.48	Identified
$G_{23}$ [GPa]	2.25	2.25	2.25	Estimated

(\*) Mass density fixed by the experimenter.

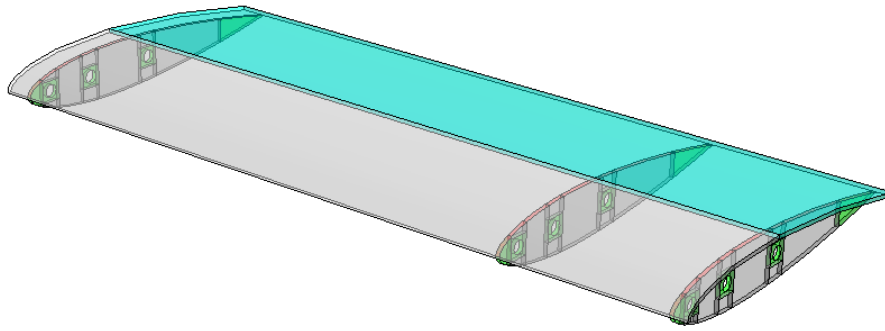


Figure 8.3 – Coloured regions by element type.

### 8.3.3 Ageing protocols

The three demonstrators were subjected to similar ageing protocols as the rectangular plates. One of the purposes of the demonstrators was to validate the statements made at the end of chapter 4, concerning the possibility to generalise the CFRP ageing model to other geometries *via* the estimation of water mass absorption. The adopted protocols are summarized in table 8.2.

1. All three protocols include humidity as a factor, and none of them includes UV radiation.
2. The water mass absorption and the consequent degradation are predicted by the multifactorial model described in section 4.5.3.
3. Demonstrator L was subjected to an ageing protocol already used in the past.

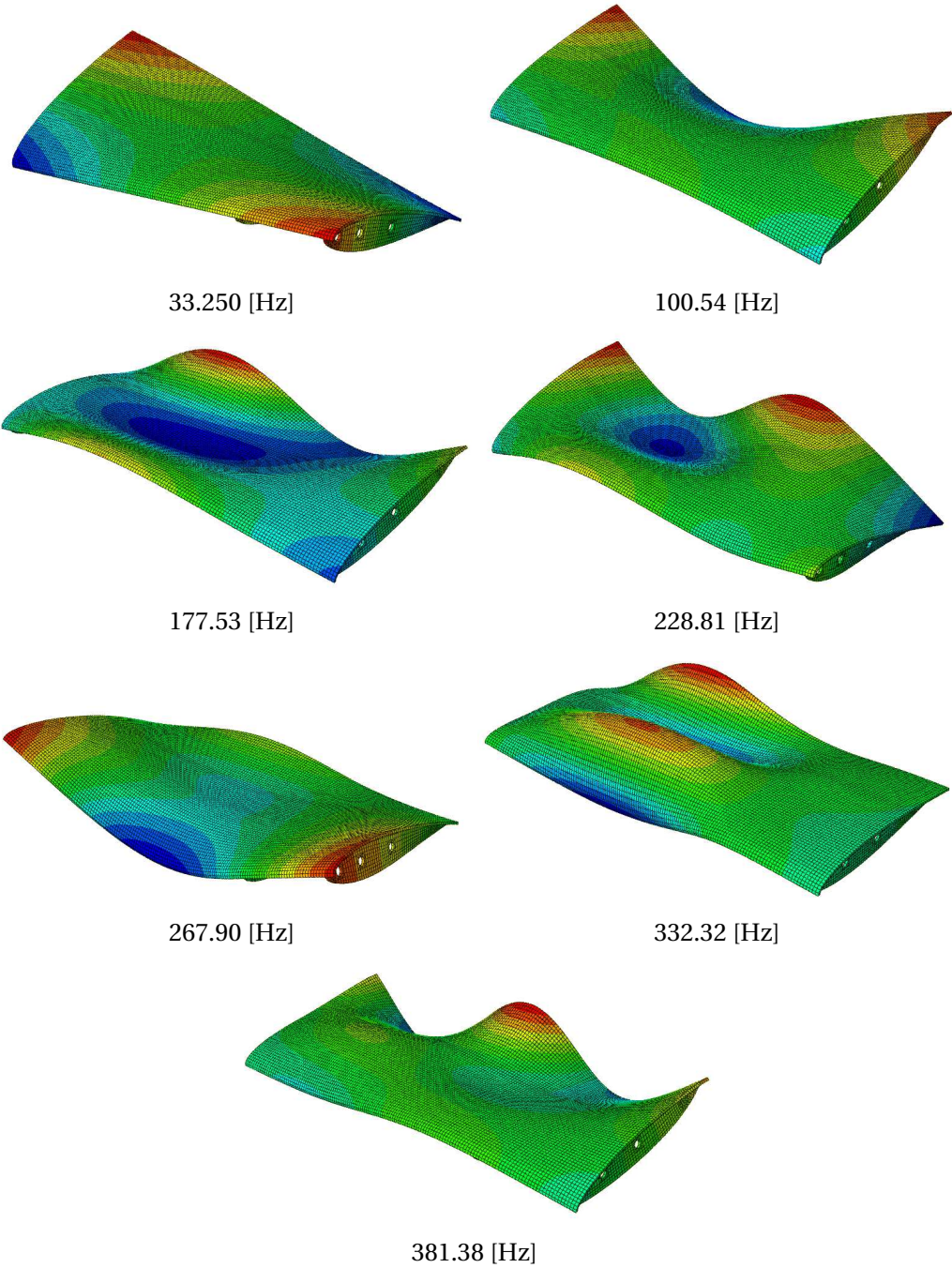


Figure 8.4 – Simulated numerical vibration modes of the demonstrator.

## Chapter 8. Application of the SHM method: Section of a plane wing

4. Demonstrator K was subjected to an ageing protocol close to one already used in the past. The reason behind subjecting it to such low humidity (15%) was to check if the prediction ability of the multifactor model would work even under very low humidity.
5. Demonstrator M was subjected to a completely new protocol, which is in the mid-point between two protocols already used.
6. The monitoring rounds occurred every 100 cycles.

The results of the protocols, if accurate, would allow validating several hypothesis and statements from the previous chapters, in particular the diffusion model (chapters 3 and 4), the multifactor ageing model (chapter 4) and the survivability of the PVDF sensors (chapter 5). Furthermore, the validation would imply that the multifactorial is adapted even in cases with different ageing protocols to those carried out in the past.

Table 8.2 – Summary of ageing protocols for the demonstrators. Monitoring rounds were carried out every 100 cycles. For all protocols,  $\Delta t_+ = \Delta t_-$ .

Series	Temperature			Relative humidity			$N_{cyc}$	$\Delta t$ [min]	$q$
	$T$ [°C]		$x_1$	$RH$ [%]		$x_2$			
	Min	Max		Min	Max				
K	45	135	1	0	15	0.16	1000	60	11
L	5	95	0	0	95	1	1000	90	11
M	25	115	0.5	0	50	0.53	900	90	10

### 8.3.4 EMA with impact hammer and Polytec interferometer

As in the case of CFRP plates analysed in the previous chapters, EMA is used as a reference modal analysis method in order to accurately measure the natural frequencies. Given the complexity of the geometry and the high modal density, it was decided to use two different EMA techniques: the impact hammer-based technique which was used in previous chapters, and the Polytec interferometer-based technique. The reason is that the Polytec offers the advantage to be semi-automatic, and allows measuring the displacement of a large number of points, and consequently giving an accurate overview of the vibration modes. These experimental modes can be easily compared to their numerical counter-parts.

As an example, the first seven modes that are shown in figure 8.5 were measured on the L demonstrator. It can be seen that they correspond to the observed modes in the FE simulation. The same modes were observed using the impact hammer, as seen in figure 8.6.

The corresponding measured FRF plots are shown together in figure 8.7, including

the extracted natural frequencies (the first plot shows the eighth natural frequency as well, which is not taken into account in further analysis). It can be verified that the differences between the extracted frequencies are not significant (the relative error is less than 0.7% in all cases). Consequently, during the ageing process, only the impact hammer technique is used to perform EMA, which results are compared to OMA results.

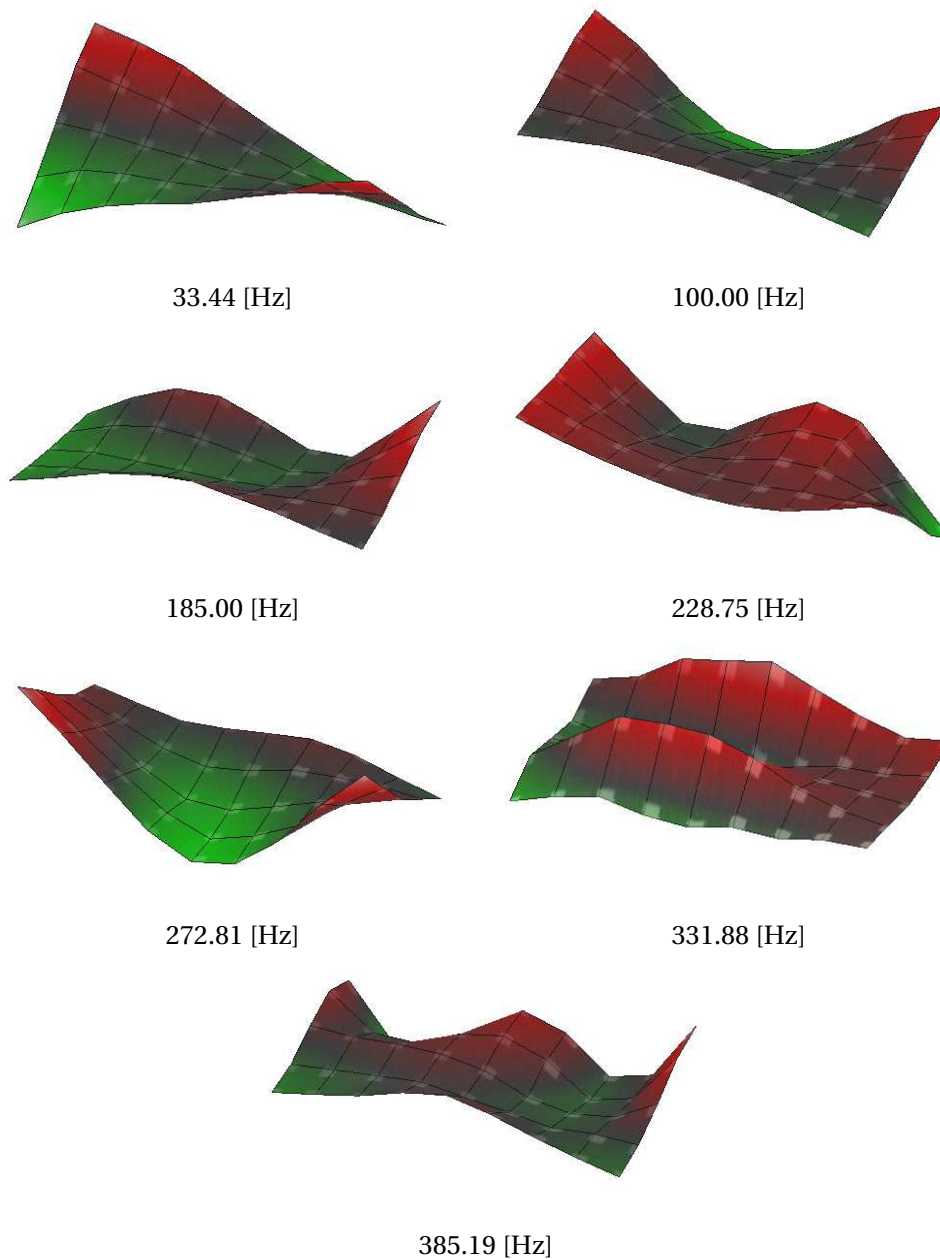


Figure 8.5 – Example: Experimentally observed vibration modes of the demonstrator L, using the Polytec interferometer.

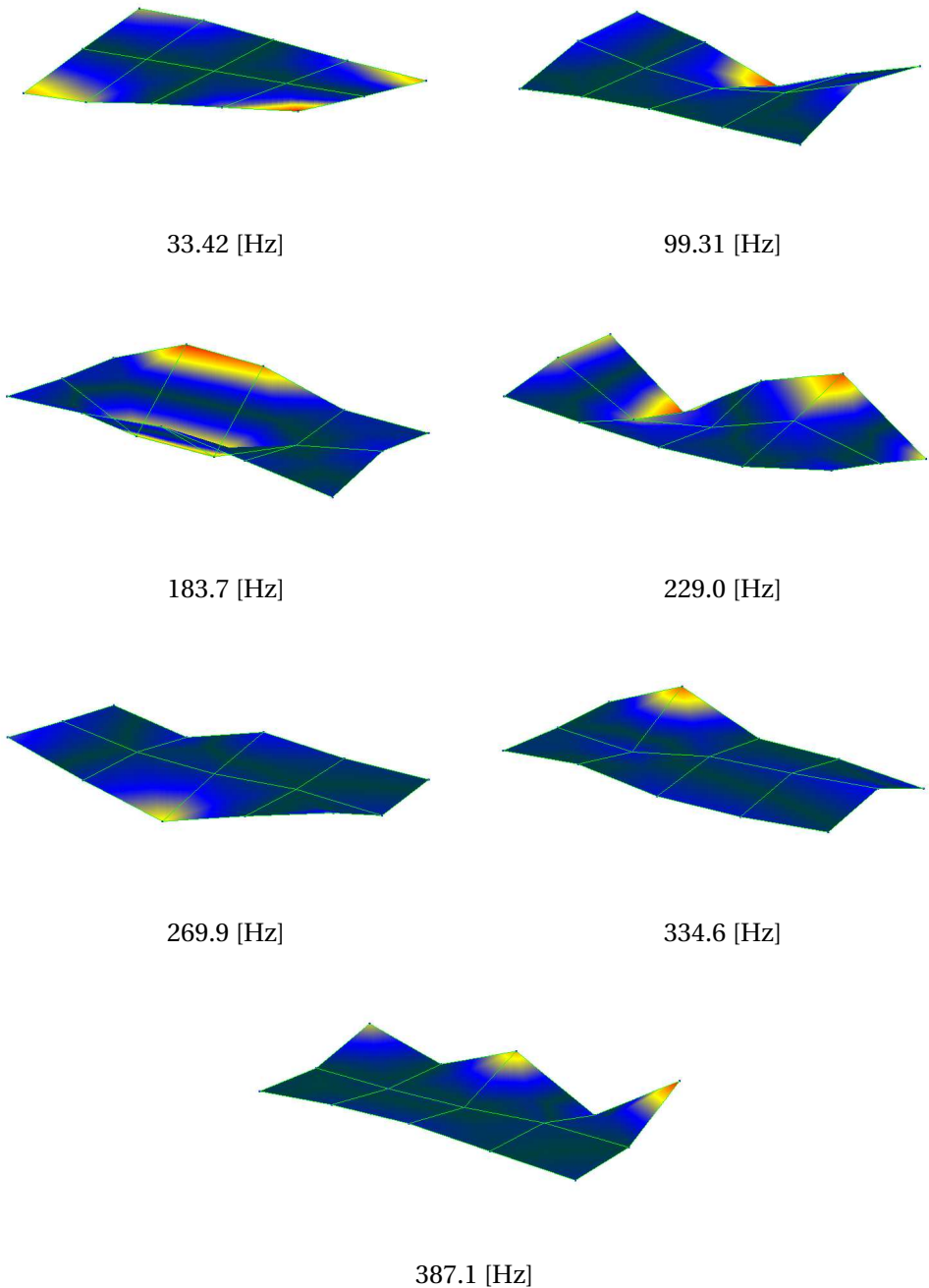
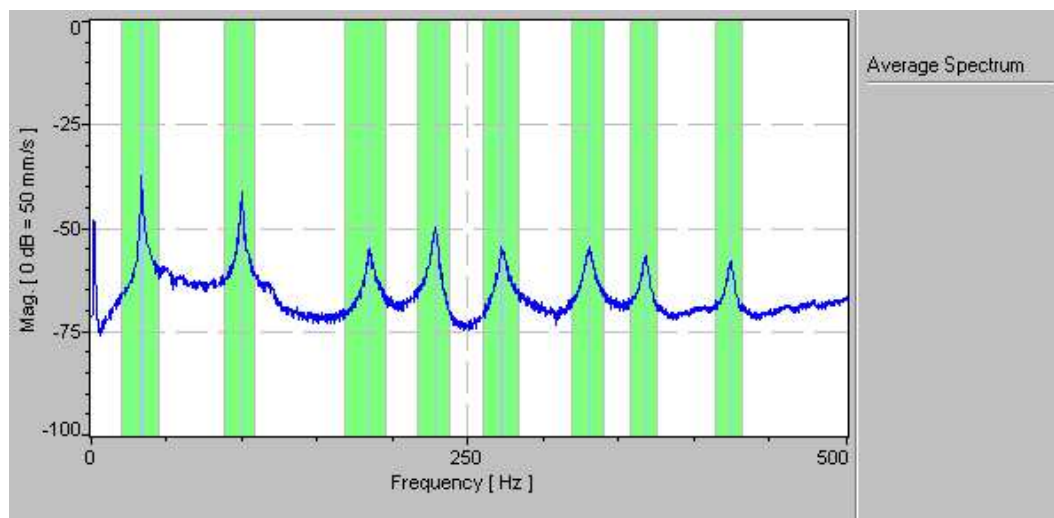
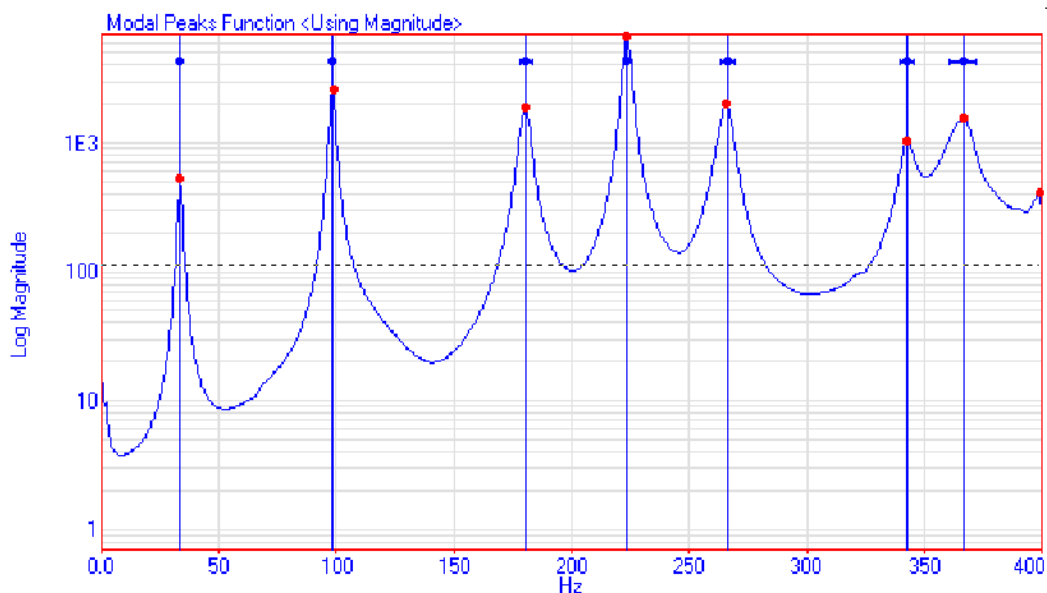


Figure 8.6 – Example: Experimentally observed vibration modes of the demonstrator L, using the impact hammer.





(a)



(b)

Figure 8.7 – Example: Experimentally measured FRF, for demonstrator L, using (a) the Polytec interferometer and (b) the impact hammer setup.

### 8.3.5 Numerical-experimental identification using vibration modes

The geometrical complexity and the high modal density (many vibration modes with close natural frequencies) make it difficult to rely only on the simulation of natural frequencies to identify accurately the elastic properties of the composite. The main reason: changes due to the ageing can cause natural frequencies to get too close to each other, to the point they are no longer accurately discerned. It can even happen that the order of the vibration modes is permuted during the ageing.

These (likely to happen in full-scale structures) eventualities considered, a new identification strategy has been proposed, that includes the comparison between the numerical and experimental frequencies, and adds an extra element to the objective function: a comparison between the numerical and experimental mode shapes *via* the MAC, which measures the colinearity between mode shapes. The objective of this criterion is then the mode pairing, to associate the FE simulated and the experimentally measured modes. The new objective function is given by the norm of the error matrix  $\epsilon$ :

$$\begin{aligned}\epsilon &= [\alpha_f \epsilon_f, \alpha_{MAC} \epsilon_{MAC}] \\ \epsilon_{f,i} &= \frac{f_{i,FE} - f_{i,Exp}}{f_{i,Exp}} \\ \epsilon_{MAC,i} &= 1 - MAC(\phi_{i,FE}, \phi_{i,Exp})\end{aligned}\tag{8.1}$$

where  $f_i$  and  $\phi_i$  denote the  $i^{th}$  natural resonance frequency (in [Hz]) and its corresponding ODS (as measured by the sensors or simulated in the location of the sensors in the FE model). The error vectors  $\epsilon_f$  and  $\epsilon_{MAC}$  are the frequency and MAC error vectors respectively. The weighing coefficients  $\alpha_f$  and  $\alpha_{MAC}$  depend on the incertitude level of each norm. In this case, the incertitude (given by the standard deviation) on the relative frequency has been estimated to around 1%, while the one for the MAC quotient is around 10%. As specified by [Cugnoli et al., 2007], the higher the incertitude, the lower the value of this coefficient must be. In the same reference, are advised  $\alpha_f = 1$  and  $\alpha_{MAC} = 0.05$ . Exaggerated high values can lead to a numerical instability of the optimization algorithm. The low value adopted for  $\alpha_{MAC}$  reduces the role of MAC in the identification process to simple mode pairing, in order to gain some accuracy in the material identification. More over, the error propagation due to MAC is estimated to be low ( $10\% \times 0.05 = 0.5\%$ ).

### 8.3.6 Local orientation of elastic properties

The material orientation is another fundamental aspect that has a particular approach in this case. In order to be coherent with which has been said in previous chapters and consequently use the conclusions about ageing modelling, it is necessary to adapt the conventions established earlier.

As in the case of plates, the thin shells manufactured for the demonstrators are unidirectional, with the fibres in the longitudinal direction for both upper skin and ribs (axis 1). The main difference with respect to the rectangular plates is that (for techni-

cal reasons) the transversal direction is tagged with number 3 this time, and normal axis is tagged with number 2. This change in the orientation implies that indexes 2 and 3 are interchanged:  $E_2$  and  $G_{12}$  moduli are replaced by  $E_3$  and  $G_{13}$  for the demonstrator. As it can be expected,  $E_3$  and  $G_{13}$ , along with  $E_1$ , are the elastic moduli that have the most influence on the dynamic behaviour of the structure. This is confirmed in subsection 8.3.7. Concerning the ageing evolution of the composite,  $E_1$  is dominated by the ageing of the carbon fibres and the carbon fibre/epoxy interfaces, while  $E_3$  and  $G_{13}$  are dominated by the ageing of the epoxy resin.

Since the upper surface of the demonstrator is curved, local reference frames need to be included in the computation of the optimal placement locations. Indeed, the PVDF sensors are chosen to be fixed on this surface. The orientation is defined in figure 8.8. This local material orientation is also used to define the material properties in the FE model of the demonstrator.

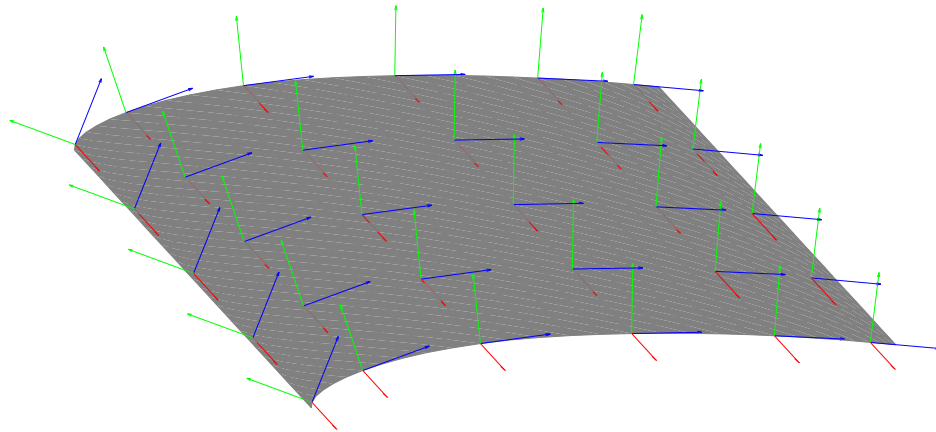


Figure 8.8 – Local orientation frames on the upper surface: red = 1, green = 2, blue = 3.

### 8.3.7 Sensitivity analysis

Another consequence of the geometrical complexity is the influence of orthotropic elastic moduli on the natural frequencies and vibration modes. The curved shape and the presence of transversal (asymmetrically disposed) ribs may change considerably the order (and shape) of the vibration modes with respect to rectangular plate samples with similar dimensions. The vibration modes are also very asymmetrical, as it can be observed in figures 8.4, 8.5 and 8.6. In such conditions, bending and torsion stiffness cannot be attributed so easily to a given set of elastic properties. Thus, a sensitivity analysis is necessary, and has been carried out for the demonstrators with the method described in subsection 2.3.3.

Furthermore, a sensitivity analysis is particularly important for another reason. By

**Chapter 8. Application of the SHM method: Section of a plane wing**

means of the statistical study of error propagation, a sensitivity matrix becomes a tool to estimate the uncertainty in the identification of elastic properties, based on the natural frequencies dispersion measurements (standard deviation for example). Thus, sensitivity works as a proportionality coefficient between standard deviation of the independent variables (natural frequencies in this case) and dependent variables (elastic properties), as referred to in equation (2.12).

For demonstrators K, L and M, the sensitivity matrix elements are represented in figure 8.9 using a bar diagram. It can be seen in this case, that only four elastic moduli have a significant influence in the vibrational behaviour of the structure:  $E_1$ ,  $E_3$ ,  $G_{12}$  and  $G_{13}$ . For the sake of simplification, influence by  $G_{12}$  is neglected since even it is significant (for the first vibration mode), its influence is much smaller than the others.

In further sections, only  $E_1$ ,  $E_3$  and  $G_{13}$  are considered. This was somehow expected, since the whole geometry of the demonstrators is constituted by thin parts.

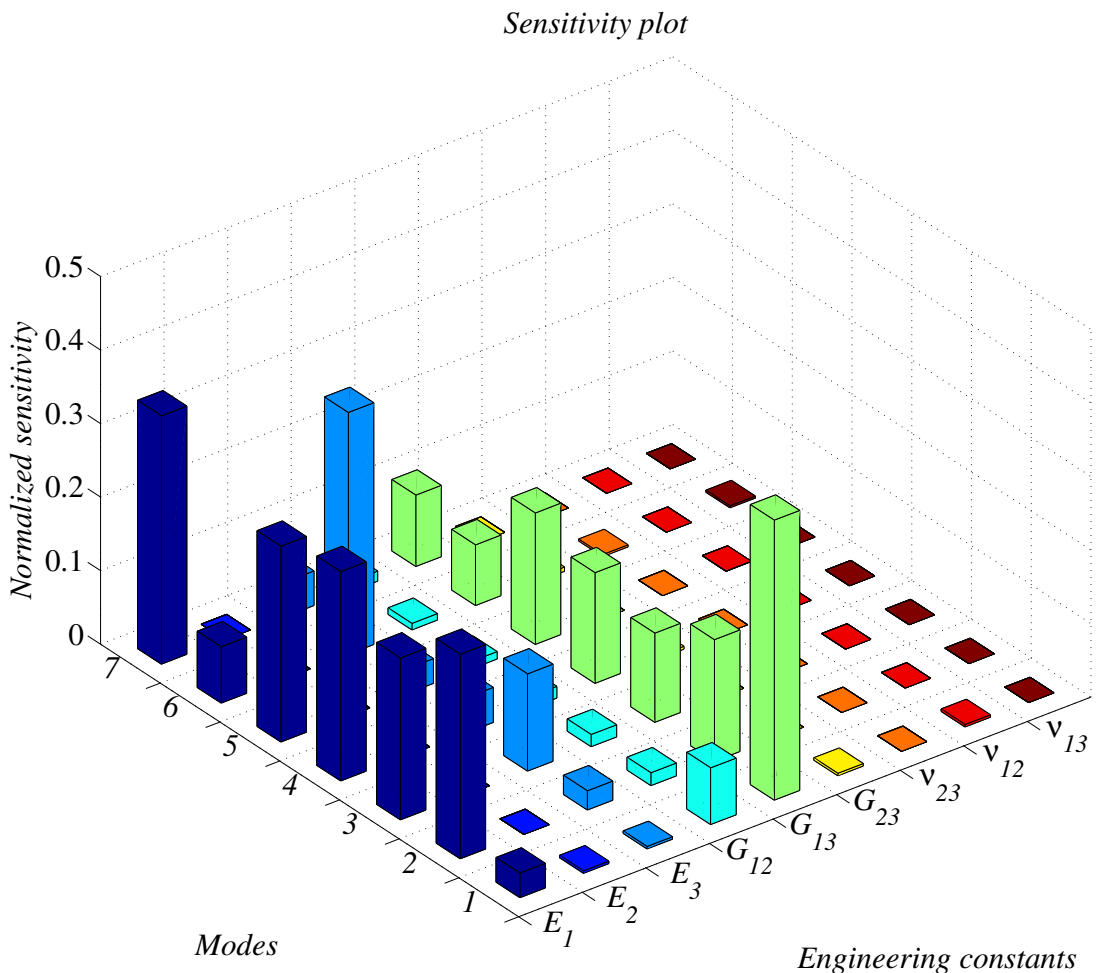


Figure 8.9 – Sensitivity coefficients for the demonstrators.

### 8.3.8 Optimal placement

The EI-based OSP tool developed in chapter 6 is adapted to the demonstrator:

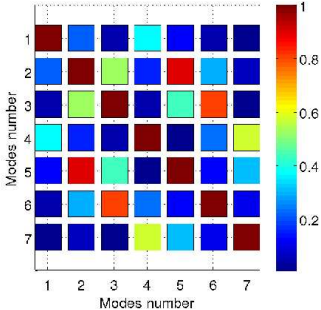
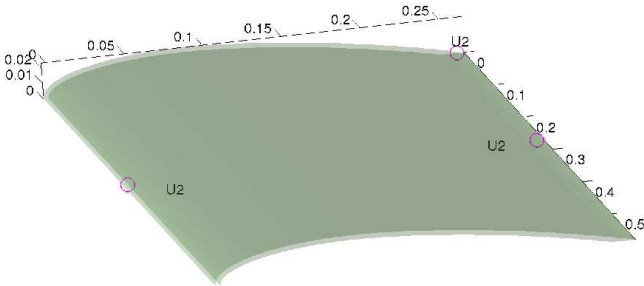
1. The interchange between indexes 2 and 3 is included in the computation.
2. For technical reasons (number of channels in the HP35670A dynamic analyser), it was preferable to find a network configuration using only three accelerometers. As it can be observed in figure 8.10 (a), the vibration modes are satisfyingly discerned. Indeed MAC coefficients between all consecutive modes are lower than 0.5, which is acceptable in these circumstances (spectral separation is at least 40 [Hz]). This configuration was successfully applied to the demonstrator, consequently with the results shown in figures 8.6 and 8.7(b).
3. Similarly, for the number of PVDF patches, a minimal configuration allowing a MAC coefficient lower than 0.5 for two consecutive modes was aimed. Direction 1 (longitudinal) was preferred since the demonstrator was most likely to be bended in this direction at the lowest frequencies (the ribs make the demonstrator stiffer in the transversal direction). Thus, in this case, the EI algorithm described in section 6.2 is applied using  $\Phi_{s_{11}}$  as modal matrix. The result of the optimisation process is a network of five sensors, which are located as shown in figure 8.10(b). The quality of spectral separation is satisfying, as it will be shown in subsection 8.5.4. Indeed, the optimisation is applied to the demonstrators (K, L and M), in sensing as well as in actuation (only M).

### 8.3.9 Manufacture

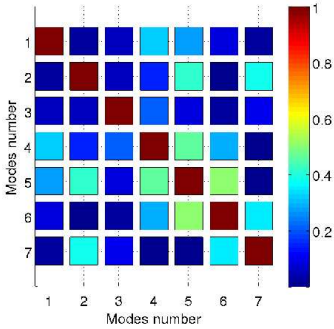
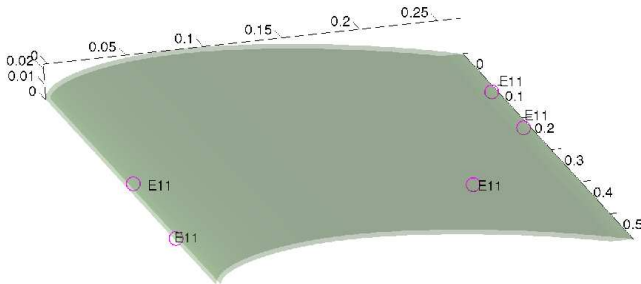
For the demonstrators, the manufacturing of the demonstrators included the use of a high temperature epoxy resin glue. The PVDF patches are integrated following the optimised locations mapping presented in subsection 8.3.8.

As for the rectangular plates, the center of the patches corresponds to the points located by the optimisation algorithm. The integration is carried out on the inner surface of the skin, mainly because it makes easier the handling of the axial cables, but also because it would be more likely to adopt that configuration in a full-scale structure. As an example, photos of the manufactured specimen are shown in figure 8.11.

In the case of demonstrator M, one additional PVDF patch per location is integrated. These additional patch is part of the actuator network. The actuators are oriented in direction 1 as well.



(a)

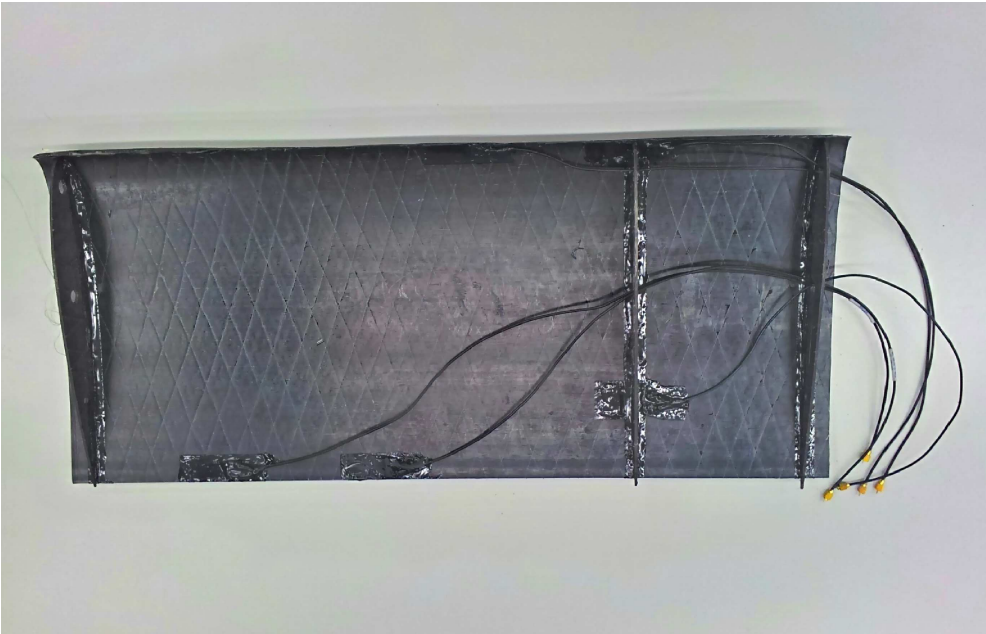


(b)

Figure 8.10 – Optimal placements, as computed for the demonstrators, using (a) 3 accelerometers and (b) 5 PVDF sensors.



(a)



(b)

Figure 8.11 – Photos of a manufactured demonstrator (L).

### 8.4 Experimental monitoring

As explained in section 8.3.7, the ageing monitoring is focused on the evolution of three elastic moduli, as it was in the case of the rectangular plates. For the sake of coherence with which has been told previously, the results are going to be expressed as the ratio between current values and initial values.

$$y_1 = \epsilon_1 = \frac{E_1}{E_{10}} \quad (8.2)$$

$$y_2 = \epsilon_3 = \frac{E_3}{E_{30}} \quad (8.3)$$

$$y_3 = \gamma_{13} = \frac{G_{13}}{G_{130}} \quad (8.4)$$

The evolution of these three dimensionless magnitudes is surveyed and subsequently compared with the ageing model, in order to verify its validity. Simultaneously, the performance of the OMA method developed in this thesis is compared with and validated by the parallel measurements using the impact hammer EMA.

#### 8.4.1 Online monitoring

The online monitoring is carried out in a similar way as for the previous chapters:

1. Monitoring frequency: as stated previously, the modal parameters are measured and recorded every 100 cycles, with the ageing protocol ending after 1000 cycles (900 cycles for M). The tests were carried out at room temperature, after a cooling down period of some minutes for the demonstrator.
2. Performed analyses: EMA is carried out with 3 accelerometers optimally placed as in figure 8.10(a). OMA is carried out with 5 PVDF sensors optimally placed as in figure 8.10(b). The mass is measured using a Mettler-Toledo weighing balance which has a resolution of 1 [g]. For weights over 200 [g], it was not possible to have a better resolution.
3. Sample sizes: for EMA,  $n = 15$  average FRFs were experimentally acquired, which gave 15 independent estimations of the natural frequencies. For OMA,  $n = 15$  because every signal is divided in 15 sub-signals (see chapter 7), which allows obtaining 15 estimations for each natural frequency.



## 8.5 Results

### 8.5.1 Moisture absorption

The absorption is measured by change of mass in the specimen. The results of the monitoring are plotted in figure 8.12, along with the predicted curves using the absorption model described in chapter 3. The "infinite" plate approximation is better suited in this case since the thickness (3 [mm]) is even smaller than in the previous cases, and a larger surface (skin and ribs) is exposed to the humidity absorption. It was expected to obtain a more accurate prediction.

The error bars represent in this context the uncertainty related to the minimal resolution of the weighing balance (1 [g]), expressed as a percentage of the total weight of the sample. It can be seen that the prediction curve passes consistently inside the uncertainty intervals. There are two exceptions to this rule: some of the last weightings of demonstrator L et M. This slight underestimation can probably be explained by the error induced by infinite plate approximation. Despite this, very satisfactory results are obtained by the prediction model. This allows to validate the cyclic diffusivity  $D_{eq}$  estimation method developed in section 4.4.

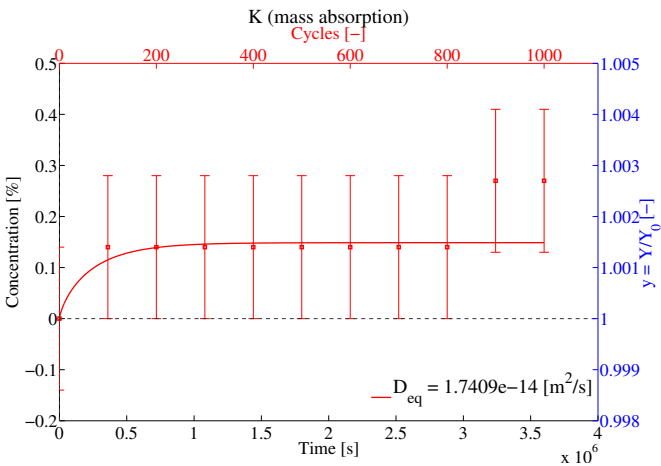
### 8.5.2 Statistical comparison between EMA and OMA

The results of the ageing monitoring are shown in figure 8.13. Each marker represents the mean estimated value for  $\epsilon_3$  and  $\gamma_{13}$ , separately by EMA and OMA. The error bars represented the corresponding standard deviations (over 15 independent estimations).

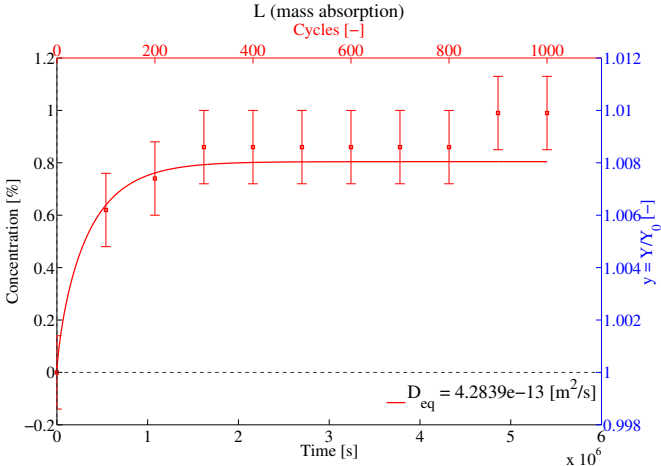
In a similar way that it was approached in chapter 5, it is necessary to compare systematically all data provided by accelerometers and sensors. However, the presence of two additional factors (sensors and modal analysis type) increases the complexity of an eventual ANOVA.

The analysis proposed here is more simple from the computational point of view and is justified by its objective: globally only a comparison between two methods: a reference method EMA carried out with non-aged sensors, and a subject method OMA carried out with integrated aged sensors PVDF, without any attempt to analyse the factors of the difference.

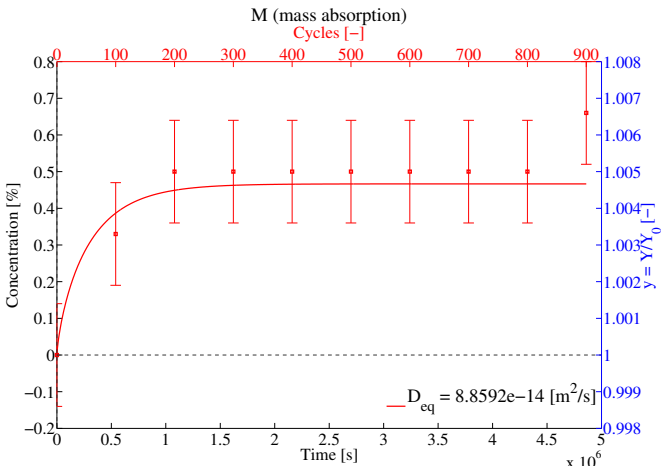
This simplified approach allows using a simple hypothesis test adapted to this case. The objective is then to compare, at each data acquisition round, that EMA and OMA data are statistically equivalent in terms of the identified  $y_i$ . In order to do so, a Welch's t-test is carried out. The test of hypothesis is formulated as follows:



(a)



(b)



(c)

Figure 8.12 – Water mass absorption prediction, and measured using separately EMA and OMA, for demonstrators (a) K, (b) L and (c) M.

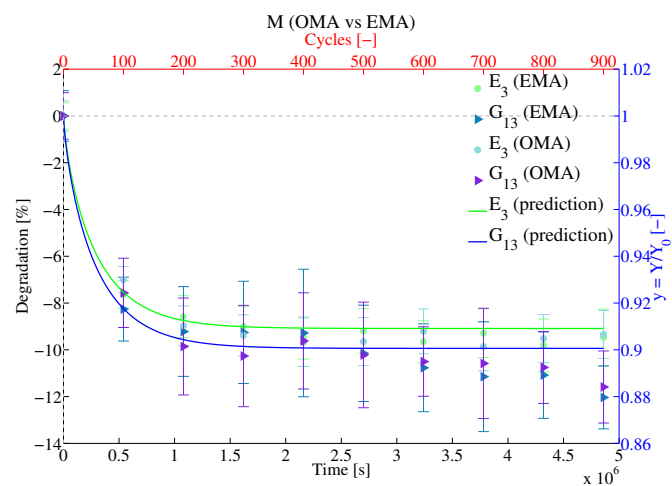
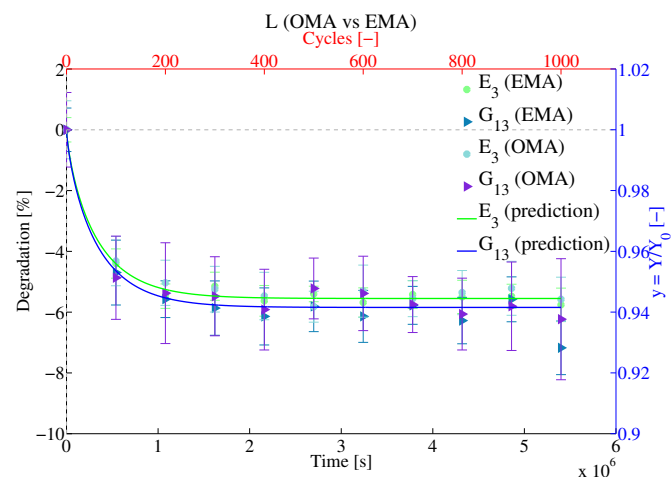
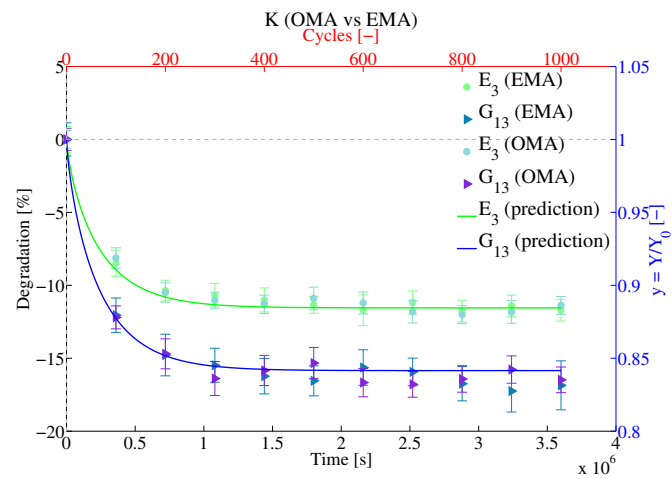


Figure 8.13 – Ageing of (a) K, (b) L and (c) M as predicted by the ageing model, and measured using separately EMA and OMA.

$$\begin{aligned} H_0 & : y_{i,EMA} = y_{i,OMA} \quad (\text{ie OMA and EMA yield equivalent results.}) \\ H_1 & : y_{i,EMA} \neq y_{i,OMA} \quad (\text{ie OMA and EMA do not yield equivalent results.}) \end{aligned} \quad (8.5)$$

where  $y_{i,EMA}$  and  $y_{i,OMA}$  denote indifferently  $y_2 = \epsilon_3$  or  $y_3 = \gamma_{13}$  as evaluated after EMA and OMA respectively, at the  $i^{th}$  measurement round. The test estimator  $t_i$  is given by:

$$t_i = \frac{|y_{i,\bar{EMA}} - y_{i,\bar{OMA}}|}{\sqrt{\frac{\sigma_{i,EMA}^2}{n_{i,EMA}} + \frac{\sigma_{i,OMA}^2}{n_{i,OMA}}}} \quad (8.6)$$

where the  $y_{i,-}$ ,  $\sigma_{i,-}$  and  $n_{i,-}$  are the mean values, the standard deviations and number of measurements for EMA and OMA. This stochastic variable follows a two-tailed t-Student distribution. To approximate the number of DoF for this distribution, the Welch-Satterthwaite equation is used:

$$\nu_i \approx \frac{\left( \frac{\sigma_{i,EMA}^2}{n_{i,EMA}} + \frac{\sigma_{i,OMA}^2}{n_{i,OMA}} \right)^2}{\frac{\sigma_{i,EMA}^4}{n_{i,EMA}^2(n_{i,EMA}-1)} + \frac{\sigma_{i,OMA}^4}{n_{i,OMA}^2(n_{i,OMA}-1)}} \quad (8.7)$$

This value is rounded up to the closest integer. For this given  $\nu$ , the critical value is estimated by the inverse t-Student distribution function  $t_{crit} = T^{-1}(\nu|\alpha)$ , where  $\alpha$ -value is the probability of refusing the equivalence between EMA and OMA data if this is true. Thus, for  $\alpha = 1\%$ , if  $t < t_{crit}$ ,  $H_0$  is accepted. The results are summarized in tables 8.3 to 8.8.

It can be seen that the null hypothesis is generally accepted, except for a few tests. In those cases, the statistic  $t$  does not exhibit an extremely distorted value. The differences between OMA and EMA can be attributed to minor factors like differences in the experimental setup (*eg* different testing supports on some occasions).

As a conclusion, EMA and OMA can be judged equivalent from the statistic point of view, which confirms the statement of the visual inspections of the plot graphs: the EMA and OMA are not significantly different. Both series of results are considered in

the following section as part of the global experimental results.

Table 8.3 – Welch’s t-test for  $E_3$  of demonstrator K.

Cycles $N_{cyc}$	Nb. of meas.		Mean $\epsilon_3$		Std. Dev.		Tests			Dec.
	$n_{EMA}$	$n_{OMA}$	$y_{EMA}$	$y_{OMA}$	$\sigma_{EMA}$	$\sigma_{OMA}$	$t$	$\nu$	$t_{crit}$	
0	15	15	0.00	0.00	0.89	0.61	0.00	25	2.79	$H_0$
100	15	15	-8.48	-8.13	0.90	0.71	1.18	27	2.77	$H_0$
200	15	15	-10.36	-10.49	0.71	0.67	0.52	28	2.76	$H_0$
300	15	15	-10.69	-11.04	0.81	0.57	1.38	25	2.79	$H_0$
400	15	15	-11.00	-11.30	0.82	0.63	1.12	26	2.78	$H_0$
500	15	15	-11.34	-10.90	0.57	0.77	1.75	26	2.78	$H_0$
600	15	15	-11.71	-11.21	1.06	0.75	1.51	25	2.79	$H_0$
700	15	15	-11.18	-11.81	0.79	0.77	2.21	28	2.76	$H_0$
800	15	15	-11.77	-12.01	0.74	0.62	0.97	27	2.77	$H_0$
900	15	15	-11.40	-11.83	0.72	0.77	1.56	28	2.76	$H_0$
1000	15	15	-11.72	-11.38	0.73	0.61	1.36	27	2.77	$H_0$

Table 8.4 – Welch’s t-test for  $G_{13}$  of demonstrator K.

Cycles $N_{cyc}$	Nb. of meas.		Mean $\gamma_{13}$		Std. Dev.		Tests			Dec.
	$n_{EMA}$	$n_{OMA}$	$y_{EMA}$	$y_{OMA}$	$\sigma_{EMA}$	$\sigma_{OMA}$	$t$	$\nu$	$t_{crit}$	
0	15	15	0.00	0.00	1.14	0.76	0.00	24	2.80	$H_0$
100	15	15	-12.05	-12.20	1.18	0.79	0.41	24	2.80	$H_0$
200	15	15	-14.78	-14.70	1.43	1.03	0.18	25	2.79	$H_0$
300	15	15	-15.48	-16.39	1.17	1.17	2.13	28	2.76	$H_0$
400	15	15	-16.23	-15.84	1.21	1.03	0.95	27	2.77	$H_0$
500	15	15	-16.55	-15.33	1.03	1.07	3.17	28	2.76	$H_1$
600	15	15	-15.64	-16.67	1.22	0.97	2.57	27	2.77	$H_0$
700	15	15	-15.94	-16.79	0.95	0.88	2.55	28	2.76	$H_0$
800	15	15	-16.74	-16.42	1.18	0.91	0.84	26	2.78	$H_0$
900	15	15	-17.25	-15.78	1.43	0.93	3.33	24	2.80	$H_1$
1000	15	15	-16.86	-16.48	1.68	0.88	0.77	21	2.83	$H_0$

Table 8.5 – Welch’s t-test for  $E_3$  of demonstrator L.

Cycles $N_{cyc}$	Nb. of meas.		Mean $\epsilon_3$		Std. Dev.		Tests			Dec.
	$n_{EMA}$	$n_{OMA}$	$y_{EMA}$	$y_{OMA}$	$\sigma_{EMA}$	$\sigma_{OMA}$	$t$	$\nu$	$t_{crit}$	
0	15	15	0.00	0.00	0.40	0.95	0.00	19	2.86	$H_0$
100	15	15	-4.40	-4.32	0.48	0.81	0.34	23	2.81	$H_0$
200	15	15	-5.47	-5.04	0.40	0.74	2.02	22	2.82	$H_0$
300	15	15	-5.15	-5.24	0.46	0.75	0.43	23	2.81	$H_0$
400	15	15	-5.63	-5.47	0.51	0.78	0.66	24	2.80	$H_0$
500	15	15	-5.40	-5.82	0.26	0.51	2.84	21	2.83	$H_1$
600	15	15	-5.68	-5.31	0.48	0.86	1.47	22	2.82	$H_0$
700	15	15	-5.42	-5.56	0.46	0.59	0.70	26	2.78	$H_0$
800	15	15	-5.50	-5.36	0.55	0.73	0.60	26	2.78	$H_0$
900	15	15	-5.48	-5.22	0.40	0.89	1.04	19	2.86	$H_0$
1000	15	15	-5.76	-5.58	0.55	0.73	0.78	26	2.78	$H_0$

## Chapter 8. Application of the SHM method: Section of a plane wing

Table 8.6 – Welch's t-test for  $G_{13}$  of demonstrator L.

Cycles $N_{cyc}$	Nb. of meas.		Mean $\gamma_{13}$		Std. Dev.		Tests			Dec.
	$n_{EMA}$	$n_{OMA}$	$y_{EMA}$	$y_{OMA}$	$\sigma_{EMA}$	$\sigma_{OMA}$	$t$	$\nu$	$t_{crit}$	
0	15	15	0.00	0.00	0.72	1.23	0.00	23	2.81	$H_0$
100	15	15	-4.70	-4.87	1.07	1.37	0.38	26	2.78	$H_0$
200	15	15	-5.57	-5.38	0.60	1.66	0.43	18	2.88	$H_0$
300	15	15	-5.87	-5.48	0.89	1.30	0.96	25	2.79	$H_0$
400	15	15	-6.14	-5.92	0.94	1.33	0.54	25	2.79	$H_0$
500	15	15	-5.81	-5.22	0.83	1.00	1.75	27	2.77	$H_0$
600	15	15	-6.14	-5.38	0.86	1.22	1.96	25	2.79	$H_0$
700	15	15	-5.78	-5.75	0.62	0.92	0.09	25	2.79	$H_0$
800	15	15	-6.28	-6.06	0.76	1.18	0.59	24	2.80	$H_0$
900	15	15	-5.58	-5.81	0.74	1.46	0.54	21	2.83	$H_0$
1000	15	15	-7.17	-6.23	0.88	1.99	1.67	19	2.86	$H_0$

Table 8.7 – Welch's t-test for  $E_3$  of demonstrator M.

Cycles $N_{cyc}$	Nb. of meas.		Mean $\epsilon_3$		Std. Dev.		Tests			Dec.
	$n_{EMA}$	$n_{OMA}$	$y_{EMA}$	$y_{OMA}$	$\sigma_{EMA}$	$\sigma_{OMA}$	$t$	$\nu$	$t_{crit}$	
0	15	15	0.00	0.00	0.56	0.65	0.00	28	2.76	$H_0$
100	15	15	-7.63	-7.00	0.59	0.56	2.96	28	2.76	$H_1$
200	15	15	-8.58	-8.97	0.90	0.85	1.23	28	2.76	$H_0$
300	15	15	-9.00	-9.38	0.85	0.87	1.19	28	2.76	$H_0$
400	15	15	-9.50	-9.67	0.90	1.04	0.50	27	2.77	$H_0$
500	15	15	-9.20	-9.65	0.95	1.03	1.24	28	2.76	$H_0$
600	15	15	-9.65	-9.21	0.89	0.96	1.31	28	2.76	$H_0$
700	15	15	-9.29	-9.86	1.05	1.04	1.50	28	2.76	$H_0$
800	15	15	-9.81	-9.52	1.13	1.02	0.75	28	2.76	$H_0$
900	15	15	-9.47	-9.34	1.21	1.02	0.30	27	2.77	$H_0$

Table 8.8 – Welch's t-test for  $G_{13}$  of demonstrator M.

Cycles $N_{cyc}$	Nb. of meas.		Mean $\gamma_{13}$		Std. Dev.		Tests			Dec.
	$n_{EMA}$	$n_{OMA}$	$y_{EMA}$	$y_{OMA}$	$\sigma_{EMA}$	$\sigma_{OMA}$	$t$	$\nu$	$t_{crit}$	
0	15	15	0.00	0.00	1.09	1.00	0.00	28	2.76	$H_0$
100	15	15	-8.26	-7.56	1.37	1.48	1.34	28	2.76	$H_0$
200	15	15	-9.22	-9.86	1.92	2.07	0.88	28	2.76	$H_0$
300	15	15	-9.26	-10.27	2.19	2.17	1.27	28	2.76	$H_0$
400	15	15	-9.28	-9.62	2.73	2.06	0.38	26	2.78	$H_0$
500	15	15	-10.15	-10.22	2.06	2.26	0.09	28	2.76	$H_0$
600	15	15	-10.77	-10.50	1.88	1.48	0.43	27	2.77	$H_0$
700	15	15	-11.15	-10.58	2.35	2.36	0.66	28	2.76	$H_0$
800	15	15	-11.08	-10.75	1.85	1.54	0.53	27	2.77	$H_0$
900	15	15	-12.04	-11.59	1.34	1.54	0.85	27	2.77	$H_0$

### 8.5.3 Ageing prediction based on the multifactorial model

The multifactor ageing model proposed at the end of chapter 4 has been used to predict the evolution of the elastic moduli as a mean to characterize ageing due to weathering agents. As a reminder, this model is based on the correlation between degradation and moisture absorption in the CFRP sample. The water concentration becomes a "state" variable, and thus the ageing is characterised by a moisture absorption model (equation 4.14) combined to a linear multifactor model with interactions (equation 4.23).

The global experimental results can be seen in figure 8.14 for  $\epsilon_3$  and  $\gamma_{13}$ . This time, the experimental uncertainty is given by the standard deviation (error bars). At first glance, the same statement as for the water mass absorption prediction can be repeated here: the prediction is in all cases inside the uncertainty interval defined by the error bars.

However, in this case, the uncertainty comes from a dispersion of the measurement. The standard deviation allows running a hypothesis test to validate more objectively the fitting of data into the ageing model, a statistical problem for which a goodness-of-fit test would be the most appropriate. Although this hypothesis test is based on a linear model assumption, it is for example mentioned by [O'Brien et al., 2009], that it is possible to adapt this test to the simple exponential model case.

The test of hypothesis can be expressed as follows:

$$H_0 : \text{The new data fit into model.} \quad (8.8)$$

$$H_1 : \text{The new data do not fit into model.}$$

The goodness-of-fit test statistic to evaluate this type of hypothesis is the Fisher F-test, similar as the one carried out in section 4.3.2. The Fisher statistic is given by the following equation:

$$F = \frac{SS_{pe}/\nu_1}{SS_{lof}/\nu_2} \quad (8.9)$$

where  $\nu_1 = Q - p = 9$  and  $\nu_2 = N - Q = 319$  (except for demonstrator M, for which  $\nu_1 = Q - p = 8$  and  $\nu_2 = N - Q = 290$ ) are the DoF of the lack-of-fit and the pure error

## Chapter 8. Application of the SHM method: Section of a plane wing

sum of squares respectively.  $Q = 11$  is the number of monitoring rounds,  $N = 330$  is the total number of measurements. The number of parameters of the model  $p = 2$  (one asymptotic value  $A$  and one time constant  $b$ ). The sum of squares are given by:

$$\sum_i \sum_j (y_{ij} - \hat{y}_i)^2 = \sum_i \sum_j (y_{ij} - \bar{y}_i)^2 + \sum_i \xi_i (\bar{y}_i - \hat{y}_i)^2 \quad (8.10)$$

$$S_{tot} = SS_{pe} + SS_{lof}$$

The statistic  $F$  is assumed to follow an F-distribution. Assuming a confidence level of 98% (*ie* there is a 2% probability to make a type I error, which means to refuse the null hypothesis even if the dataset fits into the model),  $F_{crit} = F_{0.02}(9, 319) = 2.23$ .

The results of the test are summarized in tables 8.9 to 8.11. The null hypothesis is accepted in most cases. However, in the cases where the null hypothesis is rejected, the  $F$ -value does not exhibit a totally divergent value. This goodness-of-fit could be hinted by visual inspection of figures 8.14(a),(b) and (c), since the drift between mean measured values and predicted values at each round is significantly lower than the standard deviation. Although the data measurements do not fit exactly in the ageing model, it can be stated that at least there is agreement in the trend and there is no excessive difference.

Table 8.9 – F-test for demonstrator K.

Variable	$SS_{lof}$	$SS_{pe}$	$F$	$F_{crit}$	Dec.
$\epsilon_3$	27.85	289.75	2.52	2.23	$H_1$
$\gamma_{13}$	54.84	636.37	2.21	2.23	$H_0$

Table 8.10 – F-test for demonstrator L.

Variable	$SS_{lof}$	$SS_{pe}$	$F$	$F_{crit}$	Dec.
$\epsilon_3$	3.85	195.99	0.51	2.23	$H_0$
$\gamma_{13}$	25.38	620.42	1.07	2.23	$H_0$

Table 8.11 – F-test for demonstrator M.

Variable	$SS_{lof}$	$SS_{pe}$	$F$	$F_{crit}$	Dec.
$\epsilon_3$	30.00	406.09	1.96	2.23	$H_0$
$\gamma_{13}$	149.30	1704.83	2.23	2.23	$H_0$

### 8.5.4 Sensing and actuation with PVDF transducers

This subsection focuses essentially on demonstrator M, which is the only equipped with two sets of PVDF transducers in order to perform sensing and actuation simulta-



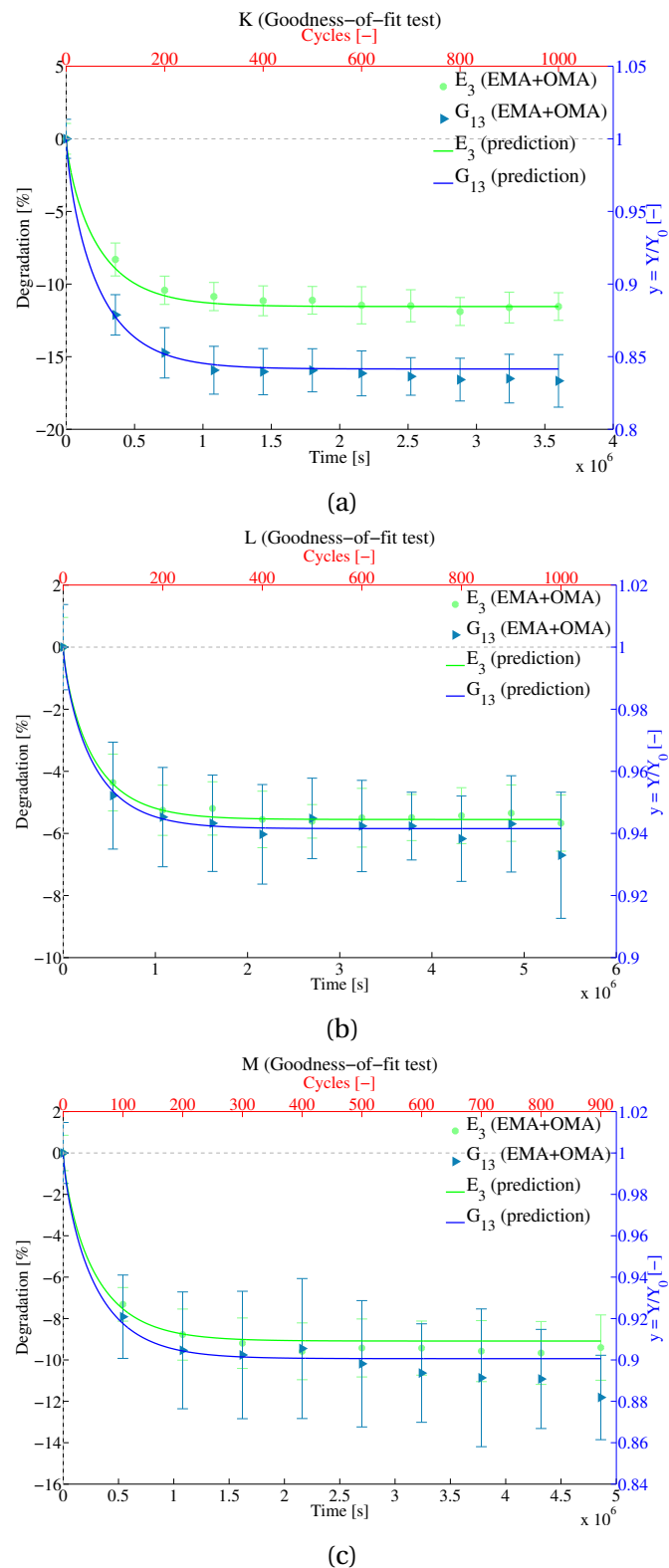


Figure 8.14 – Plot of ageing prediction curves corresponding to (a) K, (b) L and (c) M, and overall measured data (includes EMA and OMA).

neously.

It is important to check the performances of PVDF transducer networks as valid actuators. The discussion in section 6.2.1 concluded that the optimal actuator network has an optimal placement identical to that established from the sensing point of view. This statement was experimentally validated in chapter 7, for the case of a rectangular plate. Among the drawn conclusions in the same chapter, it was stated that the "natural" excitation sources (as the fan) started to show a decreasing ability to excite high-frequency modes, even if the implementation was successful for the plates anyway. On the other hand, PVDF actuators were expected to show good excitation performances rather in the high-frequency part of the spectrum, since their blocking force is very limited due to their high compliance.

In the case of rectangular plates, it was determined that both excitation sources (PVDF patches and fan) provided enough energy to the plate for the natural frequencies to be sensed. However, given the size and weight of the demonstrator, it is possible that each of these two excitation forces exhibits lower performances due to higher modal masses. In order to answer to this question, it was proposed to evaluate the performances of each actuator separately and combined. Indeed, a synergistic cooperation between the two actuators (PVDF patches and fan) can eventually improve the modal extraction accuracy.

In order to do so, an experimental campaign was designed as follows:

1. Three rounds of signal acquisition by the PVDF sensor network take place.
2. At each round, non-aged demonstrator M is excited during 5 minutes.
3. For the first round, the demonstrator is excited only by airstream of the fan. In the second, only the PVDF actuator network is the source of excitation. Each patch receives an uncorrelated white noise signal. The third round is a combination of both.
4. The experimental conditions are identical to those mentioned in chapter 7, except that the acquisition frequency band is reduced to 1 [kHz], which still englobes the frequencies of interest.

Like for the rectangular samples in chapter 7, the average bias between OMA and EMA results is statistically tested. It is assumed that the decision statistic  $t$  is defined by equation (7.10), and follows a t-Student distribution, with  $\nu = 6$  DoF. The adopted level of significance is  $\alpha = 5\%$ .

## 8.6. Conclusions about SHM method applied to the wing section

### Results

The results are summarized in table 8.12. The SVD plots and extracted frequencies are shown in figures 8.15 to 8.17. As it can be seen, the corresponding extracted frequencies are relatively close. Visually, some observations can be stated:

- Natural frequencies are satisfyingly extracted from the SVD represented graphically in the figures, in all cases. The hypothesis tests accept in all cases the null hypothesis, *ie* the extracted frequencies by OMA and EMA are statistically equal.
- As expected, the higher natural frequencies are less excited by the fan, while the low frequencies by the PVDF actuators. For the latter, the lowest natural frequency ( $\approx 33$  [Hz]) shows a weak amplification.
- In spite of the acceptance of the null hypothesis in all cases, the accuracy of the three excitation methods can be evaluated by comparing the mean relative difference with the reference, and the standard deviation. OMA3 exhibits a lower mean difference with EMA and a lower standard deviation (more accuracy).

From these statements, it can be concluded that a combined OMA including PVDF integrated actuators and external excitation forces represent an improvement with respect to an individual excitation from the point of view of the accuracy.

Table 8.12 – Statistical  $t$ -tests comparing EMA with OMA. The null hypothesis is accepted in all cases.

	Test	$\bar{\epsilon}$ [%]	$\sigma_{\epsilon}$ [%]	$t = \frac{\bar{\epsilon}}{\sigma_{\epsilon}/\sqrt{n}}$	$t_{crit}(\alpha, \nu)$	Decision
M	OMA1	2.139	2.752	2.057	2.447	$H_0$
M	OMA2	-1.728	5.101	0.896	2.447	$H_0$
M	OMA3	0.764	1.167	1.731	2.447	$H_0$

## 8.6 Conclusions about SHM method applied to the wing section

In most aspects, the application of the SHM method on the demonstrators has shown very satisfying results. The transition between the rectangular plates and the NACA-profiled demonstrator has brought under the spotlight some elements to be taken into account in future developments. Can be emphasized:

1. The need to use a numerical model of the structure as accurate as possible. For example, the inclusion of glue as a thin film layer contributed to improve enough the accuracy of the elastic properties identification.
2. Increasing geometric complexity has shown also that the natural frequencies may not be sufficient to constitute a satisfying objective function for the identi-

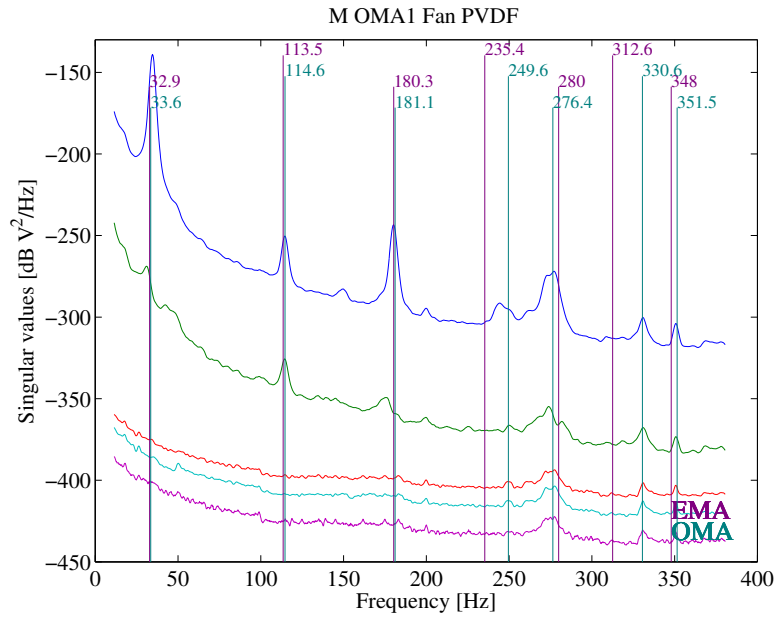


Figure 8.15 – SVD for demonstrator M, where the excitation is given by the fan.

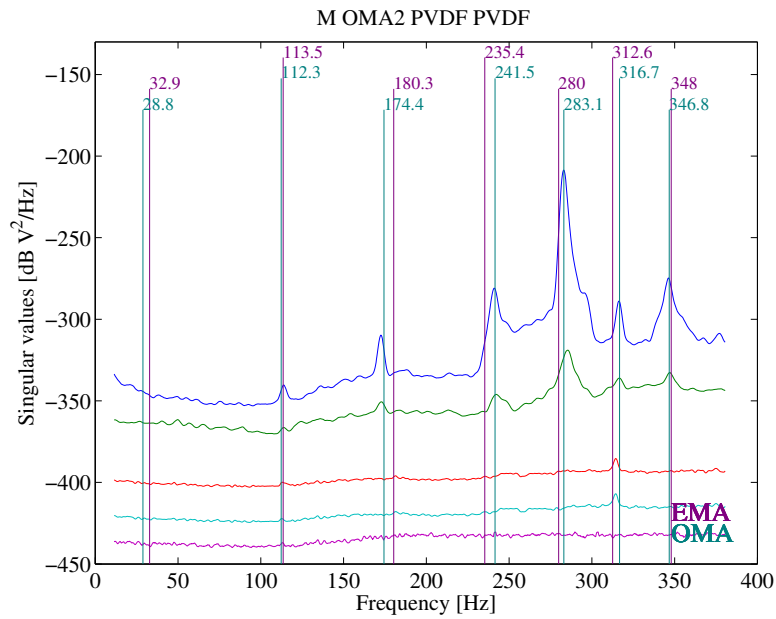


Figure 8.16 – SVD for demonstrator M, where the excitation is given by the PVDF actuator network.

fication algorithm. The closer the modes, the more difficult it becomes to spectrally discern one mode from another during the identification process. It is recommended in the case of (even slightly) complex geometries to include an additional comparison term, such as in equation 8.1, between mode shapes. MAC has shown to be an appropriate criterion.

## 8.6. Conclusions about SHM method applied to the wing section

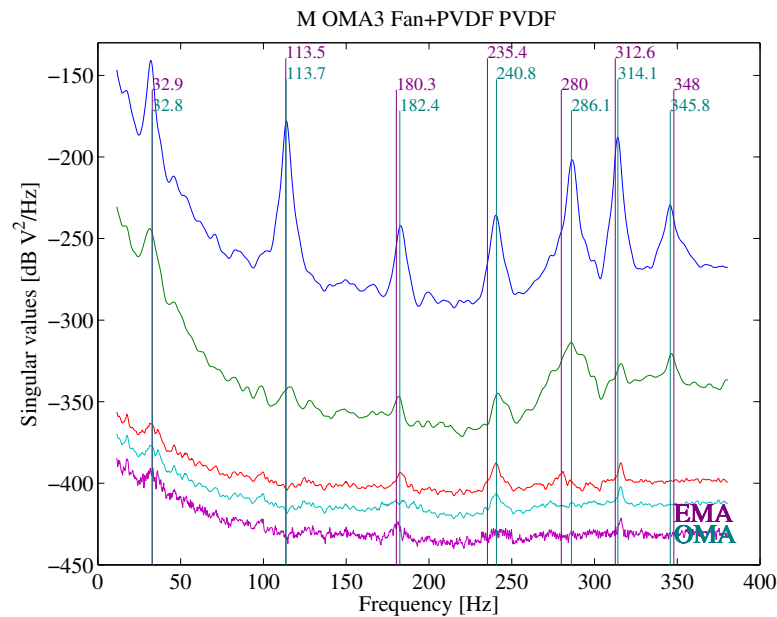


Figure 8.17 – SVD for demonstrator M, where the excitation is given by the fan/PVDF actuators combination.

3. The excitation provided by the PVDF transducers shows some difficulty to excite correctly the low frequencies. Indeed, the SVD plot in figure 8.16 shows less discernible resonance peaks. Although the statistical validation has shown an equivalence between EMA and PVDF actuators-only OMA, it is important to highlight that the extraction of lower frequencies may be inaccurate. This could turn out to be problematic since it is expected that full-scale structures show lower natural frequencies (often less than 20 [Hz] for the most representative in aircraft [Smith and Shust, 2004]). In spite of this, PVDF transducers can work as outstanding actuators at higher frequencies. It is then recommended to use a PVDF actuator network rather as complementary source of excitation. Eventually, other alternatives can be considered, like the use of several piled PVDF patches or thicker one layer PVDF patches in order to increase the block force. Depending on the application, other actuators (for example PZT patches) could carry out this task.

Globally, the SHM method has been successfully applied to the demonstrators K, L and M, and leads the way to an *in situ* validation in the future.



# 9 Conclusions

## 9.1 Synthesis

Several aspects of weathering, composite ageing and structural monitoring of composite were addressed in this thesis. The state-of-the art concerning the monitoring methods for aeronautical structures shows that there is room for potential improvement from the economic and safety points of view.

The method developed in this thesis is composed by several tools which are combined synergistically to constitute a monitoring system in its own right. These tools were designed taking into account the damage-tolerant design approach in the aeronautical industry, were proposed as original solutions to the particular problem of survey of CFRP structures using PVDF film networks, and were validated individually and then as part of the global method.

A standard method for artificial weathering has been developed. The artificial ageing protocols were inspired from results published in the literature, in particular about the ageing on real operational airframe, and artificially aged specimens as well. Concerning this matter, this thesis has focused on the influence of three factors on the ageing of CFRP specimens: exposure temperature, relative humidity and UV radiation. Most importantly, the problem this thesis has originally dealt with, is the influence of these factors simultaneously, which is an innovation with respect to most of what has been done until now.

The goal of artificial ageing is to subject the specimens to controlled ageing protocols, in order to observe changes in some of their macroscopic properties. A systematic study of the ageing process from the macroscopic point of view has been thus carried out on the rectangular specimens. Its main goal has been the establishment of a parametric mathematical model to express the evolution of elastic moduli (in particular those dominated by the epoxy resin) as a mean to monitor the ageing state and the

## Chapter 9. Conclusions

---

structural health. The mathematical model is established by means of the DoE statistical methods (specially ANOVA). This formulation includes the actions of the different ageing factors and more importantly, their interaction. From this point of view, an important and novel contribution is the use of the correlation between water concentration and degradation. A consequence of this has been the substitution of time by a state variable (water concentration) to characterise the ageing state of a structure. The purpose of this operation was to generalise the Prony series ageing model (dependent on the geometry), to a multifactor ageing model (which can be applied independently from the geometry).

The PVDF technology is a relatively new technology for strain measuring, and represents an interesting alternative to other dynamic sensors currently in use. Proving the survivability to the ageing conditions was essential to justify their integration in a composite structure, given that the solution of an integrated transducer network was most suitable to fulfil the robustness and rapidity requirements of SHM. Although the sensitivity and the piezoelectric constants were not specifically monitored, it was important to make sure that they could provide valid electric signals nevertheless. The validation has been carried out by comparing the ability of PVDF sensors to provide quality signals, which can prove to be as accurate as those from non-aged sensors and can open the possibility of a massive use of low-cost integrated PVDF sensor networks for structural monitoring applications. The statistical approach is used for this comparison, giving satisfying results about the survivability of the sensors within the frame of the designed ageing protocols.

In order to measure the elastic properties while following a line of thought compatible with SHM, it was suggested and inspired from literature, that the vibrational behaviour of the structures could provide information about its internal properties. Indeed, the physical fundamentals at the core of vibrational behaviour are given by the wave propagation theory, which proves that structural stiffness can be indirectly measured by the measurement of the vibrational features, with the mass distribution as an intermediary. However, the orthotropic nature of CFRP makes more complex this problem, and an identification algorithm intervenes to solve it. The method employed here was adapted from a numerical-experimental identification algorithm previously developed by several authors, which minimizes the difference between experimental and FE simulation results in order to identify the best estimation of the elastic properties. The objective function involves the natural frequencies and the corresponding vibration mode shapes, which constitute the "features" mentioned in the SHM axioms as information vehicles about the internal health of the structure. Moreover, the complexity of the vibration mode shapes is consequent with geometrical complexity of the specimen, and a sensitivity analysis was included in the identification process in order to determine quantitatively how the elastic properties are related to the natural modal parameters (natural frequencies and vibration modes).



Concerning the acquisition of structural data and extraction of these features, in this case the modal parameters, an output-only modal analysis (OMA) was privileged, since it carries inherently the attributes of robustness and rapidity. Moreover, the integration of low-cost sensors implies the possibility to carry out real-time (or real-near time) monitoring, which is an important step improving the monitoring capabilities on full-scale structures, especially for operational and safety reasons. In recent years, the use of output-only analyses has been justified by the difficulty (or even impossibility) to perform classic static or dynamic tests (like EMA) to extract information about the state of the structures. Among the proposed solutions, the frequency domain decomposition (FDD) technique was chosen because of the simplicity of its formulation and the remarkable results reported in the literature. This method uses the notion of singular value decomposition (SVD) to extract the necessary information exclusively from the output sensors. As an original contribution, this method was successfully applied to the rectangular specimens as well as to NACA-profiled demonstrators, and this using several sensor/actuator combinations. Again, besides the visual inspection of the results (exposed as plot graphs of the SVD), the success of the implementation has been evaluated by statistical means.

Another aspect of the transducer network implementation is obviously the problem of the spatial distribution of the sensors, as well as other design parameters like the number of sensors and the design criteria. The optimal placement problem has been extensively treated in the current state-of-the-art, including formulations based on the use of strain sensors. Among the different approaches, a simple energy-based method was chosen: the effective independence (EI) method, which was adapted to the specific case of strain patches, which has been a relatively few investigated problem. The success of the implementation has been proved and validated through the experimental tests carried out on the rectangular plates and the demonstrators. The latter showed that the method was applicable to more complex geometries than a simple flat plate.

Finally, the surveillance technique of a global SHM method has been proposed, which regroups all the elements mentioned above: the design of ageing protocols, the establishment of a multifactorial model, the verification of transducers survivability, the optimal placement of a transducer network design and optimization and feature extraction by OMA. By its constitution, the solutions it proposes and its systematic approach, this method can be presented as original.

## 9.2 Concluding statements

Let us recall the main objective of the current thesis as stated in the introduction.

To develop a novel SHM system to be applied on full-scale composite struc-

tures, primarily destined to aerospace applications, in order to monitor in real-time (or nearly real-time) the health of the structure and detect ageing-induced damage, using a transducer network and a robust, non-destructive, fast and reliable feature extraction testing technique.

From the comments and conclusions in the previous chapter, the method developed here has been successfully implemented and validated for a reduced-scale demonstrator in a laboratory controlled environment. Furthermore, the observations made throughout the different chapters point out that it should be possible to extend this method to further more complex cases, notably to be tested around *in situ* situations. It is however expected to meet problems that will require questioning previous choices in order to overcome them and ensure for the method to keep the attributes of robustness, reliability, fastness and ease of use.

### 9.3 Recommendations

The topics addressed in this thesis have been successfully implemented and showed satisfying results when applied to more or less complex geometry structures in a controlled lab environment. However, some recommendations can be addressed to future users, if further development is considered.

First of all, it has been observed that the numerical model should be as accurate as possible to represent the real structure. As it has been seen in the case of demonstrators, some details that could be considered as negligible at first sight, proved to have a real impact in the identification process.

Weighing should not be neglected in any case since the mass is necessary to link the elastic properties to the natural frequencies in the identification algorithm. It has been shown all along that a non negligible amount of water mass can easily be absorbed by CFRP structures. If for practical reasons the weighing of the full scale structure is impossible, it is suggested that one (or several) "master part" would be installed close to the full scale structure. This master part would be use as a "witness" since it would suffer for the same moisture absorption, and would consequently help to the estimation of mass absorption.

The identification algorithm should include the natural frequencies and the vibration mode shapes in the formulations, in order to identify the elastic properties as accurately as possible. Indeed, with increasing size and geometrical complexity, vibration modes can come spectrally close to each other (increasing modal density). In such cases, complementary modal criteria like MAC can be useful to improve modal discerning within the identification algorithm run.

In the same optic, close modes can be separated if a sufficient number of sensors optimally placed are integrated. The user has the possibility to visualize, through the optimal sensor placement tool, if the solution found by the algorithm leads to a satisfying separation between modes.

Another tool to detect narrowly close modes is given by OMA itself. As mentioned in chapter 7, when two (or more) modes are spectrally close, the second (third, fourth,...) order singular values can give additional information.

Concerning the prediction use of the mathematical model, its application frame is for now limited to CFRP specimens manufactured from the same raw materials and following the same curing cycles. Even if it could be adopted as a first approach to estimate degradation of similar materials, it is recommended to run some experimental campaigns in order to validate its use, eventually update the model or simply start a new ageing characterization procedure, as suggested in chapter 4.

It has also been pointed out that the actuation ability of PVDF patch networks showed some limitations due to its weak block force, which is a consequence of its high mechanical compliance. Indeed, as showed in chapter 8, the excitation by PVDF patches showed a lack of efficiency to excite the lowest natural frequencies. In order to overcome these limitations, it has been suggested to employ thicker PVDF films, or piled PVDF patch sensors, or even consider the possibility to use other actuators (such as PZT patches). In any case, the role of PVDF patches as actuators is rather supportive and would help to complete the natural excitation sources in the high frequencies. This synergy proved to add a non-negligible improvement in the feature extraction accuracy.



# A

## Influence of sensors in the dynamic behaviour

The method presented in this thesis has the quality of being non-destructive, which is highly appreciated. Since the monitoring is based on the extraction of natural frequencies, it is legitimate to question if the integration of sensors is intrusive or not. In this appendix, a summary of the results obtained to validly assume the non-intrusion hypothesis is explained.

### A.1 Experimental tests

From the experimental point of view, adding sensors would essentially shift the value of the natural frequencies. In order to measure this change, one of the rectangular samples of the G-series before ageing was used to study the influence of sensors. It is expected to observe a very small decrease of the natural frequencies due to mass increase.

The experimental procedure can be summarized as follows:

1. It starts with the sample with only one integrated PVDF sensor on the surface (low left corner). This is used to perform an EMA with impact hammer, and these results are used as reference.
2. An accelerometer is attached on the surface using mounting wax, and the measurements are still carried out using the PVDF patch (low right corner).
3. The accelerometer is removed and a second PVDF patch is mounted using glue, in the same location. The first PVDF patch still serves as the output.

Results are summarized in table A.1. It can be stated that the influence of the accelerometer is really negligible: under 0.2% for each frequency, which implies an estimation error of less than 0.4% of the mechanical properties after identification. On the other hand, the estimation error would be higher in the case of the integrated

## Appendix A. Influence of sensors in the dynamic behaviour

PVDF sensors (above 1.2% for frequencies).

Table A.1 – Experimental comparison between measurements with differently equipped samples.

Mode	1 PVDF	1 PVDF + 1 Accel		2 PVDF	
	Freq. [Hz]	Freq. [Hz]	Rel. Shift [%]	Freq. [Hz]	Rel. Shift [%]
1	224.67	224.62	-0.02	222.44	-0.99
2	362.92	362.49	-0.12	360.35	-0.71
3	564.35	564.55	0.04	557.64	-1.19
4	952.49	952.4	-0.01	948.28	-0.44
5	1053.6	1052.5	-0.10	1045.6	-0.76
6	1109.4	1108.6	-0.07	1099.3	-0.91
7	1142.9	1142.6	-0.02	1132.9	-0.87

## A.2 Numerical tests

From the simulation point of view, it is important to evaluate the error level if a PVDF sensor is included in the FE model, which is one of the heart of the identification algorithm. The question in this case is approached as follows: it is verified if the geometry of the integrated sensor needs to be included in the model. In order to do so, two FE models of the same sample plate mentioned in the previous section are compared.

Table A.2 – Numerical comparison between samples when the glue is modelled and when it is not using an FE model of the sample.

Mode	No glue model	Glue model	
	Freq. [Hz]	Freq. [Hz]	Rel. Shift [%]
1	223.02	223.38	0.16
2	364.40	365.65	0.34
3	573.72	573.81	0.02
4	975.72	977.34	0.17
5	1068.31	1071.29	0.28
6	1124.11	1125.44	0.12
7	1182.52	1184.40	0.16

As it can be seen, the influence on the frequencies is low (less than 0.4%) when compared to the experimental measurement error of the natural frequencies (around 1%). The corresponding error propagated to the elastic moduli estimation is even negligible when compared to the degradation after ageing (around 5 %).

The inclusion of the PVDF sensors and the glue to integrate them to the structure shows to have a negligible influential. However, the low error level can be explained by the low influence that surface PVDF sensors have on the global stiffness of the structure. As it has been mentioned in chapter 8, the inclusion of glue or other "mi-

nor" geometric/manufacturing details can become relevant according to the circumstances. It is therefore recommended that the extent of the influence of these details be estimated, using simulation results and/or experimental measurements, as it has been the case in this appendix.





## **B** Useful abbreviations

ANOVA = ANalysis Of VAriance

CFRP = Carbon Fibre Reinforced Plastics

DFT = Discrete Fourier Transform

DoE = Design of Experiments

DoF = Degree of Freedom

EMA = Experimental Modal Analysis

FFT = Fast Fourier Transform

FRF = Frequency Response Function

FRP = Fibre Reinforced Plastics

IFFT = Inverse Fast Fourier Transform

IRF = Impulse Response Function

MDoF = Multiple Degree-of-Freedom

ODS = Optimal Deflection Shapes

OMA = Operational Modal Analysis

PVDF = PolyVynilidene (Di)Fluoride

SDoF = Single Degree-of-Freedom

SHM = Structural Health Monitoring

## **Appendix B. Useful abbreviations**

---

EMI = Electromagnetic Interference

# Bibliography

- F Magalhães, A Cunha, and E Caetano. Dynamic monitoring of a long span arch bridge. *Eng Struct*, 30(11):3034–3044, 2008.
- M Akay. Effects of prepreg ageing and post-cure hygrothermal conditioning on the mechanical behaviour of carbon-fibre/epoxy laminates. *Compos Sci Tech*, 38(4): 359–370, 1990.
- AL Araújo, CM Mota Soares, and MJ Moreira de Freitas. Characterization of material parameters of composite plate specimens using optimization and experimental vibrational data. *Compos Part B-Eng*, 27(2):185–191, 1996.
- ASTM D5229 Standard Test Method for Moisture Absorption Properties and Equilibrium Conditioning of Polymer Matrix Composite Materials*. ASTM International, West Conshohocken, PA, 1992(2010).
- ASTM D1151 Standard Practice for Effect of Moisture and Temperature on Adhesive Bonds*. ASTM International, West Conshohocken, PA, 2000(2006).
- ASTM C581 Standard Practice for Determining Chemical Resistance of Thermosetting Resins Used in Glass-Fiber-Reinforced Structures Intended for Liquid Service*. ASTM International, West Conshohocken, PA, 2003(2008).
- ASTM G154 Standard Practice for Operating Fluorescent Light Apparatus for UV Exposure of Nonmetallic Materials*. ASTM International, West Conshohocken, PA, 2006.
- ASTM G151 Standard Practice for Exposing Nonmetallic Materials in Accelerated Test Devices that Use Laboratory Light Sources*. ASTM International, West Conshohocken, PA, 2010.
- ASTM D4762 Standard Guide for Testing Polymer Matrix Composite Materials*. ASTM International, West Conshohocken, PA, 2011.
- S Bondzic, J Hodgkin, J Krstina, and J Mardel. Chemistry of thermal ageing in aerospace epoxy composites. *J Appl Polym Sci*, 100(3):2210–2219, 2006.

## Bibliography

---

- GEP Box, WJ Hunter, and J Hunter. *Statistics for Experimenters, Design, Innovation and Discovery*. Wiley Series in Probability and Mathematical Statistics, Wiley, NY, 2nd edition, 2005.
- GP Box and DA Pierce. Distribution of residual autocorrelations in autoregressive-integrated moving average time series models. *J Amer Stat Assoc*, 65(332):1509–1526, 1970.
- R Brincker, L Zhang, and P Andersen. Modal identification from ambient responses using frequency domain decomposition. In *Proc 18th Int Modal Anal Conf*, volume 18, pages 625–630, 2000.
- R Brincker, P Andersen, and NJ Jacobsen. Automated frequency domain decomposition for operational modal analysis. In *Proc 25th Int Modal Anal Conf*, Orlando, FL, USA, February 2007. Proc SPIE(2007).
- HF Brinson and LC Brinson. *Polymer Engineering Science and Viscoelasticity: An introduction*. Springer, New York, NY, USA, 1st edition, 2008.
- CE Carraher. *Polymer Chemistry*. CRC Press Inc., New York, NY, USA, 2010.
- Z Chen, X Tan, A Will, and C Ziel. A dynamic model for ionic polymer–metal composite sensors. *Smart Materials and Structures*, 16(4):1477–1488, 2007.
- DDL Chung. Structural health monitoring by electrical resistance measurement. *Smart Mater Struct*, 10(4):624, 2001.
- J Crank. *The Mathematics of Diffusion*. Oxford science publications, Oxford, 2nd edition, 1989.
- J Cugnoni, T Gmür, and A Schorderet. Inverse method based on modal analysis for characterizing the constitutive properties of thick composite plates. *Comput Struct*, 85(17-18):1310–20, 2007.
- B Dao, JH Hodgkin, J Krstina, J Mardel, and W Tian. Accelerated ageing versus realistic ageing in aerospace composite materials – IV. Hot/wet ageing effects in a low temperature cure epoxy composite. *J Appl Polymer Sci*, 106(6):4264–4276, 2007.
- LR Deobald and RF Gibson. Determination of elastic constants of orthotropic plates by a modal analysis/Rayleigh-Ritz technique. *J Sound Vibr*, 124(2):269–283, 1988.
- SW Doebling, CR Farrar, and MB Prime. A summary review of vibration-based damage identification methods. *Shock Vibr Digest*, 30(2):91–105, 1998.
- L Euler and C Truesdell. *The Rational Mechanics of Flexible Or Elastic Bodies 1638 - 1788: Introduction to Vol. X and XI*. Number 10 in Leonhard Euler, Opera Omnia / Opera mechanica et astronomica. 1980.

- DJ Ewins. *Modal Testing: Theory, Practice and Application*. Research Studies Press Ltd., Hertfordshire, 2nd edition, 2000.
- K-E Fällström. Determining material properties in anisotropic plates using Rayleigh's method. *Polym composite*, 12(5):306–314, 1991.
- CR Farrar and K Worden. An introduction to structural health monitoring. *Philos Trans Roy Soc A: Math, Phys Eng Sci*, 365(1851):303–315, 2007.
- CR Farrar, SW Doebling, and DA Nix. Vibration-based structural damage identification. *Philos T Roy Soc A*, 359:131–149, 2001.
- EB Flynn and MD Todd. A Bayesian approach to optimal sensor placement for Structural Health Monitoring with application to active sensing. *Mech Syst Signal Pr*, 24(4):891–903, 2010.
- GC Foss and ED Haugse. Using modal test results to develop strain to displacement transformations. In *Proc 13th Int Modal Anal Conf*, volume 2460, page 112, Orlando, FL, USA, 1995. Proc SPIE(1995).
- B Fox, A Lowe, and J Hodgkin. Investigation of failure mechanisms in aged aerospace composites. *Eng Fail Anal*, 11(2):235–241, 2004.
- D Fox, M Labes, and A Weissberger. *Physics and Chemistry of the Organic Solid State*, volume II. John Wiley & Sons Inc, Wiley, NY, 1965.
- J Frieden, J Cugnoni, J Botsis, and T Gmür. Low energy impact damage monitoring of composites using dynamic strain signals from FBG sensors – part I: Impact detection and localization. *Composite Structures*, 94(2):438–445, 2012.
- RF Gibson. Modal vibration response measurements for characterization of composite materials and structures. *Compos Sci Tech*, 60(15):2769–2780, 2000.
- V Giurgiutiu. *Structural Health Monitoring with Piezoelectric Wafer Active Sensors*. Elsevier, 1st edition, 2008.
- V Giurgiutiu, A Zagrai, and J Bao. Embedded Active Sensors for In-Situ Structural Health Monitoring of Thin-Wall Structures. *J Press Vess Technol*, 124(3):293–303, 2002.
- Weiss Umwelttechnik GmbH. Optimal temperature and humidity. Brochure, 2011. URL [http://www.gigatest.net/weiss/WT\\_WK\\_E\\_neu.pdf](http://www.gigatest.net/weiss/WT_WK_E_neu.pdf).
- T Gmür. *Dynamique des structures: analyse modale numérique*. Mécanique. Presses polytechniques et universitaires romandes, Lausanne, Switzerland, 1997.
- BL Grisso and DJ Inman. Developing an autonomous on-orbit impedance-based SHM system for thermal protection systems. In *Proc 5th Int Work Struct Health Monitor*, pages 12–14, Stanford, CA, USA, September 2005.

## Bibliography

---

- M Güney and E Eskinat. Optimal actuator and sensor placement in flexible structures using closed-loop criteria. *J Sound Vibr*, 312(1–2):210–233, 2008.
- RF Guratzsch and S Mahadevan. Structural health monitoring sensor placement optimization under uncertainty. *AIAA*, 48(7):1281–1289, 2010.
- E Guzman, J Cugnoni, and T Gmür. Accelerated isothermal and cyclic ageing of carbon fibre/epoxy composite panels with integrated PVDF sensors. In *Book of Abstracts 15th Int Conf Exp Mech (ICEM15)*, pages 335–336, Porto, Portugal, 7 2012.
- E Guzman, J Cugnoni, T Gmür, P Bonhôte, and A Schorderet. Survivability of integrated PVDF film sensors to accelerated ageing conditions in aeronautical/aerospace structures. *Smart Mater Struct*, 22(6):1–12, 2013.
- E Guzmán, J Cugnoni, and T Gmür. Multi-factorial models of a carbon fibre/epoxy composite subjected to accelerated environmental ageing. *Compos Struct*, 2014.
- E Guzman, J Cugnoni, and T Gmür. Monitoring of composite structures using a network of integrated PVDF film transducers. Submitted for publication, 2014.
- FJ Harris. On the use of windows for harmonic analysis with the discrete fourier transform. *Proc IEEE*, 66(1):51–83, 1978.
- G Heo, ML Wang, and D Satpathi. Optimal transducer placement for health monitoring of long span bridge. *Soil Dyn Earthq Eng*, 16(7-8):495–502, 1997.
- KD Hjelmstad and S Shin. Damage detection and assessment of structures from static response. *J Eng Mech*, 123(6):568–576, 1997.
- TJ Holroyd. *The Acoustic Emission & Ultrasonic Monitoring Handbook*. Coxmoor Publishing Company's machine & systems condition monitoring series. Coxmoor Publishing Company, 2000.
- S Hurlebaus and L Gaul. Smart structures dynamics. *Mech Syst Signal Pr*, 20:255–281, 2006.
- SR Ibrahim. Random decrement technique for modal identification of structures. *J Spacecraft Rockets*, 11(14):696–700, 1977.
- GH James, TG Carne, JP Lauffer, and AR Nard. Modal Testing Using Natural Excitation. In *Proc 10th Int Modal Anal Conf*, pages 1209–1216, San Diego, CA, USA, 1992. Proc SPIE(1992).
- JH Jeon, SP Kang, S Lee, and IK Oh. Novel biomimetic actuator based on SPEEK and PVDF. *Sensor Actuat B-Chem*, 143(1):357– 64, 2009.
- DC Kammer. Sensor placement for on-orbit modal identification and correlation of large space structures. In *Amer Contr Conf*, pages 2984–2990, May 1990.

- DC Kammer and ML Tinker. Optimal placement of triaxial accelerometers for modal vibration tests. *Mech Syst Signal Pr*, 18(1):29–41, 2004.
- PH Kirkegaard and R Brincker. On the optimal location of sensors for parametric identification of linear structural systems. *Mech Syst Signal Pr*, 8(6):639–647, 1994.
- G Kister, B Ralph, and GF Fernando. Damage detection in glass fibre-reinforced plastic composites using self-sensing e-glass fibres. *Smart Mater Struct*, 13(5):1166–1175, 2004.
- H Ku. Notes on the use of propagation of error formulas. *J Res Natl Inst Stan*, 70(4), 1966.
- B Kumar, R Singh, and T Nakamura. Degradation of carbon fiber-reinforced epoxy composites by ultraviolet radiation and condensation. *J Compos Mater*, 36(24):2713–21, 2002.
- DS Li, HN Li, and CP Fritzen. The connection between effective independence and modal kinetic energy methods for sensor placements. *J Sound Vibr*, 305(4):945–955, 2007.
- K Liao, CR Schultheisz, DL Hunston, and LC Brinson. Long-term durability of fiber-reinforced polymer matrix composite materials for infrastructure applications: a review. *J Adv Mater*, 30(4):3–40, 1998.
- B Lin and V Giurgiutiu. Review of the in situ fabrication methods of piezoelectric wafer active sensor for sensing and actuation applications. In M Tomizuka, editor, *Smart Struct Mater: Sensor Smart Struct Technol for Civil, Mech, and Aerosp Syst (Proc SPIE 2005)*, volume 5765, pages 1033–1044, Bellingham, WA, 2005.
- B Lin and V Giurgiutiu. Modeling and testing of PZT and PVDF piezoelectric wafer active sensors. *Smart Mater Struct*, 15(4):1085, 2006.
- YC Lin and X Chen. Investigation of moisture diffusion in epoxy system: Experiments and molecular dynamics simulations. *Chem Phys Lett*, 412:322–326, 2005.
- C Liu. *Foundations of MEMS*. Pearson international edition. Pearson Prentice Hall, 2012. ISBN 9780273752240.
- AJ Lovinger, DD Davis, RE Cais, and JM Kometani. On the Curie temperature of poly(vinylidene fluoride). *Macromolecules*, 19(5):1491–1494, 1986.
- JP Lynch and KJ Loh. Summary review of wireless sensors and sensor networks for Structural Health Monitoring. *Shock Vibr Digest*, 38(2):91–128, 2006.
- D Mascarenas, M Todd, G Park, and C Farrar. Development of an impedance-based wireless sensor node for structural health monitoring. *Smart Mater Struct*, 16(6):2137–2145, 2007.

## Bibliography

---

- Piezo Film Sensors Technical Manual*. Measurement Specialties Inc., Norristown, PA, 1999.
- M Meo and G Zumpano. On the optimal sensor placement techniques for a bridge structure. *Eng Struct*, 27(10):1488–1497, 2005.
- DC Montgomery. *Design and Analysis of Experiments*. Wiley Series in Probability and Mathematical Statistics, Wiley, NY, 7th edition, 2009.
- DE Mouzakis, H Zoga, and C Galiotis. Accelerated environmental ageing study of polyester/glass fiber reinforced composites (GFRPCs). *Compos Part B-Eng*, 39(3):467–475, 2008.
- T Nestorović and M Trajkov. Optimal actuator and sensor placement based on balanced reduced models. *Mech Syst Signal Pr*, 36(2):271–289, 2013.
- TE O'Brien, S Chooprateep, and GM Funk. Encouraging students to think critically: Regression modelling and goodness-of-fit. *J Data Sci*, 7:235–253, 2009.
- C Papadimitriou. Optimal sensor placement methodology for parametric identification of structural systems. *J Sound Vibr*, 278(4-5):923–947, 2004.
- G Park, C Farrar, F Lanza di Scalea, and S Coccia. Performance assessment and validation of piezoelectric active-sensors in Structural Health Monitoring. *Smart Mater Struct*, 15(6):1673–1683, 2006.
- B Peeters and G DeRoeck. Reference-based stochastic subspace identification for output-only modal analysis. *Mech Syst Signal Pr*, 13(6):855–878, 1999.
- B Peeters, H van der Auweraer, P Guillaume, and J Leuridan. The PolyMAX frequency-domain method: a new standard for modal parameter estimation? *Schock Vibr*, 11(3):395–409, 2004.
- A Pupurs and J Varna. Modeling mechanical fatigue of UD composite: Multiple fiber breaks and debond growth. *IOP C Ser Mater Sci Eng*, 5(1):12–17, 2009.
- C Rainieri and G Fabbrocino. Automated output-only dynamic identification of civil engineering structures. *Mech Syst Signal Pr*, 24(3):678–695, 2010.
- C Rainieri and G Fabbrocino. Performance assessment of selected OMA techniques for dynamic identification of geotechnical systems and closely spaced structural modes. *J Theor App Mech*, 49(3), 2011.
- JN Reddy. A refined non-linear theory of plates with transverse shear deformation. *Int J Solids Struct*, 20(9):881–896, 1984.
- JN Reddy. *Theory and Analysis of Elastic Plates and Shells, Second Edition*. Series in Systems and Control. Taylor & Francis, 2006.



- MH Richardson and DL Formenti. Parameter estimation from frequency response measurements using rational fraction polynomials. In *Proc 1st Int Modal Anal Conf*, volume 1, pages 167–186, Orlando, FL, USA, 1982. Proc SPIE(1982).
- M Salvia and J-C Abry. Shm using electrical resistance. *Structural Health Monitoring*, pages 379–409, 2006.
- M Sanayei and MJ Saletnik. Parameter estimation of structures from static strain measurements. I: Formulation. *J Struct Eng*, 122(5):555–562, 1996.
- KB Smith and WC Shust. Bounding natural frequencies in structures I: Gross geometry, material, and boundary conditions. In *Proc 13th Int Modal Anal Conf*. Proc SPIE(2004), 2004.
- H Sohn, CR Farrar, FM Hemez, DD Shunk, DW Stinemates, BR Nadler, and JJ Czarnecki. A Review of Structural Health Monitoring Literature: 1996-2001. Technical Report LA-13976-MS, Los Alamos National Laboratories, 2004.
- H Sol, H Hua, J DeVisscher, J Vantomme, and WP De Wilde. A mixed numerical/experimental technique for the nondestructive identification of the stiffness properties of fibre reinforced composite materials. *NDT&E Int*, 30(2):85–91, 1997.
- RW Stephens and AA Pollock. Waveforms and frequency spectra of acoustic emissions. *J Acoust Soc Am*, 50:904–910, 1971.
- SM Sze. *Semiconductor sensors*. Wiley-Interscience publication. Wiley, 1994. ISBN 9780471546092.
- L Tang, X Tao, and CI Choy. Effectiveness and optimization of fibre Bragg grating sensor as embedded strain sensor. *Smart Mater Struct*, 8:154–160, 1999.
- W Tian and J Hodgkin. Long-term aging in a commercial aerospace composite sample: Chemical and physical changes. *J Appl Polym Sci*, 115:2981–2985, 2010.
- J Tichý, J Erhart, E Kittinger, and J Přívratská. *Fundamentals of Piezoelectric Sensorics: Mechanical, Dielectric, and Thermodynamical Properties of Piezoelectric Materials*. Springer e-Books. Springer, 2010. ISBN 9783540684275.
- MT Tong, SN Singhal, CC Chamis, and PLN Murthy. Simulation of fatigue behavior of high temperature metal matrix composites. Technical Report NASA-CR-204605, NASA Glenn Research Center, 1996.
- P van Overschee and LR de Moor. *Subspace identification for linear systems: Theory, Implementation, Applications*, volume 1. Kluwer Academic Publishers, 1996.
- CMA Vasques and JD Rodrigues. Active vibration control of smart piezoelectric beams: Comparison of classical and optimal feedback control strategies. *Comput Struct*, 84(22-23):1402–1414, 2006.

## Bibliography

---

- CE Ventura and T Horyna. Structural Assessment by Modal Analysis in Western Canada. In *Proc 15th Int Modal Anal Conf*, volume 3089, Orlando, FL, USA, 1997. Proc SPIE(1997).
- Polytec GmbH Waldbronn. Polytec: Technologies, 2014.
- M Wegener, R Schwerdtner, M Schueller, and A Morschhauser. Dome-like PVDF Actuators: Preparation, Phase Transformation and Piezoelectric Properties. *MRS Proceedings*, 1190, 1 2009.
- YJ Weitsman. *Fluid Effects in Polymers and Polymeric Composites*. Springer, London, UK, 2012.
- JR White. Polymer ageing: physics, chemistry or engineering? Time to reflect. *CR Chim*, 9(11-12):1396–1408, 2006.
- K Wood, T Brown, R Rogowski, and B Jensen. Fiber optic sensors for health monitoring of morphing airframes: I. Bragg grating strain and temperature sensor. *Smart Mater Struct*, 9(2):163–169, 2000.
- K Worden and A.P Burrows. Optimal sensor placement for fault detection. *Eng Struct*, 23(8):885–901, 2001.
- K Worden, CR Farrar, G Manson, and G Park. The fundamental axioms of structural health monitoring. *Proc Royal Soc A: Math, Phys Eng Sci*, 463(2082):1639–1664, 2007.
- LY Yam, TP Leung, DB Li, and KZ Xue. Theoretical and experimental study of modal strain analysis. *J Sound Vibr*, 191(2):251–260, 1996.
- SA Zaghlool. Single-station time-domain (SSTD) vibration testing technique: theory and application. *J Sound Vibr*, 72(2):205–234, 1980.
- L Zhang and R Brincker. An Overview of Operational Modal Analysis. In R Brincker and N Møller, editors, *Proc 1st Int Oper Modal Anal Conf*, pages 179–190, Copenhagen, Denmark, April 2005. Aalborg Universitet.
- L Zhang, T Wang, and Y Tamura. A frequency-spatial domain decomposition (FSDD) method for operational modal analysis. *Mech Syst Signal Pr*, 24(5):1227–1239, 2010.

Enrique René Guzmán Solares

Born on 26/05/1986

In La Paz, Bolivia

## EDUCATION

---

- 2010-2014      **PhD in Mechanical Engineering**, at the Swiss Federal Institute of Technology (EPFL), Lausanne, Switzerland.
- 2008-2010      **Master of Sciences in Mechanical Engineering**, with a minor in Space Technologies, at the EPFL, Lausanne, Switzerland.
- 2005-2008      **Bachelor of Sciences in Mechanical Engineering**, at the EPFL, Lausanne, Switzerland.

## WORK EXPERIENCE AND INTERNSHIPS

---

- 07/2009 – 09/2009      **Dassault Aviation/EPFL – Research assistant.** Practical internship as assistant in the development of the project K1000 European Suborbital Plane. Project lead by Dassault Aviation in partnership with the Swiss Space Center and the Interdisciplinary Aerodynamics Group (IAG) at the EPFL.
- 08/2009 – 09/2009      **EPFL – Research assistant.** Practical internship in the Automated Systems Laboratory (LA). Update of a code controlling the E-puck mobile robot, used as a learning tool in several courses at the School of Engineering.
- 09/2007 – 01/2010      **EPFL – Student teaching assistant** in several courses given by the School of Engineering (STI): Remote Sensing of the Earth by Satellites, Solid mechanics, Mechanics of structures, Mathematical analysis.
- 09/2007 – 03/2008      **Swiss Space Center – Assembler intern.** Internship in mechanical assembling, in order to build a test bench for the inertia wheel system included in the Swisscube satellite.
- 07/2007 – 08/2007      **Nestlé Research Center – Manufacturing trainee.** Internship in mechanical manufacturing, including the following tasks: folding, turning, drilling, welding, etc.

## SKILLS

---

- Languages      Spanish, French (bilingual), English (C1=Full professional working proficiency), German (B1=Working proficiency), Italian (A2=Limited working proficiency).
- Computing      Design software: CATIA V5, Autodesk Inventor, Solid Works, LabView. Finite element: Abaqus, Nastran. Simulation: MATLAB/Simulink, Octave, Microsoft Excel, Maple, Mathematica. Operative Systems: Windows, Linux, MacOS. Programming languages: C, C++, Java, Python. Other: Microsoft Office.
- Engineering      Modal testing, Design of experiments, Control systems design, Piezoelectric sensors, Signal processing, Flight Mechanics, Mathematical modeling, Structural mechanics, Measurement techniques, Systems engineering.

## AWARDS

---

- 2008      Excellence scholarship, granted by the EPFL to outstanding bachelor graduates, Lausanne, Switzerland.
- 2004      Higher Education Scholarship, granted by the CUSIP, Geneva, Switzerland.
- 2003      Honorable Mention, International Physics Olympiad (IPhO), Taipei, Taiwan.
- 2002      Honorable Mention, South American Mathematics Olympiad, Fortaleza, Brazil.

## R&D PROJECTS

---

- 10/2010 – 09/2014 **Doctoral thesis - Structural mechanics and Material sciences.**  
Novel structural health monitoring (SHM) system of composite materials using an embedded transducer network, to be implemented in full-scale structures for economic and safety benefits. Project is funded by the Swiss National Science Foundation (SNF) and EPFL.  
*Achievements:*
- Doctoral thesis.
  - Main author of 7 scientific papers.
  - Supervisor for 2 master theses and 9 semester projects.
  - Lecturer for the measurement techniques course in the mechanical engineering curriculum.
- 02/2010 – 08/2010 **Master Thesis - Aerodynamics/Aerothermodynamics.** Conception of a GUI for the hypersonic flow solver Eilmer3 developed by the Centre for Hypersonics (University of Queensland, Australia). Multi-physics modelling of several atmospheres in the Solar System: Earth, Titan, Mars, etc. Atmospheric re-entry simulations of real capsules: FireII, Huygens, MER. *Achievement:* Master thesis.
- 09/2009 – 01/2010 **Space technologies minor project - Aerodynamics.** Semester project in space technologies, as a part of the K1000 project led by Dassault Aviation. Complementary analysis of lateral stability. Development of a dynamic model adapted for the approach and landing. Study about ailerons efficacy.
- 02/2009 – 06/2009 **Semester project - Modeling of an ADCS.** Semester project supervised by the Swiss Space Center at the EPFL. Software has been developed to simulate the behavior of an altitude control system, being at the same time a design tool for future missions. To be implemented in a Concurrent Design Facility (CDF).  
*Achievement:* Co-author of a scientific paper.
- 09/2008 – 01/2009 **Semester project - Correction of systematic disturbances in latent-variable calibration models.** *Achievement:* Co-author of a scientific paper.

## EXTRA-PROFESSIONAL ACTIVITIES & INTERESTS

---

- Aviation **Private Pilot License (PPL)**, issued by the Swiss Federal Office of Civil Aviation (FOCA).
- Entrepreneurship **Swiss CTI training program.**
- Sports  
Basketball: Bolivian high-school championships.  
Athletics: sprinting, Bolivian high-school games.  
Tennis: EPFL staff internal championship (runner-up).  
Running: Participation to popular Swiss long-distance running events.  
Triathlon: Participation to Swiss triathlon circuit events.  
Other: snowboard, football, rock climbing, kayak.
- Music Saxophone, guitar, tropical dances.
- Associations Member of MENSA Switzerland, Swiss Triathlon, AéroClub der Schweiz, Mars Society.
- Other interests Civil aviation, history, literature, travels.

## PUBLICATIONS

---

Bozovic G, Scaglione O, **Guzman E**, Koechli C. *SwissCube: development of an ultra-light and efficient Inertia Wheel Assembly for the attitude control of pico-satellites*. 59<sup>th</sup> International Astronautical Congress (IAC2008). Glasgow, Scotland, UK, September 29<sup>th</sup> – October 3<sup>rd</sup> 2008.

Gujral P, Amrhein M, Wise B, **Guzman E**, Chivala D, Bonvin D. *Correction of systematic disturbances in latent variable calibration models*. 11<sup>th</sup> Scandinavian Symposium on Chemometrics. Loen, Norway, June 8<sup>th</sup> – 11<sup>th</sup> 2009.

Ivanov A, Noca M, Bedmar F, Belloni F, **Guzman E**, Füglistaler A, Gallay S, Triguero A, Turriere C. *Nano and Microsatellites Modeling at the Space Center EPFL*. 4th SECESA Workshop. Lausanne, Switzerland. October 13<sup>th</sup> – 15<sup>th</sup> 2010.

**Guzman E**, Cugnoni J, Gmür T. *Accelerated isothermal and cyclic ageing of carbon fibre/epoxy composite panels with integrated PVDF sensors*. 15<sup>th</sup> International Conference on Experimental Mechanics (ICEM15). Porto, Portugal, July 22<sup>th</sup>-27<sup>th</sup> 2012.

**Guzman E**, Cugnoni J, Gmür T. *Quantification of damage due to environmental conditions on carbon fibre/epoxy composite samples*. 6<sup>th</sup> International Conference on Composite Testing and Model Identification (CompTest2013). Aalborg, Denmark, April 22<sup>th</sup>-24<sup>th</sup> 2013.

**Guzman E**, Cugnoni J, Gmür T, Bonhôte P, and Schorderet A. *Survivability of integrated PVDF film sensors to accelerated ageing conditions in aeronautical/aerospace structures*. Smart Materials and Structures 22(6):065020, May 8<sup>th</sup> 2013.

**Guzman E**, Cugnoni J, Gmür T. *Use of PVDF transducers for Operational modal analysis*. International Conference on Composites/Nano Engineering (ICCE21). Tenerife, Canary Islands, Spain, July 21<sup>th</sup>-27<sup>th</sup> 2013.

**Guzman E**, Cugnoni J, and Gmür T. *Multi-factorial models of a carbon fibre/epoxy composite subjected to accelerated environmental ageing*. Composite Structures (111):179–192, January 6<sup>th</sup> 2014.

**Guzman E**, Cugnoni J, and Gmür T. *Monitoring of composite structures using a network of integrated PVDF film transducers*. Submitted to Smart Materials and Structures, September 2014.

**Guzman E**, Cugnoni J, and Gmür T. *A new Structural Health Monitoring (SHM) system using integrated polyvinylidene difluoride (PVDF) transducer networks*. 65<sup>th</sup> International Astronautical Congress (IAC2014). Toronto, Canada, September 29<sup>th</sup> – October 3<sup>rd</sup> 2014.

---